TAL
TECH

DOCTORAL THESIS

Control Dynamics and Parameters for Low Energy Heating Applications

Tuule Mall Parts

TALLINNA TEHNIKAÜLIKOOL
TALLINN UNIVERSITY OF TECHNOLOGY
TALLINN 2023

Control Dynamics and Parameters for Low Energy Heating Applications

TUULE MALL PARTS

TALLINN UNIVERSITY OF TECHNOLOGY
School of Engineering
Department of Civil Engineering and Architecture
This dissertation was accepted for the defence of the degree 20/09/2023

Supervisor: Professor Jarek Kurnitski
School of Engineering
Tallinn University of Technology
Tallinn, Estonia

Co-supervisor: Professor Martin Thalfeldt
School of Engineering
Tallinn University of Technology
Tallinn, Estonia

Opponents: Professor Alireza Afshari
Department of the Built Environment
The Faculty of Engineering and Science
Aalborg University
Aalborg, Denmark

Professor Laurent Georges
Department of Energy and Process Engineering
Faculty of Engineering
Norwegian University of Science and Technology
Trondheim, Norway

Defence of the thesis: 03/11/2023, Tallinn

Declaration:
Hereby I declare that this doctoral thesis, my original investigation and achievement, submitted for the doctoral degree at Tallinn University of Technology has not been submitted for doctoral or equivalent academic degree.

Tuule Mall Parts

_____
signature

Juhtimise dünaamika ja parameetrid madalenergia küttesüsteemides

TUULE MALL PARTS

Contents

List of publications

This thesis has been prepared on the basis of the following publications:

I   Wolisz, H., Kull, T. M., Müller, D., and Kurnitski, J. (2020) Self-learning model predictive control for dynamic activation of structural thermal mass in residential buildings, *Energy and Buildings*. Elsevier B.V., 207, p. 109542. doi: 10.1016/j.enbuild.2019.109542

II   Kull, T. M., Thalfeldt, M., and Kurnitski, J. (2020) PI Parameter Influence on Underfloor Heating Energy Consumption and Setpoint Tracking in nZEBs, *Energies*, 13(8), p. 2068. doi: 10.3390/en13082068

III Parts, T. M., Ferrantelli, A., Naar, H., Thalfeldt, M. and Kurnitski, J. (2023) Wax actuator's empirical model development and application to underfloor heating control with varying complexity of controller modelling detail, *Journal of Building Performance Simulation*, doi: 10.1080/19401493.2023.2201818

IV   Kull, T. M., Thalfeldt, M., and Kurnitski, J. (2021) Modelling of Wax Actuators in Underfloor Heating Manifolds, in E3S Web of Conferences, pp. 1–8. doi: 10.1051/e3sconf/202124611009

V   Kull, T. M., Simson, R., and Kurnitski, J. (2018). Setback Efficiency of Limited-Power Heating Systems in Cold Climate. In: Johansson, D., Bagge, H., Wahlström, Å. (eds) *Cold Climate HVAC 2018. CCC 2018. Springer Proceedings in Energy. Springer, Cham.* https://doi.org/10.1007/978-3-030-00662-4_8

Author's contribution to the publications

The author of this thesis contributed to the papers listed above as follows:

I   The author carried out the design, programming, and simulations of the control algorithms, wrote most of the method section, and reviewed the other sections. The work carried out for this article was also included in the PhD thesis of the first author [1], who was the lead author.

II–V   The author was the lead author of these articles and carried out all the analyses, simulations, and measurements.

As the surname of the author changed from Kull to Parts in 2021, both Kull, T. M. and Parts, T. M refer to the present author.

Introduction

Greater energy efficiency and the extensive use of renewable energy sources (RES) in the production of electricity are essential to the reduction of carbon emissions due to human activity [2]. However, high fluctuations in photovoltaic (PV) and wind generated electricity pose a serious problem to the power grid [3], [4]. The current inflexibility of electricity consumption and increased RES integration in the grid make it increasingly difficult to match renewable energy supply with electricity demand and therefore avoid blackouts [5]. With the drive towards power independence, the accelerated rise in the share of wind and PV in the total energy portfolio will further heighten this challenge in the coming years [6]. The swift matching of electricity demand with renewable energy supply is necessary to ensure the stability and efficiency of the distribution network and meet European goals for the Net Zero Scenario [7].

The intermittent production of renewable electricity calls for flexibility in how energy is consumed, including in consumption by buildings [8]. In Europe, buildings account for approximately 40% of final energy consumption and 36% of greenhouse gas emissions [9]. Almost half of this energy demand is incurred from heating, which is currently not available for grid balancing, as covered by sources other than electricity. The shift towards renewable energy sources and nearly zero energy buildings (nZEBs) influences the choice of technologies used for heating and its control [10], [11]. Low energy consumption makes it possible to use low-temperature heating and high-temperature cooling systems, which have lower distribution losses and higher efficiency. In modern buildings, these systems have increasingly involved the use of heat pumps, which causes electrification of heating demand [12], [13]. High targets for emission reductions and the call for energy independence further drive the electrification of thermal demand, which would make it available to the flexibility market [13]–[15] and help balance the grid. Buildings often include active (hot water tanks) or passive thermal storage, i.e., structural thermal mass (STM), such as massive floors, used often in underfloor heating (UFH) systems. The activation of these storage systems, could potentially provide thermal demand flexibility, meaning that heating times could be shifted to some extent without compromising indoor climate comfort [16]. This flexibility could also be applied in grid flexibility services [17].

Flexibility services are divided into two main types: incentive-based and price-based [7]. When applied to the space heating demand of buildings, heating power and heating times differ from that required by typical constant room temperature control. These can be altered by temperature setpoint changes, which can either reduce or increase consumption at any given time. Reducing temperature setpoints can provide flexibility and enable energy savings simultaneously, if not compensated for at later times, to ensure a suitable indoor climate [18].

When providing flexibility or energy savings using dynamic heating control, the effects on indoor thermal comfort must be carefully considered. It is especially challenging to ensure comfort in the case of low-power and inert heating systems like UFH, even with a constant setpoint. The main reason is the lengthy time constant, which prevents a reaction to sudden changes, such as fluctuations in solar or internal heat gains. The delayed reaction causes large fluctuations in indoor temperature, as thermostats respond only after a significant deviation from the setpoint. Proportional-integral(-derivative) (PI(D)) controllers could offer more precise control, but these are time-consuming to tune manually when the delay is long.

To simultaneously enable comfort and energy flexibility and energy savings in practice with dynamic setpoints, various preventive or predictive methods, e.g., model predictive control (MPC), have been developed [8], [19]. Such control algorithms need to be carefully designed, tested, and validated for applicability [20]. During initial development and testing, building performance simulations (BPS) have proven to be a suitable tool for speeding up the testing process for different building types, climates, and usage profiles. Simulations have also made it possible to compare different algorithms under the same boundary conditions.

Simulations, however, always introduce simplifications into a system. In the case of heating system control, simplifications in BPSs occur in the building model (an ideally mixed room temperature, one floor/radiator temperature, a heat emitter with an imprecise mass), in control process components (idealized pumps and valve-actuator pairs, the absence of delays), as well as in control logic (idealized control, default PID parameters). While some details have already been thoroughly discussed in previous literature, others have not had to be considered before. It is proving increasingly important to understand processes with short time spans due to emerging incentive-based flexibility methods. For example, optimal PI(D) parameters for UFH have not yet been fully considered, and there has been little discussion of thermo-electric wax actuator modelling, its effect on energy performance yet to be demonstrated (III).

In this thesis, firstly, the potential for reducing carbon emissions from the heating systems of low energy buildings by applying different dynamic control algorithms is analyzed. When the energy source includes fluctuating renewable energy, primary energy is optimized. When the energy source is constant, final energy consumption is minimized. Secondly, as an idealized control process was initially used for the heating system performance analysis, the effect of control parameters and modelling simplifications on the results is analyzed and quantified. The analysis focuses primarily on UFH as a widely used but challenging-to-control system.

The main objectives of this thesis are the following:
- To determine the energy saving potential of the applicable dynamic control algorithms of low-temperature heat emitters by analyzing the following:
  - the primary energy minimization potential of radiator heating with an MPC, based on continuous market signal and dynamic comfort limits (I),
  - potential final energy savings applying temperature setback heating and a pre-heating control methodology in nZEBs (V);
- To estimate the effect of detailed UFH control modelling on BPS results by analyzing the following:
  - the effect of UFH PI controller parameters on energy performance and indoor air temperature of the building (II),
  - the determination of PI parameters for optimal performance of UFH (II),
  - the modelling of wax actuators for HVAC applications (III, IV),
  - the effect of wax actuator modelling on BPS results (III).

Objectives were achieved primarily through the following:
- experiments carried out in a test building to calibrate building and mass flow models and experiments under laboratory conditions to calibrate the wax actuator model,
- building and component modelling in dynamic building simulation programs,

- parameter optimization in the case of PI and wax motor parameters and scenario optimization in MPC control,
- co-simulation using several different programs for the implementation of the MPC simulation framework,
- simulations to determine the influence of modelling or control changes on BPS results.

This thesis is based on three peer-reviewed journal articles and two conference papers.

In article I, we analyzed the general potential of timing the heating of a residential building according to the variable availability of renewables for decreasing primary energy demand [1]. I developed and implemented in a co-simulation framework an easy-to-apply and adaptable model-predictive control algorithm for low temperature radiators that makes it possible increase the level of renewable energy usage and employ peak shaving through preheating (or pre-cool-down) without lowering the level of comfort.

In article II, we determined PI controller parameters for UFH in different ways. Since hydronic UFH systems (especially in low-energy buildings) have long time constants, which discourage manual tuning of PI parameters, automatic methods were tested. Energy consumption and control precision were evaluated for all parameter combinations determined. Simpler methods were compared with more elaborate solutions, and optimal parameters were identified.

In article III, we developed an empirical model for a wax actuator for UFH based on extensive laboratory measurements. The modelled wax actuator, together with other control process details, was tested in BPSs. The complexity of the control process model increased with the stepwise addition of optimal controller parameters, a signal delay, a non-linear valve curve, signal modulation, and the wax actuator. Both PI and thermostat (on/off) controllers were employed.

In paper IV, we calibrated and compared physical and characteristic models for wax actuators in a simple experiment. Wax motor parameters were thus optimized, and the precision of piston displacement and volume flow modelling were evaluated in the two models.

In paper V, we developed a variation of the pre-heating control algorithm for the temperature setback approach and analyzed the resulting final energy saving potential in offices. Using estimated time constants, a suitable heat-up time was continuously calculated during night and weekend setbacks so that a temperature approaching the comfort setpoint would coincide with the occupancy start time. UFH was compared to radiators, and both well and poorly insulated constructions, as well as light and massive ones, were analyzed.

Practical outcomes and the novelty of this thesis are as follows:
- The first time-dependent empirical **model of a thermo-electric actuator** (wax motor) in BPS was developed for HVAC applications, and its effect on BPS energy results was estimated.

- **Optimal PI parameters for UFH** were determined that allow room temperature to follow the setpoint almost ideally if continuous mass flow control is applied. This made it possible to reduce energy consumption referenced to on/off control by 9%. Parameters that perform well could be achieved using a simple calculation based on data from a test running for a weekend.
- A **dynamic primary energy factor** signal instead of a price signal was applied to optimize dynamic heating operation in a simulated residential room. An MPC algorithm was developed with the dual purpose of minimizing emissions and maintaining a comfortable indoor climate.
- The algorithm developed was an **MPC that could be easily applied and adapted**, simple enough to allow for STM activation in regular residential buildings, eliminating the necessity for complex measurements, expert knowledge of the building and its control, or expensive computations.
- As a practical consideration, it was found that business-as-usual PI control simulation did not reflect actual mass flows in the system. In most cases, when PI control was used with a wax motor, mass flows were similar to on/off mass flows, making it possible to substitute PI simulations with on/off simulations with a small deadband and shifted setpoint.

Limitations of the work include the following:
- The primary energy factor was assumed to correlate directly with CO_2 emissions, though in practice, it is often determined by politics.
- Analysis of the potential of the heating control algorithms and the influence of control modeling was limited to the room level, with little simulation and analysis conducted at the whole-building level.
- Various case studies and comfort criteria were utilized in different analyses, limiting the direct comparability of the results.
- The wax motor model was developed using an extensive set of measurements, but its influence on simulation results was only tested using constant temperature setpoints.
- The performance estimation of different control algorithms and parameters was only carried out in simulations, using calibrated models, though.

Notations

Abbreviations

aFRR	Automatic Frequency Restoration Reserve
BPS	Building performance simulation
CO_2	Carbon dioxide
CP	Control parameters
D	Delay
FAT	Full activation time
FCR	Frequency Containment Reserve
FE(D)	Final energy (demand)
FFR	Fast Frequency Reserve
HR	Heat recovery
HVAC	Heating, ventilation, and air-conditioning
LS	Load shifting
MAE	Mean absolute error
MC	Modulation control
mFRR	Manual frequency restoration reserve
MPC	Model predictive control
nZEB	Nearly zero energy building
on/off	Thermostat control(ler) with binary (on or off) output
PCM	Phase change material
PE(D)	Primary energy (demand)
PEF	Primary energy factor
PI(D)	Proportional-integral(-derivative) control(ler)
PV	Photo-voltaic (solar panels)
PWM	Pulse width modulation
(V)RES	(Variable) Renewable energy sources
STM	Structural thermal mass
TABS	Thermally activated building systems
UFH	(Hydronic) underfloor heating
VC	Valve curve
WM	Wax motor

Symbols

a, b	calculated parameters
C	heat capacity
Cp	specific heat capacity
D	damping
d	displacement
E	error
g	full transmittance of solar radiation
H	heat loss coefficient
h	full hours
I	solar irradiation
K	proportional gain

k, c	estimated parameters
K_p	process gain
L	time delay (melting heat in physical WM model)
M	mass
N	number of something
n50	air change rate at a pressure difference of 50 Pascals
occ	thermal zone's occupancy
PEF	primary energy factor
Q	energy consumption
q50	air leakage of a building envelope at a pressure difference of 50 Pascals
R	thermal resistance
s	second-order transfer function from the heating signal
T	temperature
t	time
TC	temperature change speed
ti	integration time
tt	tracking time
u	control signal
U	thermal transmittance or input voltage
$\dot{V}$	volumetric flow
VI	violation index
w	angular frequency
X	exogenous variable vector
Δ	difference
τ or tau	time constant
Φ	heating power

Subscripts

auth	authority-corrected
bp	breaking point
D	delay
DAT	full deactivation time
Db	deadband
dead / d	dead
exceed	over the limit
fall / f	fall
FAT	full activation time
flu	liquid state
h	heating
H0	initial value of enthalpy
hold / h	hold
i / y	cycle counter / general index
in	indoor
melt	melting process
min	minimum
n	night
o	operative

oh	overheating
out	outdoor
out_lim	outside of limits
rise / r	rise
set	setpoint
sol / solid	solid state
sup	supply
uc	undercooling
w	wax motor
wnd	weekend

1 Background

1.1 Low energy heating applications

This thesis focuses on low energy heating applications in buildings and mostly excludes high power and high temperature energy wasting systems. Heating constitutes a large share of total building energy consumption [13]. To reduce energy consumption of buildings, the European directive on the energy performance of buildings states that all new buildings must be nZEBs [21]. This would reduce total heating consumption for new buildings, but the share would still be significant in most parts of Europe, due to cold or moderate climates.

Heating demand can be met by a variety of sources, but low carbon emissions can be ensured with the use of solar thermal, biofuel boilers, efficient district heating (DH), and heat pumps, assuming a high share of renewables in the power mix. As the efficiency of heat pumps and district heating production is higher when system water temperatures are low [22], [23], their use also assumes the use of lower temperatures in room heat emitters, and this favors the use of large surface heat emitters such as UFH and large radiators. The trend towards the use of low-temperature heat emitters is also appearing on the building side, as less heat is needed in nZEBs. People often choose UFH because it reduces thermal asymmetry and there are no visible devices.

While systems in nZEBs that use a heat pump or low-temperature DH and UFH or radiators require flow temperatures from ca 30–50 °C on the secondary side, when a traditional DH or boiler system is used, the primary side temperature is from 70–90 °C, and the secondary circuit temperature is from 40–70 °C. In the case of boiler systems, buffer tanks are usually added to stabilize the system's operation and temperature. In the case of heat pumps, tanks are used for the same purpose, though the temperature fluctuations are smaller. In the case of inverter heat pumps, the tanks are often unnecessary if the volume of the heating system is sufficiently large, as the inverter can vary the power and not overheat the water. Using the tank increases investment costs, requires additional mechanical room space, and reduces efficiency due to additional heat loss.

A typical low temperature heating system schematic is shown in Figure 1. The heat production can be provided by (inverter) heat pump, (low temperature) district heating, or, if needed, by higher temperature source and mixing the lower temperature for input. The system is assumed not to have a buffer storage tank. The parts modelled in the scope of this thesis (heat emitters, thermostats, manifold valves, and actuators) are enclosed in the red box. In the context of this thesis, the room and heat emitter and the flows in the circuit are modelled, but the interaction between different circuits and the heat source were not included.
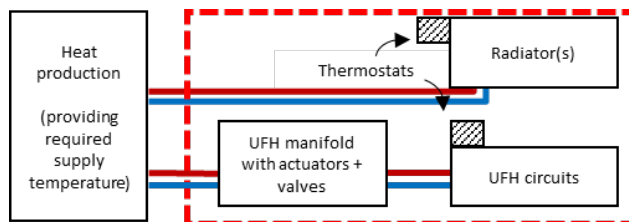

Figure 1. Low energy heating applications. The scope of the model is enclosed in the red box.

1.2 Intermittent heating control

Heat output of the hydronic systems can be influenced by supply temperature, and by the mass flow. The supply water temperature is classically adjusted to match the outdoor temperature (heating curve) to ensure that there is more heating capacity available at lower outdoor temperatures and less at higher ones with the same mass flow. The supply temperature is maintained by the heat source or by mixing higher and lower temperature water.

The mass flow is controlled using a valve for each circuit or radiator, and a manual or electric actuator opening and closing each valve. In both UFH and radiator solutions, the actuator has evolved from one with a fixed valve position, to one with room-based manual on/off or continuous control, and finally, to one with automatic feedback control using a local sensor or room controller. In the latter case, the emitters can be controlled using a set temperature value (setpoint). The setpoint can be user-defined or have a range within which a user can modify it. Newer thermostatic valve heads employ microcontrollers to gather data, learn, and use predictive control (described in section 1.4).

Energy consumption depends on external boundary conditions and internal gains, as well as on the selected room temperature (see section 1.3 for typical temperatures). Accordingly, the method of periodically decreasing the temperatures of heating systems in buildings, often called intermittent heating or the setback approach, is a widely used method for saving energy both historically and up to the present day. The temperature reduction can be applied to either the heating curve or the room temperature setpoint. Temperatures would be reduced when rooms are vacant, or the occupants are sleeping. An example usage profile for offices is shown in Figure 2A.

The optimization of intermittent heating is not a new topic [24]. In several studies, an energy saving potential of up to 20% has been demonstrated [25]–[27]. In single cases, observed reductions have been much higher or much lower, e.g., up to 70% [28] or ca 4% [29]. The main factors determining the savings potential are the thermal time constant for the building (which depends on the thermal mass of the construction, energy efficiency, and the power of the heat emitter), the outdoor temperature, the setback time, etc. In the studies mentioned, the buildings investigated were mostly moderately insulated. The effect of energy-efficiency on room temperatures during intermittent heating is shown in Figure 2B. Intermittent heating is not considered a feasible solution for massive and low energy buildings [24],[30], while a lower thermal time constant enables larger savings with intermittent heating [27].
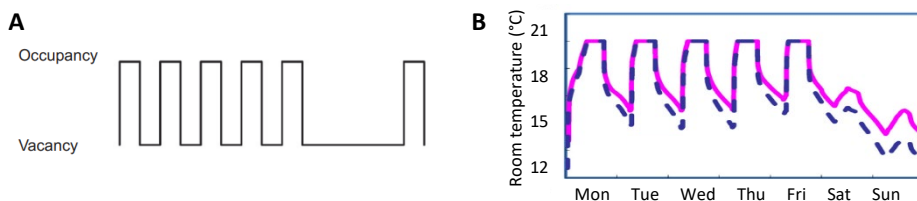

Figure 2. A: A typical intermittent occupancy/heating profile [31]; B: Typical temperature profiles for two buildings with such control; purple represents the energy-efficient building and blue, a typical building (adapted from [27]).

The use of setback control requires higher power than constant operation to ensure quick heat-up [32]. As a consequence, the dimensioning of these systems is standardized with additional power (over-dimensioning). While in the case of systems such as gas or pellet boilers, more power does not mean a significant increase in investment cost, the price of a heat pump increases significantly with an increase in power. A typical cost-reduction for modern low energy buildings is thus achieved using low peak-power heating systems. This results in systems with no extra power available for heat-up. The setback algorithms must, therefore, be able to consider both the available and required power of the heating system to perform effectively.

1.3 Thermal comfort at dynamic control

Varying the room temperature setpoint can influence the thermal comfort of the occupants. In most cases, rooms are not in constant use, and when they are not occupied, temperatures do not need to fall within the usual comfort limits. During the hours they are occupied, however, thermal comfort must be ensured. Typical usage profiles are defined by ISO 18523-2:2018 [33], and comfort limits are defined by ISO standard 16798-1 [34] according to clothing level and activity. Standard values are often defined by building class as an aid to designers. The limits, however, can vary if the activity of room occupants changes.

The indoor climate class can be estimated according to the limits defined by ISO 16798-1 and slack hours defined by ISO 16798-2 [35]. These standards allow a range of 20 to 23 °C during the heating period for a residential room with indoor climate class II (which buildings are usually designed for), where the activity level is 1.2 and the clothing level, 1. Temperatures must stay within these limits, exceeding these for up to 3% of the period of occupation during the heating period or 20% of the week (see Figure 3 for an explanation). It is assumed that the occupants will increase the temperature if it remains below this limit for a longer time. When different control algorithms are compared for energy consumption, the ensured thermal comfort should be similar. This means that the setpoint should be shifted to ensure the same climate class is achieved or that temperature control must be sufficiently precise.
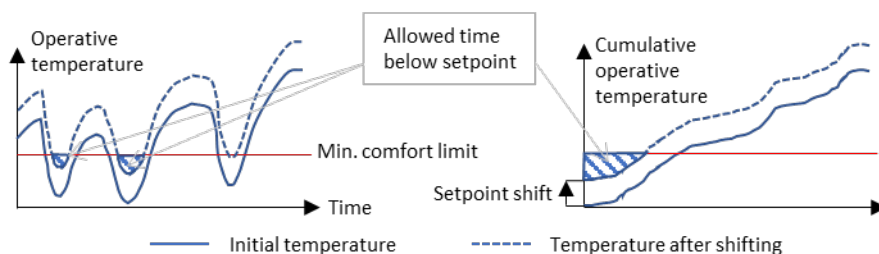
Figure 3. Allowed deviation of the room operative temperature and the required shift in temperature setpoint (adapted from [36], [37]).

1.4 Predictive control

To guarantee thermal comfort for occupants while minimizing the energy demands of dynamic heating operations, it inevitably becomes necessary to predict temperature response [1]. In buildings with simple setback control mechanisms based on pre-defined temperature setpoint schedules, there is a risk of discomfort when people arrive if the

temperature has not yet achieved its set value. On the other hand, energy is wasted if the temperature is reached too soon.

A typical solution to this problem is to predict the heat-up time. The heat-up time can be manually scheduled by the building manager or occupant as experience dictates, but this does not allow for dynamic adjustments in response to ambient temperature fluctuations and internal gains. In calculations of automatic heat-up time, the building is often simplified as a single time constant model. The time constant for the cool-down process is usually estimated, being considered dependent only on the building structure, as in ISO 52016-1:2016 (previously ISO 13790) [38]. Based on this estimated time constant and the estimated heating power, the heat-up time can be calculated.

In recent years, most intermittent heating control systems for low energy buildings include advanced control methods to ensure an acceptable level of thermal comfort and simultaneous energy savings [39]. There are several methods available to estimate the heat-up time for both single and multi-zone cases [27], [40], [41]. For at least a decade, smart thermostats for radiators have included programmable setpoints and have had the ability to learn the heat-up time. To pre-program the setpoints, the behavior of the tenants must, however, be regular and known beforehand. This mostly applies to office buildings but not to residential buildings or public buildings, such as shopping centers, concert halls, etc. In the case of residential buildings, a method by Ayr et al. locates the tenants using their smartphones and switches off the heating when the distance from home is large [42]. When the tenants approach the building, the heating is turned on again. The savings achieved using the setback approach depend heavily on the behavior patterns of tenants [43].

There are also more advanced systems that predict room temperature using different dynamic constraints, making it possible to optimize control actions. Model predictive control (MPC) solutions, for example, take comfort limits as constraints and optimize control actions using a simplified model. Different objectives can be selected, while the goal is often to achieve optimal energy consumption. The results measured are used to improve control. The general operation of MPC is shown in Figure 4. MPC control has been widely analyzed as method of building control [39]. MPCs applied to space heating, using constraints that ensure thermal comfort, have been analyzed previously in several different configurations [44]. The influence of different parameters, such as occupancy data [31], [45], and the steps necessary to implement MPC in practice have also been analyzed [46]. Still, a high level of complexity, low adaptability, and high cost are factors which keep MPCs from being more widely implemented.
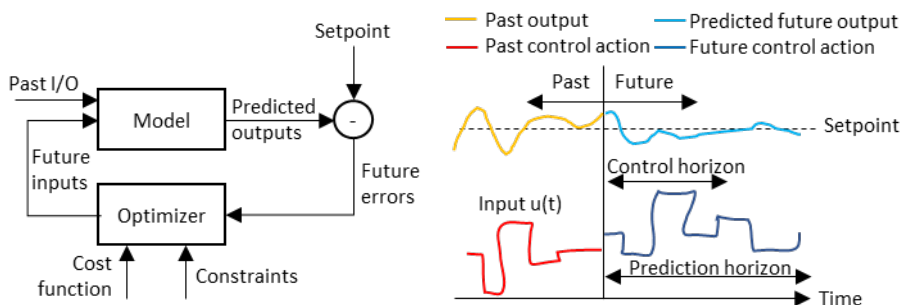

Figure 4. General concept of MPC: process flow chart [47] and timeline (adapted from [48]).

1.5 Grid-driven heating control

Not only does dynamic heating save energy, it can also be used to help balance the grid. As the share of renewable energy in the power mix is ca 28% globally and is predicted to be ca 38% by 2027 [6], the demand for energy storage [49] and demand-flexibility is expected to increase in the near future. As the building sector consumes 30% of global electrical energy [50] and thermal energy in addition to it, buildings should be considered a potential source of flexibility.

There are different ways to influence the consumption side of the grid balance [7]. Demand side management (DSM) is an established strategy for controlling energy demand, focusing on the overall energy usage of consumers and their consumption behavior over time [51]. DSM, which originated during a time when maintaining constant power from inflexible nuclear or lignite plants was paramount, has led to the practice of load shifting (LS), which includes such DSM techniques as peak clipping or valley filling. Given the fluctuating and sometimes negative electricity prices on markets like the European Energy Exchange, the DSM potential for large industrial consumers has been extensively studied [52], [53].

DSM activities are less common in a residential context, primarily involving static, daily repeating time-of-use pricing schemes to encourage nighttime consumption [54]. Residential electricity use is typically analyzed for LS involving the shifting of clothes washing times, etc. Analyses usually focus on the shifting of routine electricity use or investigate electrical HVAC consumption. The use of heat pumps for the electrification of heating can, however, combine space heating with thermal storage management (STM) as a grid balancer [16], [55].

Space heating accounts for about 20% of the EU's final energy demand [9]. Dynamically controlling residential heating systems could, therefore, offer some flexibility potential for stabilizing the grid [56]–[59]. Some heat pumps (HPs) are even now capable of operating on the basis of external signals and shutting off during peak consumption times, and there are now initial solutions for synchronizing heat pump operation with local PV generation.

The grid operator has essentially two ways to influence energy consumption: using the price of energy (see section 1.5.2) or offering special incentives to participate in grid balancing (see section 1.5.3). Their application to the thermal demand of buildings would require the dynamic control of systems that receive signals from the grid, and it would be dependent on the building's ability to shift the thermal load (section 1.5.1).

1.5.1 Potential for shifting thermal demand

Thermal demand in residential buildings is typically rigid, closely linked to interior temperatures and therefore to the thermal comfort of occupants. To harness the potential flexibility of these buildings, thermal storage is needed. This could involve the use of technical storage systems such as hot water tanks [59], [60] or the inherent structural thermal mass (STM) of the buildings themselves [61]–[63]. In the case of technical storage systems, dedicated equipment must be acquired and housed within the building. In contrast, STM is already present in the buildings and involves no additional acquisition costs or space for implementation [64]. The cost of the necessary control equipment and electronic thermostats is also significantly lower than that of hot water storage tanks or other thermal storage systems [57], [64].

Generally, the STM of a building is the total heat capacity of its construction materials. However, the thermal storage capacity of STM only becomes apparent and usable when

temperature variations within a building allow its activation, meaning the charging and discharging of a portion of that mass. This implies the need for variable setpoints or minimum and maximum limits, rather than constant room setpoints. The process of storing energy in the STM and load shifting due to temperature changes is shown in Figure 5.

Historically, thermal mass activation research had focused on commercial cooling needs, as these demanded a significant amount of electricity during peak load times in the traditional power generation system with, for example, thermally activated building systems (TABS) [65]–[68]. Heating activation was seldom discussed, as it was fueled using non-time-dependent fossil fuels [69], [70]. STM activation for electricity flexibility is now increasingly being discussed [16], [55], [63], [71]–[73]. In many studies, additional STM is provided by incorporating phase change materials (PCM) in the building construction [74].

Previous studies found that poorly insulated buildings can shift more energy but over brief periods, whereas buildings with better insulation can shift less energy but over extended periods [61], [63], [75], [76]. Further, it was shown that buildings with inadequate insulation experience greater heat losses due to STM activation. In contrast, extremely well-insulated buildings risk compromising comfort levels if STM activations are not correctly timed or if internal and solar loads are not accurately forecasted [61], [63], [77].
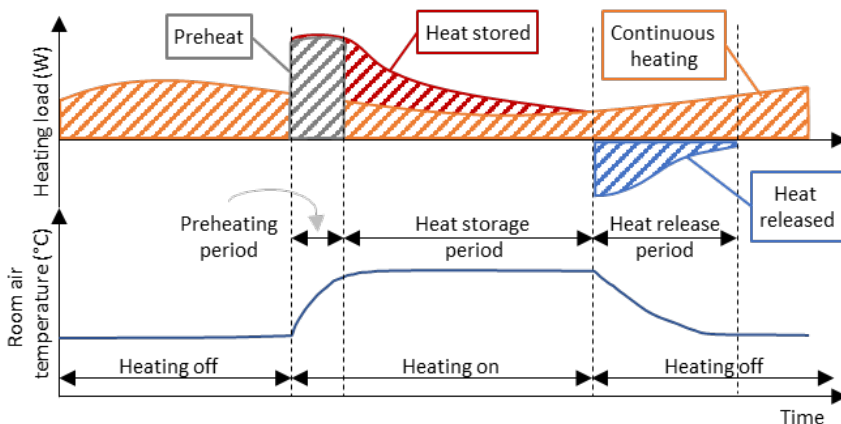

Figure 5. Energy storage and release in a building structure with constant setpoint heating alongside dynamic indoor temperatures during a heating action (adapted from [78]).

1.5.2 Price-based control

To validate the feasibility of thermal mass activation in residential buildings, suitable control algorithms need to be designed. These algorithms should facilitate STM activation in response to signals from the grid while maintaining constant thermal comfort for occupants.

Typically, the control signal is the price of electricity. Consumers can adjust their usage based on this signal to pay less for energy. In case the common two-tariff rate is applied, heating would start during the night, resulting in a control approach like the setback method. Predictive control would need to consider the day-ahead electricity spot prices. Some heat pumps already optimize their behavior on the basis of price, and more

advanced methods for heat pumps have been developed [79]. Certain control methods also ensure flexibility by exploiting a storage tank or building's STM [74].

Some studies argue that price-based MPC is not the best way to drive flexibility as it limits negative flexibility [80]. Instead, they propose a more flexible approach based more indirectly on price. Moreover, to reduce carbon emissions from the local or central grid, an ecological control signal might be preferred over an economic one. An ecological signal such as the primary energy factor could more accurately reflect the level of emissions [81].

Very few studies integrate residential building simulations with MPC and optimization strategies that control STM activations to maximize comfort and LS potential [16], [62], [82]. The LS potential of STM under model-based control is found to be lower than that of rule-based control. This is partly due to the fact that MPC minimizes comfort violations at the expense of a slightly reduced LS potential. The utility functions needed to optimize a given system's operation usually show that STM activations are only profitable for limited periods, thus also restricting LS activities.

1.5.3 Participation in frequency restoration reserve

The incentive-based approach is employed to help maintain a constant power frequency of 50 Hz across the grid throughout the day. The balance between production and demand is projected and adjusted to determine the day-ahead price. Power grids rich in renewable energy, however, often encounter sudden and unexpected intra-day production changes that can destabilize the system. Imbalances can also occur during regular operation, as a result, for example, of errors in the prediction of demand. Various frequency restoration reserves have, therefore, been established to balance these fluctuations either automatically or manually (see Table 1 for an overview of the Finnish system).

Table 1. Reserve marketplaces in Finland (adapted from [83]*)*

Abbreviation	FFR	FCR-D	FCR-N	aFRR	mFRR
Name	Fast Frequency Reserve	Frequency Containment Reserve for Disturbances	Frequency Containment Reserve for Normal Operation	Automatic Frequency Restoration Reserve	Manual Frequency Restoration Reserve
Activated	In large freq. deviations	In large freq. deviations	Used all the time	Used during certain hours	Activated if necessary
Activation speed	In 1 second	In seconds	In 3 minutes	In 5 minutes	In 15 minutes

In the Nordic countries, the reserves employed for standard operation are the Fast Frequency Reserve (FFR) and the Frequency Containment Reserve (FCR). There is also FCR for large disturbances. These reserves include production, consumption, and storage that can be automatically leveraged in seconds or within three minutes [83]. During certain hours, the automatic Frequency Restoration Reserve (aFRR), which has an activation time of 5 minutes in the Nordic countries, can also be used. The balancing market in the Baltic region is still in the development phase, so balancing services employing FFR, FCR, and aFRR have not yet been fully developed [84].

If necessary, the manual Frequency Restoration Reserve (mFRR) can also be activated. These tertiary control reserves, provided by the Transmission System Operator in most countries, are called on to help correct prolonged deviations that cannot be addressed using other upstream balancing services (FCR and aFRR) alone [85]. The mFRR is the

slowest among these products and the only one currently available in the Baltic region. In the Baltic countries, the maximum full activation time (FAT) of mFRR is 12.5 minutes [86], while in the Nordic countries, it is 15 minutes. Depending on the region, the FAT for mFRR can be even shorter (e.g., 5 minutes according to [87]). The minimum duration for which the reserve can be activated ranges from 15 minutes to 1 hour.

mFRR reserves mostly consist of safety production sources, storage options, or large consumers such as factory lines. Generally, only large consumers (representing at least 1 MW [85]) can participate in the mFRR. Aggregators (Balancing Service Providers) can, however, combine several smaller consumers (e.g., private heat pumps) into one switchable unit and therefore enable participation for everyone [88]. These units are called virtual power plants. Changing the demand of smaller consumers can be quicker and more cost-efficient than switching production or storage sources on and off. The aggregators transfer the signal to virtual power plant partners and override the default control approach. In the case of heat pumps, frequency needs be set manually [89]. The Transmission System Operator can require both upregulation of consumption to participate in the downward mFRR reserve as well as downregulation of consumption to participate in the upward mFRR reserve. In the Estonian market, the potential for both mFRR downward and upward reserves has been shown to be insufficient to balance the grid inside the country [84].

Downregulation of demand is often more difficult than upregulation for many private users. This is an opportunity for STM activation in massive and energy-efficient buildings, giving them an advantage on the market. LS and participation in mFRR downward reserve inevitably increases a building's electric energy consumption assuming that thermal discomfort is not increased. The impact of each LS action on electricity costs should be assessed for effective participation in the mFRR. It should also be ensured that modelled up- and down-regulation capacity is actually available to react to grid signals. A complete understanding of the performance of each component of the heating system on a 15-minute timescale and performance of STM activation is, therefore, needed when developing the control principles of a heating system for profitable and effective participation in the mFRR.

1.6 Modelling of control processes

Analysis of building energy performance is most often carried out using white-box simulation models. To use these models for the testing of electricity balancing control algorithms in buildings, heat emitter control modelling must be reviewed. In typical BPSs used to determine annual energy demand, heat emitters are not always separately modelled but incorporated as ideal systems with ideal control that generate exactly the heat needed to achieve the desired temperature in a room. Depending on the goal of the simulation, heat emitter models could be included, and the heating plant is sometimes modelled in detail.

When modelled, the UFH is often simplified in BPS programs, reduced to a floor layer with a different temperature, either with a specific thickness or virtually dimensionless. The layer temperature develops from the heat transfer between the piping and the layer material and is calculated according to logarithmic temperature differences. The return temperature is calculated using the room heat balance and mass flow. Floor surface temperature is estimated using the logarithmic temperature difference.

If modelled in detail, the mass flow is estimated using the design temperature drop and feedback control according to the default PID controller or thermostat. Both the

estimated room temperature fluctuations and mass flows depend, therefore, on controller parameters. Valve effects are usually omitted from UFH modelling (a linear valve curve is assumed). As most short delays in the system (valve opening delay, actuator delay, temperature sensor delay, signal transmitting delay, calculation time) are omitted, their effect is aggregated with the effect of controller parameters.

In most UFH simulations, it is not necessary to include short time delays, as the time constants for the fluid and construction mass are orders of magnitude higher. The time constant for the room temperature measurement can be as low as 2 minutes [90]. A delay of 3–5 min (the heat-up time) for the actuator-valve mechanism is normally assumed when it is being energized [91], [92]. Even together, these values are too low to have a significant effect on the annual energy consumption of a building, especially if tenants adjust the setpoint when the delay results in temperature fluctuations. Nevertheless, these short delays may prove significant, for example, in simulations aimed at testing control algorithms for rapid processes, such as reactions to grid signals from frequency markets.

Many existing studies on heating system performance and control have taken simplified approaches to the modelling of control processes, and the impact of these simplifications has not been well-documented. This thesis has thus placed a significant focus on the detailed modelling of heating system control to quantify the full effect of PI parameters (section 1.6.1) and wax motors (section 1.6.2) on UFH control.

1.6.1 PI and its tuning methods

PID is well-known as one of the best and simplest feedback controllers for any process. While PID can take different forms, the derivative part is usually dropped for buildings, and PI controllers are used instead [93]. This is because the D part is more useful for very fast processes where changes are in seconds. Even in the case of fast building processes, such as ventilation airflow control, controller producers exclude the D part from default PID parameters. Here we use the classical form (not the parallel form) of the PI controller:

$$u(t) = K \left(E + \frac{1}{ti} \int E dt \right) \tag{1}$$

where u is the (dimensionless) control signal and E is the difference between the setpoint and measured air temperature in °C and acts as the feedback to the control. K is the proportional gain, and ti is the integration time. In the case of parallel gains, the integral part's parameter integral gain Ki would be expressed as $Ki=K/ti$. The discretization of the PI(D) controller can also vary depending on the software. In IDA ICE simulation software [94], which was primarily used in this work, the implementation for each timestep is shown in Figure 6, where *hilimit* and *lolimit* are the limits for the PI output signal (0 and 1).

The PI parameters K and ti can be manually or automatically estimated (tuned), or parameters pre-set by the controller or software producer can be used. If improper PI parameters are chosen, the whole system can become unstable. Designers and researchers, therefore, often turn to optimal or predictive solutions [95]. But advanced solutions are not easy to implement, and the need for robust and reliable solutions with minimal human interaction is evident [93], [96]. Therefore, sensitivity and performance of control algorithms should be tested in very detailed realistic simulation environments [97].

```
CONTINUOUS_MODEL PIContr        E := IF Mode < 0.5 THEN
                                     (SetPoint - conv_unit*Measure)
ABSTRACT    "PI-controller.        ELSE
                                     (conv_unit*Measure - SetPoint)
Made by:    Jari Hyttinen         END_IF ;

                                EFilt := TimeConstBDF1 (tau, E, EA_S);

                                OutSignalTemp := k * (EFilt + Integ) ;

                                Integ' = EFilt/ti + (OutSignal - OutSignalTemp)/tt ;

                                OutSignal = IF OutSignalTemp > hilimit THEN
                                               hilimit
                                            ELSE_IF OutSignalTemp < lolimit THEN
                                               lolimit
                                            ELSE
                                               OutSignalTemp
                                            END_IF ;
```

Figure 6. PI controller implementation in IDA ICE software. The parameter tt is the tracking time and has a value of 30s by default. The conv_unit variable is for unit conversion if needed, and TimeConstBDF1 is for filtering. For the default tau = 0, there is no filtering, and Efilt = E.

Many simplified methods have been developed for tuning PI parameters. Approaches often rely on the first order model with time delay, where the temperature response of an input step change is given as follows:

$$T(t) = K_p \left(1 - e^{-\frac{t-L}{\tau}}\right) + T(0)e^{-\frac{t-L}{\tau}} \tag{2}$$

where $T(t)$ is room air temperature in °C at time t seconds after the step, $T(0)$ is the initial temperature before the step, K_p is the process gain (dimensionless), τ is the time constant in seconds, and L is the time delay, also in seconds. Though the underlying assumption of PI control is that the system performs linearly, it is also often applied in the case of non-linear systems. For systems performing differently at various boundary conditions (such as heating systems in different seasons), it means that the same control parameters should not be used year-round [93].

The auto-tuning of PID controllers for heating, cooling, and ventilation plants was first described several decades ago [98]–[100] and has become a current topic of interest [101]. If there is enough computational power, artificial neural network models should be capable of tuning PI parameters [102]. Self-learning PI controllers are already commonly available for radiators in new buildings. As radiators are also installed in public and commercial buildings, there is a lot of interest in and financial incentive for the development of better-performing solutions for these environments.

For hydronic UFH, only simple thermostats with a deadband of at least +/- 0.5 K are typically used even in modern buildings. When UFH is used with a thermostat, the air temperature can, however, fluctuate significantly, and occupants will raise the setpoint to avoid lower levels and meet their comfort limits. This leads to higher energy consumption. Control of UFH as a slow system with a high thermal mass is an issue of debate, and good solutions have not yet been found. Some manufacturers offer sophisticated self-learning controls, while on/off control is likely the most common implementation in practice. In some studies, self-regulating properties (no-control) have shown a level of performance similar to that of more sophisticated control solutions [103]. The high time constant for UFH is even increased by the low supply temperature from heat pumps made possible by small losses in well-insulated nZEBs with heat recovery ventilation. The high time constant means that setting PI parameters manually by trial and error, common practice for PI tuning, will take a significant amount

of time. For self-tuning controllers, simple tests are needed, but these can also prove time-consuming.

For grid-driven dynamic heating applications in low-energy buildings, a small range of temperatures can be utilized. Random fluctuations must be avoided to enable meaningful shifts. A constant (e.g., minimum) temperature level must, therefore, be held as precisely as possible. When parameters are optimized, PI control for UFH control provides a greater energy savings than standard on/off control [36], [104]. Optimal parameter values are, however, not usually revealed in the scientific literature. There is a lack of published data on PI parameter values for UFH, with some exceptions [36], [105], and the effect of different parameters values for UFH has not yet been analyzed. In the case of radiators, however, the effect of PI parameters has been studied, as there is a lot of potential for energy savings due to often untuned heating circuits [106]. Tuning radiator PI parameters using machine learning has shown a 32% reduction in heating energy consumption compared with Ziegler-Nichols tuning [107]. The current situation shows that while PID and on/off control waste energy, more advanced solutions on the market often do not ensure comfort [108]. With quality tuning, PI could both reduce energy waste and ensure comfort. Parameter optimization for UFH has been carried out extensively in simulations [36], but it is not yet known whether it is possible to obtain optimal parameters with shorter tests.

1.6.2 Wax actuator and its modelling

When dynamic heating control driven by power-grid incentives is applied, the timescale needed for UFH control decreases significantly. The start-up time for a heat pump system can generate a bottleneck that can critically impact the local system response to the grid. Even if the heat pump can be activated as quickly as required for mFRR, a heat sink is needed to keep the small amount of water in the heat pump's closed circuit from overheating. This would lead to a halt in electricity consumption and a failure to fulfill the promised bid to mFRR. In the case of inverter-based heat pump systems, large storage tanks are not typically installed, and the building structures must be used as a heat sink. This requires opened valves in the hydronic heating system, e.g., a UFH manifold.

The UFH system and its control includes several components, some of which have already been shown in Figure 1. The manifold system is shown in Figure 7 and includes valves on both the supply and the return side. Supply side valves are for initial manual balancing (e.g., with rotameters), while return side valves are often continuously electrically controlled on the basis of data received from room thermostats. In simulations, these components are often simplified as a linearly controlled volume flow with the input being calculated using the room temperature and setpoint conditions via the chosen controller (e.g., PI or on/off). In an actual system, however, the controller output would be modified in several ways before the volume flow is determined. First, there would be at least a minute delay before a change in room temperature affected the control signal. Second, volume flow does not change linearly with valve piston movement or control signal. Finally, before the heating signal is converted to water flow, an additional delay might be induced by return-side actuators. This process is shown later in Table 10.

The actuators in UFH manifolds are thermoelectric actuators that work with wax, which reacts relatively slowly. Signal delay and unsuitable control parameters can prolong the opening time even further.
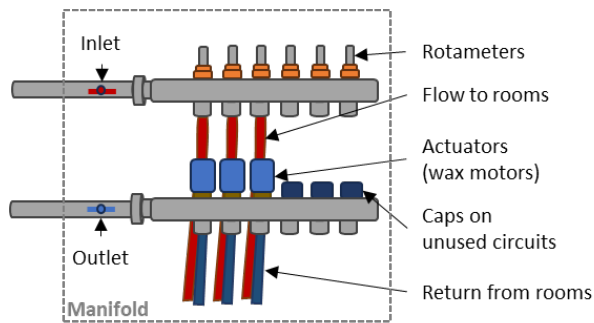
Figure 7. Components of a UFH manifold (adapted from [109]*,* [110]*).*

In the closed valve position, the system's water volume is very small and temperature limits in the heat pump circuit may be reached too quickly when the heat pump is started at full power. The slow movement of the actuator's piston with a slow opening of the valves would then hinder the aggregator's delivery of the load expected by the grid.

Thermoelectric wax actuators are electrically controlled and use paraffin wax as phase change material (PCM) for volume change [111], [112]. These actuators are known by other names as well, such as wax motors (used in this work, abbreviated as WM), wax pellet actuators, thermo-electric actuators, and thermal actuators [113]–[116]. Cross-sections of wax actuators on manifold valves in the open and closed positions are shown in Figure 8. The wax is solid at room temperature and liquid at higher temperatures. It is heated by a positive temperature coefficient (PTC) heater. In the absence of an electric heating signal, the actuator-valve system is normally closed. When voltage is applied, the wax starts melting and expanding, setting the valve's piston in motion. This process is shown in Figure 9. With the assistance of a spring, piston movement (displacement) reduces the actuator's inner height, thus opening the valve. The hysteresis of up and down movements is generated by the temperature difference between stop and start positions, due to the thermal inertia of the wax and friction of internal parts, which include a spring [117]. Such a method of valve control has been used in UFH for quite some time, as the actuators are silent and durable [118]. Slower reactions also preclude the water hammer that is associated with motorized valves. Wax actuators are also used in fan coil units in cooling systems and in pressure-independent control valves in heating systems. Radiator thermostats include similar motors, but these are often based on the expansion of a liquid or gas instead of the phase change of wax.

Some wax actuators use continuous control with voltage between 0 and 10 V. Others use discrete control with a binary heating input, i.e., no voltage for no heating and 230 V or 24 V for heating. Continuous 0–10 V wax actuators still use 24 V to power the PTC heater. Thus, if a controller with continuous output, such as a PI controller, is used to control a UFH wax actuator, the continuous signal must be modulated into a binary signal for the PTC heater. 0–10 V actuators can, theoretically, stay partially open. Partial opening control is, however, simpler for valves that have a logarithmic valve characteristic curve, i.e., a logarithmic volume flow dependency on the valve opening. In UFH manifolds, quick-opening valves are employed instead. These exhibit most of the change in volume flow when the valve is only slightly open. A partial flow would only be realized within a very small range of the extent to which the valve is open. These valves thus perform close to on/off with either actuator type, whether using continuous or discrete control. As a consequence, simpler 24-V on/off-motors are often used, as is the case in this work [117].
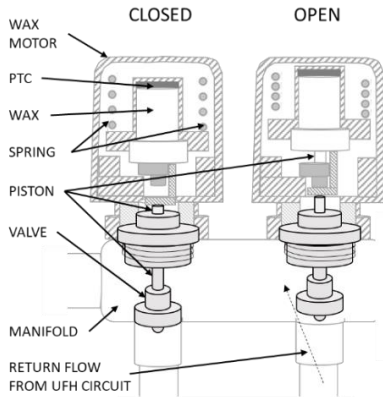
Figure 8. Valve opening with wax actuator warming visualized as part of a manifold (adapted from [119]).
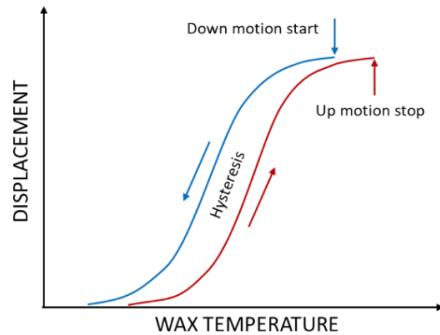
Figure 9. Theoretical piston movement (displacement) according to wax temperature (adapted from [117]).

The only available wax actuator model (described in section 2.3.2.2.4) is based on physical principles modelling the piston displacement according to ideal phase change process as shown in Figure 10. The upper graph displays the ideal wax temperature changing process presented on a time scale that is dependent on the binary heating signal. This omits the hysteresis in temperature shown in Figure 9. The lower graph in Figure 10 shows the resulting piston displacement. The linearized simplification is designed according to the ideal wax temperatures but if omitting the step of modelling the temperature, it can also include the hysteresis. In the context of this thesis, this simple linearized model is referred to as the characteristic model [92] and the different time periods shown in Figure 10 are referred to as characteristic times and defined as follows:

- Dead time (t_{dead}): solid wax heating up to the melting temperature with no volume change
- Rise time (t_{rise}): phase change of the wax from solid to liquid with expansion
- Hold time (t_{hold}): liquid wax cooling down to the melting temperature with no volume change
- Fall time (t_{fall}): phase change of the wax from liquid to solid and compression

Based on these, additional times for analysis could be calculated as well:
- Full activation time (FAT): $t_{FAT} = t_{dead} + t_{rise}$
- Deactivation time (DAT): $t_{DAT} = t_{hold} + t_{fall}$
- Overheating time (t_{oh}): the time when the valve is fully open, but the motor is still heated and liquid wax is still heating up
- Undercooling time (t_{uc}): the time when the motor is not heated, the valve is fully closed, and solid wax is cooling down

The characteristic times can be empirically estimated, and modelling of the wax actuator does not require physical modelling of the wax temperature and phase change process. This makes the method more tenable, since all physical parameters such as material properties, mass, volume, conductivities, spring properties, etc. do not have to be estimated. Wax motor models for HVAC together with their effect in BPSs have not up to now been analyzed in the scientific literature. This is a major contribution of the present study, since an implementation that allows investigation of grid-driven control with sufficient accuracy is still lacking.
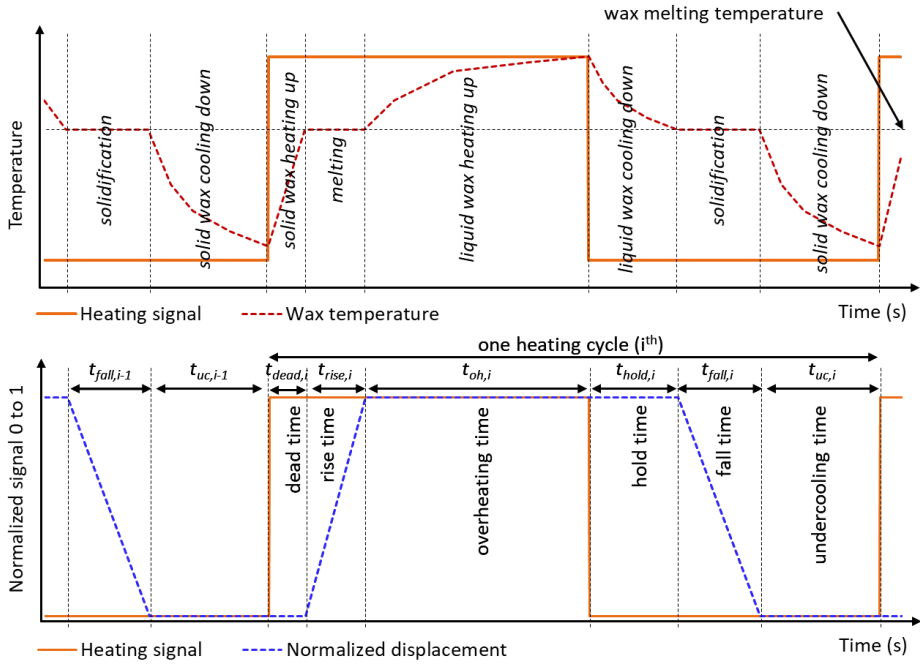
Figure 10. Definition of characteristic times for normalized linear displacement of the piston of a wax actuator or valve dependent on the heating signal; wax temperature changes during this process shown in the upper graph.

2 Methods

This work is divided into two main parts: a general evaluation of heating with dynamic setpoints in nZEBs and a detailed analysis of UFH control. This chapter is structured as follows:

- The present section provides a general overview of methods used.
- Section 2.1 describes the rooms used in the analysis.
- Section 2.2 explains the methods used in the first part of the analysis, the primary and final energy reduction algorithms, and their sensitivity analysis.
- Section 2.3 describes the methods in the second part of the work, the detailed modelling of the UFH control process, and an evaluation of its effect on BPS results.

The first task was to quantify the potential to reduce primary energy demand (PED) through the optimization of the control of low temperature radiators in buildings with different building standards (I). The combination of RES in the power grid, an increase in the energy efficiency of buildings, and the use of heat pumps suggests that there is potential for reducing carbon emissions from heating through the activation of STM. Dynamic primary energy factor (PEF) was used as the grid signal instead of spot price to make it possible to directly quantify emissions and accommodate tariff-based prices. To ensure thermal comfort, PED optimization was carried out using a control algorithm that includes MPC but is simple and can be implemented using a very small number of measurements (sections 2.2.1 and 3.1.1).

In systems with constant or only slightly varying PEF, such as fully renewable or fully non-renewable sources, final energy demand (FED) reduction is necessary for cutting PED or costs. In this case, intermittent heating control can be employed. To see its potential in modern very low energy buildings, an office room with very small losses was defined (V). Offices have a regular usage profile and long vacant periods compared to rooms in residential buildings, making it possible to quantify its full potential. Different thermal masses and both UFH and radiators were also tested to see the variance range. In addition, a well-insulated office was also compared with a less insulated one. To quantify the potential without reducing thermal comfort during occupancy, an even simpler predictive control than MPC was implemented: a pre-heating time calculation based on time constant estimation (sections 2.2.2 and 3.1.2). Theoretically, this can be realized with a prediction model like the one applied in MPC for PED reduction. Even slight complexity can, however, be a barrier to implementation and is probably not needed here.

From the results in section 3.1.2, we can see that UFH may cause overheating during day, and the potential for FED reductions with dynamic heating is, therefore, lower than that for radiators. The fact that UFH cannot maintain a defined temperature level may also reduce the potential for implementing different FED and PED reduction solutions. For a meaningful comparison and to be able to use simpler control algorithms, it is, therefore, essential to improve UFH control.

In simulations of these high-level control algorithms, PI control for UFH is usually implemented. In practice, however, thermostat (on/off) control is often installed. With on/off control, clearly, only a very small deadband would allow precise control, but due to measurement imprecision, it cannot be infinitely small. PI, therefore, has greater potential to improve control. In simulations, the BPS software's default PI parameters are often used, though it is not clear how suitable these are in practice and in the case of the simulated building. In practical applications, new parameters must be found for the specific case and given boundary conditions. In section 2.3.1, a search for optimal PI

parameters for UFH is described, and the potential influence of changed parameters on FED is analyzed (II). Section 2.3.2 investigates low-level control of UFH further, describing methods for developing a wax motor model (III and IV), as there is little to be found in the literature on wax motors in UFH applications. Two different models, a characteristic model and a physical model, were tested in one simple test scenario (IV). As the characteristic model fit the measurements slightly better and was much easier to parameterize, it was discussed and developed further in greater detail for more general use on the basis of an extensive set of experiments (III).

The effect of the resulting empirical model on FED was also discussed (III) and tested with both PI and on/off control. Beyond the wax motor itself, several accompanying effects were also considered. For PI control, both default and optimized parameters from earlier work were used. Since most wax motors only accept a binary heating signal, the PI output had to be modulated. As the valve curve is not in practice linear, a non-linear curve was used in the simulations. In all, a flow control process with gradually increasing level of detail was defined, and its effect on both temperature fluctuations and FED was estimated at each step.

The whole room temperature control process together with the regulation of the volume flow and supply water temperature of the heat emitter is shown in Figure 11. On the left, room air temperature setpoint options for different approaches are shown, including the PED and FED savings algorithms (publications I and V). The control process for volume flow based on set and measured air temperatures is shown in the middle part (publication III). Publications II and IV discussed PI control and wax motor specifics in this process. All the publications included the room and heat emitter modelling, except IV, where the room was included only in the measurement of volume flows in the UFH circuit for calibration purposes.
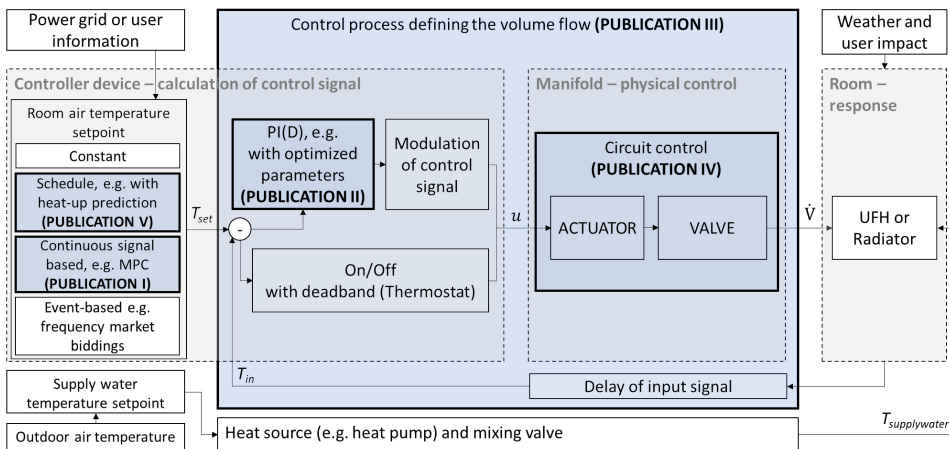

Figure 11. Overview of room heating control and which topics this thesis focuses on.

2.1 Overview of the room and building models

To evaluate the thermal conditions and energy requirements that arise when using different control strategies, comprehensive physical models of the buildings were created. In each simulation, heating operations were controlled in one room using the algorithms developed. Three different test rooms were modelled. We called these the

"German home", "Estonian home", and "Estonian office", according to their locations and usage profiles. An overview of the three rooms is shown in Table 2. In the first row, room plans are shown with windows, modelled doors, and geographical orientation with dashed lines indicating the external walls of neighboring rooms.

The rest of the table shows physical parameters for the rooms. For the sensitivity analysis, the room parameters which varied (window direction, window parameters, wall construction, etc.) are shown with slashes. The building envelope was characterized using thermal transmittance (U-value in W/m^2K), and window glazing parameters included the full transmittance of solar radiation (g-value). Infiltration was characterized using the air leakage of the external envelope at a pressure difference of 50 Pascals (q_{50}).
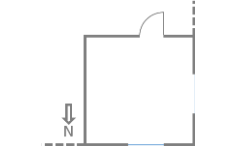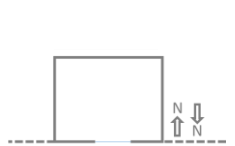
The two homes were rooms in buildings that had been used earlier to calibrate or test the simulation models [43], [104], [120]–[123]. The "German home" test room was on the first floor of the initial building model, a typical two-story single-family detached home with a heated floor area of 150 m^2. The building was constructed of aerated concrete and insulated with mineral wool. The thickness of the insulation and airtightness were varied to estimate the sensitivity of the MPC algorithm developed. The "Estonian home" was a room at the TalTech nZEB test facility, a 100-m^2 house featuring balanced heat recovery ventilation, a ground source, and an air-to-water heat pump system with radiators and UFH, among other technologies. The "Estonian home" room was called Room6/R6 in different articles. Room 5 in the same building is very similar, in fact just a mirrored version of R6. The "Estonian home" room is the subject of the detailed UFH control analysis in the second part of this work. The "Estonian office", a model modern office room, was the subject of the analysis of FED reduction with setback heating.

The office room was modelled as a single zone with adiabatic internal structures, while the adjacent zones to the other rooms were modelled to maintain a constant temperature of 21/22 °C. This approach partially ensured that the performance of the control algorithm would not be overly influenced by the selected building geometry. External boundary conditions were set using weather data from the test reference years (TRY). For the German home, the German Lower Rhine region (western Germany – TRY region number five) was used [124], and for the other two, the Estonian TRY [125].

The rooms were heated using either radiators or UFH. The table shows their power and the share of heat demand under design conditions it was defined for. Ventilation with heat recovery (HR) was included in all well-insulated cases. Average internal gains from people, lights, and equipment are also included in the table.

The IDA ICE simulation software was used in almost all cases. For the MPC analysis, a co-simulation framework was compiled using Dymola/Modelica software [94], [126], [127]. The German home was thus modelled in Modelica. Both IDA ICE and Modelica software model rooms as one ideally mixed air volume, its space enclosed by structural components. The heating system was mostly based on components available in this software. In the case of Modelica, the AixLib library was used [128], [129]. In this thesis, it was not critical to construct a detailed model of the heat generation system. Heat was produced by an ideal heat source, which was linked to the hydraulic radiator or UFH system in the test room under observation. In the context of this thesis, the room, heat emitter, and mass flows in the circuit were modelled, but the interaction between different circuits and the heat pump were excluded (see also Figure 1).

Table 2. Overview of the modelled rooms and their parameters

Visualization			
Name	**German home**	**Estonian home**	**Estonian office**
Location	NRW, Germany	Tallinn, Estonia	Tallinn, Estonia
Area	16 m²	10.4 m²	13.3 m²
Function	Residential	Residential	Office
House area	150 m²	100 m²	-
Adjacent rooms	At temperature 22 °C	At temperature 21 °C	Adiabatic int. walls
Envelope			
External env. Area	37.6 m²	30.1 m²	10.3 / 23.6 m²
External wall construction; U-value (W/m²K)	Aerated concrete, mineral wool; 0.54 / 0.28 / 0.14	Timber frame; 0.12	Timber frame / masonry; 0.8 / 0.14
Floor construction; U-value (W/m²K)	concrete floor with insulation, on ground 0.52 / 0.33 / 0.26	concrete floor (with crawlspace); 0.08	Concrete floors, adiabatic or above air Adiabatic / 0.11
Ceiling / roof; U-value (W/m²K)	timber frame ceiling; 0.21	timber frame roof; 0.08	Concrete ceiling; adiabatic
Specific heat loss W/K/floor m²	1.9 / 1.1 / 0.6 without air exchange	1.5 without air exchange	1.4 / 0.7 / 0.5 without air exchange
Windows			
Directions	N & W	S & W / N & W (R5)	N / S (modern)
Area(s)	1.8 m² x 2	3 m² x 2	3 m² x 1
Frame fraction	20%	24%	25%
U-value (W/m²K)	2.5 / 1.3 / 0.8	0.75	1.4 / 0.75
g-value	0.8 / 0.6 / 0.5	0.3	0.54 / 0.46
Air exchange			
Infiltration (q_{50} in m³/h/m²)	12 / 6 / 1.2	0.6	3 For old: in vent. Incl.
Ventilation (l/s/m²)	0.36	1.08 / 0.5	Avg. 0.58 (2 during working day)
Heat input			
Vent. Supply temperature	T_{out} (HR ca 80% reflected in smaller 0.07 l/s/m² airflow)	T_{sup} 18°C (80% HR)	T_{sup} 18°C (80% HR) old: no HR & T_{out}
Heat emitter, nominal power (W/m²)	Radiator 67 / 53 / 26 (dim. 131% /143% /260%)	UFH 68 (dim. 90% / 140%)	Radiator / UFH 125 / 33 / 21 (dim. 360% /180% /115%)
Supply/return temperatures	55/45 by design	34/29 by design	ideal
Internal gains (W/m²)	18.1 during occupancy	On average 4 (during occ. 10.4 + people)	On average 3.8 (during occ. 8.3)
Modelling			
Software	Dymola/Modelica	IDA ICE 4.8	IDA ICE 4.7.1
Utilized for:	PED reduction with MPC	PI precision, control of volume flows, WM	FED reduction with setbacks and pre-heating
In publications	I	II, III, IV	V

2.2 Effect of dynamic setpoints on energy savings

In this first part of the work, two control algorithms were developed to estimate the energy saving potential using dynamic setpoints. The following cases were analyzed:

- Primary energy saving potential in a residential building when optimizing PED using MPC (section 2.2.1)
- Final energy saving potential in an office when using a nighttime temperature setback and pre-heating time estimation based on a time constant calculation (section 2.2.2).

2.2.1 PE saving potential

2.2.1.1 Concept

An algorithm for PED minimization was developed for the "German home" room. Three building standards were compared for the sensitivity analysis. The control algorithm would dynamically identify optimal operating temperatures to guarantee thermal comfort for occupants while reducing PE demand for heating in response to a dynamic PEF [130]. Optimization would be achieved through the application of dynamic thermal comfort limits dependent on room occupancy and activity levels of the occupants [1]. Ensuring thermal comfort and PED reduction simultaneously through STM activation would require predictive capabilities, prompting the development of an MPC algorithm.

The control algorithm, which includes both rule-based and model predictive parts, was designed to operate without any prior system data and collect data required at runtime. Once enough data was gathered from the physical simulation (a white-box model), a simple black-box model was built and updated daily. This model was then used to predict thermal conditions in order to optimize heating operations.

2.2.1.1.1 Dynamic primary energy factor

The objective function of the MPC optimization algorithm was based on a dynamic PEF, making it possible to minimize PE demand for heating. The fluctuating PEF was adapted from the study by Stinner et al. [130], where it was calculated on the basis of time series data for Germany's electricity demand and renewable power generation from wind and PV in 2015. Their profiles can be scaled to reflect any given share of RES on the grid. In the present work, the PEF was scaled to reflect 80% RES, the German government's target for the year 2050 [131]. This approach ensures sufficient fluctuation to allow dynamic operation of the heating system, as required for LS and STM activation. Figure 12 illustrates the resulting dynamic PEF signal for the observed two-month period.
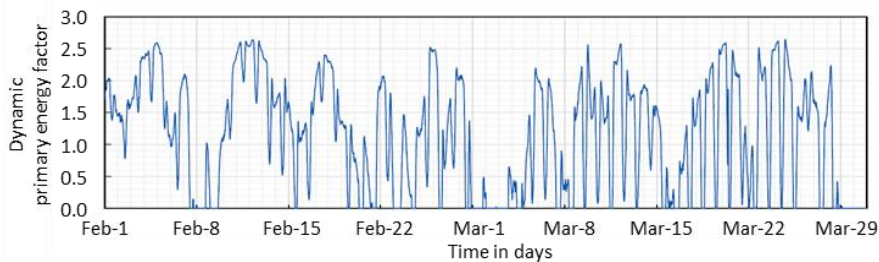

Figure 12. Dynamic PEF profile used as penalty function for optimization in MPC.

2.2.1.2 Building simulation

The "German home" was modelled using Modelica (as a white-box model) and for the reference case, and its construction was defined according to German energy conservation ordinance EnEV 2009 (referenced as EnEV 2009 or 09) [132]. This standard describes an average modern German building built or retrofitted after 2009 [132], [133]. Energy efficiency was then reduced to comply with the 1984 German thermal insulation ordinance (TIO 1984 or TIO) [134] and subsequently improved to comply with the passive house (PH) standard [135].

The room was equipped with a radiator that would provide a nominal heating load of 26 W/m^2 (PH), 52 W/m^2 (09), and 67 W/m^2 (TIO), as calculated for the observed room [32], [136]. Power included a heat-up factor of 16 W/m^2, as recommended for buildings with moderate nighttime temperature reduction. So the radiators followed the assigned air temperature setpoints, they were controlled using a conventional PI controller (K = 0.1, ti = 1000).

Room operative temperature predictions in MPC relied on a simple black-box model. An auto-regressive model with exogenous inputs (ARX) was used since ARX is often integrated with MPC to optimize energy consumption [69]. The model consists of two parts, an auto-regression calculation including the weighted sum of the variable's own previous values and the weighted sum of exogenous variables, which include the effects of other factors influencing the operative temperature from the previous and current time steps. A third order ARX model was selected based on a literature review [137]. The three previous values of the operative temperature were thus used to predict the next value. Three timesteps of the exogenous variables were also taken as inputs, with the assumption that the first predicted time step *[t+1]* values were already available. Time was quantized into 15-min steps.

The structure of this ARX model is shown in equations (3) and (4). The four exogenous variables (defined by vector $\vec{X}$) correspond to the temperature setpoint (T_{set}), solar irradiation (I), ambient temperature (T_{out}), and room occupancy (occ). T_{set} was the control variable adapted according to the optimization (see next section). In Eq. (3), T_o is the operative temperature and $c_{i,y}$ are the ARX fitting parameters estimated using the identification function 'arx' in MATLAB [138]. All $c_{i,y}$ parameters were initialized to zero.

$$T_o[t+1] = \vec{c}_{0,\vec{X}} \cdot \vec{X}[t+1] + \vec{c}_{1,\vec{X}} \cdot \vec{X}[t] + \vec{c}_{2,\vec{X}}$$
$$\cdot \vec{X}[t-1] + c_{1,T_o} \cdot T_o[t] + c_{2,T_o} \quad (3) \qquad \vec{X} = \begin{pmatrix} T_{set} \\ I \\ T_{out} \\ occ \end{pmatrix} \quad (4)$$
$$\cdot T_o[t-1] + c_{3,T_o} \cdot T_o[t-2]$$

While a perfect prediction of *I, T$_{out}$*, and *occ* was assumed to be available to the MPC, the same data was used in both the white-box and black-box models. German TRY data was applied for *I, T$_{out}$*. Occupancy was generated using Richardson's approach [139]. This method produces a statistically based irregular occupancy time-series that differs each day and distinguishes between weekdays and weekends. A two-week section of the generated profile is shown in Figure 13. According to the profile, the room was used for 34.5% of the observed time: 21.5% representing periods when the occupants were active, 11.8%, inactive periods, and 1.2%, nighttime periods.
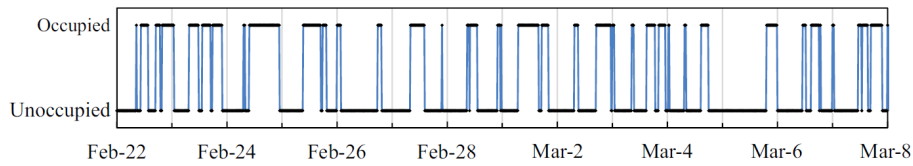
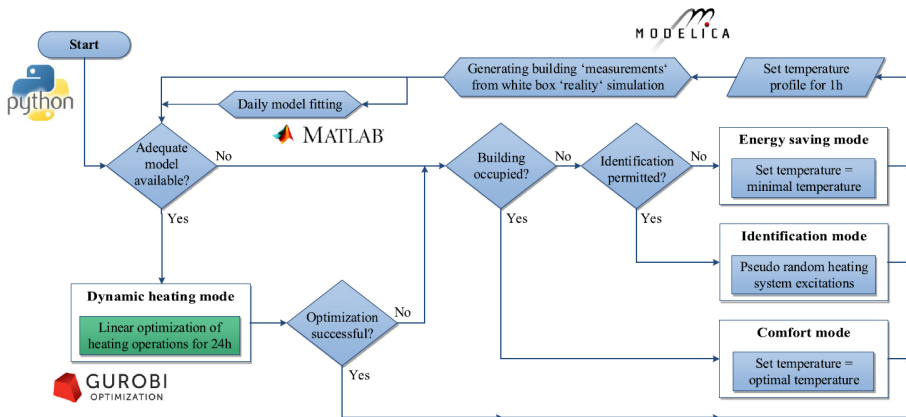*Figure 13. Sample two-week section of the occupancy profile.*

Figure 14. Flow chart for the heating control algorithm developed.

2.2.1.3 Self-learning model predictive algorithm

The control algorithm was written in the Python programming language, while MATLAB was used to fit the black-box model, Gurobi [140] to do the optimization, and Dymola/Modelica, to do the 'reality' simulations. Though it was implemented on a high-performance system, the algorithm was design to be simple enough to run on even a Rasberry Pi [141] in a typical home. The corresponding performance calculation is included in publication I.

The flow chart in Figure 14 provides an overview of the control algorithm designed. The initial part of the algorithm is rule-based, making it easier to adapt the control system to new environments. If the room is occupied, the temperature setpoint is defined as the optimal operative temperature. If not, pseudo random binary signals (PRBS) [137] are selected as temperature setpoints so that a wide range of measurement data can be gathered for model fitting. This identification mode is not permitted if the ambient temperature is higher than the minimal acceptable building temperature (19 °C) and the current PEF is higher than its yearly average value of 1. If not permitted, the energy saving mode is selected, and the temperature setpoint is defined as the minimum temperature under unoccupied conditions (19 °C). Operation modes are separately selected for all 15-minute time steps, and a temperature setpoint profile for the upcoming hour is then compiled. The control algorithm is executed once per hour.

The ARX model, based on collected measurements, is fitted when measurements for at least one week are available. New model parameters are fitted every 24 h. The model's root mean square error (RMSE) between temperature measurements and average predictions for the previous three days is evaluated. If RMSE < 1 K, the model can be implemented. If the RMSE is larger, the last suitable model is used if not older than 3 days. Otherwise, the ARX model is not used for the MPC until the next successful model fit.

If a sufficiently accurate ARX model is available, the dynamic heating mode is activated and the MPC seeks a suitable heating operation to minimize PE demand for heating according to the objective function in Eq. (5). The cost function minimizes the PEF-weighted difference between the temperature setpoint and minimum acceptable operative temperature using a time step of 15 min with a 24 h horizon. This requires the dynamic PEF from the coming 24 hr.

$$\min_{T_{set}} \left(\sum_{t=1}^{24\cdot4} PEF(t) \cdot \left(T_{set}(t) - T_{min}(t) \right) \right) \tag{5}$$

A linear optimization, employing a deterministic concurrent method [140] is performed in Gurobi (version 6.5.0) using the *gurobipy* Python package. If an optimal heating operation is found, the first hour of the optimized temperature setpoint schedule is set as the temperature setpoint profile for the heating, and the cycle is repeated hourly. If the optimization fails at first, the algorithm reduces the optimization horizon by 2 h until it reaches 12 h. If no solution is found for the observed optimization problem, and the optimization fails, then the algorithm is downgraded to rule-based control.

Finally, the compiled temperature setpoint profile for one hour is simulated in the white-box model, and the resulting operative temperatures are returned to the control algorithm as 'measurement' values for its next iteration.

2.2.1.4 Evaluation of concept and scenarios

The performance of the control algorithm was evaluated from 1 February to 31 March. This period was selected for the cold ambient temperatures, which would ensure a continuous heating demand, while the prominent role of PV generation would ensure regular fluctuations in the PEF. The simulations were performed for the three building standards described above.

To assess the potential of the algorithm developed, an MPC optimization scenario (O2b) was created. Two reference scenarios (R1 and R3) were also defined and simulated to help assess the MPC algorithm's performance. For the reference scenarios, a rule-based control was used to generate time-dependent temperature setpoint profiles. R1 would keep temperatures at a constant 22 °C for a comparison with conventional building operations. The temperature setpoints for R3 were the optimal temperatures in the dynamic comfort profile and would therefore serve as the main benchmark for the MPC algorithm. O2b implemented dynamic comfort constraints and dynamic maximum rates of temperature change that were adapted from Wolisz [1]. These vary according to occupancy and occupant activity. The rate of limiting temperature change varied from 1 to 3 K (specified in publication I), depending on tenant activity and whether the temperature was increasing or decreasing towards or away from the optimal operative temperature (R3). Specific comfort constraints for all scenarios are given in Table 3.

Table 3. Boundary conditions in the scenarios analyzed

Time range	Operative temperatures when occupants are …				Rate of change
Scenario (↓)	Not present (at any time)	Active 7 a.m.-6 p.m. 11-12 p.m.	Inactive 6-11 p.m.	Sleeping 12 p.m.-7 a.m.	At any time
R1	22 °C				≤ 4 K/h
R3	19 °C	21 °C	23 °C	20 °C	≤ 4 K/h
O2b	19-24 °C	20-23 °C	22-25 °C	19-22 °C	Dynamic

Agreement with the comfort constraints defined was evaluated by quantifying the violations of these constraints using equations (6) and (7). For each time step (t) when the operative temperature was not in the comfort range, the violation time (t_{out_lim} in 0.25 h) was multiplied by the violation's extent (ΔT_{out_lim} in K). The summation over the timesteps resulted in a temperature violation index (TVI) that represents the total constraint transgression in Kh (degree-hours). Similarly, the temperature change violation index ($TCVI$) was calculated from the extent of the violation (ΔTC_{exceed} in K) by full hour (h_{exceed} in h). The violation indices for scenario O2b were compared with those of reference scenario R3 (which had optimal temperature setpoints).

$$TVI = \sum_t \Delta T_{out\_lim} \cdot t_{out\_lim} \qquad (6) \qquad TCVI = \sum_h \Delta TC_{exceed} \cdot h_{exceed} \qquad (7)$$

2.2.2 FE saving potential

2.2.2.1 Concept

Results from the minimizing of PED using MPC control show that building energy efficiency has a significant impact on load shifting capability (see results section 3.1.1.2). It was made possible, however, by a significant increase in FED. The following analysis assesses how much it is possible to reduce FED during setback control and how much the insulation level and thermal mass of building constructions affect it in very low energy buildings. As shown previously [43], profile shape significantly influences energy consumption, as the duration of temperature setback varies. The "Estonian office" room was thus modelled to use long and regular vacancy periods to show the full savings potential.

2.2.2.2 Building simulation and scenarios

The "Estonian office" room model used for the simulations had three different energy efficiency level variants, the old, the standard, and the modern. In all cases, concrete (heavy) and wooden frame (light) constructions were used to represent different thermal masses. The old and standard rooms had one external wall with a window facing north and an external floor over outdoor air. The modern configuration had the same constructions as the standard case, but its floor was adiabatic, and it mirrored the standard case with the window facing south so the room received more solar heat gains.

We defined the internal loads and ventilation control according to Estonian norms for office simulations [142], meaning that the building would be occupied from 7 a.m. to 6 p.m. on workdays. During night, on the weekends, and on holidays, the building would be unoccupied. Ventilation airflow was 2 l/s/m^2 during periods of occupancy and for 1 hour preceding and following each of these periods. The usage profile is shown in Figure 15. This usage rate was multiplied by 5.8 W/m^2 to yield the occupant heat gain, and by 9.5 W/m^2, to yield the heat gain from lighting and electrical appliances.
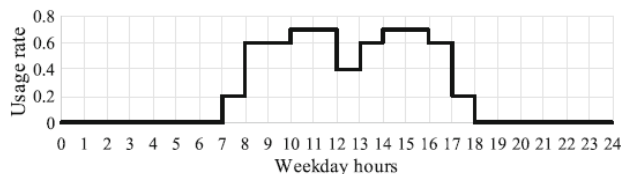

Figure 15. Usage rate (according to [142], a weighting factor for all internal gains.

Two types of limited-power heating systems were simulated: ideal air heaters and simplified floor heaters. Ideal air heaters represented the radiators (Rad) supplied by a district heating system, while floor heaters represented the underfloor heating (UFH) supplied by a heat pump. Simplified/ideal systems were used in place of the function for raising the heating curve to achieve maximum output power of the systems during heat-up; the designed power was always available if needed. The modern systems had a nominal power of 21 W/m^2, the standard systems, 33 W/m^2, and the old systems, 125 W/m^2. In the standard case, the room was also modelled with over-dimensioned radiators (according to [32]) to provide the extra power needed for weekend setbacks. It can be compared with a gas boiler supplied radiator-based heating system, which can be easily over dimensioned without a significant increase in cost. The ideal heaters in standard light offices with 51 W/m^2 and in standard heavy offices with 103 W/m^2 were simulated and defined as 'over-dim-Rad'.

10 different scenarios were created based on different combinations of the 3 insulation levels, heavy and light construction cases, 2 heat emitter systems, and the over-dimensioned radiator cases, as shown in Table 4. These were simulated over a fixed heating period (1 October to 30 April) using two control algorithms. First, a reference case with a constant setpoint of 21 ˚C tracked by PI control was simulated, and then, a setback algorithm with pre-heating was applied. The pre-heating algorithm together with the numeric parameters in the table are described in the next section.

Table 4. Scenarios and calculated input parameters used for the control algorithm

Energy-efficiency level	Str. mass	Heat emitter	Abbrev.	τ_n (h)	τ_{wnd} (h)	Φ (W)	H (W/K)	C_{20mm} (kJ/K)
Standard	Heavy	UFH	S_H_UFH	50	225	437	9	1677
Standard	Heavy	Rad	S_H_Rad	50	225	437	9	1677
Standard	Light	UFH	S_L_UFH	50	150	437	9	1561
Standard	Light	Rad	S_L_Rad	50	150	437	9	1561
Old	Heavy	Rad	O_H_Rad	25	125	1656	18	1677
Old	Light	Rad	O_L_Rad	25	75	1656	18	1561
Modern	Heavy	UFH	M_H_UFH	50	300	273	7	1677
Modern	Heavy	Rad	M_H_Rad	50	300	273	7	1677
Standard	Heavy	Over-dim Rad	S_H_O_Rad	50	225	1367	9	1677
Standard	Light	Over-dim Rad	S_L_O_Rad	50	150	684	9	1561

2.2.2.3 Pre-heating control algorithm

The aim of the setback control was to keep the air temperature at 21 °C during periods of occupancy using PI control and allow it to drop to 18 °C when the room was vacant. Pre-heating, however, also needed to be applied to ensure comfort conditions when occupancy began. A widely used heat-up time calculation was adapted for this dynamic use case.

The pre-heating or heat-up time was defined as the time the system would need to heat the room back up to 21 °C from setback. Instead of choosing a constant value for each building, a variable pre-heating time dependent on boundary conditions could be

estimated using previously calculated parameter values. From the heat balance equation for indoor temperature T_{in}:

$$C \frac{dT_{in}}{dt} = H \left(T_{out} - T_{in} \right) + \Phi \tag{8}$$

the heat-up time t up to the setpoint was calculated as the time from the current time ($t=0$) to the time targeted higher temperature T_{set} would be reached assuming current indoor air temperature to be T_{in}:

$$t = - \tau \cdot \ln \left(\frac{\Phi/H - T_{set} + T_{out}}{\Phi/H - T_{in} + T_{out}} \right) \tag{9}$$

where Φ is the constant nominal heating power in watts, H is the heat loss coefficient (W/K), and T_{out} is the external air temperature. τ is the time constant in seconds calculated as $\tau=C/H$. Parameter C represents the heat capacity of the air and structures (J/K). This rough simplification does not take into account internal gains, heat-up process dynamics, etc.

For the calculation of the time constant for the night setback, surface layers with a depth of up to 20 mm were included in the heat capacity calculation. An active layer with a depth of 100 mm was used for the weekend setback [143]. The time constants were quantized by rounding them to the closest 25 hours. This made it possible to use approximate values, as exact values are usually not known for real cases. The heat capacity values for the 100 mm layers were approximately four times higher than those for the 20 mm layers, as shown in Table 4 (7449 kJ/K for heavy and 5002 kJ/K for light).

The control algorithm developed calculated the heat-up time every 5 minutes. If the time exceeded the actual time left until the start of the period of occupancy, the temperature setpoint was changed to 21 °C, overriding the initial PI control. If the calculation resulted in a heat-up time less than the time left until the start of occupancy, the temperature setpoint was turned back to 18 °C again. The implementation of the pre-heating algorithm in the IDA ICE simulation software is shown in Figure 16.
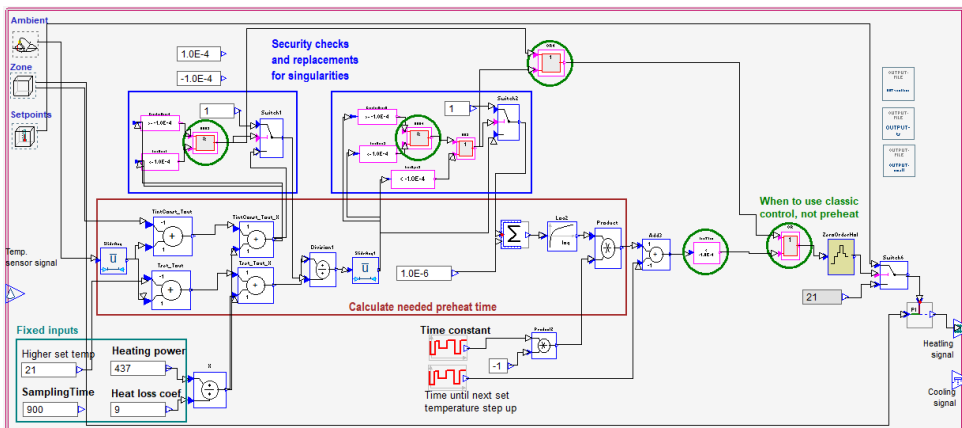

Figure 16. Implementation of the pre-heating algorithm in IDA ICE software.

2.3 Control process modelling effects on energy performance

In this second part of the work, variant models of the UFH control process were created to determine how BPS results would be affected by optimized PI parameters (section 2.3.1) and a detailed modelling of wax actuators (section 2.3.2). The modelling of wax motors also implies the modelling of the effects in detail: PI control, signal delay, valve curve, signal modulation. The analysis focused primarily on PI parameters and wax actuators, as the effect of optimal PI parameters for UFH and a parametrized wax actuator model had not been found in the previous literature. In this part, the modelled room was the "Estonian home" at the TalTech nZEB test facility.

2.3.1 PI parameter estimation for UFH
2.3.1.1 Concept
The previous analysis showed that for UFH, the use of default parameters for PI would not make it possible to maintain a constant temperature for UFH even in the simulation. The goal here was not only to optimize PI parameters for UFH but also to find simple tests that would simplify doing this in practice.

PI parameters were estimated for two test rooms in several ways according to the following process. First, input data was generated with measurements or simulations. This data was then fitted to simplified models, which were used to further estimate PI parameters with methods from the literature. Finally, the resulting parameter combinations were tested in the heating period simulation.

In another approach, PI parameters were generated by optimization in the simulations. Input data was thus generated simultaneously with the optimal parameter combination and its evaluation.

2.3.1.2 Input Data
The "Estonian home" room model used in this analysis was referred to as Room6 (R6) in preceding studies. The windows of the initial room faced south and west. In this analysis, the north-and-west facing room (Room5 / R5), essentially a mirrored version of the initial room, was also included. To generate the data used for the PI parameter estimations, six different datasets were generated. These are characterized in Table 5, according to outdoor climate, heating setpoint, room geometry, and gathering method (simulation/measurements). In all cases, the output was the room temperature that could be used in simplified models (the first four rows), or the same simulations were iterated to optimize PI parameters (last two rows).

The only measured dataset (described in [122]) consisted of measurements we carried out at the same TalTech nZEB test facility in room R5, where we performed 2-day and 3-day long temperature setbacks. The air temperature was measured while the temperature setpoint was kept at 21 °C and during the setbacks, when it was lowered to 18 °C. These temperatures are shown in Figure 17 with estimated average temperatures at the high and low levels. A commercial self-learning PI was used to control UFH, which had temperature variations below 1 K during constant operation in this room with low solar gains, while outdoor temperatures ranged between –5 and +5 °C. Heat-up times were up to a day.

Table 5. Overview of the input data for the model calculation and optimization

Dataset	Climate	Setpoint	Rooms	Generation method
A	Actual	2- and 3-day setbacks	R5	Measured
B	Constant	Shorter setbacks	R5/R6 (equal)	Simulated
C	Constant	Infinite step-up	R5/R6 (equal)	Simulated
D	Estonian TRY	PRBS	R5 and R6	Simulated
E	Estonian TRY	Constant	R5 and R6	Simulated
F	Estonian TRY	Variable (price-based)	R5 and R6	Simulated
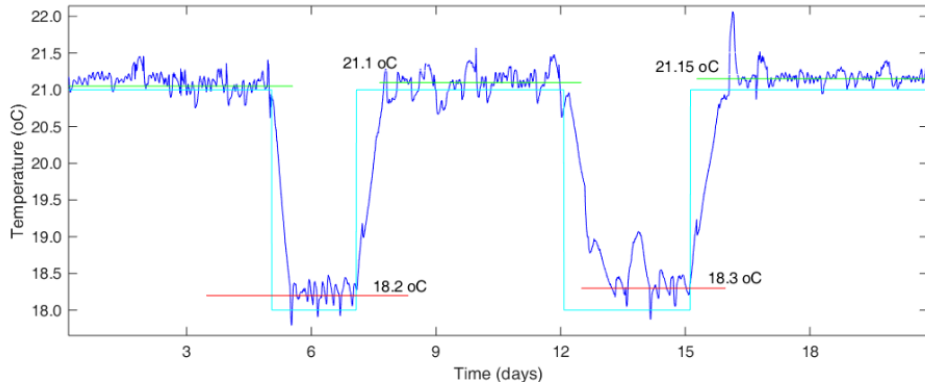
Figure 17. Measured temperatures during two setbacks at the TalTech nZEB test facility [122]

The rest of the input datasets were simulated in the previously calibrated IDA ICE model of the same building. Shorter setbacks of 1, 3, 6, 12, and 24 hours were simulated using a constant outdoor temperature of 0 °C with no solar or internal gains. Between the setbacks, the initial temperature of 21 °C was stabilized. Without solar gains, the two test rooms were equivalent, and so the estimation of PI parameters was based on only one of them. Constant outdoor conditions made it possible to get cleaner data for simplified model estimation and make it easier to tune the parameters in Matlab (see the next section).

An ideal-like step test, the only open-loop case, was also simulated using the same constant outdoor conditions. A step from no heating to full power heating was performed. The simulation period was lengthy, so that indoor air temperature stability would be achieved both before and after the step. This meant two months in simulation to stabilize it at the balance temperature, and one month after the step to reach a steady state. Simulations with outdoor conditions set using Estonian TRY and setpoints determined using pseudo-random binary signal (PRBS) were also run. For the PRBS temperature setpoint, the zero level was set at 18 °C, the maximum level at 24 °C. The simulations were carried out over two separate weeks, one week in March and one week in February: the first, a sunny week with moderate temperature (19–25 March), the second, cold week with almost no sun (29 January – 4 February). The model was fitted using both data for the entire weeks and data only for the weekends of these weeks (12 p.m. Friday to 12 p.m. Sunday).

The last two rows of Table 5 characterize the inputs for optimization of the PI parameters. The same two weeks in March and February stated above and the entire heating period from 1 October to 30 April were used as optimization times. The optimization was carried out for both a constant temperature setpoint of 21 °C and a variable setpoint temperature profile.

The variable setpoint was calculated using price data 2017–2018 [144] and a simple algorithm (from [79] that is not the best suited for therein intended purpose of load shifting but is good for producing an hourly changing profile. For the price-based control, the air temperature setpoint was changed hourly to 20, 21, or 24 °C. The lower two temperatures were comfort levels and had to be maintained, while the highest level was reserved for load shifting and did not need to be tracked, though the heating would have to have been activated at full power until the temperature was reached.

2.3.1.3 Estimating PI Parameters

For each input data combination in Table 5, the PI parameters K and ti were estimated using one or more of the following methods:

1. Calculating using a simple method (datasets A-D),
2. Tuning in Matlab/Simulink, (datasets A-C),
3. Optimizing with GenOpt [145] (datasets E,F).

In the first two cases, a simplified process model of the system was needed. Using the generated input data (see section 2.3.1.2), a first order process model with a time delay was fitted (see section 1.6.1), and parameters K_p, L, and τ were estimated. The model fitting was performed in Matlab, using System Identification Toolbox [146].

In the first method, the fitted model parameters were used to calculate PI parameters according to three widely known methods – Cohen-Coon, Skogestad IMC (SIMC), and AMIGO [147]. The formulas used by these methods to calculate the two PI parameter are shown in Table 6, where the parameter b is a dimensionless value calculated using model parameters:

$$b = L/(L + \tau) \tag{10}$$

Table 6. Formulas for calculating PI parameters in the three chosen methods.

Method	K		ti	
Cohen-Coon (CC)	$0.9 \cdot \left(1 + 0.092 \cdot \dfrac{b}{1 - b}\right)$	(11)	$\dfrac{3.3 - 3b}{1 + 1.2b} L$	(12)
Skogestad IMC (SIMC)	$\dfrac{\tau}{2K_p L}$	(13)	$\min(\tau; 8L)$	(14)
AMIGO	$\dfrac{0.15}{K_p} + \left(0.35 - \dfrac{L \cdot \tau}{(L + \tau)^2}\right) \cdot \dfrac{\tau}{K_p L}$	(15)	$0.35L + \dfrac{13L\tau^2}{\tau^2 + 12L\tau + 7L^2}$	(16)

In the second method, PI parameters were tuned in Matlab®/Simulink for the previously fitted simplified models, which were converted into transfer functions. The tuning was performed in a closed-loop process, where the input was daily periodic 6-hour setback profile. The tuning aimed for short rise time (speed) and an overshoot of no more than 5% of the desired temperature increase.

In the optimization method, PI parameters were optimized in GenOpt using a hybrid GPS algorithm [148]. The optimization was carried out for the three different time periods (the entire heating period, a cold cloudy week, and a moderate sunny week) and for both the constant and variable setpoint profiles (see section 2.3.1.2). The objective of the optimization was to minimize the mean absolute error between the setpoint temperature and the simulated temperature. The initial search was conducted with parameter values that varied by factors of 10, from 10 in power of −10 to +10.

Optimization limits were then set around the K and ti values that yielded the lowest error and the parameters were optimized more precisely.

For visualization of the results, estimated PI parameters were classified into four groups, according to the simplified models: setbacks, longer step, PRBS sL, and PRBS lL. Models generated from measured data and the ideal step were classified as "longer step", shorter setbacks, as "setbacks". Models acquired using PRBS were classified according to the resulting magnitude of the L parameter (< 1000 sec was short (sL), and > 1000 sec was long (lL)).

2.3.1.4 Evaluation tests

All the estimated PI parameter combinations were tested in simulations to evaluate heating energy consumption per square meter of floor area after thermal comfort had been ensured. Evaluations were carried out for the entire heating period (01 October – 30 April), for all combinations of PI parameters, for both rooms, and for both setpoint profiles (constant and variable). The setpoints used for the evaluation of the PI parameters were the same used in the optimization cases (see section 2.3.1.2).

It was critical that no parameter combination would result in temperatures below the given comfort setpoints. In most cases, however, this had not been achieved, and the setpoints thus had to be shifted before evaluation. The goal was to achieve temperatures equal to or above the setpoint for at least 97% of the time, as recommended by the thermal comfort standard EN 16798-2 [35].

Cumulative temperature graphs were generated on the basis of the initial simulations. In the constant setpoint case, the setpoint was shifted 3% of the time exactly as many degrees as the cumulative graph was below the setpoint (see section 1.3). In the variable setpoint case, shifts for both the 20 °C and 21 °C setpoints were calculated. For the 20 °C setpoint, the shift was 3% for 1.3% of the total time, and for the 21 °C setpoint, 45.2% of the total heating period. The maximum of the shifts calculated for these two points was applied to the entire profile.

The IDA ICE software's default values for the PI parameters, $K = 0.3$ and $ti = 300$ s, were used for the benchmark simulations. On/off controls with four different deadband widths were also evaluated for comparison: a modern controller with a deadband of 0.5 K (+/- 0.25 K), close-to-ideal versions with deadbands of 0.16 K and 0.05 K, and a conservative one with a 1 K deadband.

2.3.2 Physical control process components

2.3.2.1 Concept

In practice, in addition to PI control parameters, UFH control is also influenced by several physical components. In this part of the work, some of these effects have been evaluated. A wax actuator model, however, must be found or parametrized first, as discussed in section 1.6.2.

Initially, we tested both a characteristic and a physical model. Though results did not differ significantly, the characteristic model was much easier and more practical to estimate, and so it was chosen for further study. Dependence on previous heating actions was built into the characteristics to calibrate variability. The resulting variable empirical model was further analyzed to estimate the effect it would have on simulation results. This analysis also included other control process effects, such as delay, valve curve, and signal modulation (see Table 10 in section 2.3.2.4 for all components).

The general workflow of this part of the study is shown in Figure 18. The piston displacement, which was dependent on the electrical heating signal, was measured when

the valve was not connected to the UFH system. The displacement measurements were used to define the wax actuator model. The wax motor was then connected to a valve in the UFH manifold, and the volume flow was measured when the electric signal was known. The wax motor model from the previous step was then used to calculate the piston's linear displacement in flow measurements. The valve opening to volume flow characteristic curve (the valve curve) was then calibrated using these measurements and calculations. Finally, the wax motor model and valve curve determined from measurements were used to assess their effect in simulations.
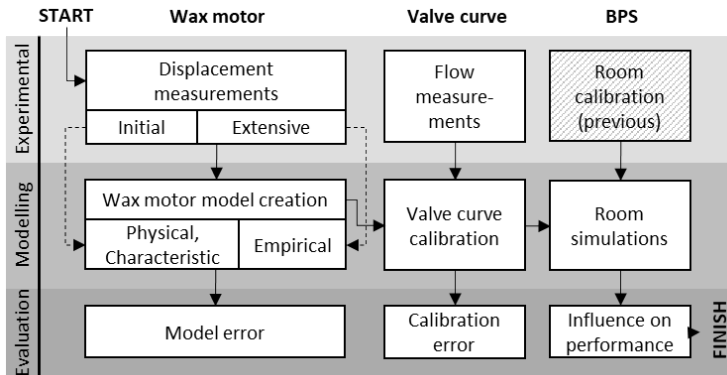
Figure 18. General overview of the research process. Room calibration was included in the previous research.

2.3.2.2 Development of the wax actuator model

2.3.2.2.1   Measured actuators

The wax actuators measured in this work were commercial products that are commonly installed in UFH manifolds in Estonian buildings. Two actuators from different producers, products A and B, were tested. In the case of product B, four different exemplars were tested to see if there were any significant differences. Assessment of potential variance was outside the scope of this work, so no more products or exemplars were considered. The datasheet for product A claimed a positioning time t_{FAT} of 3 min, a full movement range (also called 'nominal stroke') of 2.5 mm, and a positioning force of 105 N. The datasheet for product B did not include this information.

For some measurements, a quick-opening valve was screwed to the actuator (outside the manifold). In such cases, the initial position of the spring in the motor was slightly more compressed, potentially reducing the full movement range. The movement time, however, would be similar, since it depended on the wax phase change time at constant power, and it was this effect that was being analyzed. The final combinations were named A, Av, B1, B1v, B2, B2v, B3v and B4v, where the first letter indicated the product, the number, the exemplar, and 'v', the presence of the quick-opening valve. All combinations are described in Table 7. The last column is explained in the next section (2.3.2.2.2). The initial test measurements are in blue font.

Table 7. Measured wax actuator and valve combinations for clarification of combination names; the last column shows the measured heating profiles

Combination	Product	Exemplar	Valve included	Heating profiles measured (signal on - off)
A1	A	1	no	15min-15min; 15min-45min; 5min-5min
A1v	A	1	yes	15min-15min
B1	B	1	no	15min-15min; 15min-45min; etc.
B1v	B	1	yes	15min-15min
B2	B	2	no	15min-15min
B2v	B	2	yes	15min-15min; 15min-45min
B3v	B	3	yes	15min-15min
B4v	B	4	yes	15min-15min; 15min-45min; etc.

2.3.2.2.2 Displacement measurements

Displacement of the last element of the wax actuator and valve combination, either the motor's lowest surface or the valve's piston, were measured. Initial tests on B1 were measured using a digital caliper. Later, to make this measurement easier to replicate in this case and all others, a vertically fixed displacement transducer with a 10 mm measuring range was used [149]. The actuator's surface temperature, the room temperature, and the actuator's supply voltage were also measured. The measurement step was 1 second and the data was logged using an HBM CX22BW data recorder [150] and an MX840A measuring bridge [151].

In all tests, the actuators were powered and controlled using a Siemens LOGO! 24CE controller (with 24-V transistor outputs) [152], which generated the heating profiles shown in the last column of Table 7. The first value (before the dash) is the time during which the wax actuator is being heated (a 24 V signal is produced as input). The second number (after the dash) is the cool-down time between heating cycles (the signal is off). A "15min-45min" profile thus means that the voltage was 24 V for 15 minutes and was then off for 45 minutes. This was repeated periodically. The test duration for each profile is given in Appendix A of (III).

The heating profiles were chosen to ensure the complete opening and closing of the valve during each heating cycle. If this failed to happen, the tested heating profile was excluded from the study, since cycles in which the valve is not fully opened or closed are not typically used for wax actuators. Based on the literature and initial tests, at least 3–5 minutes of heating and cooling time would be needed. In this study, the cut-off limit for this exclusion remained close to 3 minutes for both heat-up and cool-down. Longer gaps between heating periods to allow the wax to cool down between cycles were tested and their effect on valve opening time was analyzed. A 15min-15min heating profile was measured for all combinations for comparison, and most heating profiles were tested on motor B1.

2.3.2.2.3 Post-processing displacement

The measured displacement was normalized for each experiment. The maximum displacement was measured at the closed cold position, when the piston was at its lowest position. When the valve opened, the piston head moved higher, and the measured values were lower. The difference between the fully open and fully closed positions, the *stroke*, was identified in each experiment to normalize the displacement as follows:

$$normDisplacement = \frac{|displacement - stroke|}{stroke} \qquad (17)$$

where $displacement$ [mm] is the measured time series during one experiment. The 0-V or 24-V input voltage was also normalized to a time series with values between 0 and 1, the heating signal. While the normalized displacement could be used directly for the physical model fitting, characteristic times had to be estimated before the characteristic or empirical model could be fitted. That process is described in section 2.3.2.2.5.

2.3.2.2.4   Physical model

The physical model used is based on first principles and was developed by Lars Eriksson at EQUA AB in 2017 for a private company. It was publicly released together with IDA ICE software [94]. The original parameter values were, however, considered proprietary not included. The model implementation is shown in Appendix .

   The model uses enthalpy levels to keep track of the wax state in the motor. The heat exchange with the ambient environment is modelled using one resistance and no capacitance. Delays due to the capacity of the plastic cover cannot, therefore, be characterized. The model does not include the springs in the system, increasing the same effect. The ambient temperature is only an input, precluding the generation of a heat balance. Heat transfer to ambient is, therefore, only dependent on the input temperature from ambient and the resistance. To be able to use the air temperature in the room where the manifold is located, the resistance would have to be large.

   To improve the model, the surface temperature was used as input instead of the air temperature. As the temperature of the motor's surface is usually not measured in typical applications and to make it possible to run the simulation with different heating signals, a model-based approach was developed for the surface temperature. It was calculated using the measured room air temperature plus a second-order transfer function y using the heating signal u:

$$y = \frac{K}{(s/w)^2 + 2D(s/w) + 1} u \qquad (18)$$

with parameters K, the gain, D, damping, and w, the angular frequency. Value ranges were estimated from time constants, as we expected the first time constant τ_1 to be close to an hour and the second time constant τ_2 to be close to a minute. As the transfer function's denominator with two poles can be expressed as $(\tau_1 s + 1)(\tau_2 s + 1)$, we can derive the following:

$$w = 1/\sqrt{\tau_1 \tau_2} \qquad (19)$$

$$D = w(\tau_1 + \tau_2)/2 \qquad (20)$$

For both the surface temperature model and physical model, the parameters, their default values, assumed ranges, and optimized values are shown in Table 8. The values were optimized to fit the experimental data measured during the initial 15min-15min and 15min-45min tests of the B1 actuator. The values for all parameters were found using GenOpt with a connection to IDA ICE parametric runs [145] minimizing the MAE (mean absolute error) between the measured and simulated values, linear piston movement in the physical wax motor model and surface temperature for the second order transfer function.

Table 8. Parameters for both the physical wax motor model and surface temperature model, their tested value ranges with reasoning, default values, initial values, and their final optimized values

Name	Description	Initial value / Default (limits)	Reasoning	Final value	Unit
N	Number of ambient connections	1 / 1	Simplest model	1	items
M	Mass of the wax	0.0008 / 0.0005 (0.0005 to 0.002)	Ca 1 cm³ of wax, density 0.8 g/cm³ [153]	0.001	kg
CP_SOL	Specific heat capacity in solid state	2100 / 1200 (2100 to 3000)	e.g. 2384 or 2604 J/(kg K) [153], or 2100 J/(kg K) [154]	2930	J / (kg K)
CP_FLU	Specific heat capacity in liquid state	2100 / 1200 (2100 to 3000)	2981 J/(kg K) [153], or 2100 J/(kg K) [154]	2910	J / (kg K)
L_SOLID	Melting heat	210000 / 200000 (200000-220000)	From 200 to 220 J/g [153]	203000	J/kg
T_H0	Initial value of wax temperature	20 / 20	As the initial value of H was not changed, default value was used.	20	°C
T_MELT	Melting temperature of wax	75 /75 (60 to 80)	Working env. temperatures up to 60 degrees [91], [155]; has to be higher	72	°C
U	Input voltage at signal 1	24 / 230	Defined by the wax motor product in use	24	V
MAXDISP VLV	Maximum displacement of the valve	3.25 / 1.5	Used the same as valve	3.25	mm
MAXDISP ACT	Maximum displacement of the actuator	3.25 / 3.5	Determined from the measurement	3.25	mm
T_CURIE	PTC heater temperature where resistance becomes infinitely large	90 / 90	Ranging from 60 to 140 °C; for thermal actuators is typically at 90 °C [156]	90	°C
R_25	PTC heater resistance at 25°C	50 / 290 (5 to 300)	50 K/W [157]	97	K/W
R	Thermal resistance between wax and cover surface	13 / 13 (0.1 to 100)	Only insulation 100 K/W, only plastic 0.3 K/W.	52	K/W
K	Surface temperature model's gain	10 (1 to 30)	Temperature change between the room and wax temperature	18.5	-
w	Surface temperature model's angular frequency	0.002 (0.0001 to 0.1)	Time constants' initial guess $\tau1$=1h and $\tau2$=1h	0.0011	-
D	Surface temperature model's damping	4 (0.1 to 10)	Time constants' initial guess $\tau1$=1h and $\tau2$=1h	0.56	-

2.3.2.2.5   Empirical model

The entire process from the measurement of displacements to the creation of the characteristic/empirical model is shown in Figure 19. In each test in Table 7, we estimated the characteristic times described in section 1.6.2. The four characteristic times, dead time, rise time, hold time, and fall time, were identified for each heating cycle.

In the initial test, the empirical model with constant characteristic times was estimated. The cut-off between time periods was defined when the minimal or maximal displacement was reached, as determined by visual inspection. Since the model would not be used later in a dynamic simulation, its response to the heating signal was set according to these identified values.

With a continuous smooth response and more data, however, the cut-off between these periods was not very clear. In the case of the dynamic empirical model, the rise and fall times were, therefore, separated by defining a minimum ramping slope. It was assumed that the linear change from 0 to 1 would take no longer than 10 min in total. For a normalized displacement, this is 10% per minute, so a slope steeper than 0.83% over 5 seconds was classified as part of the rise time. To smooth out measurement errors, the average slope was determined over a measurement of 5 seconds instead of 1 second steps. For fall classification, the slope was steeper, and therefore, a limit twice as large, -1.67% over 5 seconds, was used. These limits were chosen after qualitatively assessing whether the classified periods had discontinuities. When the displacement should have been 0, a margin of 5% was added to exclude small shift offsets. The timesteps that were not included in rise or fall times were classified as dead time, hold time, overheating time, or undercooling time according to heating signal and normalized displacement values, following the logic described in section 1.6.2. The input heating signal was recorded as 1 when greater than 0.5 and 0 when less than or equal to 0.5.
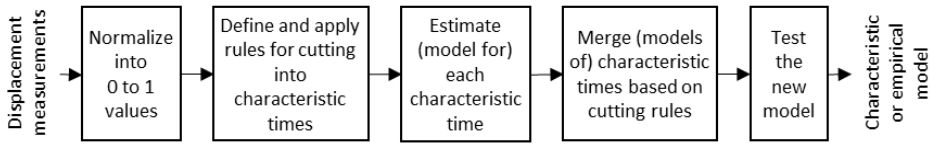
Figure 19. The process of estimating the characteristic or empirical wax motor model from displacement measurements.

It was clear from using different profiles and more data that characteristic times would vary depending on the wax temperature. For further analysis, dependence on preceding actions was then built into the parameters. Based on estimated values for one characteristic time across all tests, a regression model for calculating each characteristic time was defined by fitting the experimental data. According to wax temperature and phase change theory, the following assumptions could be made:

- dead time should be dependent on how low the temperature of the solid wax has fallen, represented by undercooling time:

$$t_{dead,n} = k_d \cdot e^{-\frac{t_{uc,n-1}}{\tau_d}} + c_d \qquad (21)$$

  where $t_{dead,n}$ [s] is the dead time at cycle n, and this depends on the undercooling (*uc*) time of the previous cycle $t_{uc,n-1}$ [s] and on the parameters k_d [s], τ_d [s], and c_d [s], where the index *d* denotes "dead" in dead time.

- hold time should be dependent on how high the temperature of liquid wax has risen, represented by overheating (*oh*) time (with similar definitions):

$$t_{hold,n} = k_h \cdot \left(1 - e^{-\frac{t_{oh,n}}{\tau_h}}\right) + c_h \qquad (22)$$

- rise and fall times should be constant for a given wax motor product at constant ambient temperature, as they represent the melting or solidification processes of the wax.

To find the parameters and test these assumptions, τ (τ_d and τ_h respectively) was first estimated. The correlation between the (one minus) exponent and the output time (t_{dead} or t_{hold} respectively) was calculated for different τ values, and the τ value with the best resulting correlation was chosen. The models based on Equations (21) and (22) were then tested using linear models (lm), and the parameter significance of k and c was tested by calculating p-values in R [158]. If the p-value for a parameter was larger than 0.001, no significance was found, and the model was not used. Otherwise, the parameters k and c were fitted.

The parameters in characteristic time models can change for each product, due to differences in wax mass and build of the motor. If no common model was significant, we used R to estimate multi-level models (lme), which varied the parameter b for the product models. Common models are, however, clearly to be preferred. Although the rise time was assumed to be constant, it can be seen by the results (section 3.2.2.2) that it was not. A model similar to Eq. (21) was, therefore, applied. The resulting models are shown in Table 9. These models were combined into a single empirical linear segments model. The implementation of this combination in IDA ICE necessitated including the detection of heating signal changes, keeping track of the duration of the last heating and cool-down periods, knowing the current status classification, calculation of the normalized displacement from the rise and fall time linear ramps. The implementation is described in detail in publication III.

The models obtained were then tested on the measured data. For each test, both the mean absolute error (MAE) and root mean square error (RMSE) were calculated, and these were used to compare motors and profiles. The linear segments model for one of the products was implemented and tested in IDA ICE. Product B was selected, as it had been installed by design at the TalTech nZEB test facility.

Table 9. Characteristic time models resulting from the analysis

Symbol	Unit	Description	Formula
$t_{dead,i}$	s	Dead time	$-192\,(3) \cdot \exp\left(-t_{uc,i-1}/780\right) + 219\,(13) \pm 13$
$t_{rise,i}$	s	Rise time	$-30(3) \cdot \exp\left(-t_{uc,i-1}/1140\right) + 142(22) \pm 21$
$t_{hold,i}$	s	Hold time	$\begin{cases} 195\,(6) \cdot \left(1 - \exp\left(-\dfrac{t_{oh,i}}{240}\right)\right) + 30\,(5), \text{for product A} \\ 82\,(3) \cdot \left(1 - \exp\left(-\dfrac{t_{oh,i}}{600}\right)\right) + 58\,(2), \text{for product B} \end{cases}$
$t_{fall,i}$	s	Fall time	$\begin{cases} 180, \text{for product A} \\ 123, \text{for product B} \end{cases}$

2.3.2.3 Calibrating the valve model
To simulate the effect of modelling the control details in a BPS, a model was needed that would map volume flow to any valve displacement. Instead of using a theoretical valve curve, an actual curve was estimated from measurements.

For measurements inside the UFH system, the wax actuator B2 was installed in the UFH manifold on the return side valve of the "Estonian home" room circuit at the TalTech nZEB test facility. While the aim was to calculate the given valve's characteristic curve for further modelling as a proof of concept, only one motor was measured. On the supply side, the circuits were set to constant position. While advanced systems can use many different methods to control pressure in the system, for this study, a constant pressure

region of the pump was used. As in previous experiments, the LOGO controller generated 15min-15min heating profiles (15-minute long heating signals with a 15-minute gap between heating cycles). The volume flow, generated from significant changes in room air temperature setpoints, was measured using the Sensus Pollustat E heat meter [159]. All other circuits were closed given the much lower setpoints. The measurements are fully described in publication IV.

The measured volume flows and the heating signal were used to estimate the valve curve. First, the empirical wax motor model developed (see section 2.3.2.2.5) was applied to estimate the valve piston's linear displacement due to the electrical heating signal from the controller. The characteristic valve curve is the relationship between this displacement and the measured volume flow. The valve curve modelling was then carried out in two steps: first, the theoretical quick opening valve curve typical of UFH valves was defined, then the valve authority effect was applied.

The theoretical normalized valve curve, the relation of the displacement d to volume flow $\dot{V}$, was here defined in a simplified way using three points [160], the minimum efficient displacement (d_{min}), the maximum efficient displacement (d_{max}), and the mid-point or breaking point (d_{bp}, $\dot{V}_{bp}$). All the parameters were chosen to minimize the MAE between the measured and calculated final volume flow using the Evolutionary Microsoft Excel Solver. The limits were set to 0.1–0.3 for d_{min}, 0.1–1 for d_{bp}, and 0–1 for $\dot{V}_{bp}$. The d_{min} was forced to be lower than d_{bp}. The parameter d_{max} was set to 1, and to model the ramp more precisely, the part where the valve opening was above 0.95 or below 0.05 was omitted from the error calculation, since the flow variation was very small. The authority effect to obtain authority-corrected volume flow $\dot{V}_{auth}$ was added according to literature sources [161], [162]. In these calculations a pressure difference across the pump of 30 kPa was assumed, and across the system without a control valve, a difference of 27.1 kPa. The pressure difference across the control valve thus resulted in 2.9 kPa. The whole process was described in detail in publication III.

2.3.2.4 Estimating the effect in simulations
To quantify the influence of the wax actuator and other control modelling details on energy performance and temperature control accuracy, several control scenarios were defined for the "Estonian home" simulation model. With UFH supply temperature and volume flow of the liquid given as inputs, the pressure and return temperature were modelled. The heating temperature curve is included in Appendix B of publication III.

The installed power was dimensioned to 140%, and the flow rate of the balanced heat recovery ventilation was set to 0.5 l/s/m². The first week of January and second week of February were the periods selected for the simulations, as heating consumption is similar while solar heat gains are different during these weeks. Heating consumption was 2.4 kWh/m²/week using IDA ICE default PI control. Solar heat gains were 0.15 kWh/m²/week and 0.82 kWh/m²/week during the first week of January and first week of February, respectively. The average dry bulb outdoor temperature was –1.9 °C in January and –6.8 °C in February. A longer period was not simulated, as the empirical wax motor model currently requires timesteps of 5 seconds, dramatically increasing both simulation time and output file size.

The on/off thermostat (O) and PI controller (P) cases were simulated for comparison, and both included a progressing level of detail. First, the business-as-usual simulations were defined (IDs O_0 and P_0), with IDA ICE default parameters, which are typical for BPS simulations. Then, adapted control parameters, signal delay, an adapted valve curve,

signal modulation, and the wax motor model were added step-by-step. The steps corresponding to the simulated scenarios are shown in Table 10. On top of the business-as-usual cases, first, in the CP step, default control parameters (CP) were added: the deadband (*Db*) for the on/off controller and proportional gain *K*, integration time *ti*, and tracking time *tt* for the PI controller. A 2-min input signal delay (D) from the room temperature sensor to the controller would not usually be considered [163] but was added starting with step D for both O_D and P_D [164]. The calibrated authority-corrected quick-opening valve curve (VC) was included next. It was estimated as described in section 3.2.2 and implemented in IDA ICE with small linear segments replacing the IDA ICE default linear control. Modulation control (MC) was then applied in step MC only to the continuous PI control, as the on/off output was already binary. Since the given 24V wax actuators could only be controlled using a binary signal, the continuous output of the PI controller was converted with an hourly modulation, where at the beginning of each hour the algorithm decided whether to heat and for how long. This is a variation of pulse width modulation (PWM). The applied modulation control principle is shown in Figure 20. Finally, the developed empirical wax actuator model for product B was included in steps O_WM and P_WM (again, the "WM" standing for "wax motor").

The most detailed steps, O_WM and P_WM, were used as the benchmark for all scenarios using the same controller. The comparison of energy consumption in the different cases is sensible only when the comfort levels are similar, since lower temperatures would clearly result in lower energy consumption for heating. All simulations were thus initially carried out with a constant air temperature setpoint, which was then shifted iteratively until the operative temperature at 0.6 m from the floor in the middle of the room was below 21 °C for up to approximately 33 hours per week. This matches the 20% limit for weekly deviation from indoor climate class boundaries (EN 16798-2:2019 standard [35]). Finally, temperature fluctuations and heating energy consumption in the different scenarios were compared.
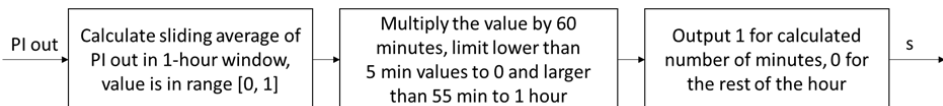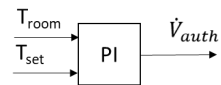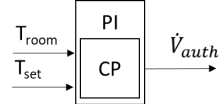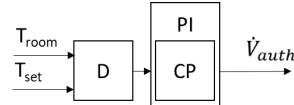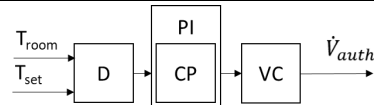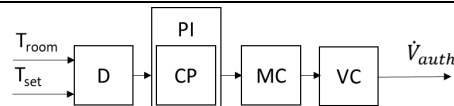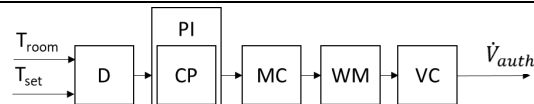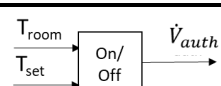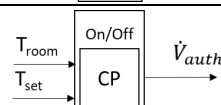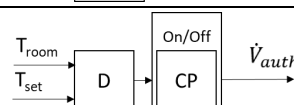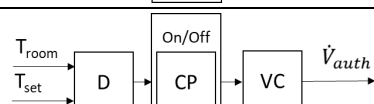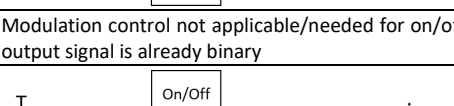

Figure 20. Implementation of the modulation of PI output into wax motor input (the heating signal s). The calculation was performed once per hour.

Table 10. Implementation of all control scenarios for both on/off (thermostat) and PI control

Step	Parameters	Modelled PI (P_) or on/off (O_) control process
P_0 (business-as-usual)	K=0.3 t_i=300s t_t=30s	T_{room}, T_{set} → PI → $\dot{V}_{auth}$
P_CP (adapted parameters)	CP : K=18 t_i=2300s t_t=30s	T_{room}, T_{set} → PI / CP → $\dot{V}_{auth}$
P_D (added delay)	Added delay t_D=2 min	T_{room}, T_{set} → D → PI / CP → $\dot{V}_{auth}$
P_VC (calibrated valve curve)	Sections 2.3.2.3 and 3.2.2.2	T_{room}, T_{set} → D → PI / CP → VC → $\dot{V}_{auth}$
P_MC (control signal modulation)	Figure 20 and Figure 38	T_{room}, T_{set} → D → PI / CP → MC → VC → $\dot{V}_{auth}$
P_WM (added wax motor)	Table 9	T_{room}, T_{set} → D → PI / CP → MC → WM → VC → $\dot{V}_{auth}$
O_0 (business-as-usual)	T_{Db}=2K	T_{room}, T_{set} → On/Off → $\dot{V}_{auth}$
O_CP (adapted parameters)	T_{Db} =0.5K	T_{room}, T_{set} → On/Off / CP → $\dot{V}_{auth}$
O_D (added delay)	Added delay t_D=2 min	T_{room}, T_{set} → D → On/Off / CP → $\dot{V}_{auth}$
O_VC (calibrated valve curve)	Sections 2.3.2.3 and 3.2.2.2	T_{room}, T_{set} → D → On/Off / CP → VC → $\dot{V}_{auth}$
O_MC	Figure 20 and Figure 38	Modulation control not applicable/needed for on/off, as the output signal is already binary
O_WM (added wax motor)	Table 9	T_{room}, T_{set} → D → On/Off / CP → WM → VC → $\dot{V}_{auth}$

3 Results

3.1 Energy performance of dynamic heating

In this section, primary and final energy savings are assessed. PED was minimized using dynamic PEF in a residential room, the "German home", with MPC and dynamic temperature constraints. FED reduction was estimated in the "Estonian office" with pre-heating estimation in setback control.

3.1.1 PED-optimized control

The MPC algorithm's performance was tested for three different building standards, EnEV 2009, TIO 1984, and the Passive House standard (PH). Results from the reference scenario R3 and MPC case O2b described in section 2.2.1.4 were compared. Scenario R1 had not achieved the same thermal comfort level (I) and is, therefore, only further considered in the discussion.

An example of the MPC algorithm's control behavior (scenario O2b and building standard EnEV 2009) is presented in Figure 21. The 'measured' and predicted temperatures differed only slightly during unoccupied phases (T_{max} = 24 °C) and at night. Larger deviations occurred during phases with significant internal or solar heat gains. The 'measured' temperature was close to the lower comfort boundary at times with high PEF and often clearly increased when PEF was low (PEF is shown in the lower part of the graph). Periods when the temperature setpoint exceeded the optimal comfort temperature were marked as STM activation periods. These phases were limited or frequently interrupted, even when the 'measured' temperature was below the upper comfort limit and PEF was low. This occurred either when the predicted temperature reached the upper boundary or when fluctuations of the predicted temperature prevented successful optimization and MPC was deactivated. Such conservative operation resulted in only a few minor comfort violations despite clear STM activation activities. Occasionally, when the identification mode was triggered, the temperature started to fluctuate significantly during unoccupied phases with a below-average PEF.
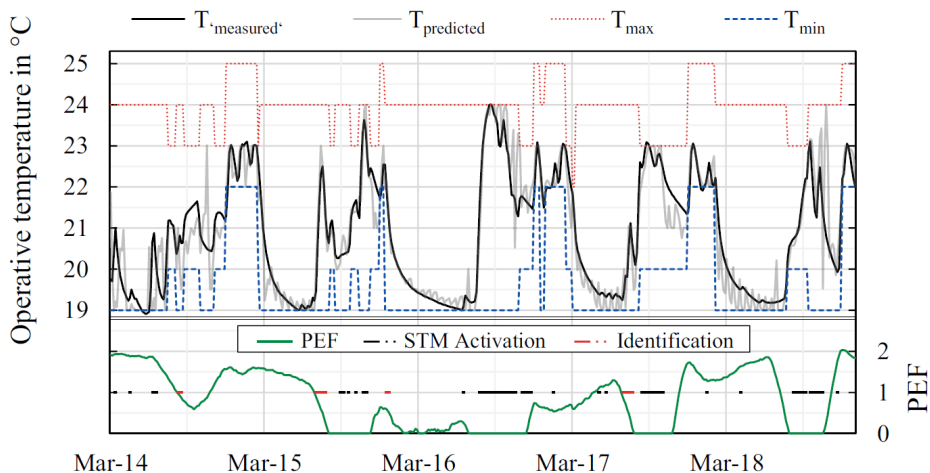

Figure 21. Example five-day sequence in the operation of the MPC algorithm.

3.1.1.1 Thermal comfort with MPC

The simulated thermal conditions for reference scenario R3 and optimized scenario O2b are shown in Figure 22. The chart shows the average operative temperatures during each occupancy phase over the entire observed period.

The average temperatures for the reference scenario differed by less than 0.5 K from the defined temperature setpoints (overlapping with optimal temperatures, indicated with red lines). For PH only, during the seldom and short periods of nighttime occupancy, and when the setpoint was low during unoccupied times, temperatures did not drop enough to achieve the targeted reduction. This shows that PI control for rule-based temperature setpoints was working properly.

The average temperatures for O2b were above the optimal and R3 temperatures for active, sleeping and unoccupied phases, showing that STM was being activated. For the inactive phase only, O2b temperatures were closer to the lower comfort boundary than R3 temperatures. O2b temperatures differed by up to 1 K from optimal temperatures for most phases, by less than 1.3 K only for the unoccupied phase (PH). Generally, average temperatures in the TIO 1984 case were lower than in the EnEV 2009 case, and average temperatures in the PH case were higher than in the EnEV 2009 case. High heat losses in the TIO 1984 case made possible stronger reactions in temperature and therefore better compliance with the dynamic temperature setpoints.
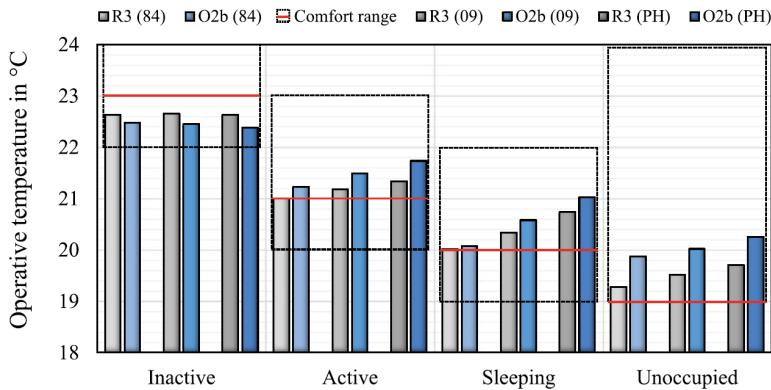
Figure 22. Sensitivity analysis across building standards of average operative temperatures for different occupancy phases.

Figure 23 shows *TVI* and the *TCVI* scores (temperature and temperature change violations) for all scenarios. For reference, a daily violation of 1 K for 1 h would result in a *TVI* or *TCVI* score of 59 Kh as the evaluated period was 59 days (1 February to 31 March). Scenario R3 was designed to keep to optimal temperatures, thus violating the comfort limits only during the transition phases between different constraints. *TVI* and *TCVI* scores for scenario R3 were, therefore, used as a benchmark, being the lowest scores that could be attained using the given PI control under the given conditions.

The violation indexes for scenario R3 increased towards that of less insulated cases due to the larger temperature fluctuations induced by the heat loss. In the MPC-controlled O2b scenario (84), these violations could be effectively mitigated, allowing a 11% reduction in *TVI* and *TCVI*, even lower than that for the EnEV or PH cases. This was primarily due to STM activations, which reduced the time for the minimum temperature setpoint in the MPC case. Temperature fluctuations decreased in the EnEV

and PH cases due to the higher insulation level and lower solar energy transmittance, leading to lower *TVI* and *TCVI* scores in reference scenario R3. In the PH case, the low *TVI* was even further reduced by using MPC, while in the EnEV 2009 case, the O2b and R3 scenarios had very similar scores. Limited improvement in *TVI* could be attributed to two possible factors: either the model's predictions were sufficiently accurate to ensure compliance with temperature constraints, or the predictions were completely unsuitable for MPC. *TCVI* scores for both the EnEV and PH cases were low and remained almost unchanged due to moderate slopes for temperature fluctuations.
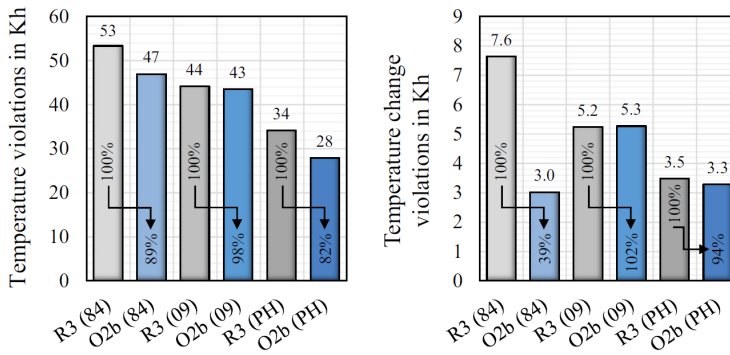
Figure 23. Sensitivity analysis of dynamic temperature/temperature change violations.

3.1.1.2 PED reduction and STM activation efficiency with MPC

After the overall ability of the MPC algorithm to maintain the desired comfort conditions was demonstrated, a comparison was made of PE and FE consumption and average PEF in the observed scenarios (see Figure 24).

The O2b cases required higher temperatures for STM activation, leading to a final energy consumption higher than that in reference scenario R3. O2b, however, exhibited a significantly lower average PEF, in the EnEV 2009 case, 8%, and in the PH case, 33% below the overall average PEF of 1.12 observed during the entire testing period. As a result, the O2b scenario was able to compensate for higher FE consumption caused by STM activation and achieve a PE consumption level below that of the R3 scenario. According to the LS efficiency calculation in publication III, more than half of the additional energy consumption associated with STM activation was wasted, mainly due to the energy used to maintain temperatures above the optimal level.

In the TIO 1984 cases, heating demand was consistent and high, leading to a PEF closer to the overall average for the reference case than in the other building standard cases. Significant heat losses limited the potential for STM activation and consequently resulted in a smaller decrease in the average PEF. Also due to the high heat losses, the energy charged into the STM could only be stored for short periods. As a result, STM activations were infrequent, and final energy consumption increased by only 16%. The slightly reduced average PEF just about compensated for the increased energy consumption from STM activation. Actual PE consumption was only 2% lower than that in the R3 scenario.

In the PH cases, low temperature fluctuations made it possible to apply MPC 61% of the observed time. Only a limited range of the available temperatures could, however, be used. The slow cool-down of the building enabled even moderate STM activations to shift heating demand over extended periods, with most of the required heating activities concentrated in phases with lower PEF. As a result, the average PEF for the PH O2b

scenario was 47% lower than that for R3. Despite the very low average PEF, PE consumption for the PH case with MPC was 15% lower than that for the R3 case, as STM activations in the low heat loss setting resulted in an increase in FE demand by 58%. Results for the EnEV 2009 case fell somewhere between the results for the two other building standards.
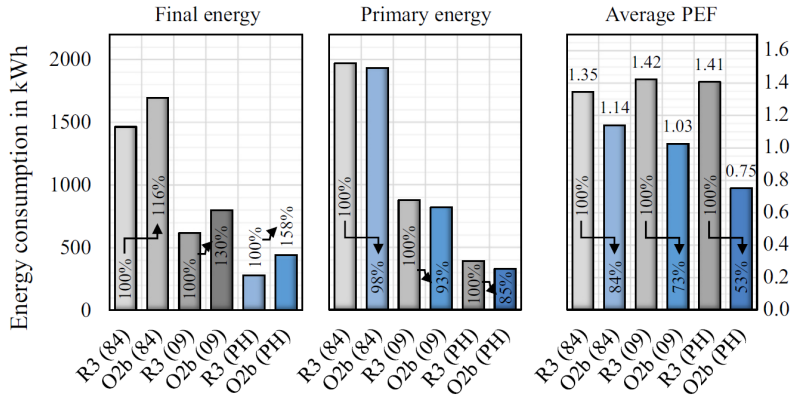

Figure 24. Sensitivity analysis of average PEF values and resulting FE and PE consumption.

3.1.2 FED-reduction with control

3.1.2.1 Temperature performance with setbacks

Simulated temperatures for the FED reducing algorithm with time-constant based pre-heating after night and weekend temperature setbacks are shown in Figure 25. Air temperature fluctuations over a two-week period in winter for all simulated cases are shown together with the occupancy-induced setpoint. Figure 25 (a) shows that for the modern well-insulated room, air temperatures did not drop below 19 °C, even with the weekend setback. With the south-side window, PI control failed to keep the temperature constant during the day after the night setback, and the room overheated, especially in the UFH case.

The same can be seen in Figure 25 (b): even with the light structure and north facing window, temperatures slightly overshot the setpoint on all days. Figure 25 (b) also illustrates the well-known fact that a room with higher heat capacity cools down more slowly. In the case of the light building structure, the temperature dropped to as low as 18 °C, even in the standard floor heating case. This never happened in the massive construction cases.

Figure 25 (c) shows that not all the time constants were accurate. Temperatures fluctuated in the standard heavy radiator case on Mondays, revealing that the algorithm had assumed heating would take longer, but the temperature rose quickly, and the temperature setpoint was lowered to its setback level. The temperature, however, also dropped quickly, need for heat-up was again calculated, and the temperature setpoint was increased again. This behavior caused a fluctuation in several other cases as well. The pre-heat algorithm, nevertheless, helped to achieve the temperature setpoint without overheating, and PI control with the radiators effectively maintained the temperature during the constant setpoint.
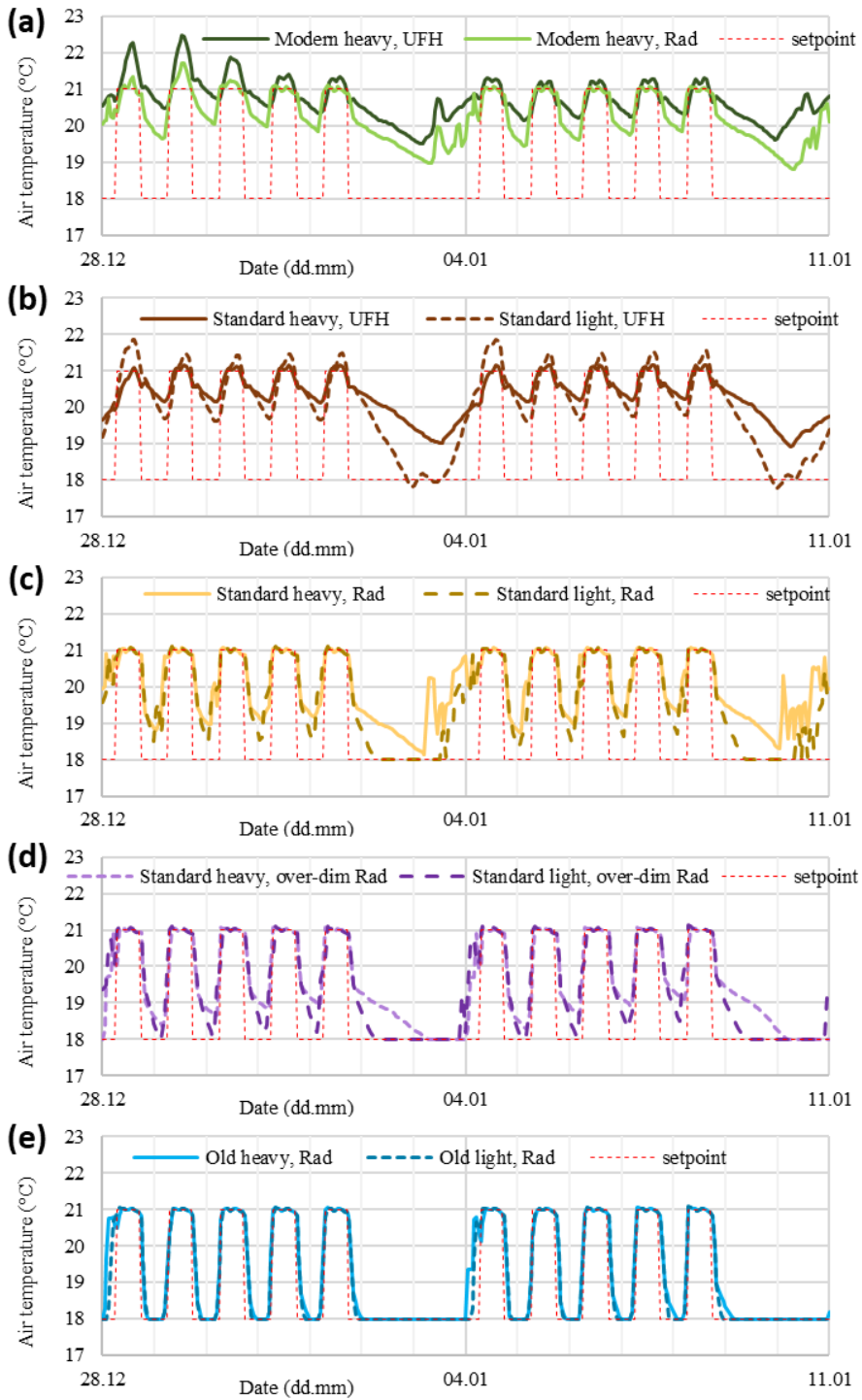
Figure 25. Air temperature fluctuations over a two week period in winter for all simulated cases.

In Figure 25 (d), we can see that in the heavy construction case with over-dimensioned heating, the temperature not only rose more quickly but also fell lower than when lower powered radiators were used instead (Figure 25 (c)). This could be attributed to less heat being stored in the construction due to a shorter reaction time. Figure 25 (e) shows that in old buildings the temperature dropped to 18 °C almost immediately and due to high available heating power, also rose quickly to 21 °C. In the old building case, therefore, the setback potential had been fully exploited.

In Figure 26, we can see that the fluctuation after the weekend setback (on Monday) was more significant than after the night setback (on Friday), strongly suggesting an over-estimated time constant. In addition to the inaccurate estimation of the heat-up time, the switching on of the ventilation at 6 a.m. also contributed to a reduction in room temperature just before occupancy started. The setpoint (21 °C) was, therefore, not attained by the start of occupancy in most of the offices on Mondays, though the temperatures were all still above 20 °C.

On Fridays, in the radiator cases (lighter grey on the graphs), the setpoint was attained by the given time. In the UFH cases (darker grey), the heat-up time was significantly under-estimated. The given algorithm resulted, nevertheless, in an overshooting of the setpoint temperature during the day and setpoint tracking with much larger fluctuations than in the radiator cases. The UFH algorithm, therefore, did not successfully carry out the setbacks, as comfort had not been ensured.
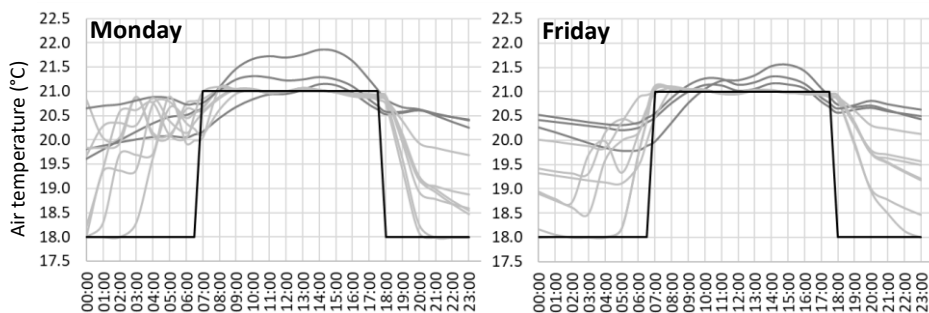

Figure 26. Temperature performance during heat-up times over the first 12 hours on Monday, 4 January (left), and Friday, 8 January (right). Darker grey: UFH, lighter grey: Rad, black: temperature setpoint.

3.1.2.2 FED reduction with temperature setbacks

Total energy consumption results are shown Table 11 (for the meaning of the scenario abbreviations, see Table 4). We can see that energy consumption for heating the supply air was almost the same for all the modern and standard cases. The slight differences were due to differences in return air temperature and thus recovered heat. In the setback cases, the consumption for air heating was 1 kWh/m^2/y higher than in the constant setpoint case. Consumption was zero for old buildings, as the supply air was not being heated. For space heating, there were three clear levels according to the energy-efficiency of the scenario, as expected. Radiator cases consumed slightly less energy than UFH cases, and the lighter cases slightly less than the corresponding massive ones. Higher consumption resulted from higher average temperatures due to imprecisions in temperature control.

The reduction in total energy consumption resulting from constant control of intermittent heating is shown in Figure 27. All the observed cases resulted in an

approximately 4%–7% reduction in heating consumption. The differences in absolute reduction, however, were significant, as the net heating demand in each of the cases ranged from 29 to 207 kWh/(m²y). For the old buildings, the reduction was, therefore, about 12 kWh/(m²y), while in the south-oriented low energy cases, the reduction was only 1 kWh/(m²y).

In all the heavy construction cases, setback efficiency was marginally less than that in the corresponding light construction cases. In these latter cases, there was, in fact, less consumption to begin with and larger reductions as well. In the floor-heating cases, consumption had been reduced more than in the comparable radiator cases. In the over-dimensioned radiator cases, consumption was the same or less than that in the standard sized radiator cases, but the reduction was larger.

Table 11. Energy consumption results in the constant and setback control cases

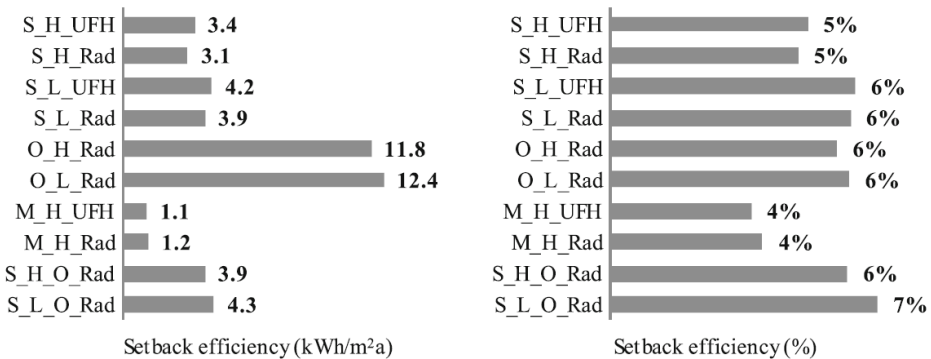|	Space heating [kWh/(m² a)]		Air handling unit [kWh/(m² a)]		Total [kWh/(m² a)]	
	21 °C	Setback	21 °C	Setback	21 °C	Setback
S_H_UFH	52	47	15	17	68	64
S_H_Rad	48	44	16	17	65	62
S_L_UFH	53	47	15	17	68	64
S_L_Rad	48	43	16	17	64	60
O_H_Rad	207	195	0	0	**207**	**195**
O_L_Rad	206	194	0	0	**206**	**194**
M_H_UFH	17	15	14	15	*31*	*30*
M_H_Rad	15	13	15	16	*30*	*29*
S_H_O_Rad	49	44	16	17	65	61
S_L_O_Rad	48	42	16	17	64	60

Figure 27. Energy performance of intermittent heating; absolute difference between given case and corresponding reference case on the left and relative efficiency on the right.

3.2 Simplification effects in modelling UFH control

In this chapter, UFH control is analyzed in more detail. In the first part, optimized PI parameters for UFH are compared with default PI parameters used in BPSs. The second part includes an estimation of the effect of modelling UFH control with different levels of detail related to energy and thermal performance as well as mass flows in short time scales. This section also describes the development and testing of wax motor models.

3.2.1 Effect of optimal PI parameters

In total, 68 PI parameter value pairs were obtained. Each of these combinations is represented in Figure 28 as a point plotted on a log10-log10 plot according to method, model, and dataset. In Figure 28 (a), the parameter estimation method is represented by the marker shape, and the model group, by the marker color. Logarithmic scaling reveals a roughly linear tendency in parameter estimation results: the lower the integration time the higher the proportional gain.

For a very small proportional gain, the integration time deviates significantly from the linear behavior shown when using the log10-log10 scale. The reason for this is partly revealed by Figure 28 (b), where we can see that these four cases had been calculated or optimized for March, in fact for the south-oriented Room 6, meaning that solar peaks were severe, and almost no heating was needed. This is why parameter values for these cases were so exceptional.

In Figure 28 (b), we see a clear separation between parameter values according to outdoor conditions. The first group (in grey) were calculated assuming constant outdoor temperatures and no solar radiation, the second group, using dynamic outdoor temperatures and realistic solar irradiation. As can be seen, there is a clear separation between the March and Jan/Feb periods, and it can be concluded that more solar gains caused the value of the K parameter to decrease and ti to be longer, while dynamic outdoor weather with normal solar gains generally increased the values of both parameters. In the optimal cases, combinations closer to the dynamic climate values were optimized for the variable setpoint, the lower values for the constant setpoint.
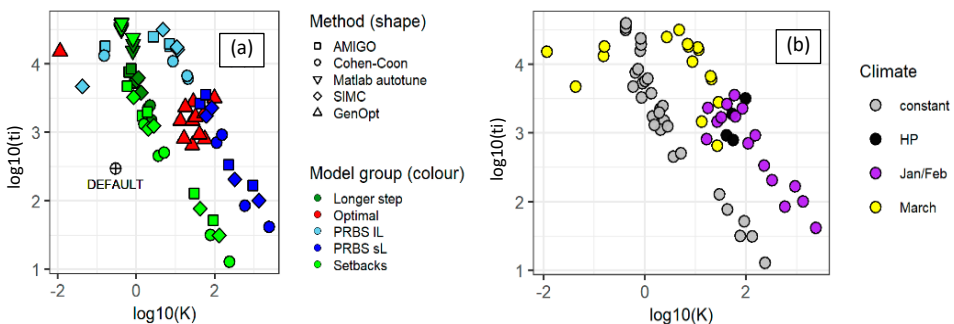

Figure 28. (a) All estimated PI parameter K and ti value combinations labelled according to calculation method and underlying model; (b) all combinations labelled according to outdoor conditions in input data (HP stands for heating period).

3.2.1.1 Temperature performance

Each parameter combination resulted in different air temperature profiles and PI output signal profiles. Four examples of both the temperature and PI output profiles for constant setpoint cases are shown in Figure 29 and four examples for variable setpoint cases for the Estonian home (Room 6), in Figure 30. In both figures, the Jan/Feb week is shown on the left and the March week, on the right. The selected parameter value combinations are ordered according to their log10 ratio. The first is the value combination that had the lowest log10 ratio, then comes the IDA ICE default combination (0.3/300), then the one that resulted in optimal energy consumption (18/2300, see section 3.2.1.2), and finally, the combination with the highest log10 ratio.

In Figure 29, the graphs on the left (Jan/Feb) suggest that it was relatively easy to maintain a constant setpoint when there were no solar gains. The small fluctuations were largest when a very small proportional gain ($K = 0.012$) with a large integration time was applied. The PI output signal readings (in black) show that the controller changed the signal too slowly. As a result, the signal remained almost constant throughout the day and even throughout the week. For the same reason, temperatures dropped below the constant setpoint in March, as shown in the graphs on the right in Figure 29, and setpoint tracking was poor in the variable cases.

Figure 29 also shows that in the constant setpoint cases, the 2400/42 combination most effectively maintained the constant setpoint. The PI output signal for this combination, however, changed the most rapidly, due to a large proportional gain and relatively short integration time. This kind of switching reduces the life span of most devices and would not be acceptable in practice. It may also be impossible to implement given the delays described in section 2.3.2. The use of optimal parameters (18/2300) led to a very similar temperature performance. In this case, the proportional gain was still large, but the integration time was longer, and as a result, the signal was a bit smoother. When the integration time was long, as in the 18/2300 case, heating started earlier and stopped sooner than in the shorter integration time default case (0.3/300), as clearly shown in the graphs for the week in March. The signal also changed more rapidly in this case due to a larger gain.

The variable setpoint cases in February (on the left in Figure 30) show that in cold weather with low solar gains, the 24 °C setpoint peaks had not been reached due to the short duration of the setpoint increase. The PI signal was 1, however, during these times, indicating that the heater was fully on, as intended for load shifting. The same graphs also show that controllers with the 18/2300 and 2400/42 combinations both effectively maintained a lower setpoint. In the latter case, however, it frequently switched on and off and had almost no other state. In March, solar peaks governed the temperatures. The March graphs (on the right in Figure 30) also show, however, that the heating had been turned on, intensifying the overheating.

All the cumulative temperature and control profiles over the heating period are shown in Figure 31. For the PI signal, only R6 is shown, as the profiles for the two rooms are very similar. The switching behavior noted before showed a clear dependency on the log10 ratio of the PI parameters. The higher the ratio, the more abrupt the changes, reflected in behavior on the cumulative graph close to on/off signals. The higher temperatures at the high-temperature end were dependent on the *ti* value, while the low-temperature end seemed to be more dependent on the *K* value. Energy consumption for a parameter combination was, therefore, mostly dependent on the *K* value, and whether there was over-heating due to disturbances was more dependent on the *ti* value.
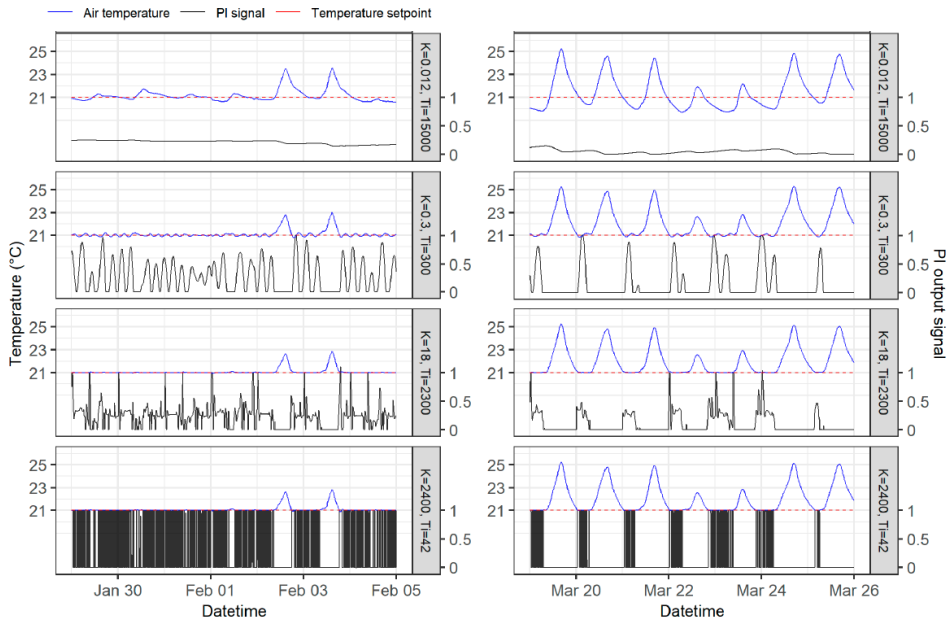
Figure 29. Air temperatures and PI output signals for the constant setpoint case over one week in January/February (left) and one week in March (right) for four pairs of parameter values.
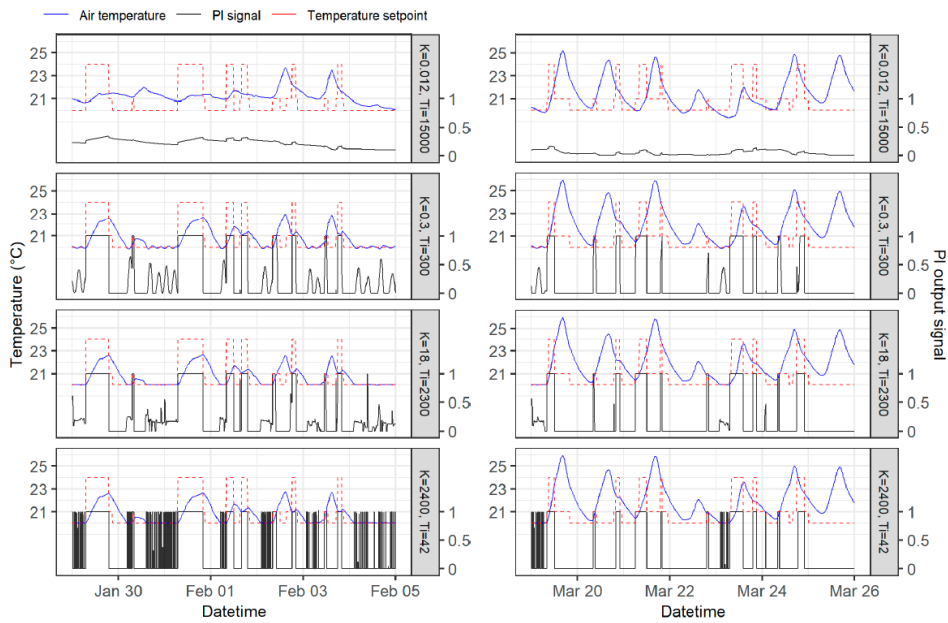

Figure 30. Air temperatures and PI output signals for the variable setpoint case over one week in January/February (left) and one week in March (right) for four pairs of parameter values.
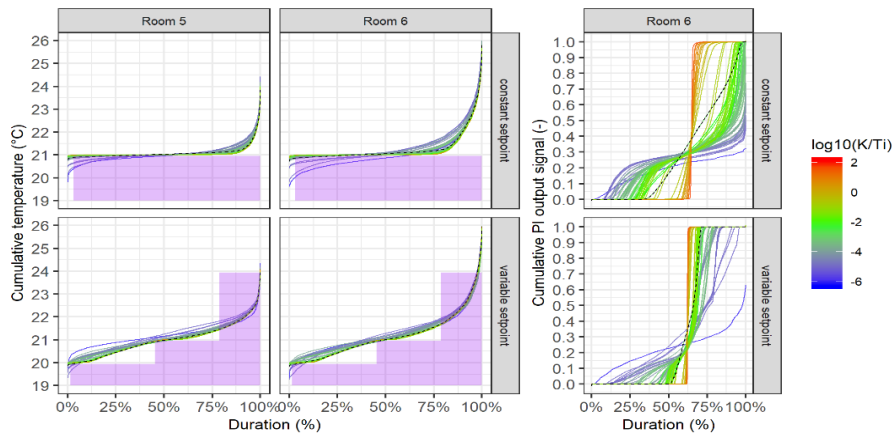
Figure 31. Duration curves for the heating period before temperature shifting. Curves for temperatures on the left and for PI output signals on the right. The purple area indicates the zone below the setpoint, and the black dashed lines show the results obtained using IDA ICE default parameters.

Some of the parameter combinations did not achieve the required temperature setpoint, and some resulted in temperatures above the setpoint. At the high temperature end, in particular, there was a clear difference in results for rooms R5 and R6, as can be seen in Figure 31. This was due to the room orientations, as south-west facing R6 experienced more solar gains than the north-west facing R5. As stated in section 2.3.1.4, setpoints were shifted in all cases so that temperatures would reach the required setpoint most of the time. The shift values were below 1 K, and they differed for R5 and R6 as well as for the constant and variable setpoint cases. After the shifting, all temperatures reached the defined setpoints over about 95%–97% of the heating period. The shifts are shown together with the energy consumption evaluations in Figure 32.

3.2.1.2 Energy consumption

Energy consumption results after setpoint shifting are shown in Figure 32. In most of the variable setpoint cases, less energy was consumed than in the constant setpoint cases, as average room temperatures were lower. The setpoints were also higher than those in the constant setpoint cases for some periods, but coincidentally, the higher setpoint temperatures often occurred during the day, when there were also solar gains, and thus influenced heating energy usage less than expected. In the constant temperature cases, a clear optimal value emerged between −3 and −1 of the log10 ratio of K/ti. In other words, in optimal cases, the K value was 10 to 1000 times smaller than ti.

The horizontal lines in Figure 32 indicate the energy performance of the benchmark on/off cases with different deadbands after setpoint shifting. From top to bottom (yellow to blue) the corresponding deadbands are 1 K, 0.5 K, 0.16 K, and 0.05 K. The color indicates the temperature shift correlating with the deadband. Optimal PI parameter value combinations resulted in energy consumption even lower than the lowest of the on/off cases with an unrealistically small dead band. In the case of the commonly used 0.5 K deadband, 2–3 kWh/m²/year more energy was consumed than in the PI cases with the variable setpoint. In the case of the constant setpoint, the lowest PI results were as high as 7 kWh/m²/year or 9% lower than results in the on/off case with the 0.5 K deadband. Excluding the cases with extremely poorly performance, total variation in energy consumption was more than 10 kWh/m²/year or 12% of consumption in the 0.5 K on/off case with a constant setpoint.

The parameter value combinations having a log10 ratio in the optimal range of −3 to −1 are shown in detail in Table 12. According to this data and data for the rest of the parameter value combinations in the Appendix of publication II, the GenOpt method produced suitable parameter value combinations in almost all tested cases. On shorter timescales, the Cohen-Coon method produced parameter values in or close to the optimal region in cases with lower solar gains (R5 and the Jan/Feb week). 6-h setpoint setbacks and PRBS also produced good results. PI parameter values obtained for the March period using the PRBS lL model and in one case using the Optimal method resulted in extremely high energy consumption. Most methods resulted in parameters that reacted more slowly than optimal over the March weekend, as almost no heating had been applied due to high solar gains. In this case, only the use of the PRBS method resulted in good parameters, while it induced additional heating.
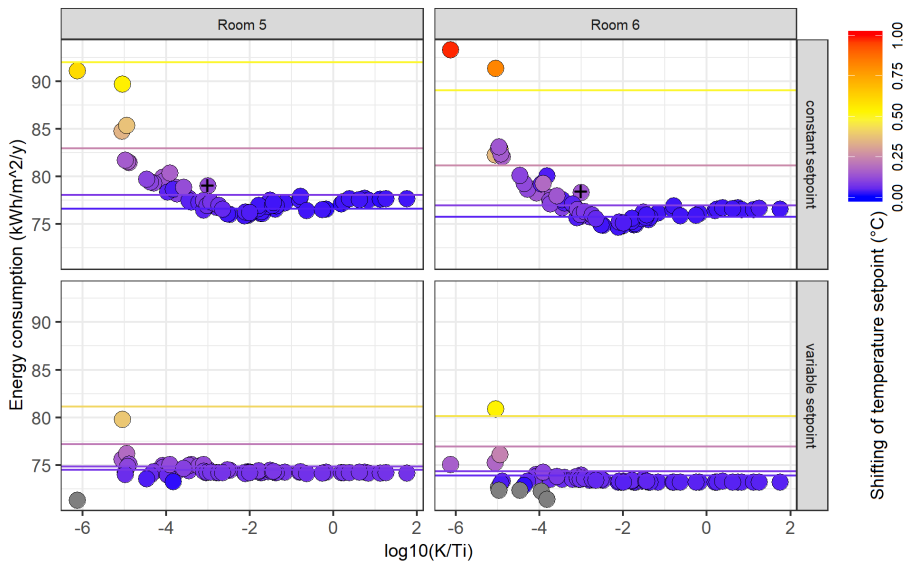

Figure 32. Influence of the PI parameter log10-ratio on energy consumption; colors indicate the setpoint shift, grey signifying that the temperature setpoints decreased (shift below 0). Horizontal lines indicate the on/off cases with different deadbands. The IDA ICE result using the default parameter ratio 0.3/300 is indicated with a black "+" on the constant setpoint markers.

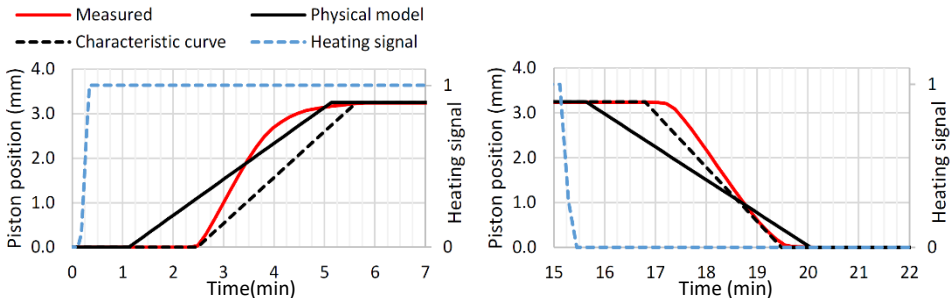| K	Ti	Model	Method	Climate	Setpoint	Room	Total Length
18	2300	-	GenOpt	TRY, Jan/Feb week	variable	R6	Inf
13	1500	-	GenOpt	TRY, March week	constant	R5	Inf
28	2800	-	GenOpt	TRY, March week	variable	R5	Inf
21	6200	11	Cohen-Coon	TRY, March weekend	PRBS	R5	2 days
20	6700	12	Cohen-Coon	TRY, March week	PRBS	R5	7 days
27	1500	-	GenOpt	TRY, Jan/Feb week	constant	R5	Inf
16	820	-	GenOpt	TRY, Jan/Feb week	constant	R6	Inf
32	1700	-	GenOpt	TRY, Jan/Feb week	variable	R5	Inf
5.2	510	4	Cohen-Coon	Const	6-h setback	equal	1.5 days
3.7	460	2	Cohen-Coon	Const	24-h setback	equal	6 days
42	2700	9	AMIGO	TRY, Jan/Feb weekend	PRBS	equal	2 days
27	650	-	GenOpt	TRY, March week	constant	R6	Inf
54	1900	-	GenOpt	TRY, heating period	variable	R5	Inf
2.8	1300	4	SIMC	Const	6-h setback	equal	1.5 days
59	3600	10	AMIGO	TRY, Jan/Feb week	PRBS	R5	7 days
61	1800	9	SIMC	TRY, Jan/Feb weekend	PRBS	R5	2 days
41	930	-	GenOpt	TRY, heating period	constant	R6	Inf
2.4	1500	1	Cohen-Coon	Const	Ideal step	equal	60 days
2.0	1100	2	SIMC	Const	24-h setback	equal	6 days
85	2300	10	SIMC	TRY, Jan/Feb week	PRBS	R5	7 days
55	800	-	GenOpt	TRY, heating period	constant	R5	Inf
98	3200	-	GenOpt	TRY, heating period	variable	R6	Inf
1.6	1300	3	Cohen-Coon	Const	12-h setback	equal	3 days

Figure 33. Piston displacement for the constant characteristic and physical models when the wax was under expansion (left) and contraction (right).

3.2.2 Effect of detailed control modelling

3.2.2.1 Initial test results

Both the physical and constant characteristic models of the wax motor were first calibrated and tested using data with constant period length. The underlying surface temperature modelling resulted in an MAE of 0.67 K. A sample of the piston movement results obtained during heat-up and cool-down processes is shown in Figure 33. The MAE for the characteristic model was 0.05 and for the physical model, 0.07 mm. This was less than 5% of the absolute maximum value but 10% and 8%, respectively, of the average displacement during the test. In the physical model, however, the actuator piston started moving more than 1 minute earlier than measurements showed when the valve was opening or closing. The characteristic curve showed good performance, as it had been fit

to the same data. It showed that the actuator was fully open 5.6 minutes after the heating started and fully closed 4.4 minutes after the heating had stopped. The characteristic times determined were as follows: t_{dead} = 144 s, t_{rise} = 192 s, t_{hold} = 102 s, t_{fall} = 162 s.

3.2.2.2 Models based on extended tests

While the dead time was almost a constant 2.4 min (144 s) during the initial test, it varied over a range of more than 3 minutes during the extended test (see Figure 34). Though initial test results lie in the same range as results in the second test, the constant characteristic curve cannot be universally applied due to a large variance in the dead and hold times. As the optimization of parameters for the physical model was a computationally expensive process, variability was included in the characteristic model by making the parameters time-dependent (see section 2.3.2.2.5). As a result, the empirical model obtained showed an MAE below 10% and an RMSE below 15% for each of the profiles, while the average MAE was 0.041 or about 4%.

Examples of the typical, best, and worst model fits for one hour are shown in Figure 35. The A1 graph shows that shape choice for the empirical model has been suitable. For motor B, the heat-up process differed, but the effective volume flow corrected the slight deviation. In the worst case, the maximum delay between the measured and simulated start of the signal ranged from 1 to 1.5 min. Because this is a close match with the results obtained with the physical model in the simple test, in future the physical model should also be considered.

The volume flow measurements and empirical model were combined to obtain the volume flow model (i.e., the valve curve). A graph showing the relation between both the measured and modelled volume flow and displacement is shown in Figure 36, with the theoretical valve curve indicated with a dashed line and the authority-corrected valve curve with a solid line. The authority-corrected valve curve best matched the measurements when the three-point quick opening characteristics had the following values: d_{bp} = 0.41, $\dot{V}_{bp}$ = 0.5, d_{min} = 0.17. For the region in question, the MAE was 1.02%.

Wax PCM effects do not explain the zero region of the valve curve in Figure 36, while linear displacement was greater than zero, indicating that the wax had already started to expand. It must have been due to some other unmodelled effect(s), such as the spring, different travel length for actuator and valve, or pressure effect. The resulting three-point characteristics also does not look very typical for a quick-opening valve. The estimated authority was, therefore, probably not precise or the different discrepancies between physics and the model behavior cancelled each other out, resulting in a good fit for the final volume flow model.
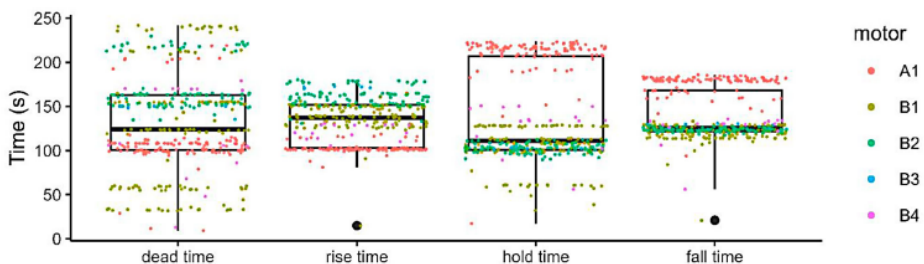

Figure 34. Characteristic times identified in all tests (motors with a valve and without grouped together).
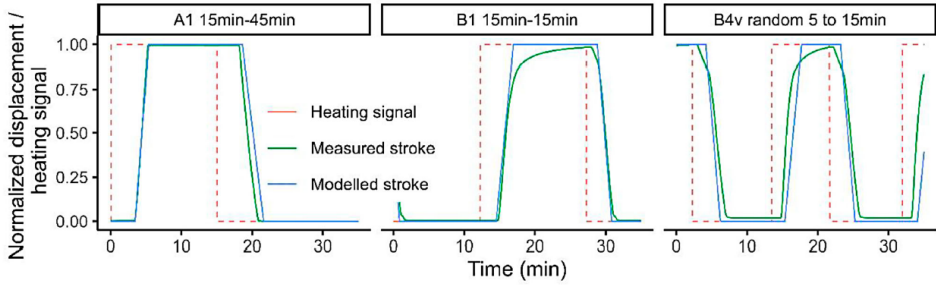
Figure 35. Performance of estimated wax motor model on the prediction of normalized displacement.
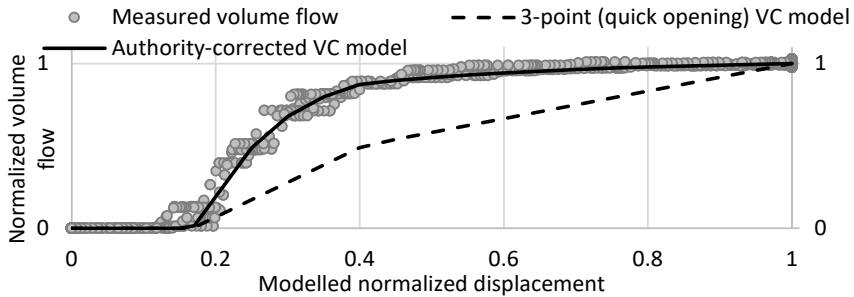

Figure 36. Valve curve modelling process and results; measured versus modelled volume flows.

3.2.2.3 Performance overview

In section 2.3.2.4, several control scenarios were defined in IDA ICE to quantify the impact of the wax actuator and other elements of the control process on energy performance and temperature control accuracy. In this section, we compare the results of the energy performance simulations. As should be recalled, the "0" case was the business-as-usual case, i.e., a simulation model with close-to-ideal control of the UFH system. This ignores the modelling of both wax motors (WM) and exact valve curves (VC), while PI control and on/off thermostats were represented using the default parameter values commonly used in BPSs. The other scenarios used adapted control parameters (CP) and then, one at a time, added a time delay (D) to the input signal, a VC, modulation control (MC), and finally, a WM. The level of modelling detail was thus gradually built up from the ideal to the WM.

To be able to compare energy consumption, air temperature setpoints were shifted so that 20% of the operative temperature remained below 21 °C (see section 2.3.2.4). The applied setpoint shifts for all cases and the resulting energy consumption are shown in Table 13. Temperature fluctuations are characterized by the air temperature shift from 21 °C (dT) and the MAE of the air temperature MAE(T). Q_h represents floor heating energy consumption per square meter of floor area per observed week, and its relative difference was calculated as $\Delta Q_h = (Q_h - Q_{h,w})/Q_{h,w}$ [%] for the given week. This difference represents the under- or overestimation of consumption in the given case, relative to the most detailed case, O_WM or P_WM.

Table 13. Temperature fluctuation and energy consumption results for all cases; air temperature setpoint deviations dT are from 21 °C, and energy consumption results Q_h are expressed in kWh/m²/week.

ID	Temperature fluctuations				Energy consumption			
	January week		February week		January week		February week	
	dT	MAE(*T*)	*dT*	MAE(*T*)	Q_h	$\Delta Q_{h,w}\%$	Q_h	$\Delta Q_{h,w}\%$
O_0	0.49	0.597	0.33	1.092	2.55	5.71%	2.42	4.84%
O_CP	0.05	0.195	-0.03	0.682	2.42	0.36%	2.32	0.41%
O_D	0.05	0.2	-0.03	0.691	2.41	-0.12%	2.32	0.25%
O_VC	0.05	0.2	-0.03	0.69	2.41	-0.12%	2.32	0.21%
O_WM	0.06	0.215	0	0.628	2.41	0.00%	2.31	0.00%
P_0	-0.03	0.128	-0.08	0.637	2.41	0.08%	2.28	0.68%
P_CP	-0.09	0.033	-0.13	0.447	2.37	-1.63%	2.20	-2.75%
P_D	-0.09	0.038	-0.13	0.453	2.37	-1.67%	2.20	-2.71%
P_VC	-0.1	0.044	-0.14	0.462	2.37	-1.67%	2.21	-2.54%
P_MC	-0.07	0.149	-0.11	0.589	2.40	-0.48%	2.24	-0.80%
P_WM	-0.05	0.150	-0.08	0.676	2.41	0.00%	2.26	0.00%

The table shows that the addition of the wax motor alone to the preceding level of model detail did not appreciably change energy consumption. There were larger changes, for example, when correcting parameter values or adding modulation. The whole process of adding modelling detail, nevertheless, led to striking changes in both temperature fluctuation and energy consumption results. The changes are discussed in detail in the following sections.

3.2.2.4 Thermal performance

The setpoint changes were negative for PI, but close to zero or even positive for on/off (Table 13). This means that the operative temperature stayed above the desired 21 °C most of the time, even after the air temperature setpoint was lowered below 21 °C for PI. In both cases, the operative temperature and air temperature had similar fluctuations, though with an offset. In the on/off case, fluctuations were much larger, and the setpoint had to be shifted higher. An example of this behavior is shown in Figure 37 (dotted lines indicate air temperature setpoint, solid lines, air temperature, and dashed lines, operative temperature).

In the on/off case, the source of temperature fluctuations was the deadband (T_{Db}) (see Table 13). The setpoint change and MAE for the O_0 case (T_{Db} = 2 K) were much higher than those for the other cases (T_{Db} = 0.5 K). While the MAE for on/off in January was generally around 0.2 K, it was around 0.6 K for the O_0 case. Due to symmetric fluctuations around the air temperature setpoint, the MAE was close to 60% of the deadband in all on/off cases. Fluctuations in the PI cases were induced by non-optimal parameters as well as modulation. While non-optimal parameters altered the continuous signal, modulation translated it to an on/off-like signal. The theoretical development of a control signal for P_WM was described in Figure 20. In Figure 38, a sample of the simulation outputs helps to visualize this translation of the PI output signal to a valve curve output.

Due to this translation from a continuous signal to a binary one, the PI cases with modulation, P_MC and P_WM, had MAEs close to those of the on/off cases from O_CP to O_WM. In Figure 39, the temperature fluctuations for the P_WM and O_WM cases are shown together with those for the benchmark cases P_0 and O_0 and the improved parameter cases P_CP and O_CP. Significantly higher fluctuations occurred with a greater

deadband in the O_0 case, and a smaller deadband in the O_CP case and onwards improved on/off control remarkably. Improved PI parameters resulted in almost ideal control, while a modulation and WM delay reintroduced the temperature fluctuations. Overall, temperature performance in cases P_0, O_CP, O_WM, and P_WM was similar, and the WM cases could be substituted by using simpler control in the simulations. The similarity between on/off and PI was due to the fact that the PI cases did not perform optimally, while the on/off cases improved significantly beyond the O_0 case. In this work, the adapted deadband for on/off was set at 0.5 K. For this to be possible, the room air temperature sensor must be precise, calibrated, and optimally positioned. The room air also must be ideally mixed. Though the vertical gradient for UFH is small [36], [104], [121], the achievement of one single uniform temperature per zone were clearly still an idealization.
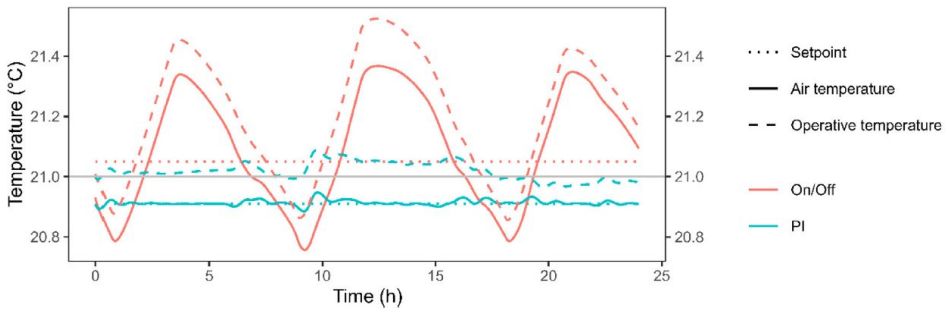
Figure 37. Air and operative temperature comparison for one January day for PI (P_CP) and on/off (O_CP) cases. The grey line shows a 21 °C reference.
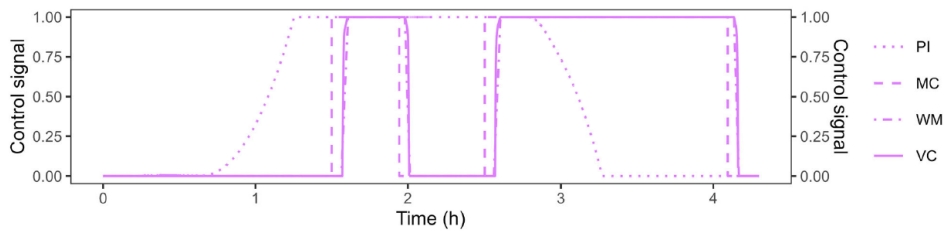
Figure 38. Control signal development for P_WM over a 4-hour period. Outputs for PI (PI), modulation (MC), wax motor (WM), and valve curve (VC) blocks from Table 10.
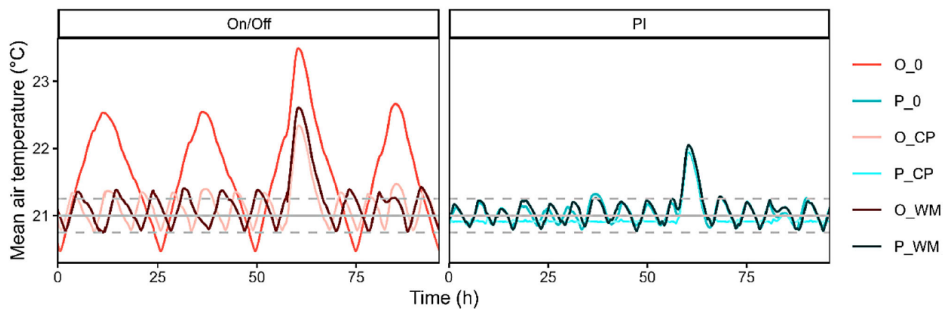

Figure 39. Air temperature fluctuations in January for detailed cases (O_WM, P_WM). For comparison, the default cases (O_0, P_0) and the cases with improved parameters (O_CP, P_CP) (grey helper lines are at 21 ±0.25°C) are also shown.

3.2.2.5 Energy consumption

Energy performance in the given scenarios varied significantly depending on the level of detail. The use of a simple wax motor model instead of continuous control (VC to WM case) resulted in an energy consumption difference of up to 2.5% over the course of the observed weeks (see Table 13). This was consistent with the literature (e.g., see [165] and its references). Over the course of a year, this would have a sizeable impact on energy efficiency.

Though the short delays and modelling of the valve curve had less of an impact on total energy performance, these resulted in different load profiles (see the next section). We found that both the choice of parameters for on/off and PI and the modulation modelling in the PI case had a significant impact. All on/off cases, except the most detailed case (O_WM), overestimated energy consumption, while all the PI cases, except the P_WM case, underestimated energy consumption.

In most cases, lower energy consumption was achieved due to smaller temperature fluctuations, which made a lower temperature setpoint possible. The step from "0" to "CP" saw a reduction in energy consumption of over 3.4% over the week in February due to the use of improved PI parameters. The reduction in temperature fluctuation due to the use of optimal PI parameters was offset by an increase in fluctuations due to the conversion of the continuous PI output to binary values, so in the step from P_VC to P_MC and with the wax motor delay, in the step from P_MC to P_WM. The step from "0" to "CP" resulted in a 2.5% higher increase over the week in February than the step from "VC" to "WM", with the addition of modulation and WM. This highlights the importance of optimal PI parameters. The parameters optimized for business-as-usual conditions, however, did not perform optimally when used with a modulation approach. The optimized parameters for continuous PI control (without modulation) could thus potentially be used for 0–10 V actuators, while the coupling of modulation with the optimization of parameters requires further research. The PI parameters specifically adapted to the applied modulation could potentially improve performance (see Appendix D of III).

In any case, for the most part, PI scenarios consumed less heating energy than the corresponding on/off cases. When on/off and PI business-as-usual cases are compared, it can be seen that PI was almost 6% more efficient for both weeks (2.41 vs. 2.55 and 2.31 vs 2.42), though there was practically no difference in the WM cases. The difference between O_WM and P_WM was generally smaller than that between the other corresponding cases, holding at 0.2% in January and 2.1% in February. For the „CP" through „VC" cases, it approached 2% in January and 5% in February. Substituting PI with WM modelling with on/off, as suggested for temperature fluctuations in section 3.2.2.4, would, therefore, not provide the same energy performance. The smallest difference was that between O_VC and P_0.

3.2.2.6 Load dynamics

In all the business-as-usual cases, energy consumption had been overestimated, keeping results on the safe side regarding system design. It was clear, however, that there were different volume flows in the circuit in the business-as-usual and the WM cases. Both overestimation of energy consumption and inaccurate mass flows may be considered non-conservative for other applications, such as grid balancing, structural thermal storage, etc.

For a better understanding of the progression of energy consumption, cumulative mass flows for the January week are shown in Figure 40. On the on/off graph, O_0 stands

out from the other on/off cases. On the PI graph, the distribution of mass flows vary for all cases, in particular, "CP", "D", and "VC". These cases otherwise performed similarly, differing by no more than 0.01 K in setpoint, 0.015 K in MAE(T), and 0.5% (0.01 kWh/m^2/week) in energy consumption over the given week. This means that adding a 2-minute delay to the input signal and correcting the valve curve did not have a significant impact on air temperature and energy performance. It did, however, change mass flow dynamics. Using the same control parameters with a different mass flow profile affected temperature performance and energy consumption. P_MC and P_WM had mass flows similar to those of the binary on/off cases, while the "CP" and "D" cases had mass flows mostly at about the 25% level. P_0 and P_VC cases were between the two extremes, with close to linear flow.
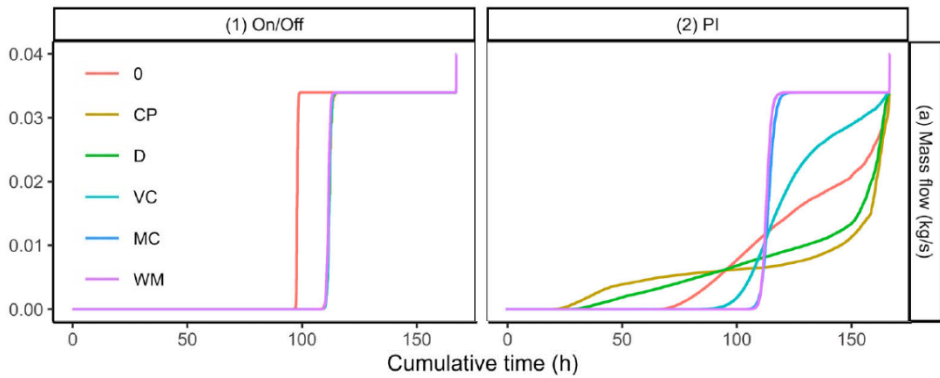
Figure 40. Cumulative mass flow performance over the week in January.

4 Discussion

4.1 Summary of influence on FED

Dynamic control of low temperature heating applications can significantly affect both thermal comfort and energy consumption in buildings. The potential effects of different control algorithms and control modelling were analyzed. In Table 14, FED and PED deviations from the corresponding benchmark are shown for all cases analyzed in previous sections. The optimization of FED for heating involves intermittent heating and the maintaining of low temperatures for as long as possible. We have shown that the temperature reduction time and energy savings for a given room are closely related [43]. For comparability, the benchmark had to be at the same comfort level as the observed scenario. In case of discrepancies in temperature setpoints, the share of time at the same comfort setpoint was given. If the difference had not been quantified, "comfort can differ" was added at the end.

PED and FED reductions are intrinsically similar in the case of constant or low variability PEF, but in the case of dynamic PEF, these could differ significantly. When PEF was variable, the potential to minimize the PED of radiator heating was demonstrated in this work. For different building standards, PED could be reduced by 2% to 15%, though FED increased by 16 to 58% in the same cases. The benchmark for PED reduction relied on a dynamic optimal temperature with a maximum of 22 °C that had to be reached 12% of the time (zone occupied but occupants inactive). The analysis in [1] shows that when applying the EnEV 2009 building standard, FED reductions achieved when moving from a constant 22 °C level (see R1 in section 2.2.1.4) to the MPC-controlled O2b and R3 scenario were 46% and 59%, respectively. While control optimization based on market price is the conventional approach, optimization based on PEF presents a solution that also accommodates tariff-based prices. Dynamic PEF has previously been taken account of in PED reduction with heat pumps [81], [130] but has been rarely used in the optimization of heating control.

In the setback analysis with pre-heating control, FED could be lowered by 4%–7%, depending on the energy efficiency level and thermal mass of the construction. The are many reasons for the reductions being lower than those seen in most of the literature. The main departure from the literature is the energy-efficiency level, as with lower level, temperatures could drop to as low as 7 degrees on the weekends [27]. Earlier sources use airflows similar to those in this study, but use outdoor air temperature for ventilation supply instead of the constant supply temperature [26]. Indoor temperatures were different due to different climates and customs, and thermal comfort was not ensured during occupancy times in all cases [25], [70]. The low reduction results, however, do not agree with some of the literature. The reduction should, for example, be larger in the Estonian climate than in the German climate [28]. A higher FED reduction should also have resulted from the selection of an office profile representing a maximum reduction scenario given the occupancy profile [29], [43]. Relative to the R1 and R3 comparison in the PED reduction analysis, the occupancy time during pre-heating control was 33% longer due to a less precise pre-heating calculation procedure. Better estimation of time constants could theoretically improve the savings potential. In the pre-heating case, low heating power and lower infiltration and ventilation rates were other factors that may contribute to lower reductions.

Findings on sensitivity across building standards agree with the previous literature [27], [59], [62], which showed that setback heating yields less FED savings in well-insulated buildings, while a long time constant poses a challenge to this approach. This contrasts with the impact of PED optimization, where load shifting would be effective, especially in the PH case. The load shifting potential of massive construction makes it possible to stabilize the comfort level. When intermittent heating is applied, however, the heat-up times are much longer, and the extra losses incurred during unoccupied hours thus reduce the potential energy savings.

Table 14 also shows the influence optimized PI parameters had on the energy consumption in comparison with IDA ICE default parameters (marked with "+" in Figure 32). The variation was –5% to +7% in the constant temperature setpoint case. Very poorly performing parameter value combinations were omitted here; otherwise the consumption increase would have been as high as 19%. In the variable setpoint case, the effect was smaller (-3% to +4%), while during activation times, PI activated full power heating, as commonly happens at significant setpoint changes.

The given range of influence of PI parameters is applicable only when UFH has continuous volume flow control. The need for modulation may alter the result. Increasing the level of detail in the control modelling (after changing the PI parameters and on/off deadband) resulted in a change of –0.4% to +2.6% in FED. 1.2% of this change can be attributed to the modulation and –0.4% to 0.9%, to the wax motor modelling. The modulation algorithm was fixed; changing it could potentially have significant effect on the energy consumption.

Table 14. Summary of the analysis of the influence of different algorithms and modelling methods on FED (and PED if marked).

Control description	Influence on FED (and PED)	Benchmark
PED optimization with MPC (O2b) and dynamic PEF (I)	FED +16% … +58% PED -15% … -2%	R3 (variable) comfort was similar
Temperature setbacks (33% at 21°C) with pre-heating control (V)	-7% … -4%	Const 21°C, comfort can differ
PI parameters, variable setpoint (II)	-3% … +4%	Default PI, variable (20% of time higher level, but not reached)
PI parameters, constant setpoint (II, III)	-5% … +7%	Default PI, const. 21°C +shifted
On/Off with 2K / 0.5K deadband (II, III)	+0.4% … +6%	Default PI, const. 21°C +shifted
Control process components, incl. wax actuator (excluding CP) (III)	-0.4% … +2.6%	Default PI or on/off, const. 21°C +shifted

4.2 Summary and suggestions for UFH control modelling

UFH is a common solution in new buildings but is a system that is also difficult to control. The variety of available advanced control algorithms and scarcity of information on low-level control in the literature raised the question about how low-level control might influence high-level control methods.

Detailed modelling of UFH control has not been common, as the thermal time constant of the system is tens of hours long, whereas differences in control are mostly in minutes. Most control details would, therefore, not significantly affect the results of annual BPSs. In the results presented above, it can, however, be seen that changing PI

parameters can increase energy consumption by up to 7%, and if extremely unsuitable parameters are chosen, the increase can reach as high as 19%. In the variable setpoint case, the increase in energy consumption was smaller, reaching 4%. In low power heating cases, therefore, the MPC approach applied in section 3.1.1 would only be slightly affected by a varying of PI parameters. The effect could potentially be much greater when using the setback approach, as constant temperatures would be maintained for a longer period.

Suitable PI parameters could be found by applying simple tests, such as 6-h setbacks applied during the night or PRBS heating activation over the weekend. For a constant setpoint, parameter values resulting in nearly ideal control were found, something that has not been reported before. The optimal ratio of gain to integration time in seconds was found to be between 1e-3 and 1e-1. Default PI parameters for temperature controllers, such as 0.3/300 and 1/540, that have ratios from around 0.001 to 0.002 are the lower end of this range [166]. Parameters obtained at different outdoor conditions clearly diverged, suggesting in accordance with literature that PI parameters should be adapted accordingly [93]. Optimized PI parameters were able to reduce energy consumption; however, if optimization was not done, default parameters for annual simulations would be able to perform well enough in practice. For dynamic operation, the available power in nZEBs is often insufficient for the parameters to be able to make a significant difference, since after each temperature setpoint change, PI controllers generally function in on or off mode.

In practice, there are other factors that can affect the performance of control algorithms, such as actuators, valves, and control signal alterations. While the effect of control parameters such as PI parameters and the on/off deadband proved to be quite significant, the effect of short signal delays turned out to be very small. While valve curves also had a low impact on energy performance, they had a significant impact on the dynamics of volume flows. The variations in volume flow could also potentially affect heat pump efficiency. It was observed that also wax motors can influence volume flows in the system as many UFH and radiator motors on the market are modulating. Continuous motors exist but are less common and more expensive.

We tested three different wax actuator models: a physical model, a characteristic model, and an empirical model. The last is essentially a characteristic model with time-dependent parameters. The first two, both previously known models, were tested using a simple periodic test. While both models performed well with MAEs below 10%, the physical model was difficult to parametrize. After a broader set of tests, it became clear that a constant characteristic model could not be universally applied, as characteristic times vary significantly. A new empirical model was, therefore, proposed, one which would make similar performance possible without known physical parameters. The new empirical model also resulted in a fit with an MAE of 10% using various heating profiles.

The effect of modelling a wax actuator in BPSs of energy consumption and temperature fluctuations had not been analyzed before. Though the effect of the wax motor alone on energy performance was found to be very small, there was a significant modulation effect. The wax motor also induced a time delay of up to 7 minutes on the opening of the valve. Manufacturer data sheets typically report 3–5 min positioning times [91], [92], [167], [168]. The longer times occurred after the wax had cooled down to room temperature and probably completely solidified. This can usually be avoided by occasionally heating the wax for a short time and thus making a warm start possible.

Modelling the wax motor delay and modulation may be important for algorithms making power-grid-driven decisions or when volume flow in time steps shorter than the hourly average is of interest, e.g., when making calibrations with measurements taken in intervals of less than 10 minutes. Modelling of the wax motor is often not necessary, as modelling a longer time delay and adding modulation with on/off control could make similar performance possible if a suitable deadband is chosen and the temperature setpoint is shifted. Non-ideal PI parameters and all further control signal alterations, including the wax motor, could then be lumped together.

4.3 Future work

The PED and FED reduction algorithms in this work illustrate some of the potential that advanced control can offer. There have been significant advancements in this area reported in the literature, and this work does not serve as an overview of it. The developed algorithms, however, have the advantage of being simple enough to be easy to apply in any building, requiring very little data and expert knowledge. While the detection of occupancy can be challenging, methods for this have been advancing rapidly. The dynamic PEF applied has also not been widely used, and the application of different dynamic PEF profiles with varied control algorithms could lead to interesting results. Here, the PEF applied was a German electricity market target of 80% for RES. Fluctuations in PEF were rapid and had a large amplitude (up to 2.5). At both a lower RE share and 100% renewable power, there would be less variability and a smaller reduction in PED. Large fluctuations are, however, characteristic of a larger RE share when the power grid is not fully renewable. In addition to the RES in the power grid, the dynamic PEF could also characterize district heating systems with mixed resources or other energy production systems with variable RE share. The dynamic control of heating in combination with dynamic PEF can have a significant impact on primary energy demand in future. The algorithms applied and their precision, therefore, deserve further analysis.

The main novelty of this work lies in the level of detail of the control modelling. A physical wax motor model was parametrized, and an empirical model was developed, and tested for UFH. The proposed empirical model performed well over heating cycles of 10–15 minutes. If the heating period was, however, shorter, so that the valve did not fully open, the model was not applicable. The physical model was needed if the PWM was shorter than the FAT of the motor. The physical model would make it possible to model not only 24 and 230 V wax motors but also 0–10 V wax actuators, which use fast modulation of the PTC heating signal (24V/230V) to achieve the required control load. Though the necessity of using 0–10 V motors in UFH manifolds should first be assessed, since with the quick-opening valves currently in use, the valve curve converts any control signal to a control close to on/off. Application of the physical model requires additional information about the materials used and the dimensions of the wax actuator. This would entail material testing or obtaining detailed manufacturer datasheets. Numerical optimization can also be carried out (see section 2.3.2.2.4). Running the optimization with different sets of variables and fixed parameters as well as different ranges, orders, and initial values, may, however, lead to different results. Further analysis involving a much larger dataset would, therefore, be required. In addition to UFH, wax motors are also used in other applications, such as on fan coil valves and on pressure-independent control valves. The developed wax motor model could be applied in analyzing the detailed control process of these systems as well.

In this thesis, PI parameters were optimized without taking the influence of wax motors into account. When optimizing PI parameters for the constant setpoint case, inclusion of the modulation algorithm and wax motor might alter the optimal result. The definition of the signal modulation should be also included before the PI parameter optimization. In this thesis, a PWM signal was determined hourly to ensure full opening and closing of the valve even at a low percentage of the signal. In the future, this time could be shortened for precision if the physical model is being used. In addition to the single UFH circuit, the interaction of several circuits with modulation control could be analyzed, as PWM [169] can be applied to distribute volume flows across circuits to ensure continuous flow in the manifold, and this may result in performance similar to that with partial flow in each circuit. The potential effect of different control algorithms on heat pump efficiency due to varying volume flows should be also investigated in the future.

As the PI parameters had only a small impact on the dynamic setpoint case, inclusion of the wax motor should not be essential in such a case. It should, however, be determined whether, when a significantly over-dimensioned UFH is being used to accommodate dynamic operation, PI parameters might have a larger effect and thus make precise control possible for constant operation as well.

5 Conclusions

In recent years, control of heating systems has seen significant developments, with advanced control methods such as model predictive control emerging for hydronic underfloor heating and radiators. These developments have, however, often overlooked the low-level details of how heating systems are controlled. This thesis addresses this gap by exploring control dynamics and parameters for low energy heating applications. This work had two main goals:

1) to analyze the energy saving potential when applying simple predictive algorithms for dynamic heating in low energy applications and
2) to analyze the effect of detailed control modelling on building performance simulation results in underfloor heating applications.

The following conclusions can be drawn regarding the former goal:

- The model predictive control algorithm developed can significantly reduce the average primary energy factor for energy consumed. Relative to rule-based control, primary energy demand can be reduced by up to 15% in the case of Passive House buildings.
- In modern buildings with slow-reacting heating systems, the relocation of final energy consumption was only possible in small absolute amounts. The use of setback control to reduce final energy demand led to a maximum savings of only 4%.
- For buildings complying with a low insulation standard, only very small improvements in primary energy efficiency could be achieved using the predictive control model. The absolute amount of relocated final energy consumption, however, was high. Nevertheless, the highest relative final energy demand reduction (7%) was achieved for a standard room with light constructions and over-dimensioned radiators.

Conclusions regarding the latter goal are as follows:

- For the first time in the scientific literature, it was shown that underfloor heating can operate similar to ideal control when using PI parameters;
- Well-performing PI (proportional-integral) parameters can be estimated using a simple automatic test over a single weekend if the test period includes significant heating actions. The test could, for example, be 6-h setbacks applied during the night or weekend-long pseudo-random changes in the setpoint signal. The mean absolute error for the air temperatures relative to the setpoint was well below 0.5 K.
- The best PI parameter combination found for the system analyzed had a proportional gain of 18 and an integration time of 2300 s, which could reduce energy consumption for heating by 9%, when compared with an on/off thermostat controller with a 0.5 K deadband, and by 5%, when compared with the default PI parameters used in IDA ICE simulation software.
- Heating energy consumption when using different estimated (not random) parameters was more than 15 kWh/m^2/year when the setpoint was constant, highlighting the importance of using suitable PI parameters;
- An empirical model of thermo-electric actuators (wax motors) used in HVAC control was developed on the basis of experiments. The model consists of four sub-models for linear segments estimating the length of characteristic times: dead time, rise time, hold time, and fall time. The final model resulted in an MAE for normalized linear displacement below 10% for all tested heating profiles.

- Business-as-usual building performance simulations over-estimated energy consumption by ca 5% for on/off and less than 1% for PI control, relative to the simulations with the most detailed level modelling of the control process. While in the on/off case, temperature fluctuations decreased when a smaller deadband was used, in the PI case, they increased due to modulation. Temperature variations thus critically affected the energy balance.
- Business-as-usual PI control did not reflect actual mass flows in the system. The detailed behavior was similar to on/off behavior, and the PI simulations could thus be substituted with on/off simulations with a small deadband and without the wax motor. The temperature setpoint in these simulations would, however, have to be more than 0.1 K higher than that in the PI simulations to ensure the same performance.

In conclusion, this thesis contributes to an understanding of control dynamics and parameters used in low energy heating applications by focusing on low-level control aspects. Our findings can inform the design and implementation of more efficient and environmentally friendly control algorithms for heating systems, as well as guide future research in this field.

List of figures

List of tables

References

[1] H. Wolisz, "Transient thermal comfort constraints for model predictive heating control," 2018.

[2] European Union, "EU Climate Target Plan 2030 Key contributors and policy Tools," 2020. Accessed: Jan. 16, 2023. [Online]. Available: https://ec.europa.eu/commission/presscorner/detail/en/fs_20_1610

[3] A. Khan, M. Hosseinzadehtaher, M. B. Shadmand, S. Bayhan, and H. Abu-Rub, "On the Stability of the Power Electronics-Dominated Grid: A New Energy Paradigm," *IEEE Industrial Electronics Magazine*, vol. 14, no. 4, pp. 65–78, Dec. 2020, doi: 10.1109/MIE.2020.3002523.

[4] C. K. Tse, M. Huang, X. Zhang, D. Liu, and X. L. Li, "Circuits and Systems Issues in Power Electronics Penetrated Power Grid," *IEEE Open Journal of Circuits and Systems*, vol. 1, pp. 140–156, 2020, doi: 10.1109/OJCAS.2020.3020633.

[5] U. Cetinkaya and R. Bayindir, "Impact of Increasing Renewable Energy Sources on Power System Stability and Determine Optimum Demand Response Capacity for Frequency Control," in *2022 10th International Conference on Smart Grid (icSmartGrid)*, IEEE, Jun. 2022, pp. 396–400. doi: 10.1109/icSmartGrid55722.2022.9848741.

[6] IEA, "Renewables 2022," 2022. Accessed: Jan. 16, 2023. [Online]. Available: https://www.iea.org/reports/renewables-2022/executive-summary

[7] IEA, "Demand Response," Paris, 2022. Accessed: Jan. 16, 2023. [Online]. Available: https://www.iea.org/reports/demand-response

[8] T. Q. Péan, J. Salom, and R. Costa-Castelló, "Review of control strategies for improving the energy flexibility provided by heat pump systems in buildings," *J Process Control*, vol. 74, pp. 35–49, 2019, doi: 10.1016/j.jprocont.2018.03.006.

[9] European Commission, "Factsheet - Energy Performance of Buildings," 2021. doi: 10.2775/03938.

[10] C. Becchio, P. Dabbene, E. Fabrizio, V. Monetti, and M. Filippi, "Cost optimality assessment of a single family house: Building and technical systems solutions for the nZEB target," *Energy Build*, vol. 90, pp. 173–187, 2015, doi: https://doi.org/10.1016/j.enbuild.2014.12.050.

[11] F. Salata *et al.*, "Heading towards the nZEB through CHP+HP systems. A comparison between retrofit solutions able to increase the energy performance for the heating and domestic hot water production in residential buildings," *Energy Convers Manag*, vol. 138, pp. 61–76, 2017, doi: https://doi.org/10.1016/j.enconman.2017.01.062.

[12] A. Thonipara, P. Runst, C. Ochsner, and K. Bizer, "Energy efficiency of residential buildings in the European Union – An exploratory analysis of cross-country consumption patterns," *Energy Policy*, vol. 129, no. March, pp. 1156–1167, 2019, doi: 10.1016/j.enpol.2019.03.003.

[13] IEA, "Heating," Paris, 2022. Accessed: Jan. 18, 2023. [Online]. Available: https://www.iea.org/reports/heating

[14] D. Bienvenido-Huertas, C. Rubio-Bellido, D. Marín-García, and J. Canivell, "Influence of the Representative Concentration Pathways (RCP) scenarios on the bioclimatic design strategies of the built environment," *Sustain Cities Soc*, vol. 72, p. 103042, 2021.

[15]   E. Guelpa and V. Verda, "Demand response and other demand side management techniques for district heating: A review," *Energy*, vol. 219, p. 119440, Mar. 2021, doi: 10.1016/j.energy.2020.119440.

[16]   G. Reynders, T. Nuytten, and D. Saelens, "Potential of structural thermal mass for demand-side management in dwellings," *Build Environ*, vol. 64, pp. 187–199, Jun. 2013, doi: 10.1016/j.buildenv.2013.03.010.

[17]   G. Masy, E. Georges, C. Verhelst, V. Lemort, and P. André, "Smart grid energy flexible buildings through the use of heat pumps and building thermal mass as energy storage in the Belgian context," *Sci Technol Built Environ*, vol. 21, no. 6, pp. 800–811, Aug. 2015, doi: 10.1080/23744731.2015.1035590.

[18]   A. Arteconi, D. Costola, P. Hoes, and J. L. M. Hensen, "Analysis of control strategies for thermally activated building systems under demand side management mechanisms," *Energy Build*, vol. 80, pp. 384–393, Sep. 2014, doi: 10.1016/j.enbuild.2014.05.053.

[19]   S. Taheri, P. Hosseini, and A. Razban, "Model predictive control of heating, ventilation, and air conditioning (HVAC) systems: A state-of-the-art review," *Journal of Building Engineering*, vol. 60, p. 105067, Nov. 2022, doi: 10.1016/j.jobe.2022.105067.

[20]   Y. Yao and D. K. Shekhar, "State of the art review on model predictive control (MPC) in Heating Ventilation and Air-conditioning (HVAC) field," *Build Environ*, vol. 200, p. 107952, Aug. 2021, doi: 10.1016/j.buildenv.2021.107952.

[21]   European Parliament, "Directive (EU) 2018/844 of the European Parliament and of the Council of 30 May 2018 amending Directive 2010/31/EU on the energy performance of buildings and Directive 2012/27/EU on energy efficiency," *Official Journal of the European Union*. 2018. Accessed: Jan. 19, 2023. [Online]. Available: http://data.europa.eu/eli/dir/2018/844/oj

[22]   H. Lund *et al.*, "4th Generation District Heating (4GDH)," *Energy*, vol. 68, pp. 1–11, Apr. 2014, doi: 10.1016/j.energy.2014.02.089.

[23]   A. Volkova, V. Mašatin, and A. Siirde, "Methodology for evaluating the transition process dynamics towards 4th generation district heating networks," *Energy*, vol. 150, pp. 253–261, May 2018, doi: 10.1016/j.energy.2018.02.123.

[24]   D. P. Bloomfield and D. J. Fisk, "The optimisation of intermittent heating," *Build Environ*, vol. 12, no. 1, pp. 43–55, Jan. 1977, doi: 10.1016/0360-1323(77)90006-3.

[25]   J. W. Moon and S. H. Han, "Thermostat strategies impact on energy consumption in residential buildings," *Energy Build*, vol. 43, no. 2–3, pp. 338–346, 2011, doi: 10.1016/j.enbuild.2010.09.024.

[26]   W. Wang, J. Zhang, W. Jiang, and B. Liu, "Energy performance comparison of heating and air-conditioning systems for multi-family residential buildings," *HVAC&R Res*, vol. 17, no. 3, pp. 309–322, 2011, doi: 10.1080/10789669.2011.568571.

[27]   B. Xu, S. Zhou, and W. Hu, "An intermittent heating strategy by predicting warm-up time for office buildings in Beijing," *Energy Build*, vol. 155, pp. 35–42, Nov. 2017, doi: 10.1016/j.enbuild.2017.08.062.

[28]   W. Guo and D. W. Nutter, "Setback and setup temperature analysis for a classic double-corridor classroom building," *Energy Build*, vol. 42, no. 2, pp. 189–197, 2010, doi: 10.1016/j.enbuild.2009.08.014.

[29]   Z. Wang, B. Lin, and Y. Zhu, "Modeling and measurement study on an intermittent heating system of a residence in Cambridgeshire," *Build Environ*, vol. 92, pp. 380–386, 2015, doi: 10.1016/j.buildenv.2015.05.014.

[30]   S. Erba and A. Barbieri, "Retrofitting Buildings into Thermal Batteries for Demand-Side Flexibility and Thermal Safety during Power Outages in Winter," *Energies (Basel)*, vol. 15, no. 12, p. 4405, Jun. 2022, doi: 10.3390/en15124405.

[31]   F. Oldewurtel, D. Sturzenegger, and M. Morari, "Importance of occupancy information for building climate control," *Appl Energy*, vol. 101, pp. 521–532, Jan. 2013, doi: 10.1016/j.apenergy.2012.06.014.

[32]   CEN, "FprEN 12831-1:2016 Energy performance of buildings — Method for calculation of the design heat load — Part 1: Space heating load." FprEN 12831-1, European Standard, 2016.

[33]   ISO, "ISO 18523-2:2018 Energy performance of buildings-Schedule and condition of building, zone and space usage for energy calculation-Part 2: Residential buildings." 2018. [Online]. Available: www.iso.org

[34]   CEN, "EN 16798-1:2019 Energy performance of buildings – Ventilation for buildings – Part 1: Indoor environmental input parameters for design and assessment of energy performance of buildings addressing indoor air quality, thermal environment, lighting and acoustics." 2019.

[35]   CEN, "EN 16798-2:2019 Energy performance of buildings – Ventilation for buildings – Part 2: Interpretation of the requirements in EN 16798-1 – Indoor environmental input parameters for design and assessment of energy performance of buildings addressing indoor air quality, thermal environment, lighting and acoustics." 2019.

[36]   K. V. Võsa, A. Ferrantelli, and J. Kurnitski, "Annual performance analysis of heat emission in radiator and underfloor heating systems in the European reference room," *E3S Web of Conferences*, vol. 111, no. 201 9, 2019, doi: 10.1051/e3sconf/201911104009.

[37]   K.-V. Võsa, A. Ferrantelli, and J. Kurnitski, "A novel method for calculating heat emitter and controller configuration setpoint variations with EN15316-2," *Journal of Building Engineering*, vol. 31, p. 101387, Sep. 2020, doi: 10.1016/j.jobe.2020.101387.

[38]   E. ISO, "52016-1. Energy performance of buildings-Energy needs for heating and cooling, internal temperatures and sensible and latent heat loads-Part 1: Calculation procedures." International Organization for Standardization: Geneva, Switzerland, 2017.

[39]   Y. Wang, J. Kuckelkorn, and Y. Liu, "A state of art review on methodologies for control strategies in low energy buildings in the period from 2006 to 2016," *Energy Build*, vol. 147, pp. 27–40, Jul. 2017, doi: 10.1016/j.enbuild.2017.04.066.

[40]   T. I. Salsbury, K. Devaprasad, R. Lutes, and A. P. Rogers, "Smarter building start – A distributed solution," *Energy Build*, vol. 282, p. 112776, Mar. 2023, doi: 10.1016/j.enbuild.2023.112776.

[41]   E. Zanetti, R. Alesci, R. Scoccia, and M. Aprile, "Floor heating pre-on/off parameters based on Model Predictive Control feature extrapolation," in *CLIMA 2022 The 14th REHVA HVAC World Congress*, 2022. doi: https://doi.org/10.34641/clima.2022.331.

[42]   U. Ayr *et al.*, "From awareness to energy saving: Using user engagement to change occupants' behaviour," *IOP Conf Ser Mater Sci Eng*, vol. 609, no. 6, 2019, doi: 10.1088/1757-899X/609/6/062008.

[43]   T. M. Kull, K. R. Penu, M. Thalfeldt, and J. Kurnitski, "Energy saving potential with smart thermostats in low-energy homes in cold climate," *E3S Web of Conferences*, vol. 172, pp. 3–9, 2020, doi: 10.1051/e3sconf/202017209009.

[44]   F. Oldewurtel, "Stochastic model predictive control for energy efficient building climate control," 2011. doi: https://doi.org/10.3929/ethz-a-007157625.

[45]   A. Mirakhorli and B. Dong, "Occupancy behavior based model predictive control for building indoor climate—A critical review," *Energy Build*, vol. 129, pp. 499–513, Oct. 2016, doi: 10.1016/j.enbuild.2016.07.036.

[46]   D. Sturzenegger, "Model predictive building climate control: Steps towards practice," 2014.

[47]   V. Tzovla and A. Mehta, "A simplified and integrated approach to model predictive control implementation," *Plant Automation.com*. ISA, Austin, TX, 2000. Accessed: Jan. 29, 2023. [Online]. Available: https://www.plantautomation.com/doc/a-simplified-and-integrated-approach-to-model-0001

[48]   X. Yang, G. Liu, A. Li, and L. Van Dai, "A Predictive Power Control Strategy for DFIGs Based on a Wind Energy Converter System," *Energies (Basel)*, vol. 10, no. 8, p. 1098, Jul. 2017, doi: 10.3390/en10081098.

[49]   M. D. Leonard, E. E. Michaelides, and D. N. Michaelides, "Energy storage needs for the substitution of fossil fuel power plants with renewables," *Renew Energy*, vol. 145, pp. 951–962, Jan. 2020, doi: 10.1016/j.renene.2019.06.066.

[50]   IEA and UNEP, *2022 Global Status Report for Buildings and Construction*. 2022. [Online]. Available: www.globalabc.org.

[51]   C. W. Gellings, "The concept of demand-side management for electric utilities," *Proceedings of the IEEE*, vol. 73, no. 10, pp. 1468–1470, 1985, doi: 10.1109/PROC.1985.13318.

[52]   M. Paulus and F. Borggrefe, "The potential of demand-side management in energy-intensive industries for electricity markets in Germany," *Appl Energy*, vol. 88, no. 2, pp. 432–441, Feb. 2011, doi: 10.1016/j.apenergy.2010.03.017.

[53]   M. H. Shoreh, P. Siano, M. Shafie-khah, V. Loia, and J. P. S. Catalão, "A survey of industrial applications of Demand Response," *Electric Power Systems Research*, vol. 141, pp. 31–49, Dec. 2016, doi: 10.1016/j.epsr.2016.07.008.

[54]   H. Wolisz, H. Harb, P. Matthes, L. Böse, R. Streblow, and D. Müller, "The new role of night storage heaters in residential demand side management," in *Fifth German-Austrian IBPSA Conference, BauSIM*, 2014. Accessed: Jan. 24, 2023. [Online]. Available: http://www.ibpsa.org/proceedings/bausimPapers/2014/p1212_final.pdf

[55]   S. Ø. Jensen *et al.*, "IEA EBC Annex 67 Energy Flexible Buildings," *Energy Build*, vol. 155, pp. 25–34, Nov. 2017, doi: 10.1016/j.enbuild.2017.08.044.

[56]   A. Arteconi, N. J. Hewitt, and F. Polonara, "Domestic demand-side management (DSM): Role of heat pumps and thermal energy storage (TES) systems," *Appl Therm Eng*, vol. 51, no. 1–2, pp. 155–165, Mar. 2013, doi: 10.1016/j.applthermaleng.2012.09.023.

[57] K. Hedegaard, B. V. Mathiesen, H. Lund, and P. Heiselberg, "Wind power integration using individual heat pumps – Analysis of different heat storage options," *Energy*, vol. 47, no. 1, pp. 284–293, Nov. 2012, doi: 10.1016/j.energy.2012.09.030.

[58] D. Müller *et al.*, "Demand side management for city districts," *Build Environ*, vol. 91, pp. 283–293, Sep. 2015, doi: 10.1016/j.buildenv.2015.03.026.

[59] S. Stinner, K. Huchtemann, and D. Müller, "Quantifying the operational flexibility of building energy systems with thermal energy storages," *Appl Energy*, vol. 181, pp. 140–154, Nov. 2016, doi: 10.1016/j.apenergy.2016.08.055.

[60] I. Dincer, "On thermal energy storage systems and applications in buildings," *Energy Build*, vol. 34, no. 4, pp. 377–388, May 2002, doi: 10.1016/S0378-7788(01)00126-8.

[61] J. Le Dréau and P. Heiselberg, "Energy flexibility of residential buildings using short term heat storage in the thermal mass," *Energy*, vol. 111, pp. 991–1002, Sep. 2016, doi: 10.1016/j.energy.2016.05.076.

[62] T. H. Pedersen, R. E. Hedegaard, and S. Petersen, "Space heating demand response potential of retrofitted residential apartment blocks," *Energy Build*, vol. 141, pp. 158–166, Apr. 2017, doi: 10.1016/j.enbuild.2017.02.035.

[63] G. Reynders, J. Diriken, and D. Saelens, "Generic characterization method for energy flexibility: Applied to structural thermal storage in residential buildings," *Appl Energy*, vol. 198, pp. 192–202, Jul. 2017, doi: 10.1016/j.apenergy.2017.04.061.

[64] S. Heinen, W. Turner, L. Cradden, F. McDermott, and M. O'Malley, "Electrification of residential space heating considering coincidental weather events and building thermal inertia: A system-wide planning analysis," *Energy*, vol. 127, pp. 136–154, May 2017, doi: 10.1016/j.energy.2017.03.102.

[65] J. E. Braun, "Load Control Using Building Thermal Mass," *J Sol Energy Eng*, vol. 125, no. 3, pp. 292–301, Aug. 2003, doi: 10.1115/1.1592184.

[66] M. Kintner-Meyer and A. F. Emery, "Optimal control of an HVAC system using cold storage and building thermal capacitance," *Energy Build*, vol. 23, no. 1, pp. 19–31, Oct. 1995, doi: 10.1016/0378-7788(95)00917-M.

[67] J. Romaní, A. de Gracia, and L. F. Cabeza, "Simulation and control of thermally activated building systems (TABS)," *Energy Build*, vol. 127, pp. 22–42, Sep. 2016, doi: 10.1016/j.enbuild.2016.05.057.

[68] M. Schmelas, T. Feldmann, and E. Bollin, "Adaptive predictive control of thermo-active building systems (TABS) based on a multiple regression algorithm," *Energy Build*, vol. 103, pp. 14–28, Sep. 2015, doi: 10.1016/j.enbuild.2015.06.012.

[69] J. Ma, J. Qin, T. Salsbury, and P. Xu, "Demand reduction in building energy systems based on economic model predictive control," *Chem Eng Sci*, vol. 67, no. 1, pp. 92–100, Jan. 2012, doi: 10.1016/j.ces.2011.07.052.

[70] J. W. Moon and S. K. Jung, "Algorithm for optimal application of the setback moment in the heating season using an artificial neural network model," *Energy Build*, vol. 127, pp. 859–869, Sep. 2016, doi: 10.1016/j.enbuild.2016.06.046.

[71] H. Johra, P. Heiselberg, and J. Le Dréau, "Influence of envelope, structural thermal mass and indoor content on the building heating energy flexibility," *Energy Build*, vol. 183, pp. 325–339, Jan. 2019, doi: 10.1016/j.enbuild.2018.11.012.

[72]   R. Yin *et al.*, "Quantifying flexibility of commercial and residential loads for demand response using setpoint changes," *Appl Energy*, vol. 177, pp. 149–164, Sep. 2016, doi: 10.1016/j.apenergy.2016.05.090.

[73]   J. Sánchez Ramos, M. Pavón Moreno, M. Guerrero Delgado, S. Álvarez Domínguez, and L. F. Cabeza, "Potential of energy flexible buildings: Evaluation of DSM strategies using building thermal mass," *Energy Build*, vol. 203, p. 109442, Nov. 2019, doi: 10.1016/j.enbuild.2019.109442.

[74]   R. Barzin, J. J. J. Chen, B. R. Young, and M. M. Farid, "Application of PCM underfloor heating in combination with PCM wallboards for space heating using price based control system," *Appl Energy*, vol. 148, pp. 39–48, Jun. 2015, doi: 10.1016/j.apenergy.2015.03.027.

[75]   H. Wolisz, A. Constantin, R. Streblow, and D. Müller, "Performance assessment of heat distribution systems for sensible heat storage in building thermal mass," in *Proceedings of the 12th CISBAT, 2013. Lausanne, Switzerland*, 2013.

[76]   H. Wolisz, H. Harb, P. Matthes, R. Streblow, and D. Müller, "Dynamic simulation of thermal capacity and charging/discharging performance for sensible heat storage in building wall mass," in *Proceedings of BS2013: 13th Conference of International Building Performance Simulation Association, Chambéry, France, August 26-28*, 2013, pp. 2716–2723.

[77]   J. Abedin, S. Firth, and P. Eames, "Simulation of domestic heat demand shifting through short-term thermal storage," in *Proceedings of BS2013: 13th Conference of International Building Performance Simulation Association, Chambéry, France, August 26-28*, 2013, pp. 3368–3374. Accessed: Jan. 25, 2023. [Online]. Available: https://www.aivc.org/sites/default/files/p_1490.pdf

[78]   Y. Li, E. Long, L. Zhang, X. Dong, and S. Wang, "Energy-saving potential of intermittent heating system: Influence of composite phase change wall and optimization strategy," *Energy Exploration & Exploitation*, vol. 39, no. 1, pp. 426–443, Jan. 2021, doi: 10.1177/0144598720969217.

[79]   J. Clauß, S. Stinner, I. Sartori, and L. Georges, "Predictive rule-based control to activate the energy flexibility of Norwegian residential buildings: Case of an air-source heat pump and direct electric heating," *Appl Energy*, vol. 237, no. December 2018, pp. 500–518, 2019, doi: 10.1016/j.apenergy.2018.12.074.

[80]   C. Karczewski, T. Henzler, and K. Stergiaropoulos, "Increasing the Energy Flexibility of Buildings controlled by Model Predictive Control," in *CLIMA 2022 The 14th REHVA HVAC World Congress*, Rotterdam, 2022. doi: https://doi.org/10.34641/clima.2022.3.

[81]   M. Jarre, M. Noussan, and M. Simonetti, "Primary energy consumption of heat pumps in high renewable share electricity mixes," *Energy Convers Manag*, vol. 171, pp. 1339–1351, Sep. 2018, doi: 10.1016/j.enconman.2018.06.067.

[82]   H. Wolisz, "Dynamic Activation of Structural Thermal Mass in A Multi-Zonal Building with Due Regard to Thermal Comfort," in *Proceedings of Building Simulation 2015: 14th Conference of IBPSA*, Dec. 2015, pp. 1291–1297. doi: 10.26868/25222708.2015.2306.

[83]   Fingrid Oyj, "Reserve products and reserve market places," 2022. Accessed: Jan. 25, 2023. [Online]. Available: https://www.fingrid.fi/globalassets/dokumentit/en/electricity-market/reserves/reserve-products-and-reserve-market-places.pdf

[84]   Elering AS, AS "Augstsprieguma tīkls," and LITGRID AB, "Baltic reserve capacity
       market study," 2021. Accessed: May 13, 2023. [Online]. Available:
       https://elering.ee/sites/default/files/2021-
       07/Market%20test%20study%20report_1.pdf

[85]   Ö. Okur, P. Heijnen, and Z. Lukszo, "Aggregator's business models in residential
       and service sectors: A review of operational and financial aspects," *Renewable
       and Sustainable Energy Reviews*, vol. 139, p. 110702, Apr. 2021, doi:
       10.1016/j.rser.2020.110702.

[86]   Elering AS, AS "Augstsprieguma tīkls," and Litgrid AB, "Baltic balancing market
       rules," 2020. Accessed: Jan. 29, 2023. [Online]. Available:
       https://elering.ee/sites/default/files/2021-
       01/Baltic%20Balancing%20market%20rules%2020201006.pdf

[87]   Artelys, *METIS Technical Note T6 - METIS Power System Module*, vol. European
       Commission. Brussels: European Commission, 2017. Accessed: Jan. 29, 2023.
       [Online].   Available: https://energy.ec.europa.eu/system/files/2017-
       07/power_system_module_0.pdf

[88]   L. Zhang, N. Good, and P. Mancarella, "Building-to-grid flexibility: Modelling and
       assessment metrics for residential demand response from heat pump
       aggregations," *Appl Energy*, vol. 233–234, pp. 709–723, Jan. 2019, doi:
       10.1016/j.apenergy.2018.10.058.

[89]   M. Lindahl, "Grid Flexible Control of Heat Pumps," *HPT - Heat Pumping
       Technologies*, 2020. Accessed: Mar. 10, 2021. [Online]. Available:
       https://heatpumpingtechnologies.org/publications/grid-flexible-control-of-
       heat-pumps/

[90]   S. Burt and M. Podesta, "Response times of meteorological air temperature
       sensors," *Quarterly Journal of the Royal Meteorological Society*, vol. 146, no. 731,
       pp. 2789–2800, Jul. 2020, doi: 10.1002/qj.3817.

[91]   Danfoss, "Actuator ABNM A5 0-10 V Proportional For Use with RA2000 Valves,"
       2016.

[92]   Ventilation Control Products Sweden AB, "Thermoelectric Valve Actuators."
       2011.   Accessed: Jan.   27,   2023.   [Online].   Available:
       http://www.ventilationcontrolproducts.net/actuators-and-valve-adaptors

[93]   T. I. Salsbury, "A survey of control technologies in the building automation
       industry," *IFAC Proceedings Volumes (IFAC-PapersOnline)*, vol. 16, pp. 90–100,
       2005, doi: 10.3182/20050703-6-cz-1902.01397.

[94]   EQUA, "IDA Indoor Climate and Energy (IDA ICE, version 4.8 SP1, Expert edition)."
       2019. [Online]. Available: https://www.equa.se/en/ida-ice

[95]   A. I. Dounis and C. Caraiscos, "Advanced control systems engineering for energy
       and comfort management in a building environment-A review," *Renewable and
       Sustainable Energy Reviews*, vol. 13, no. 6–7, pp. 1246–1261, 2009, doi:
       10.1016/j.rser.2008.09.015.

[96]   M. Royapoor, A. Antony, and T. Roskilly, "A review of building climate and plant
       controls, and a survey of industry perspectives," *Energy Build*, vol. 158,
       pp. 453–465, 2018, doi: 10.1016/j.enbuild.2017.10.022.

[97]   I. Rodríguez-Rodríguez, A. G. Vidal, A. P. R. González, and M. Á. Zamora,
       "Commissioning of the controlled and automatized testing facility for human
       behavior and control (CASITA)," *Sensors (Switzerland)*, vol. 18, no. 9, 2018, doi:
       10.3390/s18092829.

[98] K. J. Astrom, T. Hagglund, and A. Wallenborg, "Automatic tuning of a digital controller," *IFAC Symposia Series*, no. 8, pp. 285–290, 1993, doi: 10.1016/s1474-6670(17)50749-1.

[99] Q. Bi *et al.*, "Advanced controller auto-tuning and its application in HVAC systems," *Control Eng Pract*, vol. 8, no. 6, pp. 633–644, 2000, doi: 10.1016/S0967-0661(99)00198-7.

[100] Y. G. Wang, Z. G. Shi, and W. J. Cai, "PID autotuner and its application in HVAC systems," *Proceedings of the American Control Conference*, vol. 3, pp. 2192–2196, 2001, doi: 10.1109/acc.2001.946075.

[101] L. Ferrarini, S. Rastegarpour, and A. Petretti, "An Adaptive Underfloor Heating Control with External Temperature Compensation," *Proceedings of the 14th International Conference on Informatics in Control, Automation and Robotics*, vol. 1, no. Icinco, pp. 629–636, 2017, doi: 10.5220/0006432906290636.

[102] P. S. Curtiss, "Examples of Neural Networks Used for Building System Control and Energy Management," *ASHRAE Transactions*, 1997.

[103] A. Hasan, J. Kurnitski, and K. Jokiranta, "A combined low temperature water heating system consisting of radiators and floor heating," *Energy Build*, vol. 41, no. 5, pp. 470–479, 2009, doi: 10.1016/j.enbuild.2008.11.016.

[104] K. V. Võsa, A. Ferrantelli, and J. Kurnitski, "Experimental study of radiator, underfloor, ceiling and air heater systems heat emission performance in TUT nZEB test facility," *E3S Web of Conferences*, vol. 111, no. 201 5, 2019, doi: 10.1051/e3sconf/201911104005.

[105] D. D. Kukolj, S. B. Kuzmanović, and E. Levi, "Design of a PID-like compound fuzzy logic controller," *Eng Appl Artif Intell*, vol. 14, no. 6, pp. 785–803, 2001, doi: 10.1016/S0952-1976(02)00014-3.

[106] M. Ostermeier and J. Müller, "Automated investigation, evaluation and optimisation of simple heating circuits in building automation," *E3S Web of Conferences*, vol. 111, no. 201 9, 2019, doi: 10.1051/e3sconf/201911105026.

[107] M. Fiducioso, S. Curi, B. Schumacher, M. Gwerder, and A. Krause, "Safe contextual Bayesian optimization for sustainable room temperature PID control tuning," *IJCAI International Joint Conference on Artificial Intelligence*, vol. 2019-August, pp. 5850–5856, 2019, doi: 10.24963/ijcai.2019/811.

[108] F. Nägele, T. Kasper, and B. Girod, "Turning up the heat on obsolete thermostats: A simulation-based comparison of intelligent control approaches for residential heating systems," *Renewable and Sustainable Energy Reviews*, vol. 75, no. July 2016, pp. 1254–1268, 2017, doi: 10.1016/j.rser.2016.11.112.

[109] WiseWater, "Hydronic Radiant Heating Manifold Brass." 2023. Accessed: Aug. 10, 2023. [Online]. Available: https://alfaheating.com/collections/manifolds/products/8loop

[110] Warmup, "Centralised Control Hub for Water UFH Systems." Accessed: Aug. 10, 2023. [Online]. Available: https://www.warmup.co.uk/underfloor-heating/water/manifold/stainless-steel

[111] T. Barz, J. Emhofer, K. Marx, G. Zsembinszki, and L. F. Cabeza, "Phenomenological modelling of phase transitions with hysteresis in solid/liquid PCM," *J Build Perform Simul*, vol. 12, no. 6, pp. 770–788, Nov. 2019, doi: 10.1080/19401493.2019.1657953.

[112] B. Zalba, J. M. Marín, L. F. Cabeza, and H. Mehling, "Review on thermal energy storage with phase change: materials, heat transfer analysis and applications," *Appl Therm Eng*, vol. 23, no. 3, pp. 251–283, Feb. 2003, doi: 10.1016/S1359-4311(02)00192-8.

[113] CALEFFI, "Pre-assembled distribution manifolds for radiant panel systems series." Caleffi North America, Inc., 2008.

[114] B. Liu, J. Yang, Z. Zhang, J. Yang, and D. Li, "A phase change microactuator based on paraffin wax/expanded graphite/nickel particle composite with induction heating," *Sens Actuators A Phys*, vol. 275, pp. 129–136, Jun. 2018, doi: 10.1016/j.sna.2018.04.006.

[115] A. Mann, T. Germann, M. Ruiter, and P. Groche, "The challenge of upscaling paraffin wax actuators," *Mater Des*, vol. 190, p. 108580, May 2020, doi: 10.1016/j.matdes.2020.108580.

[116] P. Tautzenberger, "Thermal Actuators: A Comparison of Shape Memory Alloys with Thermostatic Bimetals and Wax Actuators," in *Engineering Aspects of Shape Memory Alloys*, Butterworth-Heinemann, 1990, pp. 207–218.

[117] Vernatherm, "Thermal Actuators (Wax Motors)," 2019. https://www.vernatherm.com/ thermal_actuators.html (accessed May 13, 2023).

[118] K. Du, J. Calautit, Z. Wang, Y. Wu, and H. Liu, "A review of the applications of phase change materials in cooling, heating and power generation in different temperature ranges," *Appl Energy*, vol. 220, pp. 242–273, Jun. 2018, doi: 10.1016/j.apenergy.2018.03.005.

[119] Ltd. Beijing MUYY Technologies Co., "Electric Thermal Actuator," 2017.

[120] A. Constantin, R. Streblow, and D. Müller, "The Modelica HouseModels Library: Presentation and Evaluation of a Room Model with the ASHRAE Standard 140," Mar. 2014, pp. 293–299. doi: 10.3384/ecp14096293.

[121] M. Maivel, A. Ferrantelli, and J. Kurnitski, "Experimental determination of radiator, underfloor and air heating emission losses due to stratification and operative temperature variations," *Energy Build*, vol. 166, pp. 220–228, 2018, doi: https://doi.org/10.1016/j.enbuild.2018.01.061.

[122] T. M. Kull, M. Thalfeldt, and J. Kurnitski, "Estimating time constants for underfloor heating control," *J Phys Conf Ser*, vol. 1343, no. 1, 2019, doi: 10.1088/1742-6596/1343/1/012121.

[123] T. M. Kull, M. Thalfeldt, and J. Kurnitski, "Optimal PI control parameters for accurate underfloor heating temperature control," in *E3S Web of Conferences*, 2019. doi: 10.1051/e3sconf/201911101081.

[124] BBSR - Federal institute for research on building, urban affairs and spatial development, "Test Reference Year (TRY) 2011: Region 5 - German Lower Rhine Region," 2011. https://www.bbsr-geg.bund.de/GEGPortal/DE/Regelungen/Testreferenzjahre/TRY2011/TRY2011Projekt/Testreferenzjahre_node.html (accessed May 14, 2023).

[125] T. Kalamees and J. Kurnitski, "Estonian test reference year for energy calculations.," *Proceedings of the Estonian Academy of Sciences. Engineering*, vol. 12, no. 1, pp. 40–58, 2006.

[126] M. Wetter, "A Modelica-based Model Library for Building Energy and Control Systems," 2009.

[127] EQUA, "IDA Indoor Climate and Energy (IDA ICE, version 4.7.1, Expert edition)." Equa Simulations AB, 2016. [Online]. Available: http://www.equa.se

[128] M. Fuchs, A. Constantin, M. Lauster, P. Remmen, R. Streblow, and D. Müller, "Structuring the building performance modelica library AixLib for open collaborative development," in *14th International Conference of the International Building Performance Simulation Association*, Hyderabad, India, 2015. Accessed: Feb. 18, 2023. [Online]. Available: http://www.ibpsa.org/proceedings/BS2015/p2202.pdf

[129] D. Müller, M. Lauster, A. Constantin, M. Fuchs, and P. Remmen, "AixLib-An open-source modelica library within the IEA-EBC annex 60 framework," in *BauSIM*, 2016, pp. 3–9. Accessed: Feb. 18, 2023. [Online]. Available: http://www.ibpsa.org/proceedings/bausimPapers/2016/A-02-3.pdf

[130] S. Stinner, T. Schlösser, K. Huchtemann, D. Müller, and A. Monti, "Primary energy evaluation of heat pumps considering dynamic boundary conditions in the energy system," *Energy*, vol. 138, pp. 60–78, Nov. 2017, doi: 10.1016/j.energy.2017.07.029.

[131] BMWi - Federal Ministry for Economic Affairs and Energy, "Energy concept. Energiekonzept für eine umweltschonende, zuverlässige und bezahlbare Energieversorgung," 2010. Accessed: May 15, 2023. [Online]. Available: https://www.bmwi.de/Redaktion/DE/Downloads/E/ energiekonzept-2010.pdf

[132] BMWi - Federal Ministry for Economic Affairs and Energy, *The German Energy Saving Ordinance (EnEV)*. 2009.

[133] BMWi - Federal Ministry for Economic Affairs and Energy, *Energy Conservation Legislation*. 2017. Accessed: May 15, 2023. [Online]. Available: https://www.bmwk.de/Redaktion/EN/Artikel/Energy/energy-conservation-legislation.html

[134] BBR - Bundesamt für Bauwesen und Raumordnung, *Thermal Insulation Ordinance 1977/1984*. 2017.

[135] Passive House Institute, "Passive House requirements & User manual for Passive Houses," 2016. https://passivehouse.com/05_service/03_literature/030300_user-manual/030300_user-manual.htm (accessed May 15, 2023).

[136] Kermi GmbH, "Therm-x2 Flachheizkörper: Profil-K/-V/-VM Heizkörperauslegung: Tested according to DIN EN 442," 2016.

[137] S. Prívara, J. Cigler, Z. Váňa, F. Oldewurtel, C. Sagerschnig, and E. Žáčeková, "Building modeling as a crucial part for building predictive control," *Energy Build*, vol. 56, pp. 8–22, Jan. 2013, doi: 10.1016/j.enbuild.2012.10.024.

[138] MathWorks, "MATLAB 'arx' function description," 2017. https://de.mathworks.com/help/ident/ref/arx.html (accessed May 18, 2023).

[139] I. Richardson, M. Thomson, and D. Infield, "A high-resolution domestic building occupancy model for energy demand simulations," *Energy Build*, vol. 40, no. 8, pp. 1560–1566, Jan. 2008, doi: 10.1016/j.enbuild.2008.02.006.

[140] Gurobi Optimization, "Continuous Models," 2017. https://www.gurobi.com/documentation/6.5/refman/continuous_models.html (accessed May 15, 2023).

[141] Rasberry Pi Foundation, "Raspberry Pi hardware guide: The Raspberry Pi 3." 2016. Accessed: Aug. 10, 2023. [Online]. Available: https://projects.raspberrypi.org/en/pathways/getting-started-with-raspberry-pi

[142] "Estonian Regulation No 58: Methodology for calculating the energy performance of buildings." Ministry of Economic Affairs and Communications, 2015.

[143] "EVS-EN ISO 13790:2008 Energy performance of buildings - Calculation of energy use for space heating and cooling," pp. 1–171, Apr. 2008, [Online]. Available: https://wiki.umn.edu/pub/PA5721_Building_Policy/WebHome/LEEDENERGYSTAR_STUDY.pdf

[144] "Nord Pool." https://www.nordpoolgroup.com/en/Market-data1/#/nordic/table (accessed May 15, 2023).

[145] M. Wetter, "GenOpt® -- A Generic Optimization Program," in *Seventh International IBPSA Conference*, Jan. 2001.

[146] "System Identification Toolbox™ Matlab®." The MathWorks, Inc.

[147] K. J. Åström and T. Hägglund, *Advanced PID Control*. ISA-The Instrumentation, Systems, and Automation Society, 2006.

[148] M. Wetter, "GenOpt. Generic Optimization Program. User Manual," *Berkeley National Laboratory*, no. c, pp. 1–108, 2011, doi: 10.2172/962948.

[149] HBM, "WI Displacement transducer Data sheet." Accessed: May 15, 2023. [Online]. Available: https://www.hbm.com/en/3060/wi-inductive-displacement-transducer-miniature-probe/?product_type_no=WI:%20Inductive%20Displacement%20Transducer%20(Miniature%20Probe)

[150] HBM, "QuantumX CX22B-W, CX22B Data recorder Data sheet." Accessed: May 15, 2023. [Online]. Available: https://www.hbm.com/en/2486/quantumx-cx22bw-data-recorder/?product_type_no=QuantumX%20CX22B-W%20Data%20Recorder

[151] HBM, "QuantumX MX840A Universal amplifier Data Sheet."

[152] A. G. Siemens, "LOGO! 24CE logic module, 6ED1052-1CC08-0BA1," in *Siemens AG*, Munich, Germany.

[153] N. Ukrainczyk, S. Kurajica, and J. Šipušić, "Thermophysical comparison of five commercial paraffin waxes as latent heat storage materials," *Chem Biochem Eng Q*, vol. 24, no. 2, pp. 129–137, 2010.

[154] M. Freund, R. Csikós, S. Keszthelyi, and G. Y. Mózes, *Paraffin Products Properties, Technologies, Applications*, vol. Volume 14. 1982. [Online]. Available: http://www.sciencedirect.com/science/article/pii/S0376736108701481

[155] Polytherm Heating Systems, "OEM-Actuator 24V." Accessed: Mar. 11, 2021. [Online]. Available: http://www.polytherm.ie/v4/0940aa0c-5421-4a9b-840d-c9a2ae5d95bb/uploads/24v Actuator Spec.pdf

[156] "Thermometrics Product Line PTC Thermistors Positive Temperature Coefficient Thermistors," 2015. Accessed: Mar. 08, 2021. [Online]. Available: www.amphenol-sensors.com

[157] R. Components, "Thermistors," 1997. https://www.thierry-lequeu.fr/data/NTC-RS.pdf (accessed Mar. 11, 2021).

[158] R Core Team, *R: A language and environment for statistical computing*. Vienna, Austria: R Foundation for Statistical Computing, 2013.

[159] Sensus, "Ultrasonic Meter for heating and cooling energy nominal sizes q p 0.6 to 60 m 3 /h PolluStat E," 2016. Accessed: Mar. 11, 2021. [Online]. Available: www.sensus.com

[160] P. Kumar, "Valve trim design using Control Valve Performer." [Online]. Available: https://www.simulationhub.com/blog/valve-trim-design-using-control-valve-performer.

[161] J. C. LTD, "Valve and Actuator Manual," in *Johnson Controls LTD*, Cork, Ireland.

[162] R. Petitjean, *Total hydronic balancing: a handbook for design and troubleshooting of hydronic HVAC systems*. Ljung, Sweden: Tour & Andersson AB.

[163] J. Wen and T. F. Smith, "Effect of thermostat time constant on temperature control and energy consumption," in *Proceedings of the First ISA/IEEE Sensors for Industry Conference*, 2001, pp. 252–257.

[164] R. Elnaklah, I. Walker, and S. Natarajan, "Moving to a green building: Indoor environment quality, thermal comfort and health," *Build Environ*, vol. 191, p. 107592, Mar. 2021, doi: 10.1016/j.buildenv.2021.107592.

[165] J. Clauß and L. Georges, "Model complexity of heat pump systems to investigate the building energy flexibility and guidelines for model implementation," *Appl Energy*, vol. 255, p. 113847, Dec. 2019, doi: 10.1016/j.apenergy.2019.113847.

[166] Jim Ford, "Initial Settings For PID Controllers," 2013. https://www.mavtechglobal.com/initial-settings-for-pid-controllers/ (accessed May 30, 2023).

[167] Siemens Switzerland Ltd, "Data sheet. Electrothermal actuators STA21.. and STA71.. for radiator valves, small valves and Combi valves," 2011.

[168] A. B. Lindab, *Lindab Actuators - Actuator 24V*. Båstad, Sweden: Lindab AB. Accessed: Mar. 16, 2023. [Online]. Available: https://itsolution.lindab.com/lindabwebproductsdoc/assets/production/ZGY3Zj kyZTItZDkyOS00Y2FmLWI4NTktMWFmNmQ0NTVkMjdi/5249629466772124848 /Actuators_GLOBAL.pdf?t=2106362828

[169] M. A. Hassan and O. Abdelaziz, "Best practices and recent advances in hydronic radiant cooling systems – Part II: Simulation, control, and integration," *Energy Build*, vol. 224, p. 110263, Oct. 2020, doi: 10.1016/j.enbuild.2020.110263.

[170] OpenAI, "GPT-4 Technical Report," Mar. 2023. [Online]. Available: http://arxiv.org/abs/2303.08774

Acknowledgements

I am profoundly grateful to all those who have supported me throughout my doctoral journey, and without whom this endeavor would not have been possible. First and foremost, I express my deepest gratitude to my supervisors Professor Jarek Kurnitski and Professor Martin Thalfeldt for their guidance, patience, and constructive feedback, which have shaped this research and my academic growth. Additionally, thank you, Martin, for the motivational support when needed, and Jarek, for always guiding me towards professionalism by your great example.

I am indebted to my colleagues and fellow researchers at the nZEB Research Group at Taltech, who have contributed to a vibrant academic environment with a very special vibe. My special thanks go to my dear deskmate Helena Kuivjõgi for all the motivational and inspirational discussions and just always being there for me. I am sincerely thankful to Raimo Simson, Karl-Villem Võsa, and Alo Mikola Simson for the help in deep-diving into the topics of HVAC, experiments, and modelling in IDA ICE. Thank you to Paul Klõšeiko and Jaanus Hallik for sharing thoughts on R/Python/statistics/visualization and being the kind hearts making me feel welcome from the start. A big thank you also goes to Professor Targo Kalamees, Kalle Kuusk, Anti Hamburg, Kristo Kalbe, Peeter Linnas, Abel Sepulveda, Andrea Ferrantelli, Hans Kristjan Aljas, Endrik Arumägi, Martin Kiil, Martin Talvik, Jevgeni Fadejev, Anni Oviir, Villu Kukk, Simo Ilomets, Professor Ergo Pikas, Ülar Palmiste, Lauri Lihtmaa, Meril Tamm, Sofia Vasman, Henri Sarevet, and many others. Thank you also to our amazing angels Laura Kadaru and Ene Pähn. I would like to extend my gratitude beyond our group to Peeter Soovik for product discussions, and Hendrik Naar for help with measurements.

I am grateful for my academic and professional growth to all my students and to all my former colleagues at the University of Tartu, at RWTH Aachen University, at the Institute of Building Research & Innovation (especially Dr. Peter Holzer), and officemates from Ingenieurbüro P. Jung in Vienna. Thank you to the former and current colleagues at Swiss Property, Amenti, and R8 Technologies for helping me to discover the building industry in practice, and for enduring my endless mumbling about "I will finish soon" and disappearing to work on my thesis. I especially thank my first supervisor and long-term mentor Dr. Tõnu Mauring, who inspired me to choose the field of energy-efficient buildings in the first place, who gave me many opportunities in my early career and has shaped several of the crucial choices I have taken in my professional life. Thank you, Dr. Henryk Wolisz, for being both a supporting mentor and a welcoming friend.

I owe a debt of gratitude to my friends and family for their love, unwavering support, understanding, and encouragement. First and foremost, thank you to Egert for enduring all the ups and downs, thank you for always undoubtedly believing in me, bringing so much wonder into our lives, and inspiring me to sometimes say "no" and always ask "why". Thank you to my parents for setting me off in the academic direction and always cheering me on, your love and support mean the world to me. Mummi, sorry for always giving you reasons to worry; thank you for keeping me afloat and enduring all the stress, you have clearly carried an important part of it. Paps, you have conveyed your drive for understanding to all of us; thank you for all the discussions, I certainly owe my argumentative and analyzing mind to your example. Thank you to Tiia, Meelis, Tiina and Karli for the technical, philosophical, and motivational dialogues, and the great role-models you all four have always been to me. Thank you to my nephews and nieces for pulling me out of my thoughts to play. Thank you, Sandhra, for being my project

manager or therapist or friend or whatever I needed. Thank you to the rest of my family and dear friends for the heart-to-heart chats, fun and laughs when I had re-appeared after a too long time apart. I am immensely grateful to such a support system having my back.

Lastly, I dedicate this work to my grandparents, (the memory of) whose endurance, grit, and wisdom inspire me and drive me forward.

Abstract
Control Dynamics and Parameters for Low Energy Heating Applications

The increase in variable renewable electricity generation and number of low-energy buildings due to energy and climate targets has been driving the electrification of thermal demand using heat pumps. To address imbalances in electricity production and consumption, the inherent thermal storage capacity of buildings has emerged as a valuable resource for load shifting. This storage potential can be tapped using heat pumps and variable room temperature setpoints.

This thesis developed and tested algorithms applying dynamic room temperature control while maintaining thermal comfort. Firstly, an easy to adapt Model Predictive Control (MPC) approach was developed based on the dynamic primary energy factor and comfort limits for radiator heating systems, making a primary energy reduction of up to 15% possible using thermal mass activation. In addition, a simple predictive pre-heating algorithm was developed for schedule-based intermittent occupancy, where a heating energy reduction of up to 7% was observed. These algorithms were tested on low-energy buildings, and results were compared with the performance of less insulated buildings. Findings agreed with the previous literature, showing that setback heating has less of an impact on energy savings in well-insulated buildings. Such buildings can, however, shift heating times over an extended period, resulting in a significant reduction in primary energy. The control of underfloor heating (UFH) systems using intermittent heating proved to be challenging with delayed heat-up and overheating.

While high-level control methods like MPC for UFH and radiators have advanced in recent years, this thesis explored the often-overlooked low-level control dynamics and parameters for low-energy heating applications. The detailed modelling of the control process in short time scales would be needed to ensure building's ability to quickly react to abrupt changes on production side. This thesis identified optimal PI (Proportional-Integral) parameters for low-energy UFH systems improving the UFH control significantly and suggested simple methods for finding them in practice. Different parameter sets were evaluated, and heating energy differences up to ca 10% were observed. Detailed control effects, such as signal delay, valve curve, and the use of wax actuators for UFH, in particular, were analyzed. Experimental work was undertaken to model the wax motor and understand its impact on simulation results. The modulation of the PI signal in UFH motors was also examined, revealing its influence on short-term performance. The modelling influence on heating energy was below 3%, but remarkably affected the flow rate.

The work in this thesis would be applicable to buildings using any limited capacity heat source with variable renewable energy share in production, such as district heat or heat pumps that are here used as an example. This thesis contributes to an understanding of control dynamics and parameters for low energy heating applications, highlighting the importance of low-level control aspects in short timescales. Results can be utilized in the design of efficient and environmentally friendly heating systems and control algorithms.

Lühikokkuvõte
Juhtimise dünaamika ja parameetrid madalenergia küttesüsteemides

Hoonete soojusvarustust on hakatud osaliselt üle viima elektripõhistele süsteemidele, soojuspumpadele. Selleks on andnud tõuke nii energia- ja kliimaeesmärkide tõttu suurenev elektri tootmine varieeruva tootlusega taastuvatest allikatest kui ka madalama energiatarbega hoonete kasvav arv. Elektri muutliku tootmise ja tarbimise tasakaalustamiseks on hoonete tarindite soojusmahtuvuse aktiveerimine osutunud energiatarbimise juhtimise väärtuslikuks ressursiks. Seda salvestusmahtu saab kasutusele võtta näiteks soojuspumpade ja ruumitemperatuuride muutuvate seadeväärtuste abil.

Käesolevas doktoritöös arendati välja ruumitemperatuuri dünaamilise juhtimise algoritmid, mis samaaegselt tagavad ka soojusliku mugavuse, ja testiti neid. Esiteks töötati radiaatorküttesüsteemide jaoks välja lihtsalt kohandatav mudelipõhine ennetava juhtimise (MPC) algoritm, mis põhines dünaamilisel primaarenergia kaalumisteguril ja dünaamilistel mugavuspiiridel. See lähenemine võimaldas konstruktsiooni soojusliku aktiveerimise abil vähendada primaarenergia vajadust kuni 15%. Lisaks töötati välja lihtne prognoosiv eelkütte algoritm perioodilise kasutusega ruumidele, kus täheldati kuni 7%-list kütteenergia vähenemist. Algoritme testiti madala energiatarbega hoonetes ja tulemusi võrreldi nende toimivusega vähem soojustatud hoonetes. Järeldused olid kooskõlas varasemate uuringutega, osutades sellele, et perioodiline küte ei võimalda hästi soojustatud hoonetes kuigi olulist kütteenergia säästu saavutada. Nendes hoonetes on aga võimalik kütmise aegu pikema perioodi jooksul nihutada, mille tulemuseks on primaarenergia oluline vähenemine. Põrandküttesüsteemide vahelduv juhtimine osutus nii ülessoojenemisega seotud hilistuste kui ka ülekütmise tõttu keerukaks väljakutseks.

Doktoritöös uuriti ka seni teaduskirjanduses vähe tähelepanu pälvinud detailsemaid komponente ja nende parameetreid madala energiatarbega küttesüsteemide juhtimisprotsessis. Juhtimise detailne modelleerimine võib vajalikuks osutuda lühikeses ajavahemikus, et tagada vajalik reageerimiskiirus hoones juhul, kui tootmise poolel toimuvad ootamatud muutused. Töös leiti optimaalsed PI (Proportsionaal-Integraal) regulaatori parameetrid põrandküttesüsteemide jaoks ja pakuti välja lihtsaid meetodeid nende tuvastamiseks praktikas. Erinevate parameetrikomplektide kasutamisel kõikus energiatarve kuni umbes 10% ulatuses. Lähemalt uuriti doktoritöös juhtimisprotsessi komponentide detailse modelleerimise mõju, analüüsides näiteks ajalist hilistuse, ventiili karakteristiku ja põrandküttesüsteemidele iseloomulike aeglaste vaha-ajamite mõju simulatsioonitulemustele. Selleks koostati katsetulemuste alusel vaha-ajami empiiriline mudel. Lisaks analüüsiti ka PI väljundsignaali moduleerimist, mis oluliselt mõjutas lühiajalist toimivust. Detailse modelleerimise mõju kütteenergiale jäi alla 3%, kuid vooluhulgad varieerusid oluliselt.

Käesoleva doktoritöö raames tehtud uuringuid saab rakendada hoonetes, mis kasutavad mis tahes varieeruval taastuvenergial põhinevat ja piiratud võimsusega küttealllikat, näiteks kaugküte või siin näitena toodud soojuspumbad. Siinne väitekiri aitab paremini mõista juhtimisdünaamika ja parameetrite mõju madala energiatarbega küttesüsteemides ning toob rõhutatult esile detailse modelleerimise olulisuse lühikestes ajaskaalades. Käesolev doktoritöö aitab planeerida tõhusaid ja keskkonnasõbralikke küttesüsteeme ning nende juhtimise algoritme.
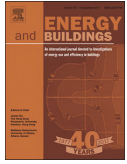
Appendix 1

Publication I

Wolisz, H., **Kull, T. M.**, Müller, D., and Kurnitski, J. (2020) Self-learning model predictive control for dynamic activation of structural thermal mass in residential buildings, *Energy and Buildings*. Elsevier B.V., 207, p. 109542. doi: 10.1016/j.enbuild.2019.109542

Self-learning model predictive control for dynamic activation of structural thermal mass in residential buildings☆

Henryk Wolisz [a,d,*], Tuule Mall Kull [b], Dirk Müller [a], Jarek Kurnitski [b,c]

[a] *RWTH Aachen University, E.ON Energy Research Center, Institute for Energy Efficient Buildings and Indoor Climate, Mathieustr. 10, Aachen 52074, Germany*
[b] *Tallinn University of Technology, Department of Civil Engineering and Architecture, Nearly Zero Energy Buildings Research Group, Ehitajate tee 5, Tallinn 19086, Estonia*
[c] *Aalto University, Department of Civil Engineering, Rakentajanaukio 4, Espoo 02150, Finland*
[d] *Drees&Sommer, Bundesallee 39-40a, 10717 Berlin, Germany*

ARTICLE INFO

ABSTRACT

Changes in the electricity supply system induce the challenge of matching the highly fluctuating and unpredictable renewable energy generation with the yet inflexible electricity demand. This leads to an increasing demand for energy storage and demand-flexibility. Electrification of residential heating systems in combination with advanced controls utilizing dynamically the structural thermal mass (STM) of buildings as thermal storage could provide some of the required demand flexibility.

In this work, a model predictive control (MPC) algorithm is developed and applied within a simulation framework to control dynamic heating operation as a measure of STM based residential load shifting (LS). The self-learning algorithm is functional without extensive measurement data or expert knowledge for parametrization. It optimizes heating operations required for LS according to a dynamic primary energy factor signal, while observing transient thermal comfort constraints. The implemented auto-regressive black-box model with explanatory variables predicts thermal conditions within the observed thermal zone with sufficient quality to support MPC. Based on that model, the control algorithm successfully activates STM as a measure of LS according to the given primary energy (PE) oriented utility function. For the observed system, the PE demand can be reduced by 3–7% while maintaining or even improving the thermal comfort.

© 2019 Elsevier B.V. All rights reserved.

1. Introduction

1.1. Motivation

The vastly growing renewable energy sector induces the challenge of highly fluctuating and unpredictable renewable energy generation from photovoltaic (PV) and wind power. Due to the current inflexibility of electricity demand, Germany has increasing difficulties to match the renewable energy generation with the electricity demand. The rising share of wind and PV in the total energy portfolio will further aggravate that challenge in the upcoming years [2]. Therefore, there will be an increasing demand for energy storage and demand-flexibility in the imminent future. Space heating of residential buildings is accountable for 18% of Germany's final energy demand (FED) [3,4] and a similar share is reported for the European Union [5]. Thus, dynamic control of residential heat-

ing systems could provide flexibility to counter the imbalances between supply and demand in the electrical grid. Since the heating demand of buildings is inherently not very flexible, thermal storages are required to actually exploit the flexibility potential of residential buildings. For this purpose, either technical storage systems such as hot water tanks can be used [6,7], or the intrinsic structural thermal mass (STM) of buildings could be actively used as a storage [8–10]. This work focuses on the latter approach since no dedicated technical storage must be purchased and accommodated within the building when using STM. However, there are several technical, social and energy policy based boundary conditions, which strongly impact the viability and the potential of employing STM as a storage in residential buildings.

Technical challenges mainly arise from the required transition from fossil fuel powered heating systems to electricity driven systems as heat pumps (HP) or direct electric heating [11,12]. Additionally, a communication infrastructure between the power grid and the potentially flexible consumers has to be established. Moreover, the energy only market (EOM) currently established in Germany and in other European countries does not provide any motivation for flexible, grid supportive electricity consumption, since

---

Nomenclature

Symbols and units

A	Surface area (m^2)
c	Specific heat capacity (J/(kg·K))
$c_{i,y}$	ARX fitting parameter (−)
clo	Clothing insulation (−)
ΔT	Temperature difference (K)
e_i	Shielding coefficient (infiltration) (−)
ϵ	Emissivity (−)
ϵ_i	Height correction factor (infiltration) (−)
η	Efficiency (%)
I	Irradiance (W/m^2)
l	Length (m or cm)
λ	Thermal conductivity (W/(m·K))
m	Mass/weight (kg)
met	Metabolic equivalent of task (−)
n_{50}	Air tightness (1/h)
occ	Occupancy (0/1)
ρ	Density (kg/m^3)
T	Temperature (K or °C)
T_o	Operative temperature (°C)
TC	Temperature change rate (K/h)
t	Time/time step (s, min or h)
V	Volume (m^3)
P	Power (W)
$\vec{X}$	Vector of exogenous ARX variables (−)

Symbols description

ARX	Auto regressive model with exogenous inputs
abs	Absolute
DSM	Demand side management
EnEV	German energy saving ordinance
EOM	Energy only market
el	Electrical
exceed	Exceedance of the rate of temperature change
FE	Final energy
FED	Final energy demand
GFLOP	10^9 floating point operations per second
HVAC	Heating ventilation and air conditioning
HP	Heat pump
heat	Heating
LS	Load shifting
LSiTD	Load shifting induced temperature drift
MPC	Model predictive control
max	Maximum
min	Minimal
NSH	Night storage heater
n	Normalized value
n/a	Not applicable
o	Operative (temperature)
out	Outside
opt	Optimal/optimization
PE	Primary energy
PEF	Primary energy factor
PH	Passive house
PI	Proportional integral (controller)
PMV	Predicted mean vote
PPD	Predicted percentage of dissatisfied
PRBS	Pseudo random binary signals
PV	Photovoltaic
p	Processor
RMSE	Root mean square error
RP3	Raspberry Pi 3

RTP	Real time pricing (electricity)
STM	Structural thermal mass
set	Set temperature
shortwave	Shortwave radiation
TABS	Thermally activated building systems
TCVI	Temperature change violation index
TIO	Thermal insulation ordinance
TOU	Time of use (electricity pricing)
TRY	Test reference year
TVI	Temperature violation index
WS	Workstation

customers pay for the consumed energy regardless of the consumption pattern. Market models have to change in order to provide incentives for customers to adapt their consumption behavior. Energy policy has to motivate a change towards innovative electricity tariffs comprising dynamic pricing, dependent on the currently available electricity generation [12,13]. Finally, appropriate control algorithms have to be developed to demonstrate the viability of thermal mass activation in the residential building sector. These algorithms have to perform STM activations based on a given economic or ecological control signal, while ensuring constantly the thermal comfort for residents.

The focus of this work is developing and evaluating the performance of such a control algorithm for STM activation. To enable adaptability of the algorithm in diverse residential buildings, the control should be functional without sophisticated measurement equipment or detailed knowledge of building specific physical parameters. Despite such simplicity, the control has to beneficially utilize the available STM, while avoiding violations of the thermal comfort boundaries.

1.2. Structure of this work

The basic foundations and literature for STM activation and residential load shifting are presented in Section 2. Furthermore, the corresponding state of research is elaborated and the field of required research is presented. The objectives and the approach for the development of the control algorithm are described in Section 3, along with the introduction of utilized tools, methods and boundary conditions employed for the performed simulation, optimization and evaluation in this work. The simulation results of the algorithm's operation are presented in Section 4, focusing on the resulting thermal comfort, the load shifting efficiency and the sensitivity to different building standards. The computational effort and energy demand of the algorithm's operation are calculated as well. In Section 5, these results are discussed and evaluated with an additional focus on the limitations of the current work and suggestions for future work. Finally, conclusions are drawn in Section 6.

2. Foundations and literature

2.1. Activation of structural thermal mass

Generally, the structural thermal mass (STM) of a building is the cumulated heat capacity of the construction materials utilized to build it. Practically, it makes also sense to consider the furnishing in a building as STM, since it contributes significantly to the thermal behavior of the total building, as discussed in [14]. However, the thermal storage capacity of the STM becomes only evident and usable when variations of the temperatures within a building enable the activation, thus the charging and discharging of some fraction of that mass. The acceptability of such required temperature

variations by the building's residents was evaluated in an extensive preceding experimental study [1]. The acceptable temperature range as well as the maximum rate of temperature change derived in that study will be applied as boundary condition for STM activations in this work. In the context of this work, the activation of STM is utilized and evaluated as an alternative thermal energy storage approach and a measure of gaining thermal flexibility in the context of load shifting (LS) and demand side management (DSM).

2.2. Load shifting in residential buildings

In the context of power supply, demand side management is the general concept of influencing the consumers' energy demand with respect to the consumed amount of energy in general and the specific time dependent consumption behavior [15]. The main purpose is to actively change the consumers' load-shape according to the current availability of electricity in the power supply system [16]. This includes consumption modifications of both, the time pattern and magnitude of the required load. The concept of DSM itself is generally not new, and many applications can be traced back to times when the constant operation of inflexible nuclear or lignite base load power plants was more important than energy efficiency. Today, many viable DSM activities are summarized with the term load shifting, since it combines several typical DSM activities as peak clipping or valley filling. Motivated by the increasingly fluctuating and partially even negative electricity prices on the European electricity markets (e.g. the European Energy Exchange), DSM potentials of large industrial customers have been widely investigated [17,18].

There are only few DSM activities for the residential sector, mostly being based on static, daily repeating time of use (TOU) pricing schemes, motivating the consumers to shift consumption towards the nighttime [19]. Today, the main application in Germany are night storage heaters. [19–22]. However, it was shown that with the dissemination of suitable heating systems, thermal demand side management in residential buildings has great potential for stabilizing the future power grid [7,20,23,24]. Exemplary, HPs are operated according to an external signal indicating shut-off periods during peak consumption times, and first solutions for coupling the heat pump operation to the local PV generation are also available [25].

The thermal demand of residential buildings is usually not very flexible itself, since it is strongly correlated with the interior temperatures and thus with the residents' comfort. Since there are currently only few incentives to invest into technical thermal storage in Germany, the active utilization of the STM in buildings could be a viable alternative enable flexible operation of heating systems. The STM is already available within the buildings and it neither induces acquisition costs nor requires additional floor space for its deployment [26]. Further costs for required control equipment and electronic thermostats are far below the investment into hot water storage tanks or any other thermal storage system [20,26].

2.3. Current state of research

Generally, thermal mass activation in the past was driven by the intermittent operation of heating, ventilation and air conditioning (HVAC) systems or thermally activated building systems (TABS). The focus was on commercial cooling demands, since they required large amounts of electricity during the peak load times of the conventional power generation system [27–30]. Seldom, STM activation was also applied to heating in commercial buildings. [31] Residential utilization of STM was rarely investigated since there was no motivation to shift the heating operation of the mostly fossil fueled, thus not time dependent, residential heat generation. There-

fore, the only common manifestation of residential STM utilization is the consideration of buildings' thermal inertia when scheduling room temperature reductions at night or in unoccupied periods [32]. However, recently a transition from fossil fuels towards renewable energy sources and electrified heating systems is observed in the residential sector, resulting in an upcoming interest in residential LS and the identification of the STM as a potential source of flexibility.

Mostly, selected archetype buildings or individual thermal zones are simulated using detailed building models, which are parametrized with prescribed set temperature patterns, to evaluate the thermal behavior when STM activations are performed [8,10,33,34]. Usually, idealized simulation boundary conditions (e.g. no internal/external loads) were used in such studies. Observed temperature ranges are either limited by standardized comfort conditions or extended above these limits to evaluate the general thermal behavior of the observed buildings. Findings indicate that poorly insulated buildings can shift a larger amount of energy for a short time, while well insulated buildings can shift a smaller amount of energy over longer periods [8,10,34,35]. Furthermore, it is observed that poorly insulated buildings have significantly higher heat losses induced by STM activation, while very well insulated buildings have a strong risk of violating comfort constraints if STM activations are not well scheduled or internal and solar loads are not predicted precisely enough [8,10,33]. Still, these studies neither suggest viable control strategies for STM activation nor allow to draw conclusions upon a realistic LS potential, since the simulated idealized conditions and the evaluated thermal patterns were usually not representative for regular building operation.

Only very few studies [9,36,37] combine residential building simulations with model predictive control (MPC) and optimization approaches controlling STM activations attempting to maximize comfort and LS potential. While the general conclusions regarding the impact of building standard could be confirmed in these studies, the resulting LS potential of STM is found to be lower for model based control when compared to rule based control [36,37]. On one hand, it is driven by the MPC operation, which minimizes comfort violations at the cost of a slightly lower LS potential [37]. On the other hand, the utility functions required to optimize the operation of a given system typically indicate profitability of STM activations only for limited periods, thus also limiting LS activities.

2.4. Field of required research

The field of STM activation in the residential sector was just recently identified and only few studies focused on the real applied potential of STM activation for residential LS. For large commercial buildings, the development of tailored control solutions for every large project can be applicable. However, for residential application the cost of designing and parameterizing an individual MPC for any given case would likely exceed potential savings by far. Still, even for the commercial sector it was found that the control concepts should become simpler, reduce the required amount of inputs and self-learning control solutions were recommended [28].

This study contributes to the field of required research by further evaluating STM activation potential in the residential sector, focusing on real life applicability and going beyond the identification of the pure physical potential to store energy in STM. A simple and easily implementable MPC approach is developed and the resulting potential of STM activation for a residential, radiator based application is evaluated. The designed approach is easily adaptable to diverse residential buildings, operational without any prior knowledge of the local building physics and capable of stand alone MPC calculations without extensive computational expenses. For testing purposes, the MPC is embedded into a detailed

physical building model representing the 'reality' feedback for the controller and allowing evaluation of the control performance with respect to energy use, storage performance and comfort compliance. The STM activation is controlled by a dynamic primary energy factor (PEF) signal, representing the expected future share of renewable energy in the German power system [38]. The underlying comfort restrictions are based on an extensive preceding experimental study, giving detailed insight into the actual acceptability of the thermal conditions resulting from residential STM activation [1]. In particular comfort criteria are taking into account the current activity of the people and incorporate the temperature change direction as an additional factor to the sole room temperature. The observed comfort restrictions are further specified in Section 3.3.2.

3. Approach

3.1. Concept and objectives

To enable the assessment of thermal conditions and energy demands resulting from different control approaches, a detailed physical building model (further explained in Section 3.2.1) is utilized to represent a real building, which would be actually controlled in reality. For a declared 'test room'[1] within the modeled building, heating operations are controlled either by the developed MPC algorithm or, for reference purposes, by a rule-based control. The MPC algorithm generates a simple black-box model based on the thermal behavior 'measured' from the physical simulation and uses that model to estimate future thermal conditions, as required for an optimized operation of the heating system. The algorithm constantly aims to find optimal operative temperatures, which ensure thermal comfort for the residents while minimizing the PE demand of heating operations, based on a dynamic PEF [38]. The performance of that control algorithm is evaluated for an observed period of two months in late winter/early spring (February 1st till March 31st). This period is selected, since the yet cold ambient temperatures induce a continuous heating demand, while the PV generation of this period is already prominent enough to ensure regular fluctuations of the PEF. The chosen period is likely to constitute favorable boundary conditions for STM activations and is therefore suitable to assess the general viability of this approach.

The control algorithm developed in this work includes a rule-based and a model predictive part. The control is designed to start functioning with no system information and collect required data during its operation. The algorithm requires the current local ambient temperature and global solar irradiation, both available with high granularity from online weather services. Further, the occupancy of the building, the heating system's set temperature and the current operative temperature is required. Solely the measurement of operative temperature is actually challenging, however, it can be approximated with sufficient precision through the indoor air temperature and inner surface temperatures, which is either measured or estimated from the indoor/ambient temperature difference [39]. Alternatively, operative temperature can be measured with a ordinary temperature sensor placed in a small matte black sphere with the size of an ping pong ball [40]. In this work, a perfect occupancy profile for the observed room is assumed to be known. In reality, such occupancy profiles can be locally generated based on collected statistical occupancy data and modeled with at least reasonable precision, as long as no person specific high level positioning is required [41,42]. For example, the required occupancy signals can be collected from simple motion detectors.

At the beginning of the algorithm's operation, the control system functions rule-based. It controls the set temperature to ensure

the comfort operative temperatures while the observed room is occupied. When the room is not occupied, pudoseudo random binary signals (PRBS) [43] are selected as set temperature for the heating system, to gather more diverse measurement data for model fitting. Based on these excitations and all other available measurements, an auto-regressive black-box model with exogenous inputs (ARX) is fitted and the resulting model is updated daily. The model's accuracy is evaluated via root mean square error (RMSE) calculation, considering the model applicable if an error of less than 1 K is identified between temperature measurements and average predictions for the last three days. This model is then used for the optimization of the heating operation and if an optimal heating schedule is found, the MPC is applied. The optimization uses dynamic constraints for comfortable temperatures and rates of temperature change [1], as well as the objective of minimal PEF. If no optimal solution can be found, the basic rule-based control is applied again. The control algorithm is written in the programming language *Python*, which executes *MATLAB* for ARX model fitting, *Gurobi* for the optimization of heating operations and *Dymola/Modelica* for the 'reality' simulation.

3.2. Building simulation

3.2.1. White box model representing the controlled building

The physical white box model used in this work to represent the controlled building and generate 'measurement' feedback for the control system was built upon the *HouseModels* Library, which is part of the *AixLib* Library made publicly available by the Institute for Energy Efficient Buildings and Indoor Climate at the RWTH Aachen University [44,45]. The thermal building models are developed in the modeling language *Modelica* and used in the simulation environment *Dymola*. These dynamic models include detailed representations of all structural components and physical properties of the utilized materials and account for the interaction with the surrounding environment. The *HouseModels* Library has been previously validated with several test cases, for example with the ASHARE Standard 140 [46].

Simulations in this work utilize a model of a generic residential two-story detached one family house with 150 m² heated floor area built out of aerated concrete and insulated with mineral wool according to the German energy conservation ordinance EnEV 2009 [47]. This standard is chosen, since it represents an average modern German building constructed or retrofitted ever since 2009 [47,48]. Still, as a measure of sensitivity analysis, the performance of the developed algorithm was also observed when changing the building's insulation thickness and air-tightness, as indicated by the German thermal insulation ordinance (TIO) 1984 [49] and passive house (PH) standard [50]. The detailed description of all construction materials and their thermal properties is given in Table A.2 through Table A.8 in the appendix, while an overview of the main U-values is given in Table 1. The layout of the first floor of the modeled building is depicted in Fig. 1. On this floor, a room with the label 'test room' can be found. This room is considered for further evaluations in this work, while the surrounding rooms are providing the thermal boundary conditions. The room is 2.6 m high and has two windows of 1.8 m² area each. The room is modeled with one air volume, its space-enclosing structural com-

Table 1
U-values in W/(m²·K) representing TIO 1984, EnEV 2009 and Passive house standard.

Standard	Window	Outer wall	Floor slab	Ceiling to attic
TIO 1984	2.5	0.54	0.52	0.21
EnEV 2009	1.3	0.28	0.33	0.21
Passive house	0.8	0.14	0.26	0.21

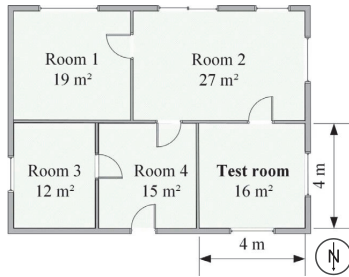[1] As depicted in Fig. 1 in Section 3.2.1.

Fig. 1. Layout of the first floor of the modeled building.

ponents and a radiator based heating system based on components of the AixLib [44,45]. The space-enclosing structural components can be distinguished in heat storing components (e.g. walls, ceilings and floor-slabs) and non-storing components such as windows and doors. The heat storing structural components are further composed of multiple material layers like plaster, flooring, aerated concrete or screed. These main materials were further subdivided into very thin layers of maximum 20 kJ/(m²·K) or 2 cm thickness for insulating materials, to ensure a very detailed representation of the thermal building behavior. All structural components and layers were connected to adjoining components, layers, the indoor air or the outer environment by the applicable means of conduction, convection, radiation or mass flows depending on the individual thermal properties of the given component.

Infiltration and ventilation air exchange represent the physical interaction of the air volume within any room with the ambient air. The resulting heat flow was calculated from the volumetric flow rate of ambient air into a room and its temperature. The flow rate of infiltration was calculated according to [51], whereas the ventilation air exchange was selected as 0.5 1/h according to the minimal air exchange rate as defined in [51]. Further parameters specifying the applicable air exchange are given in Table A.9 in the appendix. A preceding study indicated that especially under transient conditions, as induced by LS activities, the impact of furniture upon the simulated room temperature is significant [14]. Therefore, another adaption of the AixLib models was the integration of thermal structures representing the furniture within a room. The rooms furnishing was described in a simplified way by thermal capacities with properties of wood and metal, accounting for the assumed thermal mass and surface area of these materials in a given room [14]. Accordingly a correction was introduced, to account for the wall surface area covered by furnishing and therefore not included in the convective and radiative heat exchange within the room. The properties of the modeled materials, which represent the furnishing for each room of the simulated building, are given in Table A.1 in the Appendix.

For the purpose of this analysis, it is not substantial to model the heat generation system in detail. Heat is generated by an ideal heat source, which is connected to the hydraulic, radiator based heating system in the observed 'test room'. A nominal heating load of 829 W was calculated for the observed 'test room' according to [51], including a heat-up factor of 16 W/m², as suggested for buildings with a moderate nighttime temperature reduction. Therefore, the modeled 'test room' is equipped with a type 22 steel panel radiator[2] with a nominal power of 854 W. In the sensitivity analysis, the observed room's radiator is adapted to a 1065 W model for the TIO 1984 case, and a 411 W radiator for the PH according to [51] and [52]. Heat emission of the radiators is controlled by a

conventional proportional integral (PI) controller, thus assuming a high quality level of thermostatic control. The flow and return temperatures for the heating system are 55 and 45 °C respectively, as designed for a low temperature heating system according to [53]. A share of 70% convective and 30% radiative heat flow was assumed [52,54]. All other rooms in the simulated building are not equipped with radiators, but controlled by ideal heat flows to maintain constantly a temperature of 22 °C. This is crucial to enable ideally constant boundary conditions for the observed room, despite the dynamically changing weather conditions impacting also the other rooms of the building. This allows at least partially to decouple the performance of the algorithm from impacts of the chosen building geometry.

3.2.2. Black-box model for predictive control

The MPC relies on a simple ARX[3] black-box model to forecast the operative temperature within a controlled thermal zone. ARX models have been widely integrated in MPC and were successfully used to optimize energy consumption in the commercial building context [31]. However, non-linear models with higher complexity have been found to perform better [55]. Several methodologies for appropriate model choice exist [56,57], and have been consulted during the selection and development of a suitable model for the given control challenge. As a trade of between precision and simplicity an ARX model was selected in this work. The finally selected modeling approach and the structure of the ARX model are presented in the following section.

The model is designed to predict the operative temperature, as it better characterizes the comfort of the occupants. The prediction of the operative temperature required for MPC algorithm consists of two parts. First, the auto-regression calculation, which is a weighted sum of the variable's own previous values. Second, the exogenous variables, which include the impacts of other factors influencing the operative temperature, adding their weighted values from the previous and current time step. Underlying exogenous variables are the solar irradiation ($I_{shortwave}$), the set temperature (T_{set}), the ambient temperature (T_{out}), and the thermal zone's occupancy (occ). Thus, in this model, the uncontrolled heat gains within the heat balance are represented by solar irradiation and occupancy, the controlled heating power is represented by the operative temperature and the set temperature, whereas the heat losses are represented by the ambient temperature and the operative temperature. Such simple model structure was purposely chosen, to prove the model's applicability in real-life implementations with poor availability of measurements and very limited computational capacities. The choice of input variables is further supported by common gray-box and state space models, which typically utilize similar inputs for the temperature prediction in buildings [58].

The presented input variables were chosen based on the following considerations:

- Required variables are available from online sources (e.g. weather data from online services) or can be measured/estimated without complex and expensive equipment.
- Selected variables contain the minimal, though sufficient, information to formulate the total heat balance of a given thermal zone.
- The model is simple enough to be computed and optimized without the requirement of high performance computing.

A third order ARX model with 15-minute time steps is used. This means that three previous values of the operative temperature are used as the auto-regressive input for the prediction of the upcoming value. The respective time steps are referenced in square

---

[2] adapted from: Kermi therm-x2 Profil-V, [52].

[3] auto-regressive model with exogenous inputs.

Table 2
Implemented dynamic thermal boundary conditions for operative tempearture.

Occupants Time range	Not present n/a	Active 7 a.m.-6 p.m. 11–12 p.m.	Inactive 6-11 p.m.	Sleeping 12 p.m.-7 a.m.
Dynamic temperatures	in °C			
Minimal temperature	19	20	22	19
Optimal temperature	19	21	23	20
Maximal temperature	24	23	25	22
Dynamic gradients	in K/h			
Increase towards $T_{o,opt}$	no limit	3	3	1
Increase away from $T_{o,opt}$	no limit	1	2	1
Decrease towards $T_{o,opt}$	no limit	2	1	1
Decrease away from $T_{o,opt}$	no limit	1	1	1

brackets in the following, where [t] is the current time step, [t+1] the predicted time step (t+15 min), [t-1] the previous time step (t-15 min), etc. Similarly, three time steps of the exogenous variables are taken as inputs, however, here the parameters of the actual predicted time step [t+1] are assumed to be available. The model order was selected based on a literature review by [43], which indicates good performance for third order model structures. The resulting structure of the ARX model is presented in Eqs. (1) and (2). In Eq. (1), T_o is the operative temperature, $c_{i,y}$ are the ARX fitting parameters, and $\vec{X}$ is the vector of exogenous variables (specified in Eq. (2)). The parameters are computed using the ARX model identification function 'arx' in MATLAB [59].

$$T_o[t+1] = \vec{c}_{0,\vec{X}} \cdot \vec{X}[t+1] + \vec{c}_{1,\vec{X}} \cdot \vec{X}[t] + \vec{c}_{2,\vec{X}} \cdot \vec{X}[t-1]$$
$$+ c_{1,T_o} \cdot T_o[t] + c_{2,T_o} \cdot T_o[t-1] + c_{3,T_o} \cdot T_o[t-2] \quad (1)$$

$$\vec{X} = \begin{pmatrix} T_{set} \\ I_{shortwave} \\ T_{out} \\ occ \end{pmatrix} \quad (2)$$

3.3. Boundary conditions and parametrization

3.3.1. Weather data

To ensure that simulations are performed based on representative environmental boundary conditions, weather data from the test reference year (TRY) [60] for the German Lower Rhine region (western Germany - TRY region number five) was applied. This data was used for both simulations, the white box 'reality' representation and the ARX model utilized in the optimization process of the MPC. Thus, a perfect weather prediction was assumed to be available for the MPC. Taking into account that the optimization is performed for a horizon of 24 h and repeated hourly, it is likely that weather predictions with high quality would be actually available for the observed period.

3.3.2. Comfort boundaries

Comfort boundaries for the MPC were taken from a preceding experimental study focused on the perception of transient thermal conditions induced by residential load shifting activities [1]. The major findings of the named study are the impact of the peoples activity level and the relevance of the temperature change direction. Thus, whether there is a change towards a more or a less preferred temperature, has a crucial impact upon the acceptable extent and change rate of temperature deviations. This stands in great contrast to conventional comfort criteria focusing solely on the absolute temperature and treating all types of temperature changes equally. The dynamic comfort constraints adapted from [1] and used in this analysis are presented in Table 2, whereas the actual dynamic temperature profiles resulting from assumed

Table 3
Internal gains and the division into convective and radiative heat flow according to [64].

Gain	Power (W)	Convective (%)	Radiative (%)
People	125	50	50
Lights	65	50	50
Appliences	100	60	40

activity patterns are visualized in Fig. 2. Exemplary activity patterns are used to implement different comfort constraints for active, inactive and sleeping occupants. It is assumed that occupants present throughout daytime are rather active (cooking, cleaning, etc.), whereas they will have a lower activity level in the evening (watching television, reading a book, etc.). Further, it is assumed that activity increases again in the last hour before nighttime. Since the impact of LSiTD upon the thermal perception of sleeping occupant was not evaluated in the underlying study, nighttime comfort temperatures were selected according to the PMV/PPD[4] approach [61].

Conventional comfort boundaries derived from current international standards [61–63] were used for comparison in two reference and one of the observed optimization scenarios. Based on these standards, an operative temperature of 22 °C is assumed to be the optimal comfort temperature for the observed residential conditions, when generalizing across all activity conditions. Furthermore, temperature fluctuations of up to ±2 K with rates of temperature change below 2 K/h are expected to be widely acceptable, with on average less than 10% of the people being dissatisfied with the resulting thermal environment.

3.3.3. Occupancy and internal loads

Internal loads representing the heat emission of occupants, appliances and lights were determined according to [64] for the white-box 'reality' model. In this simulation, it is defined that the 'test room' is occupied by one person performing sedentary activities. All internal heat gains are described in Table 3.

The occupancy of the observed room was predefined by a generic occupancy profile, generated based on the approach of Richardson [65]. This method generates statistically based occupancy time-series with daily changing profiles and general differentiation between weekdays and weekends. Therein, occupancy is defined as the actual presence of an active person within a given zone at a given time, thus resulting profiles are suitable for most residential zones except for the bedroom. Therefore, in this work, for the case of room occupancy, all internal loads are assumed to be active, whereas no internal loads are considered when the room is unoccupied. Thus, as a simplification, potentially existing minor

---

[4] PMV: predicted mean vote, PPD: predicted percentage dissatisfied.
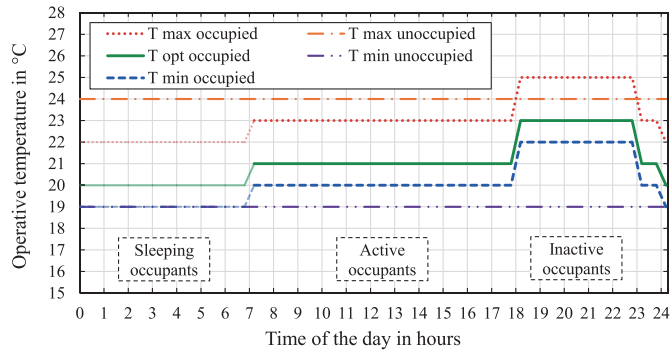
Fig. 2. Temperature boundaries implemented in the MPC.
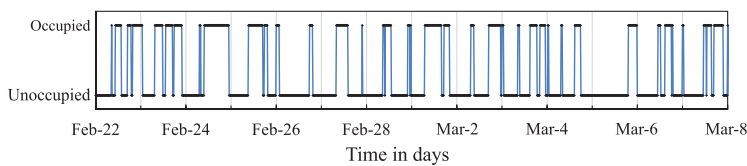
Fig. 3. Exemplary two weeks of the underlying occupancy profile.
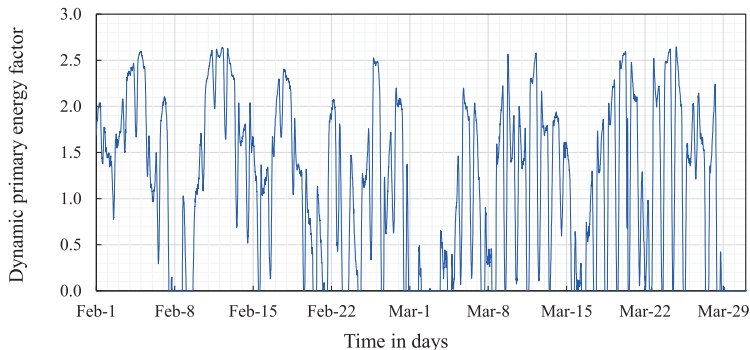
Fig. 4. Dynamic primary energy factor profile utilized for the optimization of MPC operation.

heat gains from the standby of appliances are neglected, whereas moderate lighting is assumed to be always used in the occupied room. The estimated total thermal load from appliances and lighting of 165 W is assumed to be a good approximation of average heat emissions in an occupied residential room based on [64]. Fig. 3 exemplary presents the occupancy profile for two weeks in the middle of the observed two month period. It can be seen that the profile is irregular, comprising both long periods of presence and absence as well as quick changes between these two conditions. Based on this profile, the 'test room' is on average occupied for 34.5% of the observed period, therein 21.5% in phases when occupants are considered active, 11.8% in inactive phases and since the defined zone is not a bedroom, it is only occupied 1.2% of the nighttime.

3.3.4. Dynamic primary energy factor

The utility function for the MPC algorithm is based upon a dynamic primary energy factor, enabling the minimization of the PE demand for heating purposes. This factor is adapted from the work of [38], where a fluctuating PEF is calculated based on actual time series of the German electricity demand and renewable genera-

tion from wind power and PV in 2015. The underlying time series are taken from publicly available measurement data of the four German transmission system operators [66–69], whereas the general PEF values are based on the definitions in German legislation and standardization [70]. The resulting profiles can be additionally scaled to represent any given share of renewable electricity generation in the power system. In this work the PEF is scaled for a renewable generation share of 80% as targeted by the German government for the year 2050 [11]. In this way, the utilized profile ensures enough fluctuation to actually enable a dynamic operation of the heating system, as required for LS and STM activation. The resulting dynamic PEF signal for the two-month period observed in this analysis is presented in Fig. 4, whereas average PEF values for different phases of the observed period are given in Table 4.

3.4. Model predictive control

3.4.1. Self-learning model predictive algorithm

An overview of the designed control algorithm is given as a flow chart in Fig. 5 and its functionality is described in the following. The control algorithm is executed once per hour. For every

Table 4
Average PEF for different occupancy phases of the observed period.

Occupants	Not present	Generally present	Active	Inactive	Sleeping	All phases
Average PEF	1.18	1.00	0.77	1.40	1.39	1.12

iteration, it is first evaluated whether an adequately accurate ARX model is available. If this is the case, the dynamic heating mode is activated and the MPC attempts to optimize the heating operations for a time horizon of 24 h. If an optimal heating operation is found, the first hour of the optimized set temperature schedule is used as actual set temperature profile for the heating system. It is also possible that the optimization fails, meaning that there is no solution found for the observed optimization problem. This can occur, for example, when the violation of comfort constraints within the optimization horizon cannot be successfully prevented by any possible heating control measures. One reason for that could be high uncontrollable internal or solar heat gains, making it impossible to stay within comfort constraints.

When no adequate ARX model is available or the optimization fails, one of the alternative rule-based control modes is selected. While the building is occupied, the comfort mode is activated, thus setting optimal comfort temperatures according to the current activity level of the residents. However, if the building is not occupied, the algorithm checks whether system identifications can be performed. If ambient temperature is lower than the minimal acceptable building temperature (19 °C) and the current PEF is not higher than its yearly average value of 1, the identification mode is activated. The heating system then receives pseudo random signals [43] as set temperature. Thus, the diversity of heating operations and measured temperature patterns increases, allowing generation of better fitted ARX models. When the building is unoccupied but the requirements for system identification are violated, the energy saving mode is selected and the minimal temperature for unoccupied conditions (19 °C) is defined as set temperature. The set temperature profile for the upcoming hour is then compiled from the operation modes individually selected for any 15 min time step.

Finally, the complied set temperature profile for one hour is simulated within the physical model and resulting operative temperatures are returned to the control algorithm as measurement values for its next iteration. Furthermore, once a day all gathered measurements are used for fitting of new ARX models.

The ARX model is fitted for the first time when measurement data of at least one week is available, utilizing the *arx* function [59] in *MATLAB*. The first four days of that week are used for fitting and subsequent three days to asses the model's accuracy. If more data is available, fitting horizons of 1 to 12 weeks are used to fit several models and the most accurate model of these is selected for the MPC operation. The maximum fitting horizon of 12 weeks is selected since the thermal behavior of a building is distinctly varying from season to season, thus the quality of a data-driven model fitted across many seasons is likely to decrease. Since the evaluated period in this analysis comprises only 59 days, the algorithm is provided additionally with simulated measurement data for one month before the observed period, to allow better observation of utilized fitting horizons. New model parameters are fitted every 24 h. After every fit, the model's accuracy is assessed through the calculation of the RMSE between operative temperature 'measurements' from the 'reality' simulations and estimations calculated based on the fitted model. Independently of the actually utilized fitting horizon, the data of the last three days is excluded from fitting and used for the accuracy assessment, calculating an average RMSE value for these days according to Eq. (3). If the found average RMSE is below 1 *K*, the model's accuracy is assumed adequate and the model will be used for MPC. This threshold is selected, since it represents already a decent estimation for such a simplified model, and since temperature deviations of ± 1 *K* from optimal comfort temperatures are still in the comfort range according to both the conventional and the dynamic comfort constraints. When the calculated RMSE is larger, the control will use the last model that was found accurate enough. If the currently fitted model is found inadequate and the last model fulfilling quality criteria is older than 3 days, the ARX model is not used for MPC until the next successful model fit.

$$RMSE = \frac{1}{3} \sum_{d=1}^{3} \sqrt{\frac{1}{24 \cdot 4} \sum_{t=(d-1)\cdot 24+1}^{24\cdot 4 \cdot d} (T_{predicted}(t) - T_{actual}(t))^2}$$
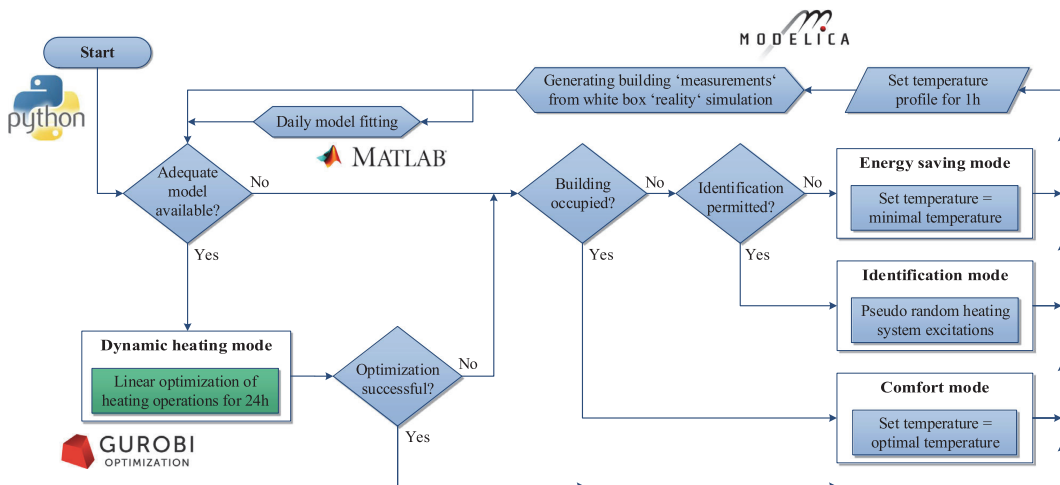
(3)

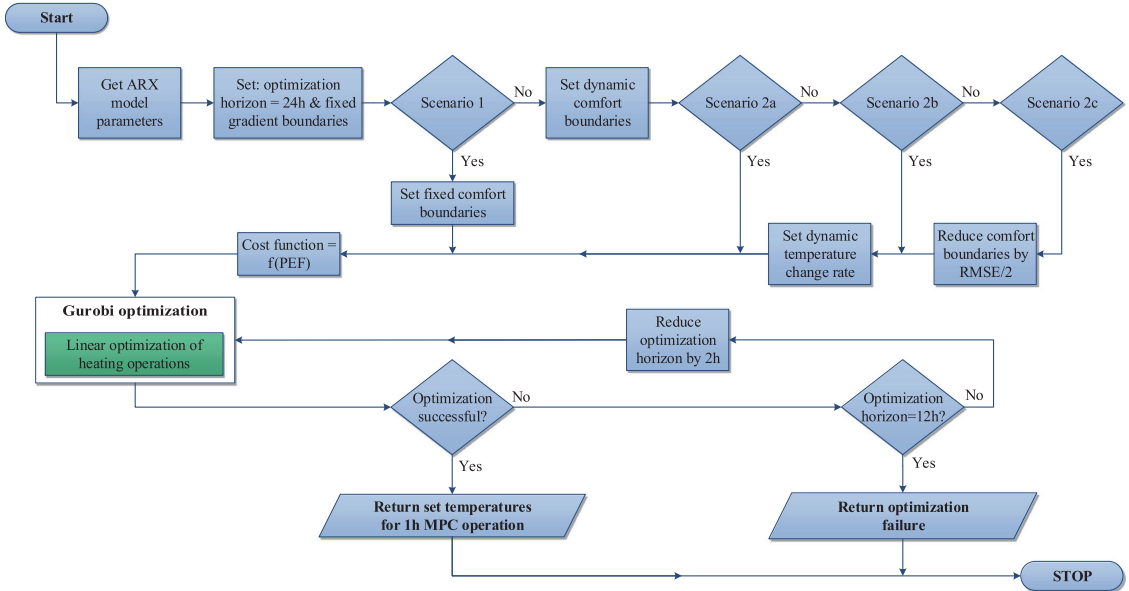**Fig. 5.** Flow chart of the implemented heating control algorithm.

Fig. 6. Flow chart of the implemented optimization procedure.

3.4.2. Optimization

When an applicable ARX model is available, the dynamic heating mode is activated, thus the control algorithm attempts to perform heating operations based on the MPC, minimizing the PE demand for heating. An overview of the optimization procedure is given as a flow chart in Fig. 6, while the individual steps of the approach are explained in the following.

Generally, the optimization minimizes the PE required for the heating operation by minimizing the PEF weighted difference between the set temperature and the actually minimal acceptable operative temperature at all times. The utilized hourly changing PEF based on the findings of [38] allows correlating the chosen set temperature and the actual PE demand in the cost function given in Eq. (4). The dynamic PEF for the upcoming 24 h is expected to be known and available for the optimization. The cost function is minimized over a horizon of 24 h with a time step of 15 min. However, only the outcomes of the first optimized hour are returned as set temperatures for the MPC, while the optimization is repeated once every hour.

$$\min_{T_{set}} \left(\sum_{t=1}^{24 \cdot 4} PEF(t) \cdot (T_{set}(t) - T_{min}(t)) \right) \qquad (4)$$

Four different optimization scenarios are implemented to test the potential of the developed algorithm, each with different static or flexible thermal comfort constraints. In scenario O1, fixed conventional comfort constraints are applied at all times, being 22 ± 2 °C, with maximal temperature changes of 2 K/h. The dynamic comfort constraints (as presented in Fig. 2), which change according to occupancy and occupant activity, are utilized in scenario O2a together with the conventional temperature change restriction of 2 K/h and in scenario O2b with the dynamic rates of temperature change. Finally, in scenario O2c, the calculated RMSE is utilized to improve the model's compliance with the comfort limits. Thus, the applicable dynamic constraints are narrowed by subtracting half of the currently calculated RMSE from the higher and adding RMSE/2 to the lower limit. Since the maximal allowed RMSE is 1 K and the range of acceptable temperatures in occupied times is 3 K, a reduction of this range by more than 2·RMSE/2 would strongly reduce the potential for STM activation. Thus, half of the currently calculated RMSE is chosen as a trade-off between comfort improvement and optimization potential. The specific comfort constraints for all optimization scenarios are given in Table 5.

For all scenarios, a linear optimization is performed in Gurobi (version 6.5.0) utilizing the Python *gurobipy* package, both developed by Gurobi Optimization Incorporation. Thereby, a deterministic concurrent method [71] is employed for this optimization. This approach starts different solvers on different threads simultaneously and chooses the results of the method that finishes first. The deterministic version of the optimization method is utilized, thus under equal boundary conditions always the same optimal solution is found. If the optimization should fail, the algorithm reduces the optimization horizon in 2 h steps down to a minimal scope of 12 h. Only if these scope reductions still do not render the problem solvable, the total optimization actually fails. It was also evaluated, whether the introduction of a slack variable making the comfort constraints slightly flexible would increase the chance of finding optimal solutions. In case that no solution for the optimization was found, the slack variable increased the comfort constraints by as much as the current RMSE, thus up to 1 K. However, this relaxation of the permissible temperature range did not noticeably increase the chance of finding an optimal solution and was therefore rejected.

3.4.3. Evaluation concept

To enable a precise evaluation of the control algorithm's performance, three reference scenarios were defined and simulated. For all reference scenarios, a rule-based control is used to implement time-dependent temperature profiles. References 1 and 2 allow the comparison of the developed algorithm with conventional building operations, keeping temperatures either constant at 22 °C (scenario R1) or reducing them in phases without occupancy and at night to 20 °C (scenario R2). In turn, reference scenario R3 is constantly

Table 5
Boundary conditions of the analyzed scenarios.

Boundary conditions	Operative temperatures when occupants are:				Rate of change
Time range	Not present n/a	Active 7 a.m.-6 p.m. 11–12 p.m.	Inactive 6-11 p.m.	Sleeping 12 p.m.-7 a.m.	at all times
Reference scenarios	in °C				in K/h
R1: Constant temperature	22				≤ 4
R2: Setback temperatures	20	22	22	20	≤ 4
R3: Optimal temperatures	19	21	23	20	≤ 4
MPC optimized scenarios	in °C				in K/h
O1:　Fixed constraints	22 ± 2 K				≤ 2
O2a: Dynamic temperatures	19–24	20–23	22–25	19–22	≤ 2
O2b: Dynamic constraints	dynamic, as in O2a				dynamic
O2c: Reduced constraints	dynamic as in O2a, but constraints reduced by RMSE/2				dynamic

following the optimal temperatures of the dynamic comfort profile and serves therefore as the main benchmark for the MPC algorithm. Table 5 presents all thermal constraints for these reference cases as well as for the optimization scenarios described in the optimization Section 3.4.2.

The compliance with the defined dynamic comfort constraints was evaluated by quantifying the violations of these constraints for each scenario and comparing them against the optimal temperature oriented reference scenario R3. For each time step (t) when the operative temperature was outside of the comfort range, this violation time (t_{out} in 0.25 h) was multiplied with the extent of the violation (ΔT_{out} in K), thus resulting in the temperature violation index (TVI), giving the total constraint transgression in Kh. Similarly, the violations of the dynamic rate of temperature change are observed, however now on a hourly base. Thus, for all full hours (h) when the rate of temperature change is exceeded (h_{exceed} in h), the extent of the violation (ΔTC_{exceed} in K) was cumulated, resulting in the temperature change violation index (TCVI) likewise in Kh.

$$TVI = \sum_t \Delta T_{out} \cdot t_{out} \tag{5}$$

$$TCVI = \sum_h \Delta TC_{exceed} \cdot h_{exceed} \tag{6}$$

To quantify the load shifting potential resulting from STM activations in an observed thermal zone, absolute amounts of stored or shifted energy are frequently stated [10]. However, such a measure is sensitive to the actually prevailing ambient conditions and the extent of the STM activation achievable for any individual occasion. In particular, the storage potential is impacted by the activation times and the temperature profiles throughout the activation phases, which are different on any single occasion when operated by an optimized MPC. Finally, with such control it is seldom possible to identify individual STM activation phases, which could be considered independent from the preceding utilization of the STM. It is therefore not viable to define an actual LS potential for individual activation phases. Thus, the potential of MPC operated LS should be quantified for a representative longer period of time, comprising a wide range of diverse STM activation, as applied by [8,9]. Also, it can be questioned if the frequently used normalization of the LS potential per m² of considered floor space is meaningful. Especially, when dynamic occupancy and activity oriented temperature profiles are utilized for MPC of STM activation, it is likely that different utilization patterns of a thermal zone will have different resulting LS potentials per m². As a result, relative measures describing the overall performance of the observed thermal zone throughout the whole observation period are chosen to quantify the LS potential in this work. Nevertheless, some absolute and m² normalized values of the LS extent will also be presented to enable comparability with existing studies.

It depends on the motivation of LS activities, whether the impact upon final energy or primary energy[5] is of larger interest. Grid-services, for example, require large FE shifting potentials, while the focus of environmentally motivated LS is on PE. Therefore, the LS performance of the MPC is evaluated based on three efficiency measures, which observe separately the absolute LS efficiency as well as the LS performance with respect to FE and PE. The absolute load shifting efficiency is defined according to Eqs. (7)–(9). This value (η_{LS}) indicates which share of additional heating energy utilized for STM activation in the MPC scenarios is actually utilized to reduce the heating demand of the room at later times, taking the heating operations in scenario R3 as a reference. Thereby, all time steps (t) when scenario R3 requires less FE than an MPC case are defined as charging phases, whereas when R3 requires more FE than the MPC case, this is observed as a discharging phase.

$$\eta_{LS} = \frac{FE_{\text{MPC discharged}}}{FE_{\text{MPC charged}}} \tag{7}$$

$$FE_{\text{MPC discharged}}$$
$$= \begin{cases} \sum_t (FE_{R3}(t) - FE_{MPC}(t)) & \forall t \in FE_{R3}(t) > FE_{MPC}(t) \\ 0 & \forall t \in FE_{R3}(t) \le FE_{MPC}(t) \end{cases} \tag{8}$$

$$FE_{\text{MPC charged}}$$
$$= \begin{cases} \sum_t (FE_{MPC}(t) - FE_{R3}(t)) & \forall t \in FE_{MPC}(t) > FE_{R3}(t) \\ 0 & \forall t \in FE_{MPC}(t) \le FE_{R3}(t) \end{cases} \tag{9}$$

Further, the final energy demand change, which compares the total FE demands in the MPC scenarios against the FE demand in scenario R3 is defined according to Eq. (10). And finally, the primary energy demand change, a similar comparison of the PE demands of the MPC scenarios against R3, is presented in Eq. (11).

$$FE_{\text{demand change}} = \frac{\sum_t (FE_{MPC}(t) - FE_{R3}(t))}{\sum_t FE_{R3}(t)} \tag{10}$$

$$PE_{\text{demand change}} = \frac{\sum_t (PE_{MPC}(t) - PE_{R3}(t))}{\sum_t PE_{R3}(t)} \tag{11}$$

---

[5] FE: final energy, PE: primary energy.

3.5. Computational performance evaluation

One of the main objectives for the development of the MPC algorithm is such simplicity that would allow implementing the suggested concept of MPC for STM activation in regular residential buildings without complex measurements, expert knowledge and expensive computations. Therefore, the actual computational effort of the performed model fittings and optimizations is estimated, being related to the expected calculation effort of a simple residential energy management system. The developed algorithm was operated on a workstation (WS) with a 64-bit Intel Xeon E5-2667 6-core CPU clocked at 2.9 Ghz, 32 GB RAM running a 64 bit version of Windows 7 Enterprise. The processor utilized in the WS has a computational capacity of 139 GFLOP[6] [72] per core. It was estimated which calculation effort would result if the developed algorithm would be operated on a Raspberry Pi 3 B (RP3) single-board computer. The system is chosen for comparison, since it is widely available at a low price,[7] has high connectivity[8] [73] and its Linux based operation system allows the usage of diverse programming and optimization codes [74]. The system selected for comparison is equipped with a 64-bit ARM Cortex-A53 4-core CPU clocked at 1.2 GHz, 1 GB RAM, running a 64-bit version of Raspbian and requiring 1.8 W in idle and 4.4 W at full load [74]. The processor of the RP3 has a computational capacity of 6.4 GFLOP, when equipped with an additional passive heat sink [74].

For this evaluation, the WS computation times for the *Matlab* based model fitting and the optimizations performed with *Gurobi* were calculated using a single core and assuming the worst case computation effort feasible in the developed algorithm. Thus, for the fitting problem, a maximal availability of fitting data was assumed, resulting in 12 ARX models that need to be calculated. For the optimization, the worst case was defined by an optimization failure, since the 7 possible optimization horizons between 12 and 24 h are calculated in this case. The actually measured computation times of the WS were converted to estimated computation times of the RP3 according to three factors, one for the utilized processor and two for the utilized software. The actually observed additional RAM requirement of approx. 400 MB when running fitting or optimization routines was not expected to be a limiting factor.

The processor oriented factor f_p is calculated based on the computational capacity of the observed platforms as a ratio of their GFLOP scores. The software oriented factors are necessary, since the utilized software *Matlab* and *Gurobi* require expensive licenses and are not operational on a RP3. Therefore, alternative software which is freely available and functioning on the Linux based RP3 is selected for this computation time estimation. Is is assumed that model fitting would be performed on the RP3 with *GNUOctave* [75], a free scientific programming language, which is widely compatible with *Matlab* syntax and scripts. According to a comparison based on 50 benchmarks [76] *Matlab* is 2.5 times faster than the *GNUOctave* software, resulting in a f_{fit} factor of 2.5. Similarly, it is assumed that the linear optimization would be performed with *Cbc* [77], which is an open-source linear programming solver. According to a comparison based on 87 optimization problems [78], *Gurobi* is up to 32 times faster than *Cbc*, resulting in a f_{opt} factor of 32. Calculation times for RP3 were estimated by multiplying the calculation times measured on WS by the presented factors.

The required FE and PE demand for the operation of the RP3 were estimated as well to compare these to the energy savings. It was assumed that the RP3 is operating in full load throughout the

optimization and fitting routines and stays idle all the remaining time. Finally, it is stressed that the described performance estimation is expected to be suitable as a rough estimation for the calculation effort the developed algorithm would require, when recoded to be operated with freely available software on a distinctly simpler hardware. The actually implemented code is not operational on the soft- and hardware described in this evaluation.

4. Results

4.1. General performance of the ARX model and MPC algorithm

All implemented scenarios are viable and the underlying control mechanisms are able to control the operative temperature within the 'test room' in a meaningful way over the total observed period. For the MPC algorithm controlled scenarios, an adequately precise ARX model was available at all times. The worst observed RMSE in accuracy estimation is 0.56 K and still well below the threshold of 1 K. A total of 1680 individual ARX models were fitted by the algorithm across all MPC based scenarios, whereof 236 were actually selected for MPC operation. Fig. 7 presents a histogram of the RMSE values achieved by all actually selected models in the accuracy estimation process. Most models selected for MPC had a RMSE in the range of 0.2-0.3 K, and 90% of the chosen models had a RMSE below 0.35 K. The average fitting data horizon utilized for the ARX models is 2.3 weeks, with a slight tendency towards longer horizons as more fitting data is available. Fig. 8 depicts the average fitting horizon of the selected ARX models in dependence
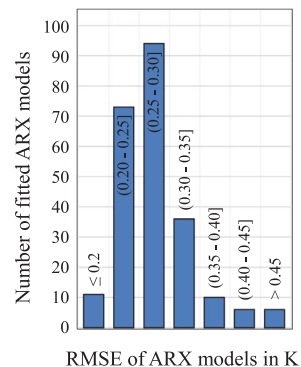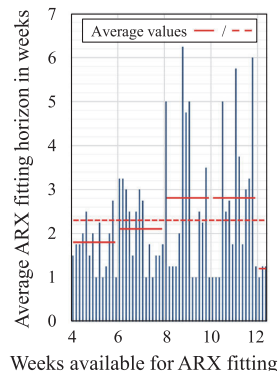
Fig. 7. RMSE of utilized ARX models.

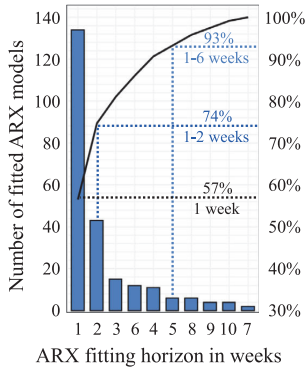**Fig. 8.** Average ARX fitting horizons.

Fig. 9. Histogram of fitting horizons.

of the actually available fitting data. It can be seen that even in the last weeks of the observed period, when more than 10 weeks of fitting data are available, the average selected fitting horizon is 2.8 weeks. A histogram of the fitting horizons of selected ARX models is given in Fig. 9, depicting that 57% of the utilized models are fitted only with the data of the past week and 74% with two previous weeks, even though data of at least 4 weeks is available for all fitting iterations. Probably, the temperature fluctuations resulting from both STM activations and building identification yield well excited measurement data for model fitting, being the reason for the observed short fitting horizons [79]. Nevertheless, 7% of selected models have fitting horizons of even more than 6 weeks. In total, 43% of the selected models were based on fitting horizons longer than one week. Thus, the approach of creating models with different fitting horizons and selecting individually the best performing model proves to be viable and superior to a fixed definition of the fitting horizon.

The dynamic heating mode is active for more than 40% of the evaluation period in all optimized scenarios, reaching a share of 64% for the O1 scenario. System identification is performed for approx. 6% of the time across all scenarios. When neither MPC operation nor identification were possible, heating is operated in comfort or energy saving mode according to the occupancy status. A full overview of the employed individual control modes is given in Fig. 10 for all optimized scenarios. When further specifying the operation times of different control modes, it can be calculated that scenario O1 operated 69% of the occupied times in MPC mode, whereas O2 scenarios were just able to find optimal control paths for 27–38% of occupied phases. Thus it can be derived that the optimization problem is distinctly easier to solve for static comfort constraints.

An exemplary sequence of the algorithm's control behavior is presented in Fig. 11 for the O2b scenario. The 'measured' and predicted temperatures are well aligned in unoccupied phases (when T_{max} is set to 24 °C) and at nighttime, with increasing deviations in phases with uncontrollable internal or solar heat gains. Still it can be recognized that the 'measured' temperature is close to the lower boundary in phases with high PEF and increases clearly when PEF is low. Periods when the set temperature is above the optimal comfort temperature are marked as STM activation phases in the lower part of the graph. These STM activations are frequently interrupted or limited, even when the 'measured' temperature is still well in the comfort range and the PEF is low. This happens either when the predicted temperature reaches the upper boundary, or when strong fluctuations of the predicted temperature prevent successful optimization and MPC is deactivated. However, due to such conservative operation, only few minor comfort violations are visible despite the distinct STM activation activities. On few occasions, the identification mode is activated, inducing significant temperature fluctuations at unoccupied phases with a PEF below average.

4.2. Resulting thermal comfort

The thermal comfort is a crucial focus point in the evaluation of dynamic STM activation, since the compliance with comfort constraints is a vital condition for the general acceptance of such LS operations. Therefore, the simulated thermal conditions of all observed scenarios are presented and evaluated in the following, with a major focus on the impact of the suggested dynamic comfort constraints upon thermal comfort. Fig. 12 depicts the resulting average operative temperatures for the individual occupancy phases over the total observed period for all evaluated scenarios. The average values for the reference scenarios are well aligned with their defined temperature profiles, not diverging more than 0.5 K from set temperatures of the active, inactive and unoccupied phases. Solely throughout the seldom and short periods of occupancy during the nighttime, scenario R2 does not reach the targeted temperature reduction. It can be concluded that the rule-based control utilized for the reference scenarios is working properly. As expected, thermal conditions in scenario R3 are well aligned with the optimal temperatures throughout all occupancy phases. Therefore, scenario R3 is meaningful as the main benchmark for the further evaluation of the observed MPC scenarios. To improve clarity, the results of reference scenarios R1 and R2 will not be further presented in the following, however they can be found in [1]. All optimized cases keep the average temperatures above the optimal temperature for active, sleeping and unoccupied phases, indicating that STM activations are actually performed. Only throughout the inactive phase, the optimized temperatures are close to the lower comfort boundary. Scenario O1, which is actually not limited by the dynamic comfort constraints, violates
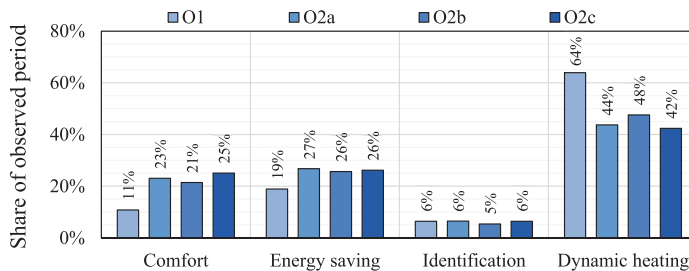
Fig. 10. Distribution of heating operations across the different control modes.
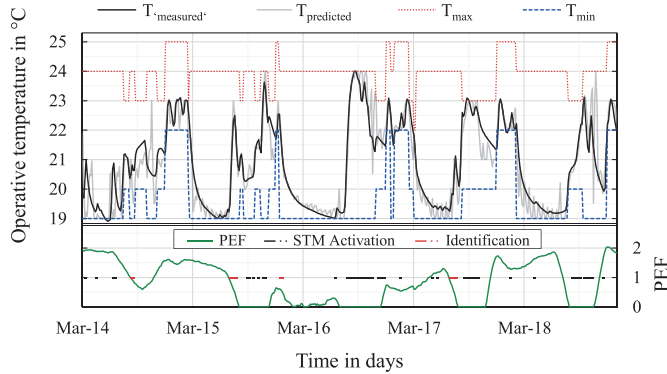
Fig. 11. Exemplary five day sequence of algorithm operation for scenario O2b.
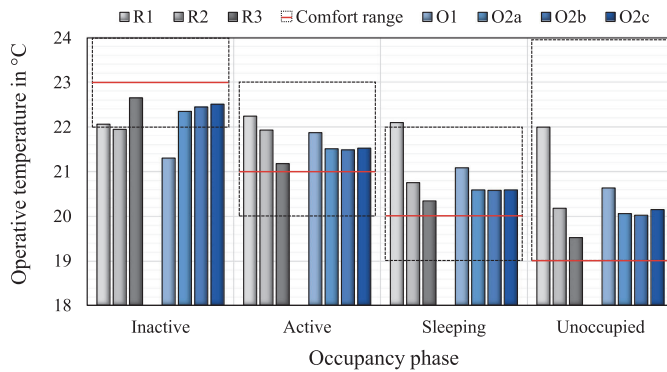
Fig. 12. Comparison of average operative temperatures across all scenarios.
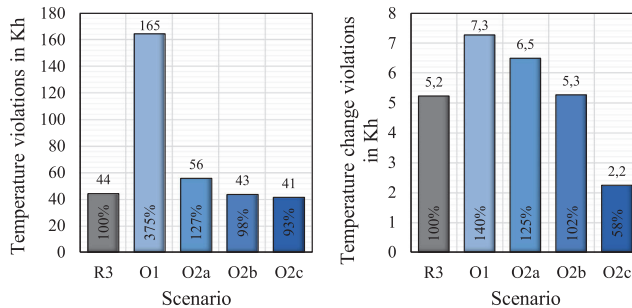
Fig. 13. Violations of dynamic temperature/temperature change constraints.

on average the minimal temperature for inactive occupants. All other MPC scenarios are on average not more than 0.7 K away from optimal temperatures for the occupied phases.

Fig. 13 depicts the TVI and the TCVI scores for all scenarios. As a benchmark, a daily temperature or temperature change violation of 1 K for 1 h would result in a TVI/TCVI score of 59 Kh for the evaluated 59-day period. Scenario R3 follows optimal temperatures at all times, thus violating given temperature limits only in the transition phases between different dynamic constraints. Thus, the TVI and TCVI values of scenario R3 can be seen as a benchmark for the lowest values, which can be reached when a rule-based control follows the dynamic temperature constraints.

MPC scenario O1, which is controlled according to conventional comfort constraints, has the highest TVI score of all scenarios and the highest TCVI rating among the MPC scenarios. It is actually not unexpected that scenario O1 performs poorly on criteria not implemented into its control. Still, the results are emphasized to indicate that a conventional STM activation approach would result in far-reaching comfort violations according to the dynamic comfort constraints applied in this work. Scenario O2a exceeds the comfort violations of scenario R3 by approx. 25% for both TVI and TCVI, whereas scenario O2b has very similar scores than R3. Finally, in scenario O2c, the adaptive limitation of the comfort range by the value of the current RMSE reduces TVI by 7% and TCVI even by
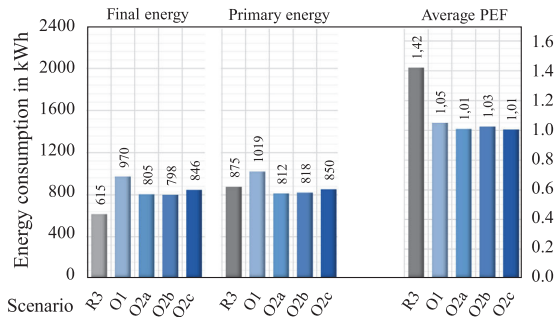
Fig. 14. Comparison of energy consumption and average PEF.

42%. TVI improvement is limited probably because model predictions were either good enough to ensure the adherence of temperature constraints anyway, or the predictions were not suitable for MPC at all. However, the adaption of comfort constraints resulted in an overall reduction of the applicable temperature range, thus limiting temperature fluctuations and clearly improving the TCVI.

4.3. Energy consumption and load shifting efficiency

Having shown that the MPC algorithm is generally capable of ensuring required comfort conditions, now the energy consumption of the individual scenarios is compared and impacts upon the final energy consumption, the average PEF and the resulting primary energy consumption are observed. Fig. 14 depicts these values for all scenarios. The MPC with conventional comfort constraints (scenario O1) has final and primary energy consumption well above these of scenarios with dynamic comfort constraints. However, the exemplary defined occupancy and activity periods in this analysis have a strong impact upon the resulting heating requirements and the choice of different periods could potentially change the results. Therefore, no general conclusion upon the energy consumption impact of conventional or dynamic temperature constraints can be made. Nevertheless, the assumption of higher occupancy and lower occupant activity in the evenings seems generally reasonable. This indicates the general challenge of increased heating demand in the evening, thus at times with hardly any PV generation and therefore higher average PEF values in the utilized profile, as presented in Table 4.

Due to the increased temperatures required for STM activation, the FE consumption of all MPC scenarios are clearly higher than in the reference scenario R3. In turn, they have significantly reduced average PEF factors, being even 6–10% below the average value of the total observed period. As a result, all O2 scenarios are able to compensate the higher FE consumption induced by the STM activation and reach PE consumption below the level of scenario R3. Solely, potentially limited through the overall smaller range of temperature fluctuations, scenario O1 can not compensate the high FE consumption with its reduced PEF. Scenarios with a PE consumption reduction (O2a-c) reached absolute FE LS volumes of 137–156 kWh for the observed 59-day period. When normalized to the size of the modeled 'test room' of 16 m^2, the LS potential is 8.6–9.8 kWh/m^2 or on average daily 146–166 Wh/m^2. Fig. 15 presents the associated LS performance of STM activation for all scenarios controlled by the MPC algorithm, always in relation to the optimal temperature scenario R3 (as defined in Section 3.4.3). The actual absolute LS efficiency is below 50% for all MPC scenarios, thus more than half of the additional FE consumption for STM activation is lost. Most of the energy is spent for maintaining temperatures above the optimal level, as indicated by the average temper-

atures presented in Fig. 12. Consequently, also the FE consumption increases with FE consumption changes in the range of 30–58%. However, driven by the reduced average PEF values, the PE consumption is reduced for all MPC scenarios controlled according to dynamic comfort constraints, reaching up to 7% lower PE consumption than scenario R3.

Fig. 16 exemplifies one of the most prominent STM activation phases within the evaluated period. The operative temperatures of scenarios O2b and R3 are compared in the upper part of the diagram, whereas the respective heating power and the current PEF are depicted in the lower part, being normalized between 0 and 1. The MPC increases the temperature substantially for a period of 12 h while the PEF is 0. As a result, the heating consumption is significantly reduced throughout the subsequent occupancy phases, which occur at times with an increased PEF. The FE consumption for the 31 h period presented in Fig. 16 is 21.7 kWh in the R3 scenario and 42.5 kWh for the O2b case. The PE consumption is 15.0 kWh for R3 and 12.1 kWh for O2b. This results in an FE consumption increase of 96% and an PE consumption reduction of 19% for the observed period. Due to the STM activation in the first 12 h of the depicted period, the FE consumption of the subsequent 19 h is reduced by 4.3 kWh, yielding an η_{LS} of 21%. If the resulting storage capacity is reported in Wh/m^2 as suggested by [8], the resulting capacity would be 269 Wh/m^2 of the final energy and 176 Wh/m^2 of the primary energy.

4.4. Sensitivity to building standard

The sensitivity of the MPC algorithm's performance with respect to the building standard is evaluated based on a comparison of EnEV 2009, TIO 1984 and the Passive House standard[9] for the reference scenario R3 and the MPC case O2b. Generally, average temperatures for the different occupancy phases are lower as in EnEV 2009 for the case of TIO 1984 and higher for PH as depicted in Fig. 17. The high heat losses in TIO 1984 enable stronger temperature fluctuations and thus better adherence to the dynamic set temperatures. However, for the reference case R3 (84), these fluctuations also induce more temperature and temperature change violations, as depicted in Fig. 18. These violations can be well mitigated in the MPC controlled O2b (84) scenario, reaching even distinctly lower temperature change violations than in the EnEV case, mainly because the MPC induced STM activations reduce the frequency of maximal permissible temperature reductions. The higher insulation level of the building envelope and the lower solar energy transmittance of the windows in the PH reduce the extent of temperature fluctuations. This also reduces temperature and temperature change violations in the reference case R3 (PH) (Fig. 18). The low temperature violation level can be even further reduced by the MPC, while temperature change violations are low in any PH scenario due to the moderate slopes of temperature fluctuations.

For the TIO 1984 standard, the heating demand is generally larger and rather continuous, resulting in a lower PEF for the reference case, since the heat up phase in the evening is not that predominant anymore. In turn, the high heat losses are minimizing the potential for STM activation and therefore also the average PEF decreases just slightly. Due to the high heat losses, the MPC has generally difficulties to predict and control the rapid temperature fluctuations, as indicated by an MPC share of just 40%, as compared to 48% in the EnEV 2009 case. Additionally, the energy charged into the STM can be just stored for short periods due to the high heat losses. Therefore, STM activations are seldom performed and

---

[9] 'EnEV 2009' or '09' refers to the energy conservation ordinance 2009, 'TIO 1984' or '84' refers to the thermal insulation ordinance 1984, 'PH' refers to the Passive House standard.

Fig. 15. Comparison of the load shifting performance across all MPC scenarios.

Fig. 16. Heating operation for an exemplary STM activation sequence in scenario O2b.

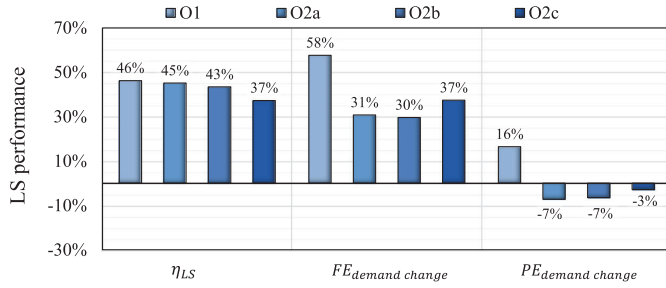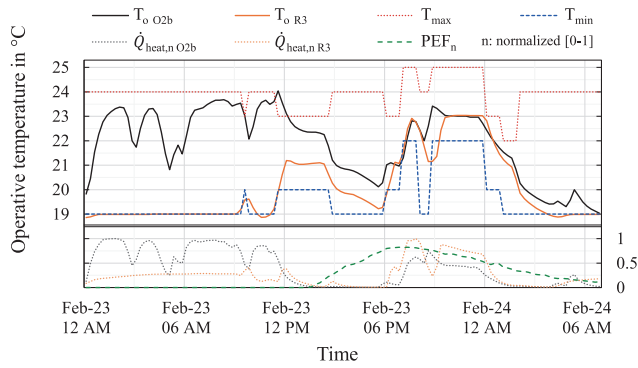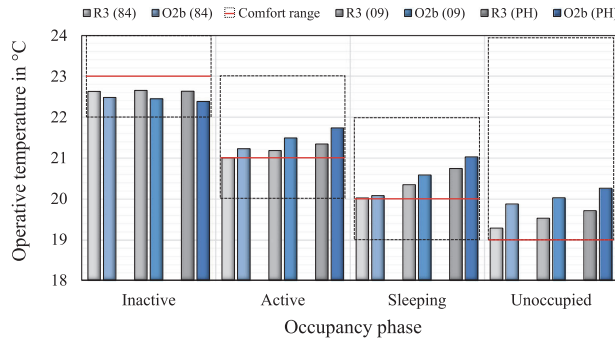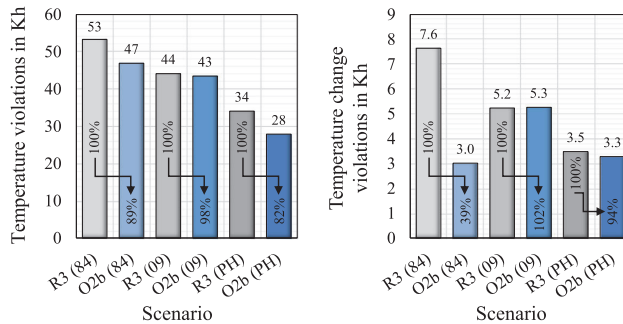**Fig. 17.** Sensitivity analysis of average operative temperatures.

Fig. 18. Sensitivity analysis of dynamic temperature/temperature change violations.
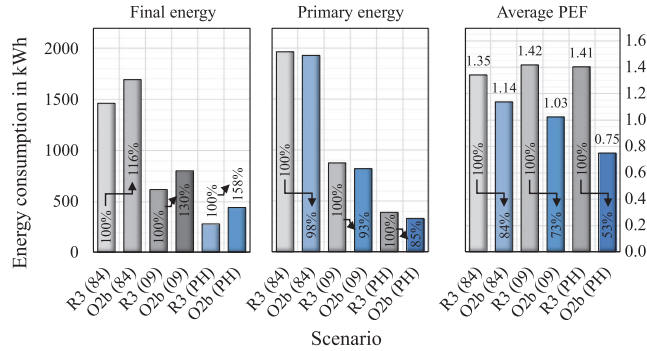
Fig. 19. Sensitivity analysis of average PEF values and resulting FE and PE consumption.

FE consumption just increases by 16%, as depicted in Fig. 19. As a result, the reduced average PEF just compensates the increased energy consumption for STM activation. The actual PE consumption is solely 2% lower than the reference scenario (Fig. 19).

In the case of the PH, the reduced temperature fluctuations enable MPC operation at 61% of the observed time, however only a limited part of the available temperature range can be actually used. Since the building cools down very slowly, even the moderate STM activation can shift heating demand across substantial periods, thus being able to concentrate most of the required heating activities in phases with lower PEF. The resulting average PEF is 47% lower than in the PH reference and even 33% lower than the average of the observed period. Still, due to the low general heating demand, the performed STM activations increase the FE demand by 58%. However, that increase is overcompensated by the very low average PEF, resulting in a 15% lower PE consumption for the PH with MPC (Fig. 19).

Despite of these differences, the absolute LS efficiency (η_{LS}) calculated from Eq. (7) is constantly in the range of 41–46% for all MPC scenarios, indicating that not the building standard dependent heat losses to the ambient, but the increase of operative temperatures above the optimal level are the main driver for the poor absolute LS efficiency.

4.5. Computational effort required for the MPC based STM activation

The ratio between the GFLOP scores of the WS and RP3 is calculated as shown in Eq. (12). Thus, it is estimated that the RP3 is 22 times slower than the actually utilized hardware.

$$f_p = \frac{139\ GFLOP}{6.4\ GFLOP} \approx 22 \tag{12}$$

Table 6 presents the actually measured calculation times of the WS and the estimated calculation times for the RP3, based on the software factors presented in Section 3.5. It can be seen that even for the worst case of the hourly optimization a calculation time of approx. 0.3 h could be expected, being well below the available time-frame of one hour. The estimated time for the worst case of daily ARX model fitting is 0.5 h, thus enabling that even both routines, the optimization and model fitting could be performed in

just one hour. This leaves enough calculation capacity to either optimize further thermal zones, increase optimization frequency, increase the number of fitted black-box models or provide entirely different smart home services.

The required energy demand for the operation of the RP3 is estimated in Eq. (13), assuming that the RP3 is operating in full load throughout the optimization and fitting routines and stays idle all the remaining time. The resulting energy demand of 3.7 kWh$_{el}$ is adjusted with the average PEF of the observed period (1.12) to calculate an estimated PE demand of 4.1 kWh$_{PE}$ for the operation of the RP3. This PE demand accounts for 7–16% of primary energy savings observed in the MPC controlled scenarios with dynamic comfort constraints, thus even in that worst case estimation of the computation effort, the MPC operation would be still beneficial.

$$W_{el} = (1416\frac{opt}{59\,d} \cdot 0.3\frac{h_{load}}{opt} + 59\frac{fit}{59\,d} \cdot 0.5\frac{h_{load}}{fit}) \cdot 4.4\frac{W_{el}}{h_{load}}$$
$$+962\frac{h_{idle}}{59\,d} \cdot 1.8\frac{W_{el}}{h_{idle}} \approx 3.7\frac{kWh_{el}}{59\,d} \tag{13}$$

5. Discussion

5.1. Viability of residential STM activation for LS activities

STM activations have regularly absolute LS efficiencies well below 50%, being lower than values of 50–90% observed by [8,10,79] for individual STM activation phases of more than 12 h. Still, the clearly higher FE demand resulting from long phases with increased temperatures is overcompensated by the reduction of the average PEF. The scenario with the best balance between comfort and LS performance (O2b) in the regular building standard reaches a PE demand reduction of 7%, while maintaining the comfort level of the optimal comfort reference (R3). The application of MPC driven STM activations can be therefore recommended based on the defined boundary conditions.

For the building with lower thermal standard (TIO 1984) the LS potential is very limited since the PE demand reduction is just 2%. Such a minor improvement might not outweigh the effort required to implement MPC based STM activation. Nevertheless, since the observed PE demand reduction come along with a minimization

Table 6
Measured and estimated worst case computation times of the MPC algorithm.

Computation time	Hourly optimization routine	Daily model fitting routine
Workstation (measured)	1.5 s	35 s
Raspberry Pi 3 (estimated)	$1.5\ s \cdot f_{opt} \cdot f_p = 1056\ s \approx 0.3$ h	$35\ s \cdot f_{fit} \cdot f_p = 1925\ s \approx 0.5$ h

of comfort violations for that building standard, the application of MPC might still be considerable. Furthermore, the absolute amount of shifted FE equals 71% of the total FE demand of the PH reference scenario R3 (PH). Especially if LS activities are considered as potential grid services, such a large absolute energy shifting potential might be valuable. For the future oriented PH standard, a PE demand reduction of 15% is reached, while even limiting comfort violations. Thus, even though the absolute amount of shifted FE is rather low, it is clearly advisable to perform MPC based STM activations in such buildings.

Although, this study proofs the proposed LS concept, considering that the results have been obtained for just two month of LS activities in a single room, the found percentages can only be seen as an indication of the potential performance. In addition to the impact of thermal standards evaluated in this work, other parameters can affect the LS potential of STM activation. Among others, the type of heating system, building materials, the occupancy schedule and the selected utility function (here PEF) will have strong impact upon the algorithms performance and resulting LS potential. Thus, before the results can be generalized to all residential buildings, several follow-up studies, favorably including field-tests, should be done.

5.2. MPC based on a simple ARX model

Both the implemented simple black box model and the developed self-learning MPC algorithm proved to be functioning and together capable of controlling STM activations in a residential building zone without any prior model parametrization. Due to temperature fluctuations, self-induced by the algorithm's operation, the measurement data covers a wide range of possible thermal conditions and allows computing accurate ARX models based on very short fitting horizons. These short horizons are likely a reason for the good accuracy of the models, because the weather conditions of the fitting data are close to these in the predicted phase. The resulting models perform well when neither internal nor solar heat loads are present, while the prediction quality deteriorates when these impacts increase. It can be concluded that these models are best suitable for thermal zones with intermittent occupancy and particularly throughout seasons with limited solar irradiance. Both criteria can be assumed to be fulfilled for the observed case of residential LS in winter. However, it can be expected that the utilized black-box models would not perform similarly well if adapted for air conditioning based LS in summer or incorporated in zones with strong and hardly predictable internal loads. Generally, the performance of the model improves when the overall amount of uncontrollable temperature fluctuations decreases. This becomes evident in the sensitivity analysis, by the increasing share of MPC operation for the building with higher insulation standard and lower solar energy transmittance through the windows.

If required for other cases of applications, the quality of the model could be significantly improved as suggested in several identification approaches by other authors [56,57]. However, in this work identifying a high-quality model was not required and not in focus. The less accurate model is compensated by a prediction quality estimation and a small (one-hour) step in recalculating the optimal heating schedule. Generally, the required frequency of re-optimization depends on the quality of the available predictions and is limited by the models complexity and resulting calculation times. In this study we show that even a very simple model with robust predictions can be beneficially used for STM activation. Due to that model simplicity the execution of the algorithm requires minimal calculation effort, whilst it is required to re-optimize more frequently. Taking a more sophisticated model would reduce the amount of required re-optimizations. It could be evaluated and discussed in future work, whether an optimum between model complexity and optimization frequency can be found.

5.3. Trade-off between comfort and LS

Operation of the heating system according to dynamic temperature constraints generally increases the risk of temperature and temperature change violations. Nevertheless, the temperature profile of the dynamically controlled reference scenario R3 is on average closer to the defined optimal temperatures than the static scenario R1 or the set-back scenario R2. It can therefore be assumed that despite a slightly increased number of comfort violations, the overall thermal conditions are not worsened by the implementation of dynamic temperature profiles. The developed algorithm is generally capable of operating according to dynamic or conventional temperature constraints. Assuming the validity of the dynamic comfort constraints applied in this work [1], STM activations according to conventional comfort constraints are clearly not recommended, since the amount of comfort violations increased strongly in comparison with any other scenario. When STM activations are performed within dynamic comfort limits, the MPC can ensure or even improve the adherence to defined dynamic comfort constraints. This indicates that despite the increased control complexity resulting from a variety of dynamically changing temperatures and temperature change constraints, the simple MPC algorithm can manage both STM activations and comfort conditions. This corresponds with the expectations formulated for model predictive STM activation by [8,9]. However, it was found than an increasing comfort performance always reduces the viable LS potential, thus indicating a trade-off between strict comfort observance and the extent of feasible STM activations.

The utilized dynamic PEF profile indicates the challenge of increasing PEF values in the evenings, when PV generation is discontinued, while the heating demand increases at the same time. Especially the higher dynamic comfort temperatures in the evening, driven by the assumed inactivity of the residents, can aggravate that imbalance. However, the developed MPC algorithm is capable to counterbalance that effect by shifting the heating demand to periods with lower PEF, typically earlier in the day.

6. Conclusion and future work

In this work, an MPC algorithm was developed and used to control dynamic heating operation in one room of a simulated residential building. The algorithm aimed to optimize required heating operations according to a dynamic primary energy factor signal, while observing dynamic comfort constraints defined in a preceding experimental study [1]. One of the main objectives for the development of the MPC algorithm was such level of simplicity that implementing the suggested concept of MPC for STM activation in regular residential buildings would be possible without complex measurements, expert knowledge and expensive computations. Therefore, the developed algorithm utilizes a simple ARX black-box model, which is fitted and assessed based on few simple input signals. Several rule based reference scenarios and MPC operated optimized scenarios were compared, leading to the following key findings.

- The observed absolute load shifting efficiency of the MPC algorithm was below 50% for all optimized scenarios, thus clearly increasing the required final energy demand. However, the algorithm can distinctly reduce the average PEF of the consumed energy, reaching up to 7% lower primary energy demands than the rule-based reference, for scenarios controlled according to dynamic comfort constraints. A trade-off between thermal comfort and the load shifting potential of STM activations was

observed, which leaves potential for individual user specific calibration of the STM activation extent.

- In comparison with conventional heating operation, any heating control according to the suggested dynamic comfort constraints increased the extent of comfort violations, due to the existence of the transition phases between the applicable constraints. However, on average the resulting temperatures of dynamically controlled heating operations were closer to the suggested optimal comfort temperatures. STM activations according to dynamic comfort constraints result in a similar or even lower extent of comfort violations than the optimal temperature oriented rule-based control according to these constraints. However, STM activations according to conventional standardized comfort constraints increase the extent of comfort violations distinctly.
- The utilized simple black-box model could successfully predict thermal conditions within the observed room with sufficient quality to support MPC. The control algorithm based on that model was capable to activate STM as a measure of LS according to the given utility function. However, the model's prediction quality was found to be sensitive to dynamic internal and solar loads, therefore the suitability beyond the winterly residential scope is likely limited.
- For buildings with lower insulation standard, only very small improvements of the primary energy efficiency can be reached, however the absolute amount of relocated final energy consumption is high. Buildings comparable to the Passive House standard have a clearly higher increases of primary energy efficiency, while only small absolute amounts of final energy consumption can be relocated.
- The low computational effort of the developed MPC enables an implementation on simple and affordable hardware, as the Raspberry Pi 3. The primary energy demand resulting from the computations was estimated to be distinctly lower than the potential savings due to the utilization of the MPC.

In summary, the general concept to perform STM activations in residential buildings is viable. However, to ensure thermal comfort of residents while maximizing the extent of STM activation potential, at least a simple MPC is required. The performance of such control depends on the knowledge about few resident-specific factors as the expected presence in the controlled zone or the current and expected activity level. Assumptions of these factors can be either static, or defined according to time-based schedules, ensuring at least an approximation of their impact. Just few rough assumptions indicating a repeatable daily occupancy and activity pattern, can enable meaningful load shifting activities and even improve comfort conditions. Furthermore, future smart building, communicating with the residents' smart appliances, could actually gain precise knowledge of these factors. Thus, it is likely that the potential for residential STM activations will increase in the future. Control algorithms for STM activation have to be further developed by improving the MPC models, adapting them for other heat delivery methods than hydraulic radiators, and evaluating different utility function types. Finally, since it was shown that the required control can be easily implemented utilizing simple hardware, field tests should be targeted.

Declaration of Competing Interest

We wish to confirm that there are no known conflicts of interest associated with this publication and there has been no significant financial support for this work that could have influenced its outcome.

Appendix

Table A.1
Material properties of modeled furniture.

Parameter	Density	Heat capacity	Conductivity	Emissivity	Surface/ volume	Volume
	ρ	c	λ	ϵ	A/V	V
Unit	kg/m^3	J/(kg·K)	W/(m·K)	–	m^2/m^3	m^3
Wood	650	1900	0.14	0.85	105	0.8
Metal	5300	670	160	0.5	200	0.02

Table A.2
Properties of windows representing TIO 1984, EnEV 2009 & Passive house standard.

Window type Unit	U-value in W/(m^2·K)	G-value in %	Emissivity in %	Frame fraction in %
TIO 1984	2.5	80	90	20
EnEV 2009	1.3	60	90	20
Passive house	0.8	50	90	20

Table A.3
Properties of outer walls representing TIO 1984, EnEV 2009 & Passive house standard.

Construction material from outside to inside Unit	Total thickness in m	Sub-layers n	Heat capacity in J/(kg·K)	Conductivity in W/(m·K)	Density in kg/m^3
Lime cement	0.050	5	1000	1.000	1800
Mineral wool (TIO 1984)	0.000	0	1030	0.035	120
Mineral wool (EnEV 2009)	0.060	3	1030	0.035	120
Mineral wool (PH)	0.180	9	1030	0.035	120
Aerated concrete	0.175	14	1000	0.110	350
Gypsum plaster	0.015	1	1000	0.510	1200

Resulting U-values: TIO 1984: 0.54, EnEV 2009: 0.28 and Passive house: 0.14 W/(m^2·K)

Table A.4
Properties of load bearing inner walls.

Construction material from outside to inside Unit	Total thickness in m	Sub-layers n	Heat capacity in J/(kg·K)	Conductivity in W/(m·K)	Density in kg/m^3
Gypsum plaster	0.015	1	1000	0.510	1200
Aerated concrete	0.175	10	1000	0.315	1000
Gypsum plaster	0.015	1	1000	0.510	1200

Table A.5
Properties of simple inner walls.

Construction material from outside to inside Unit	Total thickness in m	Sub- layers n	Heat capacity in J/(kg·K)	Conductivity in W/(m·K)	Density in kg/m³
Gypsum plaster	0.015	1	1000	0.510	1200
Aerated concrete	0.115	8	1000	0.315	1000
Gypsum plaster	0.015	1	1000	0.510	1200

Table A.6
Properties of floor slabs representing TIO 1984, EnEV 2009 & Passive house standard.

Construction material from outside to inside Unit	Total thickness in m	Sub- layers n	Heat capacity in J/(kg·K)	Conductivity in W/(m·K)	Density in kg/m³
Foam glass	0.060	3	1000	0.040	140
Reinforced concrete	0.250	32	1000	2.300	2300
Mineral wool (TIO 1984)	0.000	0	1030	0.035	120
Mineral wool (EnEV 2009)	0.040	2	1030	0.035	120
Mineral wool (PH)	0.160	8	1030	0.035	120
Screed	0.060	6	1000	1.400	2000
Flooring	0.006	1	1500	0.070	500

Resulting U-values: TIO 1984: 0.52, EnEV 2009: 0.33 and Passive house: 0.26 W/(m²·K)

Table A.7
Properties of the ceiling between floors.

Construction material from outside to inside Unit	Total thickness in m	Sub- layers n	Heat capacity in J/(kg·K)	Conductivity in W/(m·K)	Density in kg/m³
Gypsum plaster	0.015	1	1000	0.510	1200
Reinforced concrete	0.160	20	1000	2.300	2300
Mineral wool	0.040	2	1030	0.035	120
Screed	0.060	6	1000	1.400	2000

Table A.8
Properties of the ceiling towards unheated attic.

Construction material from outside to inside Unit	Total thickness in m	Sub- layers n	Heat capacity in J/(kg·K)	Conductivity in W/(m·K)	Density in kg/m³
Gypsum plaster	0.0150	1	1000	0.510	1200
Drywall	0.0125	1	1000	0.250	800
Mineral wool between wooden panels	0.2000	10	1300	0.045	194
Particle board	0.0200	1	1700	0.100	300

Table A.9
Infiltration parameters and air exchange rates employed in simulations.

Building standard Unit	n_{50} in 1/h	e_i –	ϵ_i –	resulting infiltration in 1/h	ventilation air exchange in 1/h %
TIO 1984	6	0.03	1	0.36	0.5
EnEV 2009	3	0.03	1	0.18	0.5
Passive house	0.6	0.03	1	0.04	0.1[a]

[a] 0.1/h with ambient air representing 0.5/h provided by a ventilation system with heat recovery.

References

[1] H. Wolisz, Transient thermal comfort constraints for model predictive heating control, published by the E.ON Energy Research Center, Aachen, 2018. ISBN:978-3-942789-63-9.

[2] T. Boßmann, I. Staffell, The shape of future electricity demand: exploring load curves in 2050s germany and britain, Energy 90 (2) (2015) 1317–1333, doi:10.1016/j.energy.2015.06.082.

[3] AGEB, Arbeitsgemeinschaft Energiebilanzen. Evaluation Tables of the Energy Balance for Germany 1990 to 2015, 2016. http://www.ag-energiebilanzen.de/10-1-Evaluation-Tables-on-the-Energy-Balance.html.

[4] BMWi, Federal Ministry for Economic Affairs and Energ. Energy Data: Complete Edition, 2016. http://www.bmwi.de/Redaktion/EN/Artikel/Energy/energiedaten.html.

[5] P. Capros, A.D. Vita, N. Tasios, D. Papadopoulos, P. Siskos, E. Apostolaki, M. Zampara, L. Paroussos, K. Fragiadakis, N. Kouvaritakis, EU Energy, transport and GHG emissions: Trends to 2050: Reference scenario 2013, Publications Office of the EU, Luxembourg, 2014.

[6] I. Dincer, On thermal energy storage systems and applications in buildings, Energy Build. 34 (4) (2002) 377–388, doi:10.1016/S0378-7788(01)00126-8.

[7] S. Stinner, K. Huchtemann, D. Müller, Quantifying the operational flexibility of building energy systems with thermal energy storages, Appl. Energy 181 (2016) 140–154, doi:10.1016/j.apenergy.2016.08.055.

[8] J. Le Dréau, P. Heiselberg, Energy flexibility of residential buildings using short term heat storage in the thermal mass, Energy 111 (2016) 991–1002, doi:10.1016/j.energy.2016.05.076.

[9] T.H. Pedersen, R.E. Hedegaard, S. Petersen, Space heating demand response potential of retrofitted residential apartment blocks, Energy Build. 141 (2017) 158–166, doi:10.1016/j.enbuild.2017.02.035.

[10] G. Reynders, J. Diriken, D. Saelens, Generic characterization method for energy flexibility: applied to structural thermal storage in residential buildings, Appl. Energy 198 (2017) 192–202, doi:10.1016/j.apenergy.2017.04.061.

[11] BMWi, Federal Ministry for Economic Affairs and Energy. Energy concept. Energiekonzept für eine umweltschonende, zuverlässige und bezahlbare Energieversorgung, 2010. https://www.bmwi.de/Redaktion/DE/Downloads/E/energiekonzept-2010.pdf.

[12] H. Wolisz, C. Punkenburg, R. Streblow, D. Müller, Feasibility and potential of thermal demand side management in residential buildings considering different developments in the german energy market, Energy Convers. Manage. 107 (2016) 86–95, doi:10.1016/j.enconman.2015.06.059.

[13] H. Wolisz, T. Schütz, T. Blanke, M. Hagenkamp, M. Kohrn, M. Wesseling, D. Müller, Cost optimal sizing of smart buildings' energy system components considering changing end-consumer electricity market models, Energy (2017), doi:10.1016/j.energy.2017.06.025.

[14] H. Wolisz, T.M. Kull, R. Streblow, D. Müller, The effect of furniture and floor covering upon dynamic thermal building simulations, Energy Procedia 78 (2015) 2154–2159, doi:10.1016/j.egypro.2015.11.304.

[15] C.W. Gellings, The concept of demand-side management for electric utilities, Proc. IEEE 73 (10) (1985) 1468–1470, doi:10.1109/PROC.1985.13318.

[16] A. Arteconi, N.J. Hewitt, F. Polonara, State of the art of thermal storage for demand-side management, Appl. Energy 93 (2012) 371–389, doi:10.1016/j.apenergy.2011.12.045.

[17] M. Paulus, F. Borggrefe, The potential of demand-side management in energy-intensive industries for electricity markets in germany, Appl. Energy 88 (2) (2011) 432–441, doi:10.1016/j.apenergy.2010.03.017.

[18] M.H. Shoreh, P. Siano, M. Shafie-khah, V. Loia, J.P.S. Catalão, A survey of industrial applications of demand response, Electric Power Syst. Res. 141 (2016) 31–49, doi:10.1016/j.epsr.2016.07.008.

[19] H. Wolisz, H. Harb, P. Matthes, L. Böse, R. Streblow, D. Müller, The new role of night storage heaters in residential demand side management, in: Proceeding of the 5th BauSIM Conference, 2014, pp. 611–616. Aachen, Germany.

[20] K. Hedegaard, B.V. Mathiesen, H. Lund, P. Heiselberg, Wind power integration using individual heat pumps – analysis of different heat storage options, Energy 47 (1) (2012) 284–293, doi:10.1016/j.energy.2012.09.030.

[21] R. D'hulst, W. Labeeuw, B. Beusen, S. Claessens, G. Deconinck, K. Vanthournout, Demand response flexibility and flexibility potential of residential smart appliances: experiences from large pilot test in belgium, Appl. Energy 155 (2015) 79–90, doi:10.1016/j.apenergy.2015.05.101.

[22] S. Zurmühlen, H. Wolisz, G. Angenendt, D. Magnor, R. Streblow, D. Müller, D.U. Sauer, Potential and optimal sizing of combined heat and electrical storage in private households, Energy Procedia 99 (2016) 174–181, doi:10.1016/j.egypro.2016.10.108.

[23] D. Müller, A. Monti, S. Stinner, T. Schlösser, T. Schütz, P. Matthes, H. Wolisz, C. Molitor, H. Harb, R. Streblow, Demand side management for city districts, Build. Environ. 91 (2015) 283–293, doi:10.1016/j.buildenv.2015.03.026.

[24] A. Arteconi, N.J. Hewitt, F. Polonara, Domestic demand-side management (DSM): role of heat pumps and thermal energy storage (TES) systems, Appl. Thermal Eng. 51 (1–2) (2013) 155–165, doi:10.1016/j.applthermaleng.2012.09.023.

[25] SMA Solar Technology AG, Sunny Home Manager 2.0, 2017. http://www.sma.de/en/products/monitoring-control/sunny-home-manager-20.html#Downloads-259054.

[26] S. Heinen, W. Turner, L. Cradden, F. McDermott, M. O'Malley, Electrification of residential space heating considering coincidental weather events and building thermal inertia: a system-wide planning analysis, Energy 127 (2017) 136–154, doi:10.1016/j.energy.2017.03.102.

[27] M. Kintner-Meyer, A.F. Emery, Optimal control of an HVAC system using cold storage and building thermal capacitence, Energy Build. 23 (1995) 19–31.

[28] J.E. Braun, Load control using building thermal mass, J. Solar Energy Eng. 125 (3) (2003) 292–301, doi:10.1115/1.1592184.

[29] M. Schmelas, T. Feldmann, E. Bollin, Adaptive predictive control of thermo-active building systems (TABS) based on a multiple regression algorithm, Energy Build. 103 (2015) 14–28, doi:10.1016/j.enbuild.2015.06.012.

[30] J. Romaní, A.d. Gracia, L.F. Cabeza, Simulation and control of thermally activated building systems (TABS), Energy Build. 127 (2016) 22–42, doi:10.1016/j.enbuild.2016.05.057.

[31] J. Ma, J. Qin, T. Salsbury, P. Xu, Demand reduction in building energy systems based on economic model predictive control, Chem. Eng. Sci. 67 (1) (2012) 92–100, doi:10.1016/j.ces.2011.07.052.

[32] J.W. Moon, S.K. Jung, Algorithm for optimal application of the setback moment in the heating season using an artificial neural network model, Energy Build. 127 (2016) 859–869, doi:10.1016/j.enbuild.2016.06.046.

[33] J. Abedin, S. Firth, P. Eames, Simulation of domestic heat demand shifting through short-term thermal storage, in: Proceeding of the 13th International Conference of the International Building Performance Simulation Association, 2013, pp. 3368–3374. Chambéry, France.

[34] H. Wolisz, H. Harb, P. Matthes, R. Streblow, D. Müller, Dynamic simulation of thermal capacity and charging/discharging performance for sensible heat storage in building wall mass, in: Proceeding of the 13th International Conference of the International Building Performance Simulation Association, 2013, pp. 2716–2723. Chambéry, France.

[35] H. Wolisz, A. Constantin, R. Streblow, D. Müller, Performance assessment of heat distribution systems for sensible heat storage in building thermal mass, in: Proceedings of the 12th CISBAT, 2013. Lausanne, Switzerland.

[36] G. Reynders, T. Nuytten, D. Saelens, Potential of structural thermal mass for demand-side management in dwellings, Build. Environ. 64 (2013) 187–199, doi:10.1016/j.buildenv.2013.03.010.

[37] H. Wolisz, P. Block, R. Streblow, D. Müller, Dynamic activation of structural thermal mass in a multi-zonal building with due regard to thermal comfort, in: Proceeding of the 14th International Conference of the International Building Performance Simulation Association, 2015, pp. 1291–1297. Hyderabad, India.

[38] S. Stinner, T. Schlösser, K. Huchtemann, D. Müller, A. Monti, Primary energy evaluation of heat pumps considering dynamic boundary conditions in the energy system, Energy 138 (2017) 60–78, doi:10.1016/j.energy.2017.07.029.

[39] H. Wolisz, J. Graf, D. Müller, Verfahren zur Beheizung von mehreren Zonen eines Gebäudes: Patent application, Nr. DE 10 2017 005 872, 2017.

[40] ISO 7726, EN ISO 7726: Ergonomics of the thermal environment - Instruments for measuring physical quantities, 2002.

[41] A. Mahdavi, F. Tahmasebi, Predicting people's presence in buildings: an empirically based model performance analysis, Energy Build. 86 (2015) 349–355, doi:10.1016/j.enbuild.2014.10.027.

[42] X. Feng, D. Yan, T. Hong, Simulation of occupancy in buildings, Energy Build. 87 (2015) 348–359, doi:10.1016/j.enbuild.2014.11.067.

[43] S. Prívara, J. Cigler, Z. Váňa, F. Oldewurtel, C. Sagerschnig, E. Žáčeková, Building modeling as a crucial part for building predictive control, Energy Build. 56 (2013) 8–22, doi:10.1016/j.enbuild.2012.10.024.

[44] D. Müller, M. Lauster, A. Constantin, M. Fuchs, P. Remmen, Aixlib - an open–source modelica library within the IEA-EBC annex 60 framework, in: Proceedings of BauSIM, 2016. Dresden, Germany.

[45] M. Fuchs, A. Constantin, M. Lauster, P. Remmen, R. Streblow, D. Müller, Structuring the building performance modelica library aixlib for open collaborative development, in: Proceedings of the 14th International Conference of the International Building Performance Simulation Association, 2015. Hyderabad, India.

[46] A. Constantin, R. Streblow, D. Müller, The modelica housemodels library, presentation and evaluation of a room model with the ASHRAE standard 140, in: Proceedings of the 10th International Modelica Conference, 2014. Lund, Sweden.

[47] BMWi, Federal Ministry for Economic Affairs and Energy. The German Energy Saving Ordinance (EnEV), 2009. http://www.bbsr-energieeinsparung.de/EnEVPortal/EN/Archive/EnEV/enev_node.html.

[48] BMWi, Federal Ministry for Economic Affairs and Energy. Energy Conservation Legislation, 2017. https://www.bmwi.de/Redaktion/EN/Artikel/Energy/energy-conservation-legislation.html.

[49] BBR, Bundesamt für Bauwesen und Raumordnung. Thermal Insulation Ordinance 1977/1984, 2017. http://www.bbsr-energieeinsparung.de/EnEVPortal/EN/Archive/ThermalInsulation/thermalinsulation_node.html.

[50] Passive House Institute, Passive House requirements & User manual for Passive Houses, 2016. http://passivehouse.com/05_service/03_literature/030300_user-manual/030300_user-manual.htm.

[51] EN 12831, DIN EN 12831: Heating systems in buildings - Method for calculation of the design heat load, 2003.

[52] Kermi GmbH, therm-x2 Flachheizkörper: Profil-K/-V/-VM Heizkörperauslegung: Tested according to DIN EN 442, 2016. https://portal.kermi.de/DownloadCenter2/kermi_de/de/de/h/c/heating/documents/11.

[53] EN 12098, DIN EN 12098-1: Controls for heating systems - Part 1: Control equipment for hot water heating systems, 2013.

[54] D.E. Watkins, Heating Services in Buildings: Design, Installation, Commissioning & Maintenance, John Wiley & Sons, 2011.

[55] M. Jimnez, H. Madsen, Models for describing the thermal characteristics of building components, Build. Environ. 43 (2) (2008) 152–162, doi:10.1016/j.buildenv.2006.10.029.

[56] S. Prívara, J. Cigler, Z. Váňa, E. Žáčeková, J. Cigler, Building modeling: selection of the most appropriate model for predictive control, Energy Build. 55 (2012) 341–350, doi:10.1016/j.enbuild.2012.08.040.

[57] J. Ma, J. Qin, T. Salsbury, Model predictive control of building energy systems with balanced model reduction, in: Proceedings of 2012 American Control Conference (ACC), 2012, pp. 3681–3686, doi:10.1109/ACC.2012.6315516.

[58] G. Reynders, J. Diriken, D. Saelens, Quality of grey-box models and identified parameters as function of the accuracy of input and observation signals, Energy Build. 82 (2014) 263–274, doi:10.1016/j.enbuild.2014.07.025.

[59] MathWorks, MATLAB 'arx' function description, 2017. https://de.mathworks.com/help/ident/ref/arx.html.

[60] BBSR, Federal institute for research on building, urban affairs and spatial development, Test Reference Year (TRY) 2011: Region 5 - German Lower Rhine Region, 2011 http://www.bbsr-energieeinsparung.de/EnEVPortal/EN/Regulation/TRY/testreferenceyears_node.html.

[61] ISO 7730, DIN EN ISO 7730: Ergonomics of the thermal environment - analytical determination and interpretation of thermal comfort using calculation of the PMV and PPD indices and local thermal comfort criteria, 2005.

[62] EN 15251, DIN EN 15251: Indoor environmental input parameters for design and assessment of energy performance of buildings addressing indoor air quality, thermal environment, lighting and acoustics, 2007.

[63] ASHRAE 55, ANSI/ASHRAE Standard 55–2013: Thermal Environmental Conditions for Human Occupancy, 2013.

[64] VDI 2078, VDI 2078: Calculation of thermal loads and room temperatures, 2015.

[65] I. Richardson, M. Thomson, D. Infield, A high-resolution domestic building occupancy model for energy demand simulations, Energy Build. 40 (8) (2008) 1560–1566, doi:10.1016/j.enbuild.2008.02.006.

[66] 50Hertz, Grid data: Actual generation output, 2016. http://www.50hertz.com/en/Grid-Data.

[67] Amprion, Grid data: Generation in control area, 2016. https://www.amprion.net/Grid-Data/.

[68] Tennet, Transparency: Network figures, 2016. http://www.tennettso.de/site/en/Transparency/publications/network-figures/overview.

[69] Transnet BW, Transparency: Key figures, 2016. https://www.transnetbw.com/en/transparency/market-data/key-figures.

[70] DIN V 18599, DIN V 18599-1: Energy efficiency of buildings; Part 1: General balancing procedures, terms and definitions, zoning and evaluation of energy sources, 2016.

[71] I. Gurobi Optimization, Algorithm used to solve continuous models: Method paramter, 2017. http://www.gurobi.com/documentation/7.5/refman/method.html#parameter:Method.

[72] Intel Corporation, Intel Xeon Processor E5-2600 Series: E5-2667 base frequency GFLOP, 2012. http://download.intel.com/support/processors/xeon/sb/xeon_E5-2600.pdf.

[73] Raspberry Pi Foundation, Raspberry Pi hardware guid: The Raspberry Pi 3, 2016. https://www.raspberrypi.org/learning/hardware-guide/components/raspberry-pi/.

[74] M. Cloutier, C. Paradis, V. Weaver, A raspberry pi cluster instrumented for fine-grained power measurement, Electronics 5 (4) (2016) 61, doi:10.3390/electronics5040061.

[75] J.W. Eaton, GNU Octave - Scientific programming language, 2017. https://www.gnu.org/software/octave/.

[76] R. Baudin, Run time comparison of MATLAB, Scilab and GNU Octave on various benchmark programs, 2016. http://roland65.free.fr/benchmarks/benchmarks-0.2.pdf.

[77] J. Forrest, Cbc: Coin-or branch and cut: Open-source mixed integer programming solver, 2016. https://projects.coin-or.org/Cbc/wiki.

[78] H. Mittelmann, Mixed integer linear programming benchmark (Sept. 2017), 2017. http://plato.asu.edu/ftp/milpc.html.

[79] G. Reynders, J. Diriken, D. Saelens, A generic quantification method for the active demand response potential of structural storage in buildings, in: Proceedings of the 14th International Conference of the International Building Performance Simulation Association, 2015. Hyderabad, India.

Publication II

Kull, T. M., Thalfeldt, M., and Kurnitski, J. (2020) PI Parameter Influence on Underfloor Heating Energy Consumption and Setpoint Tracking in nZEBs, *Energies*, 13(8), p. 2068. doi: 10.3390/en13082068

PI Parameter Influence on Underfloor Heating Energy Consumption and Setpoint Tracking in nZEBs

Tuule Mall Kull [1,*] 📵**, Martin Thalfeldt** [1] **and Jarek Kurnitski** [1,2] 📵

[1] Nearly Zero Energy Buildings Research Group, Tallinn University of Technology, Ehitajate tee 5,
    19086 Tallinn, Estonia; martin.thalfeldt@taltech.ee (M.T.); jarek.kurnitski@taltech.ee (J.K.)
[2] Department of Civil Engineering, Rakentajanaukio 4 A, Aalto University, FI-02150 Espoo, Finland
* Correspondence: tuule.kull@taltech.ee

Abstract: In rooms with underfloor heating (UFH), local on–off controllers most often regulate the air temperature with poor accuracy and energy penalties. It is known that proportional–integral (PI) controllers can regulate most processes more precisely. However, hydronic UFH systems have long time constants, especially in low-energy buildings, and PI parameters are not easy to set manually. In this work, several potential PI parameter estimation methods were applied, including optimizing the parameters in GenOpt, calculating the parameters based on simplified models, and tuning the parameters automatically in Matlab. For all found parameter combinations, the energy consumption and control precision were evaluated. Simpler methods were compared to the optimal solutions to find similar parameters. Compared with an on–off controller with a 0.5 K dead-band, the best PI parameter combination found was with a proportional gain of 18 and an integration time of 2300 s, which could decrease the energy consumption for heating by 9% and by 5% compared with default PI parameters. Moreover, while GenOpt was the best method to find the optimal parameters, it was also possible with a simple automatic test and calculation within a weekend. The test can be, for example, 6-h setbacks applied during the nights or weekend-long pseudo-random changes in the setpoint signal. The parameters can be calculated based on the simplified model from these tests using any well-known simple method. Results revealed that the UFH PI controller with the correct parameters started to work in a predictive fashion and the resulting room temperature curves were practically ideal.

Keywords: IDA ICE; building simulation; intermittent heating; model predictive control (MPC); heat pumps; proportional–integral–derivative (PID) control; thermostats

1. Introduction

The change towards nearly zero-energy buildings (nZEBs) and renewable energy sources influences the technologies used for heating and its control [1,2]. The intermittent production of renewable electricity calls for flexibility in all consumers, including buildings [3]. Space heating is responsible for up to 70% of the final energy demand in residential buildings [4]. Therefore, it has a high potential for flexibility. In modern buildings, the use of heat pumps has intensified [5]. Only electricity-based heating is relevant to the power grid, therefore, heat pumps are a clear target.

To be exploited when the grid needs it, heat pumps should use an electricity price or other signal for optimizing their performance. Some of the heat pumps already optimize their behaviour according to the price. As one solution to improve the flexibility, model predictive control (MPC) can be used [6,7]. It enables the use of historic and forecasted data to predict the most optimal course of action. At the occurrence of renewed data, the optimization can be corrected. For an MPC for a single-family house,

the input signal is, for example, the electricity price or other signal from the grid and the output of the optimization are the air temperature setpoints of the rooms [3].

The setpoints in rooms have to be tracked by room-based controllers, such as thermostats or proportional–integral–derivative (PID) controllers, as the supervisory control can deal with optimization but not with the local fast changes [8]. PID is commonly known to be one of the best and easiest feedback controllers for any process. For buildings, as a relatively slow system, the derivative part is usually dropped and PI controllers are used instead. However, choosing improper PID gains (parameters) could result in making the whole system unstable. Therefore, designers and researchers often turn to optimal or predictive solutions [9].

However, advanced solutions are not easy to implement and the need for robust and reliable solutions with minimal human interaction is evident. [10,11]. To simplify or avoid technicians' inputs to the systems, the control algorithms can be tested in realistic environments [12]. Also, building blocks have been developed to be compatible with detailed modelling so that engineers can do the tuning. However, the process is still not fully automated [13]. Auto-tuning of PID controllers for heating, cooling, and ventilation plants have been described both several decades ago [14–16] and more recently [17]. If there is enough computational power, artificial neural network models could theoretically tune their PID parameters [18].

Self-learning PI controllers are already commonly available for radiators in new buildings. As radiators are also installed in public and commercial buildings, there is a lot of interest and financial capability to develop better-performing solutions for these environments. In homes, hydronic underfloor heating (UFH) has become more popular, being a low-temperature solution that matches with heat pumps in nZEBs. For hydronic underfloor heating, even in modern buildings, only simple thermostats with a dead-band of at least 0.5 K are often used. However, using UFH with a thermostat, the air temperatures fluctuates significantly and, therefore, the users can easily raise the setpoints to avoid lower levels and to meet their comfort limits. This ends up in a higher energy consumption.

Control of underfloor heating as a slow system with a high thermal mass is a debated question, where good solutions have not been found yet. Some manufactures offer sophisticated self-learning controls, while on–off is likely the most common implementation in practice, and in some studies, self-regulating properties (no-control) have shown similar performance with more sophisticated control solutions [19]. The long time constant of UFH is even increased by a low supply temperature from heat pumps and this is due to the small losses in well-insulated nZEBs with heat recovery ventilation. This means that setting PI parameters manually by trial and error, which is the common practice for PI tuning, would take a lot of time. For self-tuning controllers, simple tests would be needed but also these can be too time-consuming.

When the gains are optimized, PID control can save energy in UFH control compared with the standard on–off control [20]. However, the optimal parameter values are usually not revealed. There is almost no previous published data on PI parameter values for UFH, with rare exceptions [21]. Furthermore, the effect of different parameters has not been analyzed for UFHs. However, the effects of PI parameters have been analyzed for radiators, as the heating circuits are, in reality, often not tuned and there is a lot of potential for energy saving [22]. Tuning radiator PID parameters with machine learning has shown a 32% reduction in heating energy consumption compared with Ziegler–Nichols tuning [23]. The current situation shows that while PID and on–off control waste energy, more advanced solutions on the market do not ensure comfort [24]. With quality tuning, PID could both reduce wasting energy and ensure comfort. The parameter optimization for UFH has been performed in extensive simulations [20], but it remains unknown whether it is possible to obtain the optimal parameters with shorter tests.

Therefore, the aim of this work is two-fold. Firstly, to determine how UFH control can be improved by the application of PI parameters specifically derived for underfloor heating in nZEB with various tests and methods. Secondly, to find whether it is possible to determine the PI parameters which perform close to optimal, when using short tests and simple methods. This work estimates the PI

parameters for UFH in nZEB and analyzes their effect on the energy performance and indoor air temperature of the building. PI performance is compared with a traditional thermostat's performance in the same situation. Both an accurate temperature tracking performance and a considerable energy saving compared with conventional control are expected. The results may be utilized in the design of UFH systems with accurate temperature control and energy savings compared with conventional UFH systems.

2. Materials and Methods

2.1. The Building

The work is based on a test building at TalTech University campus, which is described in detail in several previous publications [25–27]. Two almost identical rooms with a floor area of 10.4 m² were analyzed, except that one of them (Room 6 or R6) has two 4 m² windows facing south and west, while the windows of the other (Room 5 or R5) face north and west. The floor plan of the building is shown in Figure 1 with the two test rooms highlighted with red rectangles. Previously, the test house model in IDA ICE 4.8 software [28] was calibrated against measured air temperatures in the test room R5 during temperature setback cycles with varying durations [27]. As a result, the heat losses and thermal mass of the room structures are adequately defined in the model. This model was used for the simulations in the current work. In the simulations, all of the other rooms were heated constantly with ideal heaters to the setpoint of 21 °C.
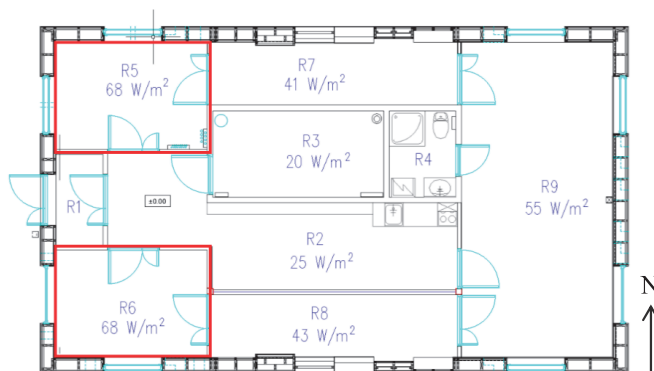
Figure 1. Layout of the test building; the two test rooms are shown in red rectangles.

The building has wooden-frame walls, a wooden-frame roof, and concrete floors with a crawl space below. The total heat-up time constant for the rooms is around 85 h and the effective time constant for temporary setbacks is around 12 h [27]. The absolute cool-down time constant of one test room is around 24 h when the other rooms are heated constantly. The time constant for the whole building cool-down is ca. 100 h. The time constants are long mainly due to the concrete floor and highly insulated building envelope. The values were confirmed by the experimental data presented in [27].

2.2. Outline of the Work

The PI parameters were estimated for the two test rooms in several different ways. Firstly, they were optimized in GenOpt with the aim of minimal setpoint tracking errors both for the constant and variable setpoints (Section 2.5). Secondly, they were calculated and estimated using simplified models. The data used for the model fitting are described in Section 2.3 and the model fitting process is described in Section 2.4. The models were used to either autotune the parameters in Matlab or to calculate the parameters using well-known methods such as AMIGO, SIMC, and Cohen–Coon. Both

of these approaches are also clarified in Section 2.5. The performance of all the gained parameters was cross-checked in both rooms over the whole heating period. The analysis is described in detail in Section 2.6.

2.3. Input Data

All the data used for the PI parameter calculations are summarized in Table 1. In this section, only the grey area is described, the rest is tackled in the following sections. Here, the data from [27] were used, where the authors performed temperature setbacks with different lengths in the test building. The air temperature during setbacks with durations of 2 days and 3 days was measured in room 5, where the temperature setpoint was normally kept at 21 °C and during the setbacks was lowered to 18 °C. In the calibrated IDA ICE model, shorter setbacks of 1, 3, 6, 12, and 24 h were simulated using a constant outdoor temperature of 0 °C, with no solar and internal gains. Between the setbacks, the initial temperature of 21 °C was stabilized. Without solar gains, the two test rooms are equivalent and therefore, the PI parameters estimation is based on only one of them.

Table 1. Overview of the input data for the model calculation (grey area) and optimization as well as the methods for getting the proportional–integral (PI) parameters.

Climate	Setpoint	Room	Source	Estimation Basis	Method
Actual	2-3-day (long) setbacks	R5	Measured	Simplified model	Calculation methods + tuning in Matlab
Constant	Shorter setbacks	R5/R6 (equal)	Simulated	Simplified model	Calculation methods + tuning in Matlab
Constant	Infinite/ideal step	R5/R6 (equal)	Simulated	Simplified model	Calculation methods + tuning in Matlab
Estonian TRY	PRBS	R5 and R6	Simulated	Simplified model	Calculation methods
Estonian TRY	Constant	R5 and R6	Simulated	Optimization	GenOpt
Estonian TRY	Variable (price-based)	R5 and R6	Simulated	Optimization	GenOpt

In addition, an ideal-like step test was simulated with the same constant outdoor conditions. A step from no heating to full power heating was performed. The simulation period was prolonged for so long that the stability of the indoor air temperature was achieved both before and after the step. This meant two months in simulation to stabilize at the balance temperature, and one month after the step for reaching a steady state.

Additionally, simulations with Estonian test reference year (TRY) [29] and pseudo-random binary signal (PRBS) as setpoints were used. For the PRBS temperature setpoint, the zero level was set on 18 °C and the maximum level on 24 °C. The simulations were done for two separate weeks, one in March and one in February:

- A sunny week with moderate temperature (19–25.03);
- A cold week with almost no sun (29.01–04.02).

The model fitting was done both on the entire weeks and only on the weekends of these weeks (12 p.m. Friday to 12 p.m. Sunday).

For the optimization (the last two rows in Table 1), the same two weeks of Estonian TRY were used as well as the whole heating period from 1 October to 30 April. The setpoints for the optimization cases are the same as used for the evaluation and are described in Section 2.6.

2.4. Model Fitting

A simplified process model of the system is needed to use most of the PI parameter calculation methods. Based on the generated input data, a first order process model with a time delay was fitted. Therefore, the temperature response of an input step change is

$$\theta(t) = K_p \left(1 - e^{-\frac{t-L}{T}}\right) + \theta(0) e^{-\frac{t-L}{T}} \tag{1}$$

where $\theta(t)$ is room air temperature in °C at time t seconds after the step, $\theta(0)$ is the initial temperature before the step, K_p is the process gain (unitless), T is the time constant, and L is the time delay, both in seconds. The model fitting was performed in Matlab using System Identification Toolbox [30].

2.5. Estimating PI Parameters

The PI parameters K and T_i were estimated, where K is the proportional factor and T_i is the integration time of the integral part of the PI in its ideal form:

$$u(t) = K \left(E + \frac{1}{T_i} \int E dt\right) \tag{2}$$

where u is the control signal (unitless) and E is the difference between the setpoint and measured air temperature in °C that is feedback to the control. For all the cases in Table 1, the PI parameters were estimated by one or more of the following methods:

1. Optimized using GenOpt;
2. Tuned in Matlab/Simulink;
3. Calculated from an applicable simple method.

In the optimization method, the PI parameters were optimized in GenOpt using a hybrid GPS algorithm [31]. The optimization was carried out for the three different periods described previously and two different setpoint profiles, which are also used for the evaluation and are described below in Section 2.6. The objective of the optimization was to minimize the average absolute difference between the setpoint temperature and the simulated temperature.

In the second method, the PI parameters were auto-tuned in Matlab®/Simulink for the previously fitted simplified models (described in Section 2.4). The tuning was performed aiming for a short rise time (speed) and overshoot of no more than 5% of the desired temperature increase.

In the third method, all the models that had been fitted based on the different input data were used to calculate the PI parameters. Three widely known methods—Cohen–Coon, Skogestad IMC (SIMC), and AMIGO—were used for that. The PI parameters K and Ti are calculated according to these methods as follows [32]:

Cohen–Coon (CC):　$K = 0.9 \cdot \left(1 + 0.092 \cdot \frac{\tau}{1-\tau}\right)/$　(3)　$Ti = \frac{3.3-3\tau}{1+1.2\tau} L$　(4)

Skogestad IMC (SIMC):　$K = T / \left(2 K_p L\right)$　(5)　$Ti = \min(T; 8L)$　(6)

AMIGO:　$K = \frac{0.15}{K_p} + \left(0.35 - \frac{L \cdot T}{(L+T)^2}\right) \cdot \frac{T}{K_p L}$　(7)　$Ti = 0.35L +$　(8)　$\frac{13LT^2}{T^2+12LT+7L^2}$

where Kp, L and T are the parameters from the fitted models with the general representation in Equation (1). The parameters a and τ are unitless parameters:

$$a = \left(K_p L\right)/T \tag{9}$$

$$\tau = L/(L+T) \tag{10}$$

2.6. The Evaluation Tests

All the estimated PI parameter combinations were tested in simulations in both test rooms. The accuracy of the setpoint tracking was assessed on both the constant and variable setpoints. The constant setpoint was chosen to be 21 °C and the variable setpoint was calculated from price data 2017–2018 [33], based on the simple algorithm given in [34] that does not perform the best for their purpose of load shifting but gives us an hourly changing setpoint profile. In the price-based control, the air temperature setpoint is changed hourly between 20, 21, and 24 °C. The lower two levels are meant for comfort and have to be met at all times, the highest level is implemented for load shifting and does not need to be tracked. All evaluations were done for the whole heating period (01 October–30 April). All combinations of PI parameters, both rooms, and both setpoint profiles were evaluated based on:

- The average absolute error (AAE) of the air temperature from the setpoint;
- The heating energy consumption per square meter of the floor area.

For the energy consumption comparison, it is important that no parameter combinations would result in temperatures lower than the given comfort setpoints. In most cases, this was not achieved and, therefore, the setpoints had to be shifted. The goal was to achieve temperatures equal or above the setpoint for at least 97% of the time, as suggested in the thermal comfort standard EN 16798-2 [35]. Based on the initial simulations, cumulative temperature graphs were generated. In the constant setpoint case, the setpoint was shifted exactly as much as the cumulative graph was, below the setpoint at 3% of the time. For the variable setpoints, shifts for both the two 20 °C and 21 °C setpoints were calculated. The 3% of the 20 °C was at 1.3% of the total time and for the 21 °C setpoint at 45.2% of the total heating period length. The maximum of the shifts calculated for these two points was applied to the whole profile.

2.7. Benchmarks

The simulation software IDA ICE's default PI parameter values $K = 0.3$ and $T_i = 300$ s were used for the benchmark simulations. Furthermore, on–off controls with four different dead-band widths were evaluated for the comparison. A modern one with a dead-band of 0.5 °C was used, but also close to ideal versions, with dead-bands of 0.16 °C and 0.05 °C and a conservative one with a 1 °C dead-band, were used as well.

2.8. PI Implementation in IDA ICE and PI Mechanics

As the PI controller can be implemented in various formats, the implementation in IDA ICE is shown in Figure 2. The example code in Figure 2A is modified for the case where error filtering is turned off, the mode is heating, and the conversion unit equals 1. The parameter *tt*, the tracking time, is set to 30 s.

The *hilimit* and *lolimit* are the limits for the PI output signal. In this work, the PI output signal is the fraction of the nominal mass flow to the UFH and is, therefore, limited from 0 to 1. In Figure 2B, an increase in the sample air temperature over the setpoint, i.e., due to solar gains, can be observed. In Figure 2C,D, the calculation of the script can be followed. The lines are colored according to the variable text colors in the script.

In Figure 2C, it can be observed that, even though the temperature is over the setpoint between 3 a.m. and 5 a.m. (Figure 2B), the PI signal is not zero. It only gets to zero when the integral part also decreases so much so that the sum of the integral and error parts is less or equal to zero. Although the *OutSignal* is limited, the negative values of *OutSignalTemp* are still used for the calculation. This enables the effect, which looks like prediction in some cases. This effect is further discussed in Section 3.3.

A.

$$E := \text{SetPoint} - \text{Measure};$$ (Figure B)

$$\text{OutSignalTemp} := K * E + K * \text{Integ} ;$$ (Figure C)

$$\text{Integ}' = E\ /Ti + (\text{OutSignal} - \text{OutSignalTemp})/tt;$$ (Figure D)

$$\text{OutSignal} = \text{IF } \text{OutSignalTemp} > hilimit \text{ THEN}$$ (Figure C)

$$hilimit$$

$$\text{ELSE\_IF } \text{OutSignalTemp} < lolimit \text{ THEN}$$

$$lolimit$$

$$\text{ELSE}$$

$$\text{OutSignalTemp}$$

$$\text{END\_IF} ;$$

B.

C.

D.
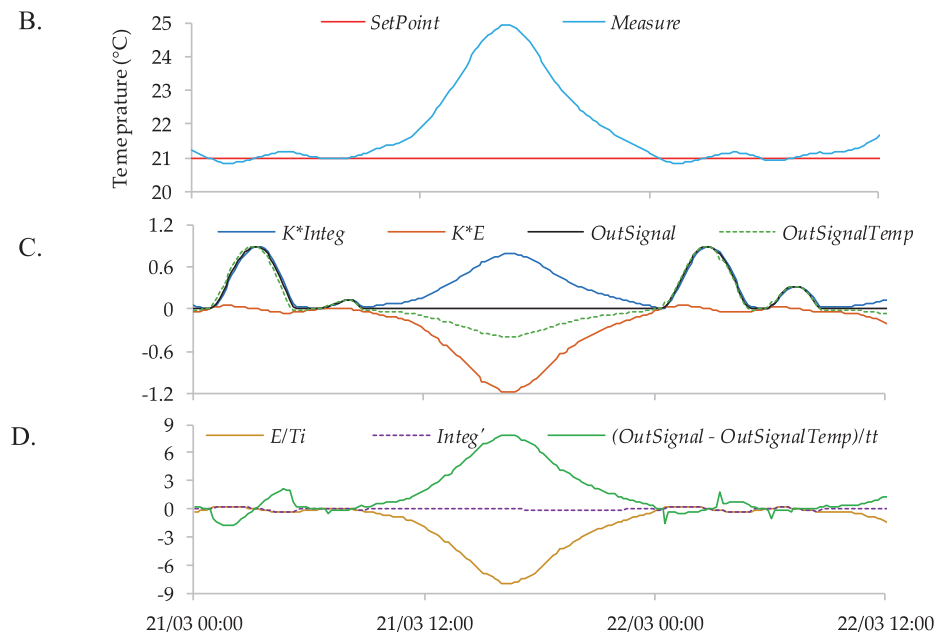
Figure 2. PI implementation in IDA ICE and example signals. In (**A**), variables in the script are colored after each line it is referred where the example signals are visualized. Lines in (**B**–**D**) graphs use the same color-coding.

3. Results

3.1. Found Simplified Models

The simplified model of the system that is needed for the parameter calculation was estimated for 16 different cases. All three parameters of the gained models varied between all cases. The used cases and exact parameter values are included in Table 2 with parameter values also visualized in Figure 3. The process gain (K_p) has two clearly different orders and altogether three different levels. The values were around 1 for all cases where the PRBS signal was used as the setpoint and were much larger for

other cases. For the ideal step and measured setbacks, the K_p value was around 20, for all other setback cases, around 40.

Table 2. List of all used models and their parameters.

Based on Room	Model Number	Model Group	Model Source	K_p	L (Seconds)	T (Seconds)
R5 & R6	1	Longer step	Ideal step	21.842	476	27,892
	2	Setbacks	24-h setback at 0 °C	41.063	141.12	23,652
	3	Setbacks	12-h setback at 0 °C	42.649	410.58	30,141
	4	Setbacks	6-h setback at 0 °C	44.717	156.96	38,648
	5	Setbacks	3-h setback at 0 °C	42.664	9.66	35,191
	6	Setbacks	1-h setback at 0 °C	41.446	3.9	42,130
R5	7	Longer step	2-day measured setback	24.256	720	33,720
	8	Longer step	3-day measured setback	21.472	780	41,820
	9	PRBS sL	2-day PRBS in February	1.0123	218.4	27,152
	10	PRBS sL	1-week PRBS in February	1.03	286.8	50,122
	11	PRBS lL	2-day PRBS in March	1.0555	2034	48,950
	12	PRBS lL	1-week PRBS in March	1.0599	2226.6	51,845
R6	13	PRBS sL	2-day PRBS in February	1.03	25.8	17,237
	14	PRBS sL	1-week PRBS in February	1.042	12.6	34,930
	15	PRBS lL	2-day PRBS in March	1.0973	3996	41,990
	16	PRBS lL	1-week PRBS in March	1.1035	50,084	4737
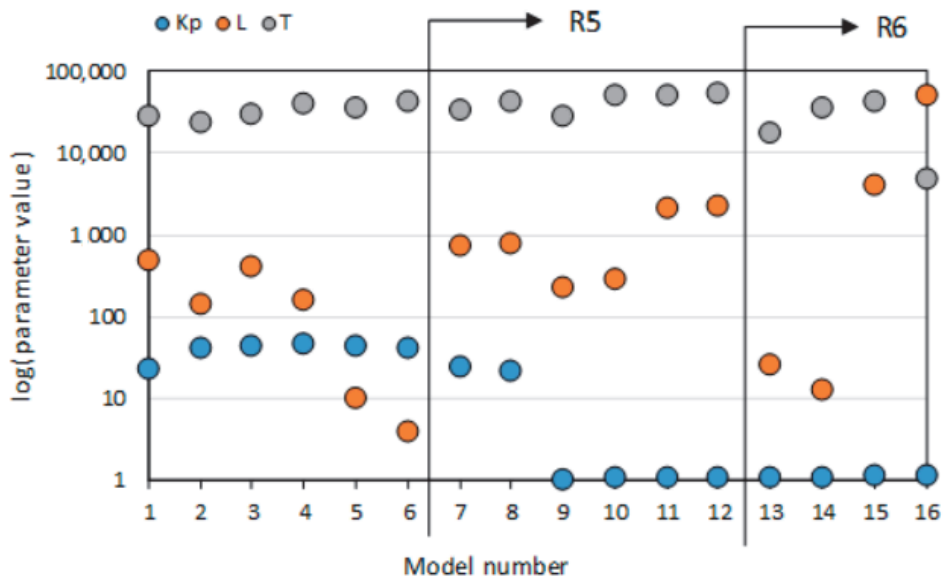
Figure 3. Log-value of all model parameters shown in Table 2.

The time delay (L) values for the PRBS cases had around a 100 times difference between the March week and February week values in R5, and the same difference was larger than 1000 times in R6, the southern room with more solar gains. L was smaller than 10 s for the two shortest setbacks, between 10 and 30 s for the February PRBS tests in R6, and larger than 100 in all other cases. There was

ranging from 140 to 4000 (around 2 m to 1 h) and in one case (1-week PRBS in March for R6, model 16) it was over 50,000 s (around 14 h).

The *T* values varied least of the parameters, i.e., between 10,000 and 100,000 s (between around 4 and 15 h). Only in the same model 16 case, where an extra-large *L* value occurred, the *T* value was a lot lower at a bit less than 5000. So exceptionally, for this model, *L* is larger than *T*.

Based on mostly the K_p and *L* values, the models are divided into four groups, shown in Table 2. The setbacks and longer step groups are self-evident from above. The PRBS models are divided into models with a short *L* (PRBS sL) and a long *L* (PRBS lL). These groups will be used below for visualization.

3.2. Identified PI Parameters

In total, 68 PI parameter value pairs were obtained. All the parameter values are included in Appendix A, Table A1. However, all the parameter combinations are also visualized in Figure 4a, where each point on the graph is a parameter combination. The scales are the logarithms of the parameter values with base 10. The graphs in Figures 4b and 5 follow the same logic. In Figure 4a, the parameter estimation method is shown by the marker shape and the model group is shown by the marker color. In the logarithmic scales, the tendency in the parameter estimation results seems to be roughly linear, so the lower the integration time the higher the proportional gain.
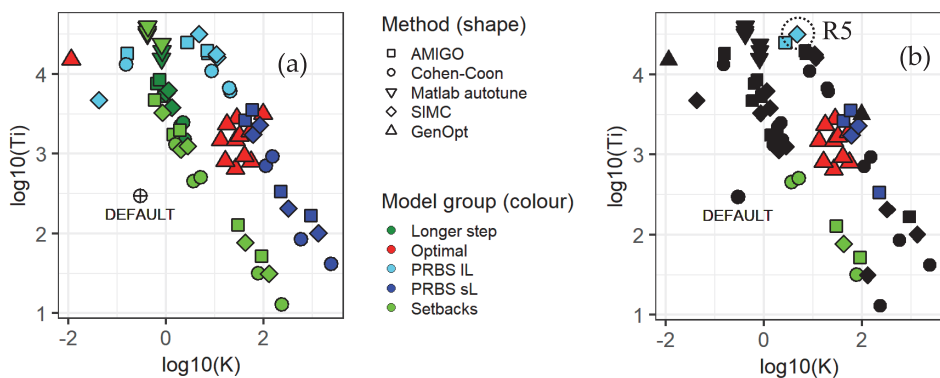
Figure 4. All PI parameter value pairs (*K, Ti*) on log-valued axes colored based on the method, in (**a**) the default black circle with cross is the PI parameters pair used in IDA ICE by default, in (**b**) the black points are the ones that would not result in acceptable temperatures for R6 without setpoint shifting.
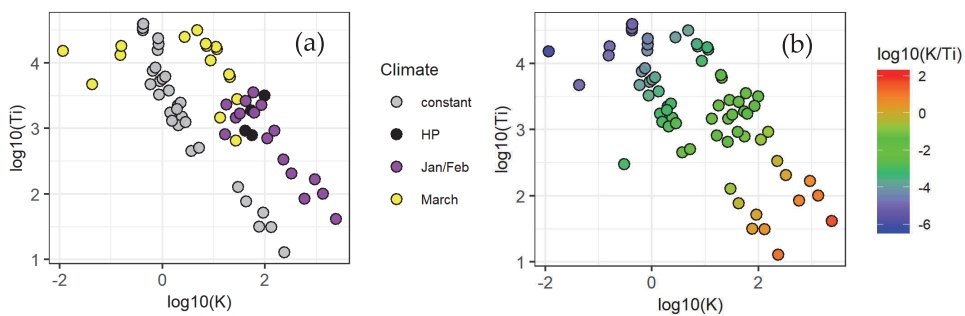
Figure 5. Graph (**a**) shows the underlying climate data and graph (**b**) shows the log-ratio values of all the PI parameter pairs. In (**a**), the constant climate is at 0 °C with no solar radiation, HP stands for heating period and all the dates are covered in Section 2.

For the very small proportional gain, the integration time varies significantly from this otherwise linear behavior in the log10-log10 scale. The reason for this is depicted partly in Figure 5a. As can be seen, this covers the four cases calculated or optimized for March. Actually, these were all achieved for Room 6. This means that the solar peaks have been severe and almost no heating was needed. Therefore, these cases resulted in obscure parameters.

The clear separation between parameters is evident. The two sets of parameters with both blue and red (optimal) results made up one group and both green ones the other. This is also the difference in outdoor conditions, as can be seen in Figure 5a. The first group was generated at dynamic outdoor temperatures and realistic solar irradiation, while the second group bordered constant outdoor temperatures and no solar radiation. Here, also the separation between the March and Jan/Feb periods is clear, so it can be assumed that more solar gains causes the K parameter to be smaller and T_i to be longer. For the optimal cases, the combinations closer to the blue ones are optimized for the variable setpoint, the lower values for the constant setpoint.

In Figure 4b, the parameter combinations, which do not achieve the needed setpoints in Room 6 for at least 97% of the time (with a slack of 0.05 °C), are colored black. Both the one constant and two variable setpoint levels are checked and the coloring shows if any of the three are violated. If the graph would be for R5, all of the points, except the one with a dashed circle around it, would be black. This means that only one parameter combination would achieve the required temperatures in R5, if the setpoints were not shifted, as it was described in Section 2.6.

In Figure 5b, all the K-T_i pairs are colored by the log10 (K/T_i) value. This logarithm is further used for describing the pairs, as this is a clear indicator whether the pair is in the lower right or upper left corner of the log10-log10 graph.

3.3. Setpoint Temperature Tracking and PI Output Signal Behaviour

Each parameter combination results in different air temperature profiles and PI output signal profiles. There are four examples of the temperature and PI output profile combinations shown in Figure 6 for the constant setpoint cases and in Figure 7 for the variable setpoint cases in Room 6. In both figures, the Jan/Feb week is depicted on the left and the March week on the right. The parameter combinations are chosen as the ones with minimum and maximum log10 ratios of the parameters, the IDA ICE default combination, and the one which resulted in optimal energy consumption (see Section 3.5). The combinations are ordered by the log10 ratio of the parameters with the minimum ratio at the top and the maximum ratio at the bottom. The IDA ICE default combination is the second (0.3/300) and the optimal is the third from the top (18/2300). Here, the parameter values were rounded to two significant numbers.

In the first column of Figure 6, most of the controllers show results that suggest maintaining a constant setpoint in the situation with no solar gains is an easy task. The small fluctuations are largest when a very small proportional gain ($K = 0.012$ in Figure 6a) with a large integration time is applied. This controller changes the signal too slowly, as its PI output signal in black shows. The signal stays almost constant throughout the day and even throughout the week. Due to the same effect, temperatures drop below the constant setpoint in March in Figure 6b and the setpoint tracking is poor in the variable cases. The level at which the signal is constant depends on the season, as there is a clear difference between February and March.
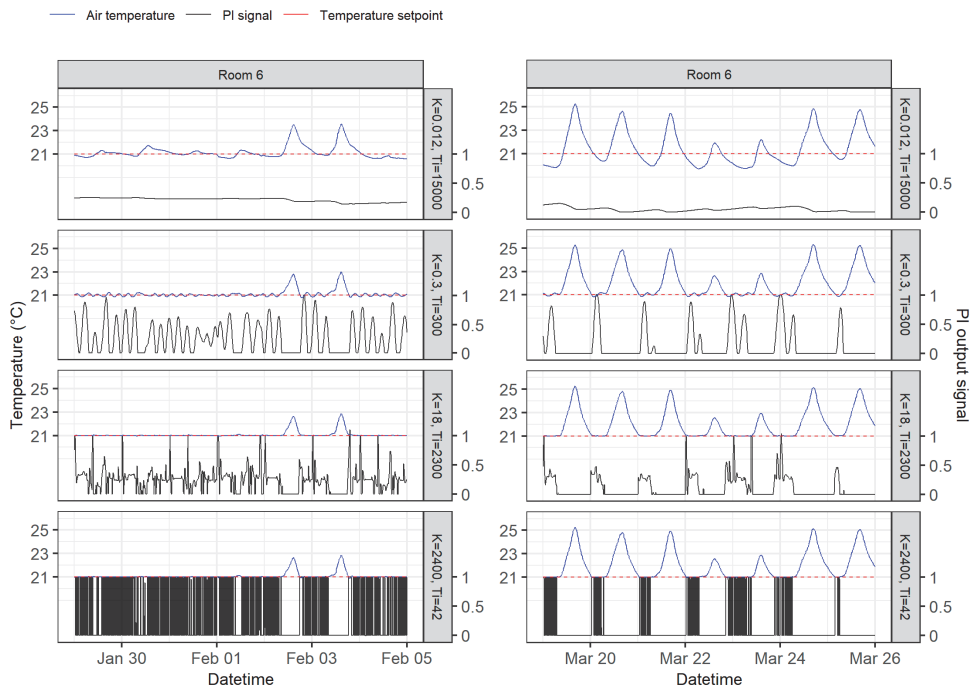
Figure 6. Air temperatures and PI output signals for the constant setpoint case during one week in January/February (**left**), and in a week in March (**right**) for the chosen four pairs of parameters.
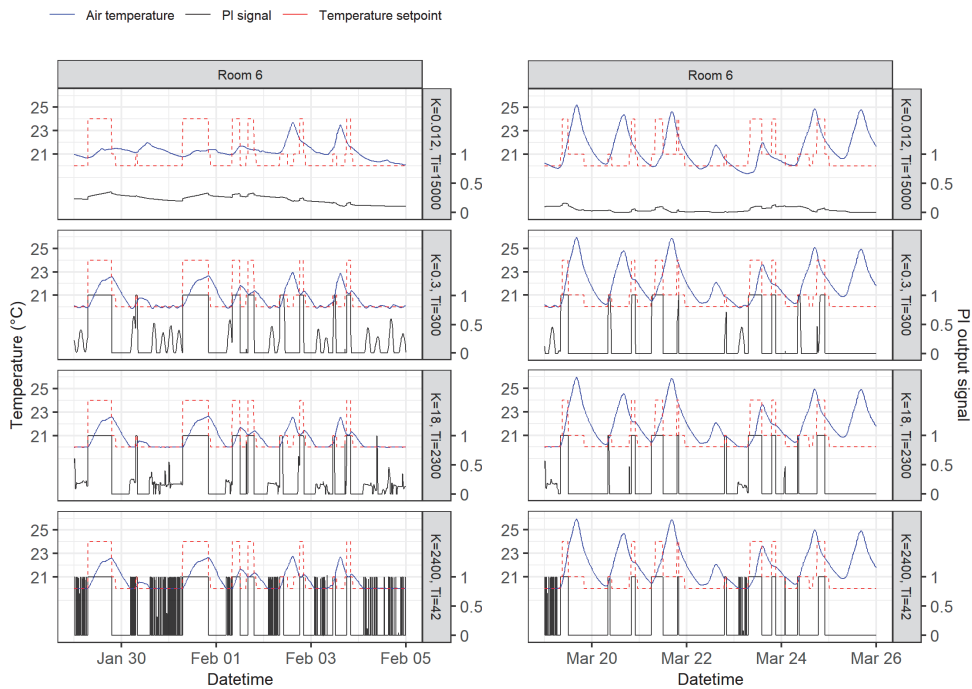
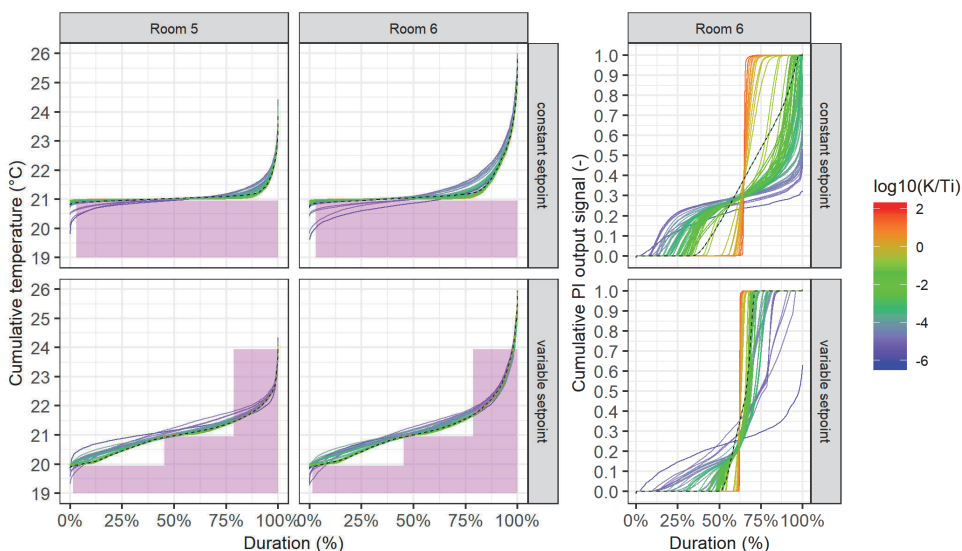**Figure 7.** Air temperatures and PI output signals for the variable setpoint case during one week in January/February (**left**), and in a week in March (**right**) for the chosen four pairs of parameters.

　　　The constant setpoint cases in Figure 6 show that 2400/42 manages to maintain the constant setpoint the best. However, there is no significant difference for the variable setpoint cases. However, the PI output signal in the same case changes most rapidly. Both a large proportional gain and relatively small integration time contribute to this. Such switching reduces the life span of most of the devices, so this would not be acceptable in practice. For the case with also a large proportional gain but with a large integration time as well (18/2300), the signal is a bit smoother. In the long integration time cases, the heating starts earlier and stops sooner than for the shorter integration time. It can be observed that the PI signal turns on before the temperature lowers below the setpoint generating a prediction effect. This is especially clear for 18/2300 during the March week.

　　　The variable setpoint cases in February in Figure 7's first column show that in cold weather with no solar peaks, the 24 °C setpoint peaks were not reached due to the short duration of the setpoint increase. Therefore, setpoint tracking during high setpoints is clearly not good but is also not required. However, the PI signal is 1 during these times, which means the heater is fully on as is the aim for load shifting. In this figure, again controllers 18/2300 and 2400/42 both maintain the lower setpoint well. However, the latter is switching on and off often and has almost no other state. In March, the solar peaks govern the temperatures. However, the second column of Figure 7 shows that the heating is turned on as well.

　　　All the cumulative profiles over the heating period are shown in Figure 8. For the PI signal, only R6 is shown as the profiles look very similar for the two rooms. The switching behavior indicated before is clearly dependent on the log10 ratio of the PI parameters. The higher the ratio, the more abrupt the changes, as the cumulative graph indicates behaviors close to on–off signals. As shown in Figure 9, a zoom-in on R6's constant setpoint graph, the higher temperatures at the high-temperature end are clearly dependent on the Ti value. The low-temperature end seems to be more dependent on the K value. Therefore, the energy consumption of the parameter combination is mostly dependent on the K value and avoiding over-heating at the disturbances is more dependent on the Ti value. This effect was also observed in the analysis.

Figure 8. Duration curves over the heating period for temperatures on the left and PI output signals on the right. The purple indicates the temperatures below the setpoint and the black dashed line shows the results of the IDA ICE default parameters.
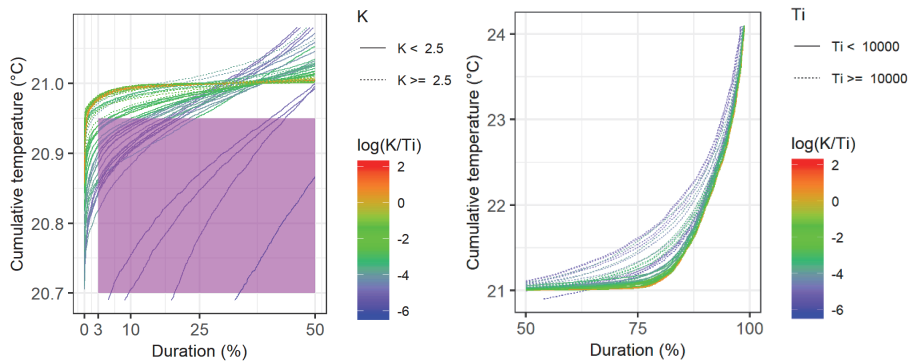
Figure 9. (**Left**): Zoom-in on Figure 8's lower temperature end of the constant temperature graph of R6; (**right**): Zoom-in on the temperature end of the same graph.

3.4. Setpoint Shifting

It is clear, that some of the parameter combinations did not achieve the required temperature setpoint and some resulted in higher temperatures above the setpoint. Especially at the high temperature end, there was also a clear difference between rooms R5 and R6, as can be seen from Figure 8. This was caused by the room orientations as the R6 faces south-west and gets more solar gains than the north-west orientated R5. As declared in Section 2.6, the setpoints were shifted for all cases in the way that temperatures would reach the required setpoint for at least 97% of the time. The shift values were different for R5 and R6 as well as for the constant and variable setpoint cases. As a result, all temperatures reached the given setpoints at around 95–97% of the heating period. This accuracy was considered satisfactory. The shifts are shown together with the energy consumption evaluation in Figure 10.
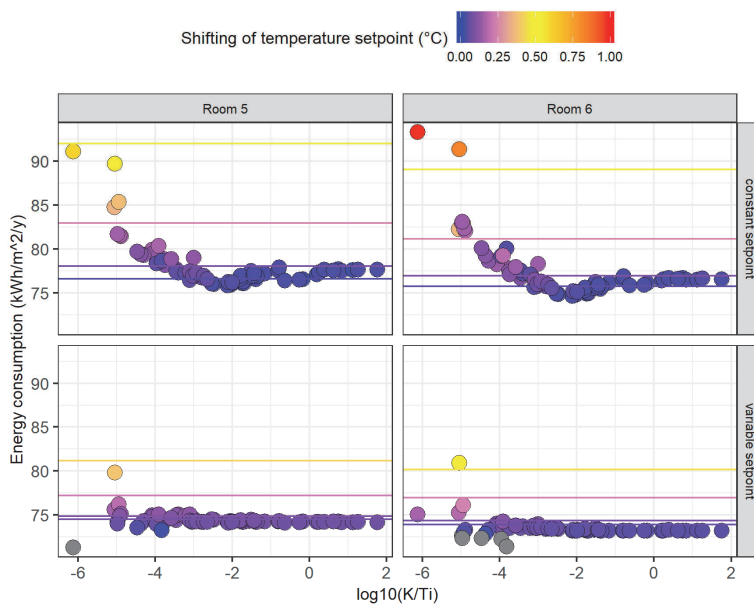
Figure 10. Influence of the log10 of the PI parameters ratio *K/Ti* on energy consumption in the 10.4 m^2 rooms; color-scale shows the setpoint shift; the grey values are below 0 which means that the temperature setpoints have been decreased. The horizontal lines depict the setpoint shifts and energy consumption of the on–off cases with different dead-bands.

3.5. Energy Performance and Total Setpoint Tracking Accuracy

The energy consumption results after setpoint shifting are shown in Figures 10 and 11. It is clear that the variable setpoint cases consumed less energy. This is because the average room temperatures were lower. The setpoints were also higher than the constant cases in some periods but coincidentally the higher setpoint temperatures often occurred during the day and the lower setpoints occurred during the night, so this does not influence heating energy use much. Also, the high setpoints were not actually reached. In the constant temperature cases, a clear optimum emerged between the log10 ratio of −3 and −1. This means that in optimal cases, the K value was 10 to 1000 times smaller than *Ti*.
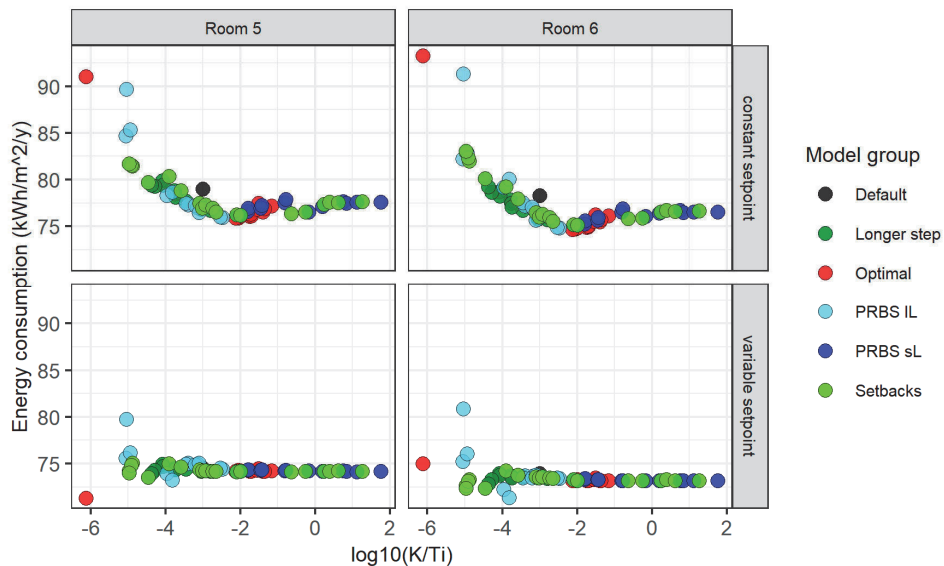
Figure 11. Influence of the log10 of the PI parameters ratio *K*/*Ti* on energy consumption; colors visualize the underlying model group.

The horizontal lines in Figure 10 represent the shifted energy performance at the benchmark for the on–off cases with different dead-bands. From top to bottom (yellow to blue) the corresponding dead-bands are 1 K, 0.5 K, 0.16 K, and 0.05 K. The optimal PI parameter combinations result in a lower energy consumption than even the lowest of the lines with an unrealistically small dead-band. The commonly used dead-band of 0.5 K consumes 2–3 kWh/m^2/year more energy than the PI cases for the variable setpoint. For the constant setpoint, the lowest PI results are up to 7 kWh/m^2/year or 9% lower than for the on–off with a 0.5 K dead-band, which, for example, in R6 is at 81 kWh/m^2/year. Omitting the extreme poorly performing cases, the total variation in energy consumption is more than 10 kWh/m^2/year or 12% in the constant setpoint case.

Figure 11 shows the same data colored by the model group. The IDA ICE default parameter is at one edge of the optimum range with exactly 1000 times difference. The energy consumption is already around 5 kWh/m^2/year or 5% higher on that edge compared with the optimal case. The parameters optimized for setpoint tracking are also close to an optimal energy consumption. The PRBS sL group performs well almost in all cases but not optimally, while in all other groups some combinations perform poorly. The optimal range of parameters is shown in detail in Table 3. Most of the optimal values were calculated using TRY climate data but the methods varied.

Table 3. Optimal parameter combinations from log10 ratio from −3 (excluded) to −1. Ordered in increasing energy consumption values for the R6 constant setpoint.

K	Ti	Model	Method	Climate	Setpoint	Room	Total Length
18	2300	-	GenOpt	TRY, Jan/Feb week	variable	R6	Inf
13	1500	-	GenOpt	TRY, March week	constant	R5	Inf
28	2800	-	GenOpt	TRY, March week	variable	R5	Inf
21	6200	11	Cohen-Coon	TRY, March weekend	PRBS	R5	2 days
20	6700	12	Cohen-Coon	TRY, March week	PRBS	R5	7 days
27	1500	-	GenOpt	TRY, Jan/Feb week	constant	R5	Inf
16	820	-	GenOpt	TRY, Jan/Feb week	constant	R6	Inf
32	1700	-	GenOpt	TRY, Jan/Feb week	variable	R5	Inf
5.2	510	4	Cohen-Coon	Const	6-h setback	equal	1.5 days
3.7	460	2	Cohen-Coon	Const	24-h setback	equal	6 days
42	2700	9	AMIGO	TRY, Jan/Feb weekend	PRBS	equal	2 days
27	650	-	GenOpt	TRY, March week	constant	R6	Inf
54	1900	-	GenOpt	TRY, heating period	variable	R5	Inf
2.8	1300	4	SIMC	Const	6-h setback	equal	1.5 days
59	3600	10	AMIGO	TRY, Jan/Feb week	PRBS	R5	7 days
61	1800	9	SIMC	TRY, Jan/Feb weekend	PRBS	R5	2 days
41	930	-	GenOpt	TRY, heating period	constant	R6	Inf
2.4	1500	1	Cohen-Coon	Const	Ideal step	equal	60 days
2.0	1100	2	SIMC	Const	24-h setback	equal	6 days
85	2300	10	SIMC	TRY, Jan/Feb week	PRBS	R5	7 days
55	800	-	GenOpt	TRY, heating period	constant	R5	Inf
98	3200	-	GenOpt	TRY, heating period	variable	R6	Inf
1.6	1300	3	Cohen-Coon	Const	12-h setback	equal	3 days

The AAE of the temperatures for rooms R5 and R6 are shown in Figure 12. The AAE is clearly dependent on the room and setpoint but not on the parameter combination. The AAE is constantly at 0.5 K for R5 and around 0.7 for R6 in the variable setpoint cases. The accuracy here depends mostly on the solar gains. For the constant setpoint case, the optimal region is everything, with a *Ti* lower than 10^4 and a *K* higher than $10^{0.5}$. The error is around 0.2 K for all the simulations in R5, for R6 the error ranges from 0.25 to 0.6 K, and in extreme cases to 1 K.
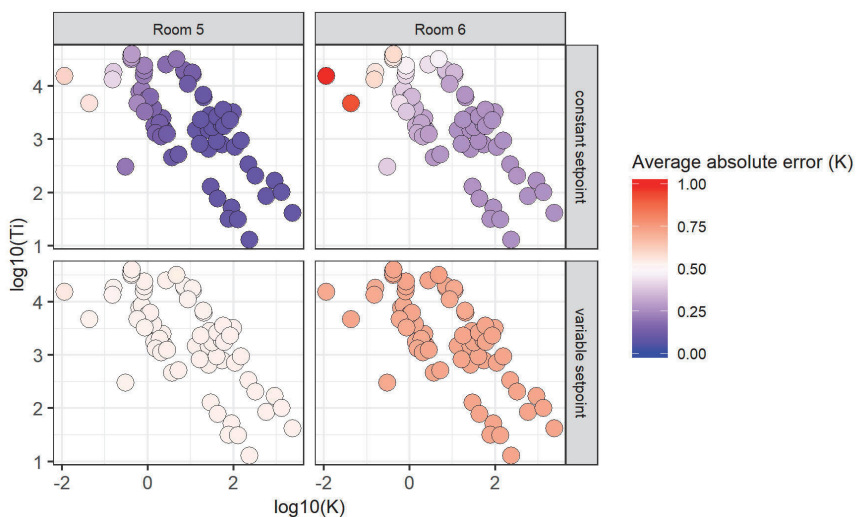
Figure 12. Absolute average error (AAE) of the air temperature compared to the setpoint.

4. Discussion

Different PI parameter estimation methods were applied on various periods and control profiles. An optimal region of the parameter ratio was determined where the energy consumption was the lowest. Half of the parameter combinations in the optimal region for energy consumption were found via GenOpt, although they were optimized for the minimal temperature setpoint tracking error. Although most reliably well-performing, this approach is not always suitable in practice as it requires an advanced model of the building. Therefore, it is practical that the other half of the parameter combinations in the optimal region were found using only short tests and simple calculations.

For all these other methods, simplified models were identified. In the optimal region, all the tested simplified methods were represented: Cohen–Coon, AMIGO, and SIMC. The results tuned in Matlab were not represented, probably due to the chosen goal being speed for that methodology. The models underlying these calculations were obtained from the week or weekend pseudo-random temperature setpoint (PRBS) data or setbacks of 6, 12, or 24 h. It is clear that the longer the setback, the easier it is to identify a simple model on it. This is probably the reason why the 1- and 3-h setbacks resulted in less desirable parameters. Still, conducting 24-h setbacks would probably not be comfortable for the occupants. Therefore, it is beneficial that 6-h setbacks could suffice. For example, these could be conducted during the night when the outdoor conditions are less variable with no solar gains. The suitable PRBS cases included both the January and March data, indicating that it is possible to get quality parameters in various weather conditions.

The optimal parameter combinations resulted in an annual heating energy reduction of up to 9% or 7 kWh/m^2/year. The comparison of heat emitters and controllers in the European standard room shows similar results with 5% to 10% savings for the PI controlled UFH compared with the on–off control [20]. This does not compare to the 32% achieved for radiators in [23], however, the actual difference is difficult to compare as the baselines are different. The reduction of 7 kWh/m^2/year here can be seen as highly significant as this can be achieved with only parameter correction, which does not require intensive computation when the simple tests are applied. Accounting for the more expensive thermostat head with variable parameters option, the payback time of this change is around 5 years. This saving can be achieved without setpoint reductions, which means no penalty on comfort. On the contrary, due to less fluctuation, comfort could even improve.

The methodology used here could be applied in any UFH system. In public and office buildings, a detailed model often exists and optimization of the parameters could be possible. Due to the large floor areas in these buildings, the absolute savings could be significant compared with the on–off control. Even more evident would be the saving in outdoor UFH systems installed under garage runways or stadiums to keep them clear from ice and snow.

Evidently, the parameter value results apply to the studied building, and future research can determine possible variation of the parameters in buildings with a smaller or higher thermal mass, insulation level, and maximum heating power. However, the wide range of well-performing parameter combinations and the fact that the suitable region is the same for both the north and south facing rooms provides an indication that the parameters from this region could be suited to different buildings as well. This should be confirmed by future studies on the subject.

5. Conclusions

Several combinations of the input data and PI parameter estimation methods were applied with the aim to improve UHF temperature control, resulting in 68 different PI parameter combinations. Based on the results and discussion above, most importantly concluded is that:

- For the first time in the scientific literature, it is shown that UFH can operate with determined PI parameters similar to ideal control;
- A performance close to optimal could also be achieved by parameters achieved from shorter tests, e.g., weekend pseudo-random setpoints, and 6- to 24-h setbacks which were shown to be suitable;
- The optimal PI parameters improved the room temperature control accuracy considerably, and that the results show that the UFH PI control with the correct parameters started to work in a predictive fashion and the resulting room temperature curves were practically ideal;
- The optimal PI parameters reduced the energy consumption for heating by up to 9% (7 kWh/m^2/year) in comparison with the on–off control (at around 80 kWh/m^2/year) and by 5% in comparison with the default PI parameters;
- The variation amplitude of the heating energy needed using different estimated (not random) parameters was more than 15 kWh/m^2/year for the constant setpoint, which stresses the importance of having the correct PI parameters;
- The optimal PI parameters included combinations with log10 *(K/Ti)* between −3 and −1, in these combinations, the proportional gain *K* ranged from 2 to 100 and the integration time *Ti* from 500 to 6700 s, and thus higher gain and longer integration time values than are conventionally used are recommended;
- For the variable setpoint, using the PI control had a similar effect to decreasing the dead-band and the variation in the PI parameters did not have a significant further effect on the energy consumption, except for when they were extremely poorly tuned;
- The average absolute error for the air temperatures from the setpoint was well below 0.5 K for the constant setpoints, but above for the variable setpoints.

Appendix A

Table A1. All obtained parameter values, which were not already shown in Table 3, sorted by log10 ratio from largest to smallest.

K	Ti (s)	Model	Method	Climate	Setpoint	Room	Total Length (Days)
2400	42	14	Cohen-Coon	TRY, Jan/Feb week	PRBS	R6	7
235	13	6	Cohen-Coon	Const	1-h setback	equal	0.25
1300	100	14	SIMC	TRY, Jan/Feb week	PRBS	R6	7
580	85	13	Cohen-Coon	TRY, Jan/Feb weekend	PRBS	R6	2
930	170	14	AMIGO	TRY, Jan/Feb week	PRBS	R6	7
130	31	6	SIMC	Const	1-h setback	equal	0.25
77	32	5	Cohen-Coon	Const	3-h setback	equal	0.75
91	52	6	AMIGO	Const	1-h setback	equal	0.25
320	210	13	SIMC	TRY, Jan/Feb weekend	PRBS	R6	2
230	340	13	AMIGO	TRY, Jan/Feb weekend	PRBS	R6	2
43	77	5	SIMC	Const	3-h setback	equal	0.75
30	130	5	AMIGO	Const	3-h setback	equal	0.75
150	940	10	Cohen-Coon	TRY, Jan/Feb week	PRBS	R5	7
110	710	9	Cohen-Coon	TRY, Jan/Feb weekend	PRBS	R5	2
1.9	2000	4	AMIGO	Const	6-h setback	equal	1.5
2.3	2500	8	Cohen-Coon	Actual	3-day measured	R5	3
2	2300	7	Cohen-Coon	Actual	2-day measured	R5	2
1.4	1800	2	AMIGO	Const	24-h setback	equal	6
8.7	11,000	15	Cohen-Coon	TRY, March weekend	PRBS	R6	2
11	16,000	11	SIMC	TRY, March weekend	PRBS	R5	2
11	18,000	12	SIMC	TRY, March week	PRBS	R5	7
7.2	18,000	11	AMIGO	TRY, March weekend	PRBS	R5	2
7	20,000	12	AMIGO	TRY, March week	PRBS	R5	7
1.3	3800	1	SIMC	Const	Ideal step	equal	60
0.9	3300	3	SIMC	Const	12-h setback	equal	3
1.1	6200	8	SIMC	Actual	3-day measured	R5	3
1	5800	7	SIMC	Actual	2-day measured	R5	2
0.9	5300	1	AMIGO	Const	Ideal step	equal	60
4.8	32,000	15	SIMC	TRY, March weekend	PRBS	R6	2
0.6	4700	3	AMIGO	Const	12-h setback	equal	3
2.7	25000	15	AMIGO	TRY, March weekend	PRBS	R6	2
0.7	8500	8	AMIGO	Actual	3-day measured	R5	3
0.6	7700	7	AMIGO	Actual	2-day measured	R5	2
0.81	16,000	1	tuned in Matlab	Const	Ideal step	equal	60
0.83	20,000	7	tuned in Matlab	Actual	2-day measured	R5	2
0.82	24,000	8	tuned in Matlab	Actual	3-day measured	R5	3
0.82	24,000	2	tuned in Matlab	Const	24-h setback	equal	6
0.41	32,000	3	tuned in Matlab	Const	12-h setback	equal	3
0.41	34,000	5	tuned in Matlab	Const	3-h setback	equal	0.75
0.15	13,000	16	Cohen-Coon	TRY, March week	PRBS	R6	7
0.43	40,000	6	tuned in Matlab	Const	1-h setback	equal	0.25
0.41	39,000	4	tuned in Matlab	Const	6-h setback	equal	1.5
0.043	4700	16	SIMC	TRY, March week	PRBS	R6	7
0.16	18,000	16	AMIGO	TRY, March week	PRBS	R6	7
0.012	15,000	-	genopt	TRY, March week	variable	R6	Inf

References

1. Salata, F.; Golasi, I.; Domestico, U.; Banditelli, M.; Basso, G.L.; Nastasi, B.; Vollaro, A.D.L. Heading towards the nZEB through CHP+HP systems. A comparison between retrofit solutions able to increase the energy performance for the heating and domestic hot water production in residential buildings. *Energy Convers. Manag.* **2017**, *138*, 61–76. [CrossRef]

2. Becchio, C.; Dabbene, P.; Fabrizio, E.; Monetti, V.; Filippi, M. Cost optimality assessment of a single family house: Building and technical systems solutions for the nZEB target. *Energy Build.* **2015**, *90*, 173–187. [CrossRef]

3. Péan, T.; Salom, J.; Castello, R.C. Review of control strategies for improving the energy flexibility provided by heat pump systems in buildings. *J. Process. Control.* **2019**, *74*, 35–49. [CrossRef]

4. EU Buildings Factsheets. Available online: https://ec.europa.eu/energy/eu-buildings-factsheets_en (accessed on 20 April 2020).

5. Thonipara, A.; Runst, P.; Ochsner, C.; Bizer, K. Energy efficiency of residential buildings in the European Union—An exploratory analysis of cross-country consumption patterns. *Energy Policy* **2019**, *129*, 1156–1167. [CrossRef]

6. Kummert, M.; Andre, P.; Nicolas, J. Optimal heating control in a passive solar commercial building. *Sol. Energy* **2001**, *69*, 103–116. [CrossRef]

7. Wolisz, H.; Kull, T.M.; Müller, D.; Kurnitski, J. Self-learning model predictive control for dynamic activation of structural thermal mass in residential buildings. *Energy Build.* **2020**, *207*, 109542. [CrossRef]

8. Astrom, K.; Hägglund, T. The future of PID control. *Control. Eng. Pr.* **2001**, *9*, 1163–1175. [CrossRef]

9. Dounis, A.I.; Caraiscos, C. Advanced control systems engineering for energy and comfort management in a building environment—A review. *Renew. Sustain. Energy Rev.* **2009**, *13*, 1246–1261. [CrossRef]

10. Royapoor, M.; Antony, A.; Roskilly, T. A review of building climate and plant controls, and a survey of industry perspectives. *Energy Build.* **2018**, *158*, 453–465. [CrossRef]

11. Salsbury, T.I. A SURVEY OF CONTROL TECHNOLOGIES IN THE BUILDING AUTOMATION INDUSTRY. *IFAC Proc. Vol.* **2005**, *38*, 90–100. [CrossRef]

12. Rodríguez-Rodríguez, I.; González-Vidal, A.; González, A.R.; Izquierdo, M.A.Z. Commissioning of the Controlled and Automatized Testing Facility for Human Behavior and Control (CASITA). *Sensors* **2018**, *18*, 2829. [CrossRef] [PubMed]

13. Seidel, S.; Haufe, J.; Majetta, K.; Blochwitz, T.; Liebold, E.; Hintzen, U.; Klostermann, V.; Clauß, C. Modelica based Design and Optimisation of Control Systems for Solar Heat Systems and Low Energy Buildings. In Proceedings of the 11th International Modelica Conference, Versailles, France, 21–23 September 2015; Volume 118, pp. 401–410.

14. Astrom, K.; Hägglund, T.; Wallenborg, A. Automatic tuning of a digital controller. In Proceedings of the 4th IFAC Symposium on Adaptive Systems in Control and Signal, Grenoble, France, 1–3 July 1992; Volume 25, pp. 285–290. [CrossRef]

15. Wang, Y.-G.; Shi, Z.-G.; Cai, W.-J. PID autotuner and its application in HVAC systems. In Proceedings of the 2001 American Control Conference. (Cat. No.01CH37148), Arlington, VA, USA, 25–27 June 2001; pp. 2192–2196. [CrossRef]

16. Bi, Q.; Cai, W.-J.; Wang, Q.-G.; Hang, C.-C.; Lee, E.-L.; Sun, Y.; Liu, K.-D.; Zhang, Y.; Zou, B. Advanced controller auto-tuning and its application in HVAC systems. *Control. Eng. Pr.* **2000**, *8*, 633–644. [CrossRef]

17. Ferrarini, L.; Rastegarpour, S.; Petretti, A. An Adaptive Underfloor Heating Control with External Temperature Compensation. In Proceedings of the 14th International Conference on Informatics in Control, Automation and Robotics, Madrid, Spain, 26–28 July 2017; pp. 629–636. [CrossRef]

18. Curtiss, P.S. Examples of Neural Networks Used for Building System Control and Energy Management. *ASHRAE Trans.* **1997**, *103*, 909.

19. Hasan, A.; Kurnitski, J.; Jokiranta, K. A combined low temperature water heating system consisting of radiators and floor heating. *Energy Build.* **2009**, *41*, 470–479. [CrossRef]

20. Võsa, K.-V.; Ferrantelli, A.; Kurnitski, J. Annual performance analysis of heat emission in radiator and underfloor heating systems in the European reference room. *E3S Web Conf.* **2019**, *111*, 111. [CrossRef]

21. Kukolj, D.D.; Kuzmanović, S.B.; Levi, E. Design of a PID-like compound fuzzy logic controller. *Eng. Appl. Artif. Intell.* **2001**, *14*, 785–803. [CrossRef]

22. Ostermeier, M.; Müller, J. Automated investigation, evaluation and optimisation of simple heating circuits in building automation. *E3S Web Conf.* **2019**, *111*, 111. [CrossRef]

23. Fiducioso, M.; Curi, S.; Schumacher, B.; Gwerder, M.; Krause, A. Safe Contextual Bayesian Optimization for Sustainable Room Temperature PID Control Tuning. In Proceedings of the Twenty-Eighth International Joint Conference on Artificial Intelligence, Macao, 10–16 August 2019. [CrossRef]

24. Nägele, F.; Kasper, T.; Girod, B. Turning up the heat on obsolete thermostats: A simulation-based comparison of intelligent control approaches for residential heating systems. *Renew. Sustain. Energy Rev.* **2017**, *75*, 1254–1268. [CrossRef]

25. Maivel, M.; Ferrantelli, A.; Kurnitski, J. Experimental determination of radiator, underfloor and air heating emission losses due to stratification and operative temperature variations. *Energy Build.* **2018**, *166*, 220–228. [CrossRef]

26. Võsa, K.-V.; Ferrantelli, A.; Kurnitski, J. Experimental study of radiator, underfloor, ceiling and air heater systems heat emission performance in TUT nZEB test facility. *E3S Web Conf.* **2019**, *111*, 111. [CrossRef]

27. Kull, T.M.; Thalfeldt, M.; Kurnitski, J. Estimating time constants for underfloor heating control. *J. Phys. Conf. Ser.* **2019**, *1343*. [CrossRef]

28. IDA ICE 4.8 SP1, Expert Edition. 2019. Available online: https://www.equa.se/en/ida-ice (accessed on 20 April 2020).

29. Kalamees, T.; Kurnitski, J. Estonian test reference year for energy calculations. *Proc. Est. Acad. Sci. Eng.* **2006**, *12*, 40–58.

30. Ljung, L. *System Identification Toolbox: User's Guide*; MathWorks Incorporated: Natick, MA, USA, 1995.

31. Wetter, M. *Generic Optimization Program User Manual Version 3.0.0*; Lawrence Berkeley National Lab. (LBNL): Berkeley, CA, USA, 2009; pp. 1–108. [CrossRef]

32. Åström, K.J.; Hägglund, T. *Advanced PID Control*; ISA-The Instrumentation, Systems, and Automation Society: Research Triangle Park, NC, USA, 2006; Volume 461.

33. Nord Pool. Available online: https://www.nordpoolgroup.com/historical-market-data/ (accessed on 20 April 2020).

34. Clauß, J.; Stinner, S.; Sartori, I.; Georges, L. Predictive rule-based control to activate the energy flexibility of Norwegian residential buildings: Case of an air-source heat pump and direct electric heating. *Appl. Energy* **2019**, *237*, 500–518. [CrossRef]

35. *EN 16798-2, Energy Performance of Buildings—Part 2: Indoor Environmental Input Parameters for Design and Assessment of Energy Performance of Buildings Addressing Indoor Air Quality, Thermal Environment, Lighting and Acoustics*; EPB Center: AN Rotterdam, The Netherlands, 2019.

Publication III

Taylor & Francis
Taylor & Francis Group

Check for updates

Wax actuator's empirical model development and application to underfloor heating control with varying complexity of controller modelling detail

Tuule Mall Parts [a,b], Andrea Ferrantelli [a,b,d], Hendrik Naar [c], Martin Thalfeldt [a,b] and Jarek Kurnitski [a,b,d]

[a]FinEst Centre for Smart Cities (Finest Centre), Tallinn University of Technology, Tallinn, Estonia; [b]Nearly Zero Energy Buildings Research Group, Tallinn University of Technology, Tallinn, Estonia; [c]Mechanics and Fluids and Structures Research Group, Tallinn University of Technology, Tallinn, Estonia; [d]Department of Civil Engineering, Aalto University, Aalto, Finland

ABSTRACT

This paper investigates how a simulated room's energy and temperature performance are affected if its underfloor heating control is modelled with increasing detail. Experiments were performed to develop and calibrate an empirical model of wax motor and to calibrate the valve curve. These models were used to implement and test the On/Off and proportional-integral (PI) control processes at various levels of modelling detail. Controllers were implemented by gradually adding optimized control parameters, signal delay, calibrated valve curve, signal modulation, and actuator modelling. The On/Off control dead band and PI parameters exhibited the largest impact, reducing energy use (1%–5%) and temperature fluctuations (ca 1 K). Modulating the PI output signal increased temperature fluctuations to the same amplitude as On/Off with 0.5 K dead band, increasing space heating demand by 1.3%. The wax actuator counted for less than 1%; however, it increased time delays to maximally 7 min and remarkably changed the mass flows.

1. Introduction

Buildings are responsible for 36% of greenhouse gas emissions and for about 40% of the total energy consumption, of which 1/3 goes into heating (Bienvenido-Huertas et al. 2021). Extensive involvement of renewables in the energy production is important for reducing carbon emissions (Rogelj 2018), but it poses serious problems to the electricity grid, due to the highly fluctuating nature of photovoltaic and wind generated energy. To guarantee stability and efficiency of the distribution network in the imminent future, matching electricity demand and renewable energy generation needs to be realized rather swiftly (Boßmann and Staffell 2015).

Electricity-based heating systems, such as heat pumps together with hydronic underfloor heating (UFH), are increasingly used in residential buildings to reduce heating demand. These provide both electrification of the heating demand as well as structural thermal storage. Balancing the power grid of high shares of renewable energy is thus possible, to some extent, through demand-side management (Wolisz et al. 2020; Zhang, Good, and Mancarella 2019). Dynamic control of these systems exploits indeed the buildings' intrinsic structural thermal mass to shift both heating and cooling timing, without reducing

the indoor climate quality (Wolisz et al. 2020; Le Dréau and Heiselberg 2016; Pedersen, Hedegaard, and Petersen 2017; Reynders, Diriken, and Saelens 2017). Importantly though, the thermal fluctuations in the enclosure critically affect the charging and discharging of some fraction of this thermal mass. An accurate balance of the power grid via structural thermal storage should thus be accomplished through several control methods (Zhang, Good, and Mancarella 2019; Wolisz et al. 2016, 2020).

One way to participate in the balancing of the power grid is bidding on the so-called manual Frequency Restoration Reserve, which helps stabilizing the electricity grid by restoring the required frequency of the grid. Open for public participation is in most countries the manual Frequency Restoration Reserve, which is provided by the Transmission System Operator. This is a tertiary control reserve, which steps in to correct longer lasting deviations that cannot be fixed by the other upstream balancing services alone (Okur, Heijnen, and Lukszo 2021). At least 1 MW is often required for bidding (Okur, Heijnen, and Lukszo 2021), but intermediators aggregating several heat pumps could provide enough power (Zhang, Good, and Mancarella 2019). In such Frequency Restoration Reserve market, the providers must be able to switch

---

their loads within 5 to 15 min (Artelys 2017; Fingrid Oyj 2022). To this aim, heat pumps require manual intervention and overwritten control (Lindahl 2020); the start-up time of the heat pump system could also generate a bottleneck that is critical to the local system response to the grid. Even if the heat pump can be activated as fast as within 5 min, a heat sink is needed for its energy to avoid overheating the small amount of water in the heat pump's closed circuit. This would lead to stopping the electricity consumption and not fulfilling the bid. In case of inverter-based heat pump systems, large storage tanks are typically not installed, and the building structures should be used as a heat sink. This requires opened valves in the hydronic heating system, e.g. UFH manifold. However, valves in UFH systems are controlled by thermoelectric actuators with solid wax, which react relatively slowly. In closed valve positions, the system volume is very small and temperature limits in the heat pump circuit may be reached too quickly when the heat pump is started at full power. A slow movement of the actuator's piston with slow opening of the valves would then hinder the aggregator from delivering the bidden load for the grid.

To ensure energy flexibility and thermal comfort simultaneously in real applications, the control algorithms need to be carefully designed, tested, and validated. For initial development and testing, building performance simulations (BPS) are a suitable tool for speeding up the testing for different heating systems, building types, climates, usage profiles. Simulations are also needed to compare different algorithms at exact same boundary conditions. However, BPS are well known to simplify the control process to close-to-ideal, ignoring control parameter tuning, signal time delays, actual valve characteristic, and actuators. Usually, modelling of these is omitted as the control time constant is several orders of magnitude smaller than that of the whole system. The room temperature measurement time delay could be as large as 2 min (Burt and de Podesta 2020). Additionally, a delay of 2−3 min for the actuator-valve mechanism is normally assumed (Danfoss A/S 2017; Ventilation Control Products Sweden AB 2022). Even together, these timescales are too small to significantly alter the annual energy consumption of the building, especially if the users adapt the setpoint in response to temperature fluctuations induced by the delay. This timescale could still be important in simulations aimed at testing control algorithms that include logic for bidding or experimental situations for analysing the valve effects on volume flows.

Modelling the control in a detailed manner requires, among other details, a wax motor model. This is a major contribution of the present study, since an implementation that allows investigating the above systems' control

with sufficient accuracy is still missing. Additional applications of PCMs into the buildings' design are currently implemented into BPS with a broad scope, from, e.g. thermally activated wall panels (Klimeš, Charvát, and Ostrý 2019) to PCM tanks (Li et al. 2020). These have often been modelled as thermal hysteresis (Goia, Chaudhary, and Fantucci 2018). Sometimes, the actuators are simply modelled as a delay in BPS (Wetter 2009), or more commonly also as hysteresis, modelling their movement (Rizzello, Naso, and Seelecke 2019). To our knowledge, there can be found only one detailed wax actuator model for HVAC applications, namely a physical enthalpy-based model in IDA ICE (EQUA AB 2020), which was tested in Kull, Thalfeldt, and Kurnitski (2021). The study calibrated the physical wax motor model by numerically optimizing the parameters and compared the calibrated model error to a simple characteristic model. The calibration and comparison were performed only on a short and periodic signal. It was concluded that the parameters of the simple model should be variable, to perform well also in other situations. In this constant case the characteristic model induces slightly smaller errors than the physical model. The main limitation of the physical model lies however in the extensive amount of material testing or optimization required to determine all the properties of each wax motor product in practice.

Overall, scientific publications on the experimental as well as the modelling aspect of wax actuators are indeed very scarce. The effect of wax motors on BPSs has not been shown in the literature. In this study, we attempt at filling this compelling research gap that is entailed from the above discussion by developing a characteristic model with variable parameters and testing its effect on simulation results in a realistic control process. Motivation is given by both formal advancements and possible effects of the modelling on energy performance predictions, control algorithm testing and power grid balancing.

More into detail, several research questions emerge:

1. How can we characterize HVAC wax actuators with limited material testing? This study proposes a new empirical wax actuator model (with discrete hysteresis) for simulations in IDA ICE.
2. How much time does the valve opening with wax motors take? Can it be managed within 5 min, so that it would match the limit imposed by the frequency market for energy grids?
3. In the modelling of UFH for testing temperature control algorithms, the control is often assumed to be continuous (e.g. PI). However, the actual control is often On/Off (modulated) and exhibits a wax motor delay. How much are temperature control accuracy and energy performance then affected?

4. How do wax motor and modulation effects compare to performance differences from other modelling simplifications such as non-optimal control parameters, no delays in signals and linear valve characteristic?

To address these problematics, in this study we first performed experiments on wax motors to develop and calibrate an empirical model of wax actuator. Then, measurements were performed to estimate the valve performance in one UFH circuit and calibrate the valve curve. The wax actuator and the valve curve models were then used in BPS to implement and test the various levels of detail in modelling the control algorithms.

The paper is organized as follows. In Section 2, we provide a short overview of wax actuators and their modelling. Section 3 explains our methodology, featuring wax motor model development, valve curve estimation, and setup of room simulations. Section 4 fully reports experimental and simulation results, including a discussion at each stage. Finally, we draw our conclusions in Section 5, and include some additional experimental inputs and results in the Appendix.

2. Wax actuators

Thermoelectric wax actuators are electrically controlled and use paraffin wax as phase change material (PCM) for volume change (Burt and de Podesta 2020; Danfoss A/S 2017). The wax is solid at room temperature and liquid at higher temperatures. It is heated by a positive temperature coefficient (PTC) heater. These actuators are known by other names as well, such as wax motors (used in this work, abbreviated as WM), wax pellet actuators, thermo-electric actuators, or thermal actuators (Ventilation Control Products Sweden AB 2022; Klimeš, Charvát, and Ostrý 2019; Li et al. 2020; Goia, Chaudhary, and Fantucci 2018). In the absence of an electric heating signal, the system actuator-valve is normally closed. When voltage is applied, the wax starts melting and expanding, thus moving the valve's piston. By the action of a system of springs, the piston movement reduces the actuator's inner height, thus opening the valve. Such method of valve control has been used in UFH for a long time, as the actuators are silent and durable (Wetter 2009). Slower reactions also avoid the water hammer that is associated with motorized valves. Additionally, wax actuators are used before fan coils in cooling systems, and for pressure-independent control valves in heating systems. Radiator thermostats also include similar motors; however, these are often based on the expansion of liquid or gas instead of the phase change of the wax.

Some wax actuators use a continuous control with voltage between 0 and 10 V. Others use discrete control with a binary heating input, namely no voltage for no heating and 230 V or 24 V for heating. Continuous 0–10 V wax actuators still use 24 V to power the PTC heater. Therefore, if a controller with continuous output such as a PI controller is used to control the UFH wax actuators, the continuous signal must be modulated into a binary signal for the PTC heater.

The 0–10 V actuators can theoretically stay partially open. However, the partial opening control is easier for valves that have a logarithmic valve characteristic curve, i.e. a logarithmic volume flow dependency on the valve opening. In UFH manifolds, quick-opening valves are instead applied. These exhibit most of the change in volume flow when the valve is only slightly open. The partial flow would be realized only in a very small range of valve opening; therefore, these valves perform close to On/Off with either actuator, by using continuous or discrete control. Simpler 24-V On/Off-motors are often applied, which is the case of this work.

The actuator's cross section, valve, and part of the manifold are shown in Figure 1. The piston movement in function of the wax temperature change is shown in Figure 2. The hysteresis of up and down movements is generated by the temperature difference at the movement start and stop on both ends, caused by thermal inertia of the wax and friction of the internal parts that include a spring (Vernatherm 2023). The hysteresis in temperature can be linearized for simplification and presented on a time scale that is dependent on the binary heating signal, as shown in Figure 3. This linearized simple model was called 'characteristic model' in Kull, Thalfeldt, and Kurnitski (2021). Of course, the opening and closing process can be non-linear according to Figure 2. In the context of this paper, the different time periods in Figure 3 are called 'characteristic times' and defined as follows:

- Dead time (t_{dead}): solid wax heating up to the melting temperature, no volume change.
- Rise time (t_{rise}): phase change of the wax from solid to liquid and expansion.
- Hold time (t_{hold}): liquid wax cooling down to the melting temperature, no volume change.
- Fall time (t_{fall}): phase change of the wax from liquid to solid and compression.

Based on these, additional times for analysis could be calculated as well:

- Full activation time (FAT): $t_{FAT} = t_{dead} + t_{rise}$
- Deactivation time (DAT): $t_{DAT} = t_{hold} + t_{fall}$
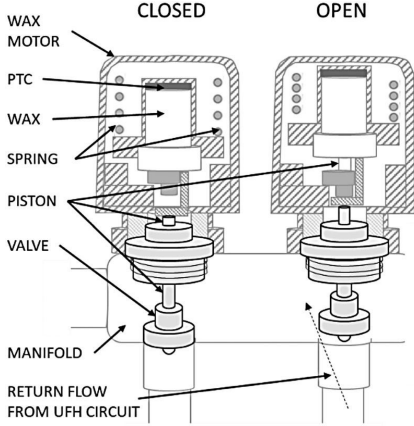
Figure 1. Valve opening with wax actuator warming visualized with part of manifold, figure parts adapted from (Beijing MUYY Technologies Co., Ltd 2023) and (The Underfloor Heating Site 2023).
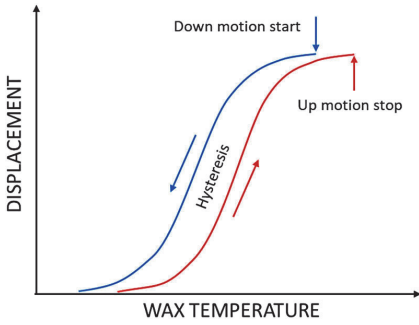
Figure 2. Theoretical piston movement (displacement) according to wax temperature, adapted from (Vernatherm 2023).

- Overheating time (t_{oh}): the time when the valve is fully open, but the motor is still heated, liquid wax is heated up
- Undercooling time (t_{uc}): the time when the motor is not heated, and the valve is fully closed, solid wax is cooling down

The characteristic times could be empirically estimated and do not need physical modelling of the wax temperature and phase change process to make the wax actuator model. This would make the method more approachable than estimating all physical parameters such as material properties, mass, volume, conductivities, spring properties, etc. In Kull, Thalfeldt, and Kurnitski (2021), the characteristic times were constant. In this work, the models are fitted for each characteristic time depending on previous actions. The following assumptions can be drawn:

- The dead time should be dependent on how low the temperature of solid wax has fallen, represented by the undercooling time:

$$t_{dead,i} = a_{dead} \cdot e^{-\frac{t_{uc,i-1}}{\tau_{dead}}} + b_{dead} \qquad (1)$$

where $t_{dead,i}$ [s] is the dead time at cycle i, which depends on the undercooling time of the previous cycle $t_{uc,i-1}$ [s] and on the empirically fitted parameters a_{dead} [s], τ_{dead} [s], and b_{dead} [s], where τ represents the time constant, a and b are the linear regression parameters.

- The hold time should be dependent on how high the temperature of liquid wax has risen, represented by the overheating time (with similar definitions):

$$t_{hold,i} = a_{hold} \cdot \left(1 - e^{-\frac{t_{oh,i}}{\tau_{hold}}} \right) + b_{hold} \qquad (2)$$
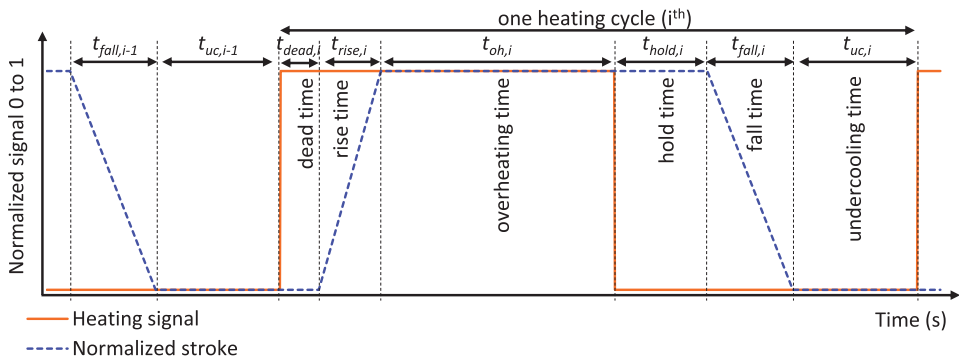

Figure 3. Definition of characteristic times for the normalized linear displacement of the piston of wax actuator or valve.

- The rise and fall times should be constant for a given wax motor product and at constant ambient temperature, as the wax amount is constant and therefore so is the amount of energy given with the heating signal through PTC during melting, or the heat loss during solidification.

3. Methods

A visualization of the general workflow of the study is depicted in Figure 4. The model of wax motor and the valve curve achieved from measurements were used to estimate their effect in simulations. The *displacement*, the linear movement or position of the piston dependent on the given electric signal, was measured without the valve being connected to the UFH system, see Figure 5. The displacement measurements were used to define the empirical model of the wax actuator. Then, we installed the wax motor on a valve in the UFH manifold and measured the volume flow while knowing the electric signal, see Figure 1. The wax motor model from previous step was then used to calculate the piston's linear displacement in flow measurements. The valve opening to volume flow characteristic curve – the valve curve – could be calibrated from these measurements and calculations. The resulting models were used to assess the effect of the wax actuator in BPS.

We have divided the experiments into (i) displacement measurements of the actuator but not in the UFH system, and (ii) flow measurements within the system, for two main reasons. First, a separate wax motor model would
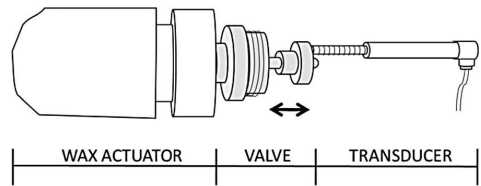
Figure 5. Visualization of a wax actuator functioning and measurements when not installed in the manifold (HBM Finland 2022), in measurement the system was vertical (90 degrees turned).

enable applying any valve model on top of the wax motor model. As valve characteristics are quite well known and modelled, this would result in a broader field of application, possibly with no further measurements. Secondly, it was not possible to directly measure the wax motor position in the same experiment as flow measurements, since measuring the piston displacement inside the manifold's pipes or through transparent piping during execution is not commonly available.

The main physical difference between the two experiments was the existence of water flow. In the flow measurement case, there was water flow against the piston, driven by circulation pump. In the displacement measurement case, there was none. Still, we assumed that this water flow had insignificant influence on the movement of the piston, thus we used the wax motor model generated from the displacement measurement case on the flow measurement case without modifications. This
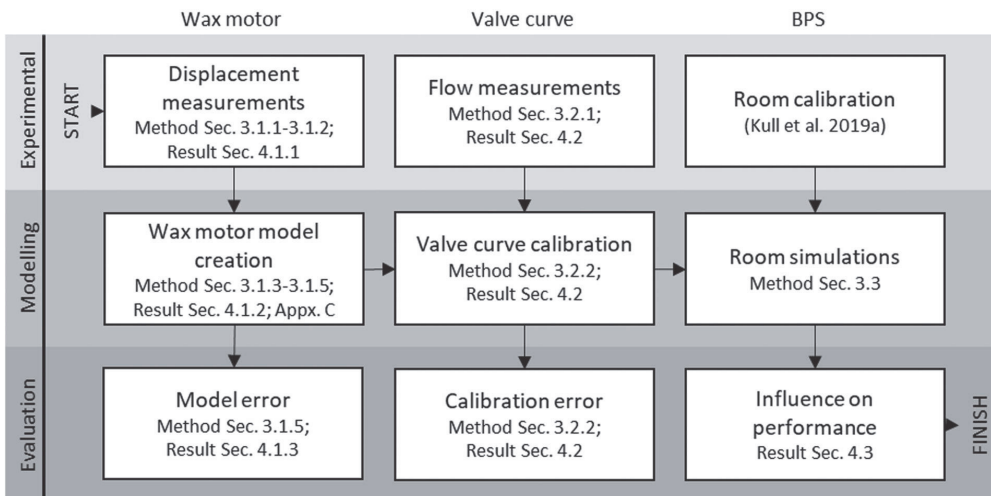
Figure 4. General overview of the research process.

assumption was supported by a comparison of pressures. The pump in the small measured system generated maximally a 30 kPa pressure head in the example volumetric flow measurements. The wax motor, on the other hand, generates 1000 kPa while expanding. If we assume a 1 cm^2 valve head cross section, the force is ca 100 N. This was confirmed by some data sheets where the force was claimed to be, i.e. 100 N $\pm$ 5% (Lindab 2021). Therefore, the force that is generated on the valve by the pump (3 N) was over 30 times lower than the force applied by the wax motor (100 N). The piston movement would not be affected significantly by the pressure difference that is generated by the circulation pump.

3.1. Wax motor model development

3.1.1. Measured actuators

The wax actuators that were measured in this work were commercial products that are commonly installed in the UFH manifolds in Estonian buildings. Products A and B, originating from separate producers, were tested. For product B, four different exemplars were tested just to see whether products and exemplars were different. Describing the whole potential range of variance was out of the scope of this work, so no more products nor exemplars were included. In the data sheet of product A, the positioning time t_{FAT} is claimed to be 3 min, the full movement range (also called 'nominal stroke') is 2.5 mm, and the positioning force is 105 N. The data sheet of product B does not include these details.

In some measurements, a quick-opening valve was screwed to the actuator as shown in Figure 5. In such case, the initial position of the spring in the motor is slightly more compressed, therefore the full movement range could be smaller. However, the movement time should be similar as it depends on the time of wax phase change at constant power. This is the effect that was analysed. As a result, the combinations are named A, Av, B1, B1v, B2, B2v, B3v and B4v, where numbers label the exemplars, and 'v' stands for the quick-opening valve if attached. The explanation of all measured combinations is shown in the first four columns of Table 1. The last column is explained in the next section (3.1.2.).

3.1.2. Displacement measurements

We measured the displacement of the wax actuator and valve combination's last element as shown in Figure 5. The sensor was a vertically fixed displacement transducer with 10-mm measuring range. Additionally, the actuator's surface temperature, the room temperature and the actuator's supply voltage were measured. The measurement step was 1 s and the data was logged by an HBM CX22BW

Table 1. Measured wax actuator and valve combinations for clarification of combination names; in the last column are the measured heating profiles.

Combination	Product	Exemplar No.	Valve included	Heating profiles measured (signal on–off)
A1	A	1	no	15 min–15 min
				15 min–45 min
				5 min–5 min
A1v	A	1	yes	15 min–15 min
B1	B	1	no	15 min–15 min
				15 min–45 min;
				30 min–30 min
				10 min–10 min
				18 min–6 min
				3 min–3 min
B1v	B	1	yes	15 min–15 min
B2	B	2	no	15 min–15 min
B2v	B	2	yes	15 min–15 min
				15 min–45 min
B3v	B	3	yes	15 min–15 min
B4v	B	4	yes	15 min–15 min
				15 min–45 min
				random 5 to 15 min

data recorder (HBK 2022) through a MX840A measuring bridge (HBK 2021).

In all experiments, the actuators were powered and controlled by a Siemens LOGO! 24CE controller with 24-V transistor outputs (Siemens 2021), which generated the heating profiles as shown in the last column of Table 1. The first value before the dash is the heating time during which the wax actuator is heated, with the 24 V signal given as input. The second number after the dash is the cool-down time in between two heating cycles. Therefore, a '15min-45min' profile means that the voltage was 24 V for 15 min, then turned off for 45 min. This was repeated periodically and the test duration for each profile is given in Appendix A.

The heating profiles were chosen to ensure complete opening and closing of the valve during each heating cycle. If this did not happen, the tested heating profile was excluded from this study, since those cycles where the valve is not fully opened or closed are typically not used for 24-V actuators. Based on literature and initial tests, at least 3–5 min of heating and cooling time was needed. In this study, the cut-off limit for this exclusion remained close to 3 min for both heat-up and cool-down. Longer gaps between heating charges were tested, for allowing the wax to cool down between cycles and to analyse its effect on valve opening time. A 15 min–15 min heating profile was measured for all combinations to enable comparison, and most heating profiles were tested on the motor B1.

3.1.3. Post-processing and cut-off conditions

The measured displacement was normalized for each experiment. The maximum displacement is the closed

cold position when the head was at the lowest position. When the valve opened, the head moved higher, and the measured values were lower. The difference between the fully open and fully closed positions, the stroke, was identified in each experiment for normalizing the displacement as follows:

$$\text{normDisplacement} = \frac{|\text{displacement} - \text{stroke}|}{\text{stroke}} \quad (3)$$

where displacement [mm] is the measured time series during one experiment. The 0-V or 24-V input voltage was also normalized to a time series with values between 0 and 1, the heating signal.

For each heating cycle in each experiment, we estimated the characteristic times described in Section 2. For an ideal trapezoid displacement as shown in Figure 3, all these times are clearly defined. However, for continuous smooth response, the cut-off between these periods is not clear. In this work, the rise and fall times were separated from the rest by defining a minimum slope of the ramping. We assumed that the linear change from 0 to 1 would take no longer than 10 min in total. For a normalized stroke, this is 10% in a minute, so a slope steeper than 0.83% in 5 s was classified to be part of the rise time. To smoothen out measurement errors, an average slope for 5 seconds was used instead of a 1-second measurement step. For fall classification, the slope was steeper and therefore a twice as large limit of −1.67% change in 5 s was used. These limits were chosen by qualitatively assessing that the classified periods did not have discontinuities (example result in Section 4.1.2, Figure 10). When the stroke should have been 0, a slack of 5% was applied to exclude small shift offsets. The timesteps that were not included into rise or fall times were separated into dead time, hold time, overheating time, and undercooling time according to heating signal and normalized displacement values, according to the logic described in Section 2. The input heating signal was accounted to be 1 when larger than 0.5, or 0 when equal to 0.5 or lower.

3.1.4. Models of characteristic times
The four characteristic times – dead time, rise time, hold time, and fall time – were identified for each heating cycle, and a regression model for calculating each characteristic time could be defined by fitting the experimental data. The models for all non-constant characteristic times in Section 2 can be given as

$$t_{\text{out}} = a \cdot f(t_{\text{in}}/\tau) + b \quad (4)$$

where t_{in} is t_{uc} in Equation (1) and t_{oh} in Equation (2), and t_{out} is t_{dead} or t_{hold} correspondingly. The parameters τ, a and b are empirical parameters and need to be fitted.

To find the parameters and to test these assumptions, τ was first estimated. The correlation between $f(t_{\text{in}}/\tau)$ and the output time t_{out} was calculated for different τ values, and the τ value with best correlation was chosen. The assumed models from Equations (1) and (2) were then tested by using linear models (lm) and the parameter significance was tested according to p-values in R (R Core Team 2020). If the p-value for any parameter was larger than .001, no significance was found and the model was not used. If significant, the parameters a and b were fitted.

The parameters in characteristic times' models can change for each product, due to a different wax mass and build of the motor. If no common model was significant, we applied multi-level models (lme) in R, which vary the parameter b for the product models. However, common models are clearly to be preferred. Although the rise time was assumed to be constant, it can be seen in the results (Section 4.1.2) that it was not. A similar model as in Equation (1) was therefore applied.

The entire fitting process was based on the results from Sections 4.1.1 and 4.1.2, and is described into detail in Appendix C. The resulting models are shown in Table 2 with yellow background. These models were compiled into one as the next section describes.

3.1.5. Empirical model of wax motor
The entire process from displacement measurements to empirical model is shown in Figure 6. The final empirical linear-segments model of a wax motor was a combination of the four characteristic time models – dead time, rise time, hold time, and fall time – each with product-specific parameter values. For implementation, the characteristic time lengths need to be calculated into displacement at any given time. This concluding implementation is shown in Table 2 as a calculation process from the heating signal to the linear movement of the wax motor valve. Figure 3 helps with the visualization of the different time periods and notation. Based on the heating signal $s(t)$ and the same signal delay – $d(t)$, jumps in the signal were determined as its slope $k_s(t)$. Based on the heating signal and its slope, the last 'On' and 'Off' times of the heating signal were calculated. The undercooling time was found in one heating cycle, when both the normalized displacement and the heating signal were zero. Then, it was used in the obtained formulas to estimate the dead time and rise time for the next cycle.

When the normalized displacement rose to 1 or its gradient slowed down, the overheating time started and was registered until the heating signal dropped to 0. The following hold time was calculated according to this overheating time. The fall time was a constant for a given

Table 2. Empirical wax motor model with its calculation process.

	Symbol	Unit/range	Description	Logic expression in IDA ICE
IN	s	0/1	Heating signal	Input
	s_D	0/1	Delayed heating signal	s lagged by 5 sec
	k_s	[-1,1]	Signal slope	$s - s_D$, hold for 4 sec
	t_{ls1}	s	Last On-time	Integrate s, reset when $k_s > 0.5$
	t_{ls0}	s	Last Off-time	Integrate 1-s, reset when $k_s < -0.5$
	$t_{uc,i-1}$	s	Last undercooling time	Integrate 1-s when not($t_{DAT} > t_{ls0}$ & s_D ==0), reset when $k_s < -0.5$, $t_{uc,i-1}$=0 until t_{DAT} available
	$t_{dead,i}$	s	Dead time	$-192\,(3) \cdot \exp(-t_{uc,i-1}/780) + 219\,(13) \pm 13$
	$t_{rise,i}$	s	Rise time	$-30(3) \cdot \exp(-t_{uc,i-1}/1140) + 142(22) \pm 21$
	$t_{oh,i}$	s	Overheating time	Integrate s when not($t_{FAT} > t_{ls1}$ & d==1), reset when $k_s > 0.5$, $t_{oh,i}$=0 until t_{FAT} available
	$t_{hold,i}$	s	Hold time	$\begin{cases} 195\,(6) \cdot \left(1 - \exp\left(-\dfrac{t_{oh,i}}{240}\right)\right) + 30\,(5), \text{ for product A} \\ 82\,(3) \cdot \left(1 - \exp\left(-\dfrac{t_{oh,i}}{600}\right)\right) + 58\,(2), \text{ for product B} \end{cases}$
	$t_{fall,i}$	s	Fall time	$\begin{cases} 180, \text{ for product A} \\ 123, \text{ for product B} \end{cases}$
	$t_{FAT,i}$	s	Full activation time	$t_{dead,i} + t_{rise,i}$
	$t_{DAT,i}$	s	De-activation time	$t_{hold,i} + t_{fall,i}$
	c_{dead}	0/1	Is this currently dead time?	$t_{dead,i} > t_{ls1}$ & s_D ==1
	c_{rise}	0/1	Is this currently rise time?	$t_{FAT,i} > t_{ls1}$ & s_D ==1 & not c_{dead}
	c_{fall}	0/1	Is this currently fall time?	$t_{DAT,i} > t_{ls0}$ & s_D ==0 & not c_{hold}
	k_{rise}	1/s	Rise ramp	Integrate $1/t_{rise}$ when c_{rise}, reset every 3 min, [0, 1]
	k_{fall}	1/s	Fall ramp	Integrate $1/t_{fall}$ when c_{fall}, reset every 3 min, [0, 1]
	c_{hold}	0/1	Is this currently hold time?	$t_{hold,i} > t_{ls0}$ & s_D ==0
OUTPUT	h	[0,1]	Wax motor (+ valve piston's) normalized linear movement, limited between 0 and 1	If c_{dead}: h=0 Else if c_{rise}: h=k_{rise} Else if c_{hold}: h=1 Else if c_{fall}: h=k_{fall} Else: h= s_D

The leftmost vertical label spanning the calculation rows reads: Empirical model of wax actuator: calculation process.

wax motor product. After the normalized displacement had reached 0, the undercooling time started again. The final normalized displacement value was set to 0 during dead time and to 1 during the hold time. During rise time and fall time the value should be ramping up or down. Therefore, the ramping speed was calculated and
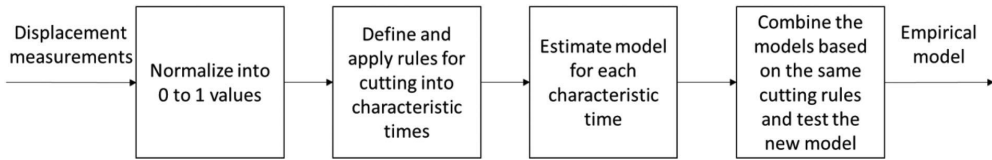
**Figure 6.** The process of estimating the empirical wax motor model from the displacement measurements.

integrated from the start of the given period, to get the output displacement.

The obtained models were then tested on the measured data. For each experiment, both the mean absolute error (MAE) and root mean square error (RMSE) were evaluated, and these were compared between motors and profiles. The linear segments model for one of the products was implemented and tested in IDA ICE. Product B was chosen as it was installed by design in the test facility discussed in the next section.

3.2. Valve curve estimation

3.2.1. Volume flow measurements

To simulate the effect of modelling the control details on BPS, the characteristic curve of the valve was needed. Instead of using a theoretical curve, an actual curve was estimated from measurements (see Section 3.2.2). For the measurements inside the UFH system, the wax actuator B2 was installed in the UFH manifold of the TUT nZEB test facility. This is a 100-m^2 house that was constructed for testing nZEB solutions. It features balanced heat recovery ventilation, a ground source, and an air-to-water heat pump system with both radiators and UFH, among other technologies. The building model has been previously built and calibrated in the IDA ICE software, as detailed in Kull, Thalfeldt, and Kurnitski (2019a). The floor plan of the test facility is shown in Figure 7 and the key parameters for modelling the building are listed in Table 3.
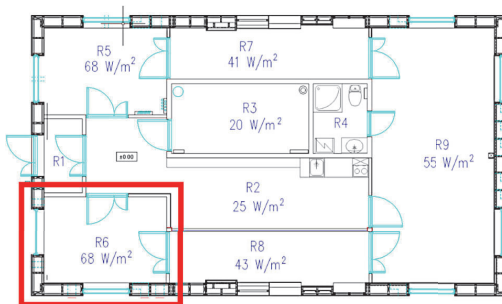
Figure 7. Floor plan of the test facility, experiment room R6 marked in red.

The aim was to calculate the given valve's characteristic curve for further modelling as a proof of concept, so only one motor was measured. In the experiment, the LOGO controller (see Section 3.1.1) generated 15 min–15 min heating profiles – 15 min-long heating signals, with a 15-min gap between heating cycles. The volume flow was generated by significant setpoint changes in one UFH circuit that serves a 10-m^2 room, marked with a red box in Figure 7, which was controlled as described in Section 3.3. The volume flow was measured by the heat metre Sensus Pollustat E (Sensus Inc. 2021). All other circuits were closed due to much lower setpoints. The measurements are fully described in Maivel, Ferrantelli, and Kurnitski (2018; Võsa, Ferrantelli, and Kurnitski 2019; Kull, Thalfeldt, and Kurnitski 2019b).

3.2.2. Valve curve and authority correction

The measured volume flows and the heating signal were used to estimate the valve characteristic curve for the given UFH circuit. First, the empirical model developed according to Sections 3.1.4 and 3.1.1 was applied to estimate the linear valve displacement due to the electrical heating signal from the controller. The *characteristic valve curve* is the relationship between this displacement and the measured volume flow.

To apply a valve curve for simulations, a model is needed for mapping volume flow to any valve displacement. The measured valve curve develops in two parts. First, the linear valve opening creates open area which in ideal case would be linearly correlated to volume flow. However, this theoretical valve curve is changed by valve authority, which describes how well the valve can control the volume flow.

The valve curve model was estimated in two steps: first we defined the theoretical quick opening valve curve, which is typical of UFH valves, then the valve authority effect. All the parameters were chosen such that the final volume flow best fits the measurements.

The *quick opening valve curve* is where most of the volume flow increase happens at low opening values. There are no precise values defined, so the theoretical normalized valve curve, here relation h to $\dot{V}$ was here defined in a simplified way with three points (Kumar 2017),

Table 3. Main building parameters.

Parameter	Value and unit	Comment
Floor area	100 m²/10.4 m²	House/room
Room window area	2 × 3 m²	south and west
Windows U-value	0.75 W/m²K	total
Glazing g-value	0.3	
External walls U-value	0.12 W/m²K	timber-frame
Floor U-value	0.08 W/m²K	concrete, above outdoor air
Avg. thermal bridges	0.031 W/K/m²	area of external surface
Infiltration at △p 50 Pa	0.6 m³/h/m²	area of external surface
Fixed infiltration flow	0.0048 L/s/m²	area of external surface
Internal walls	Adiabatic	
UFH PEX piping	20 × 2.0 mm	300 mm intervals, wet install
Floor cover upon piping	40 mm of screed	no cover on top
UFH power	68 W/m²	nominal heat output
Design temperatures	34/29°C	heating curve in Appx. B
Over-dimensioning	40%	

- The minimum efficient displacement (h_0) – the normalized displacement from which the volume flow starts to increase
- The maximum efficient displacement (h_{max}) – the normalized displacement starting from which the volume flow does not increase further
- The mid-point ($h_p, \dot{V}_p$) – the point from which quick opening stops and slower opening continues

where h is the normalized shift from 0 to 1, and $\dot{V}$ is the normalized volumetric flow. The valve authority can significantly change the theoretical valve curve. To take this into account, the theoretical curve $\dot{V}$ was modified by the valve authority N into normalized and authority-corrected volume flows ($\dot{V}_{auth}$) (Johnson Controls LTD 2020) with

$$\dot{V}_{auth} = \sqrt{\frac{\frac{1}{N}}{\frac{1}{N} - 1 + \frac{1}{\dot{V}^2}}} \quad (5)$$

where $\dot{V}$ is the theoretical valve curve and N is the valve authority. The valve authority can be calculated from the following formula (Petitjean 1994),

$$N = \frac{dp_v}{dp_{pump}} = \frac{dp_{pump} - dp_{sys}}{dp_{pump}} \quad (6)$$

where dp_v, dp_{pump}, dp_{sys} are the pressure differences across the control valve in kPa, the pump, or the rest of the system with a fully open valve. dp_{sys} can be estimated by adding up pressure drops across each component in the system. In our tested configuration, we estimated that the system consists of both the circuit's straight components (1.1 kPa) and the bends in its pipe (7.1 kPa), a heat metre (4.5 kPa), a balancing valve on the main pipe

(10.8 kPa), and balancing valves on each circuit's supply side (3.6 kPa). Altogether, dp_{sys} results in 27.1 kPa. The pump works at second speed and generates 30 kPa, therefore dp_v results in 2.9 kPa.

As the theoretical curve consists of linear segments, the Evolutionary Microsoft Excel Solver was applied to minimize the MAE between the measured and calculated $\dot{V}_{auth}$ numerically. The parameters h_0, h_p and $\dot{V}_p$ were varied to find the optimum. The limits were set as 0.1 to 0.3 for h_0, 0.1 to 1 for h_p, and 0 to 1 for $\dot{V}_p$. The h_0 was forced to be lower than h_p. The parameter h_{max} was set to 1 and the part where the valve opening was above 0.95 or below 0.05 was excluded from the error calculation, since although carrying many points, the flow variation was very small.

3.3. Room control simulations

To quantify the influence of the wax actuator and other control modelling details on energy performance and temperature control accuracy, several control scenarios were defined in the IDA ICE building simulation model. The modelled building and room were described in Section 3.2.1. The UFH in the room was modelled with an 'HCFloor model', which is basically a floor layer with different temperature (CEN 2008). The layer temperature develops with heat transfer from the piping to the layer material calculated according to logarithmic temperature differences. The supply temperature and volume flow of the liquid were given as inputs, the pressure and return temperature were modelled. The heating curve is included in Appendix B.

The installed power and schedules of internal gains defined by the Estonian legislation for energy performance calculations (Majandus-ja taristuminister 2015) were used, with an average internal heat gain of 4 W/m². The flow rate of the balanced heat recovery ventilation was 0.5 l/s/m². The supply air temperature was 18°C and the ventilation was constantly working. The Estonian Test Reference Year climate data for Tallinn (Kalamees and Kurnitski 2006) were applied. The first week in January and the second week in February were chosen to be simulated, as these have similar heating consumption but different solar heat gains. The heating consumption was 2.4 kWh/m²/week with IDA ICE default PI control. The solar heat gains were 0.15 kWh/m²/week and 0.82 kWh/m²/week in the January and February weeks respectively. The average dry bulb outdoor temperatures were −1.9°C in January and −6.8°C in February. A longer period was not simulated, as the empirical wax motor model currently requires timesteps of 5 s, which dramatically increases both simulation time and output files size.

The On/Off thermostat (O) and PI controller (P) cases were simulated for enabling comparisons, and both included a gradual increase in the level of detail. First, the business-as-usual simulations were defined, with IDA ICE default parameters that are typical for BPS simulations, corresponding to IDs O_0 and P_0. Then, step-by-step adapted control parameters, signal delay, adapted valve curve, signal modulation, and wax motor model were added. The process listing the sequential steps that correspond to the simulated scenarios is depicted in Table 4. On top of business-as-usual cases, first, the default control parameters (CP) were adapted in step CP. These are dead band (Db) for the On/Off controller and proportional gain K, integration time Ti and tracking time Tt for the PI controller. A 2-min delay (D) of input signal from the room temperature sensor to the controller, which is usually not considered (Wen and Smith 2001), was added starting from step D in cases O_D and P_D (Elnaklah, Walker, and Natarajan 2021). The calibrated authority-corrected quick-opening valve curve (VC) was then included. It was estimated as described in Section 3.2.2 and implemented in IDA ICE with small linear segments replacing the IDA ICE default linear control. Modulation of the continuous PI control signal, the modulation control (MC) was then applied in step MC on PI only as the On/Off output is already binary. Since the given 24 V wax actuators can only be controlled by a binary signal, the continuous output of the PI controller was translated with an hourly modulation, where at the beginning of each hour the

algorithm decided whether and for how long to heat. The applied modulation control principle is shown in Figure 8. Finally, the developed empirical wax actuator model of product B was finally included in the cases O_WM and P_WM (where 'WM' stands again for 'wax motor').

The most detailed cases O_WM and P_WM were used as the benchmark for all scenarios of the same controller. The comparison of energy consumption between different cases is sensible only at similar comfort levels, since lower temperatures would clearly result in lower energy consumption for heating. All simulations were thus initially carried out with a constant air temperature setpoint, which was then shifted iteratively until the operative temperature at 0.6 m from the floor in the middle of the room was below 21°C for up to approximately 33 h per week. This corresponds to the 20% limit for weekly deviation from the indoor climate class boundaries (EN 16798-2:2019 standard (CEN 2019)). Finally, the temperature fluctuations and heating energy consumption of the scenarios were compared.

4. Results and discussion

4.1. Wax motor modelling

4.1.1. Displacement measurements
The displacement is the linear movement of the actuator's piston triggered by electric signal, and its measurements described in Section 3.1 were used to define

Table 4. Implementation of all control scenarios for both On/Off (Thermostat) and PI control.

An initial controller (On/Off or PI) is always included, the other components/parameters are gradually added or adapted. T_{Db} is the dead band, K is the proportional gain, t_i is the integration time, t_t is the tracking time, and t_D is the time delay. Adapted PI parameters taken from Kull, Thalfeldt, and Kurnitski (2020).
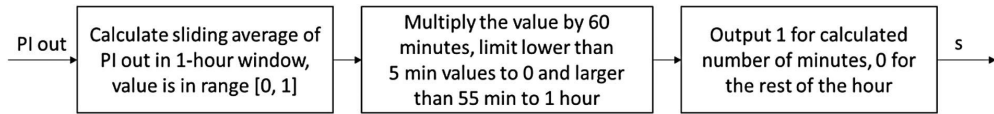
Figure 8. Implementation of the modulation for the PI output into wax motor's input, the heating signal s. The calculation is performed once per hour.

the empirical model of the wax actuator. Some examples of the displacement during a 15 min–15 min heating profile for each of the measured actuators are shown in Figure 9. There was a clear difference between the first period (left) and the following periods (visualized on top of each other on the right), as the motors were not conditioned identically before the beginning of each experiment. The figure shows that the wax in motor B1 was already warmed up before the first cycle. There has been a slight movement in the measuring device during the first cycle for B2. However, the first period conditions the motors and we can see that the following periods performed very similarly within each motor's measurements. There was almost no difference for cases with and without valve for the same motor either. Larger differences were found between different products, and small differences existed among instances of the same product. In the observed cases, the response for motor A1 looked like a trapezoid, while the product B motors had a slight movement even during the overheating. Quite likely, these differences could be caused by different general builds, covers, materials, etc. The product A's datasheet states that the cover is made of polycarbonate, this is not known for product B but the diameter of the motor B cover is 15% smaller. The actuator heights are very similar. The smooth change in displacement for product B makes it challenging to separate the rise time and overheating

time, which is why the limits for ramps were defined as in Section 3.1.3.

4.1.2. Cut-offs for characteristic times

The characteristic times of a wax motor – dead time, rise time, hold time, and fall time – were defined in Section 2 and summarized in Figure 3. Their estimation relied on the definition of the cut-off conditions for the periods. A sample result of the cut-off conditions is shown for a 15 min–15 min period of motor B3v in Figure 10. After filtering out some cases where the estimation failed as one or more of the characteristic times were estimated to be zero, 380 periods remained to be analysed. All resulting characteristic times are shown in Figure 11, where they are coloured according to the motor. The rise and fall times varied less than the dead and hold times. This was expected, as these should be constant for one product at the same room temperature. However, while the fall time shows to be mostly constant for one motor, the rise time has a more than 1-min variance for product B.

For heat pump inclusion in grid balancing, it is also important that the valves would open within 5 min. The full activation time t_{FAT} was calculated by adding up the dead and rise times. In most cases, the t_{FAT} was very close to 5 min, as shown in Figure 12. However, there were some cycles when t_{FAT} exceeded 5 min, yet staying below 7 min. For product B, these were of experiments where
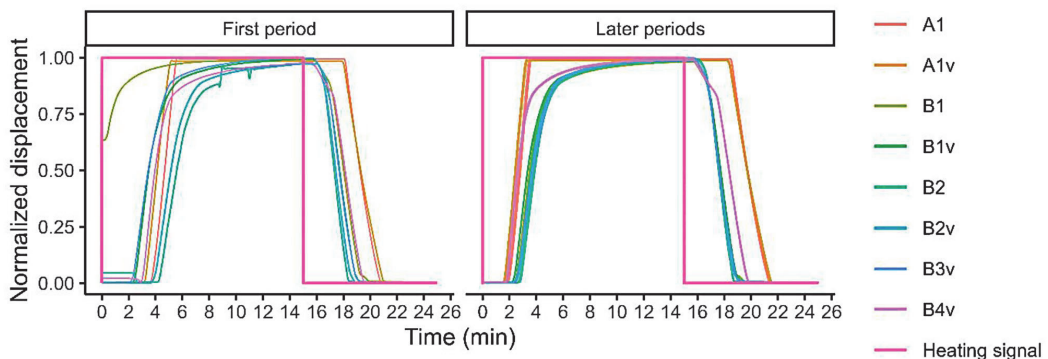
Figure 9. Different wax motors' normalized displacement dynamics in the 15 min–15 min profile as shown by the heating signal (normalized voltage).
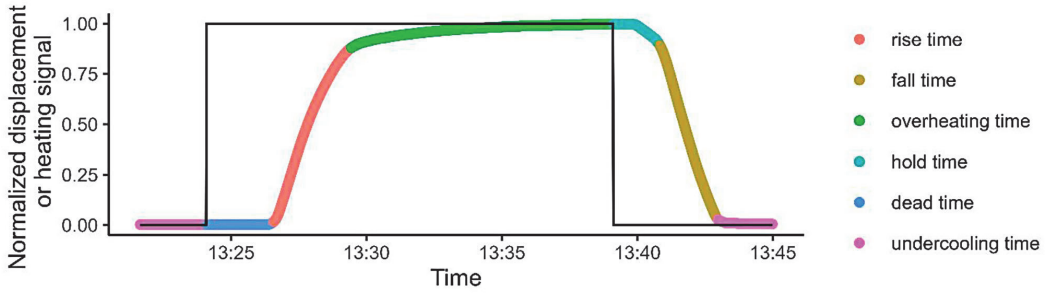
Figure 10. Example of how the characteristic times have been separated with cut-off definitions. The black line indicates the heating signal.
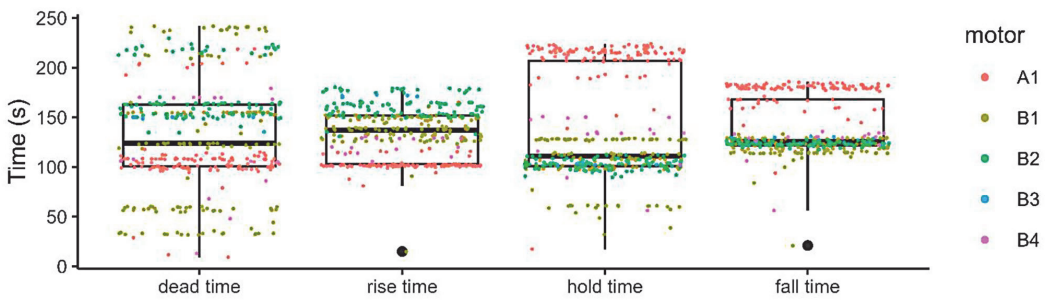
Figure 11. Characteristic times identified from all experiments, motor with and without valve grouped together.

the cool-down time was 30 min or 45 min, and the wax could cool down more. The limit was exceeded also for the first period of 10 min–10 min and first three periods of 15 min–15 min profiles, due to the previous longer cool-down. For product A, even the 15 min–45 min profile's cycles were very close to the limit. However, falling to either side of the limit depended heavily on the definition of allowed ramp definitions. These influenced the cut-off

between rise time and overheating time. For reaching below 5 min for all profiles, standby heating could be activated. The control would need to keep the wax at higher than room temperature with short heating pulses, which do not open the valve. The suitable pattern for standby heating should be determined either by experiments or with a physical model, which can handle profiles with short heating times.
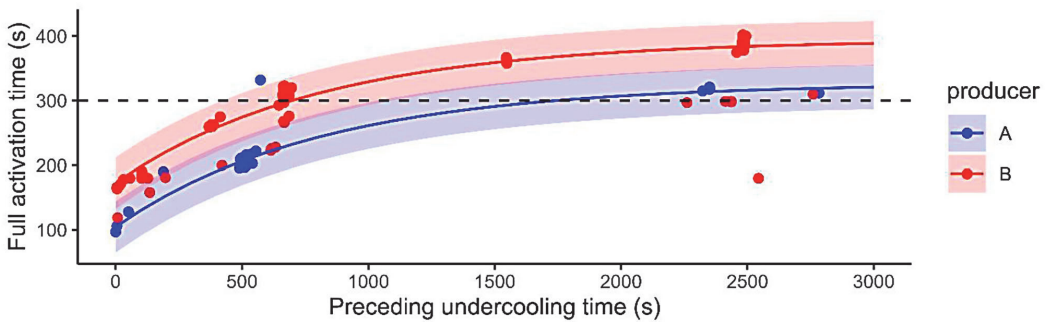
Figure 12. FAT dependence on preceding undercooling time and motor's producer. The points are measured values, the lines show modelled values, the shaded area the modelling errors; the dashed line indicates the 5-min limit.

4.1.3. Empirical model performance

The mean absolute errors between measured and modelled displacement for some profile-motor combinations are shown in Figure 13. On the left, the examples from motor B1 show that there was a tendency for lower error in longer profiles, where undercooling and overheating dominate in the period. At these times the displacement is the easiest to model, as it is almost constant and close to 0 or close to 1. Therefore, the error is also the smallest, reducing the average error. The graph on the right illustrates the differences between experiments with and without the valve. No clear conclusion can be drawn from the slight differences. Results for motor A were more precise and there were slight differences between different samples of the same B motor. All the fitting errors are shown in Appendix A, Table A1. For all the profiles, the MAE remained below 10% (0.1) and the RMSE below 15% (0.15); the average MAE is 0.041 or about 4%. Examples of the typical, the best, and the worst performance for

one hour are shown in Figure 14. The graph for A1 shows the suitable shape choice for the empirical model. For motor B, the heat-up process differed, but the effective volume flow corrected the slight difference, as shown in the next section. In the worst case, the maximum delay between the measured and simulated signal start was 1 to 1.5 min.

4.2. Volume flow modelling

We recall that the volume flow model, i.e. the characteristic curve of the valve, was needed to estimate the effect of modelling the volume flow in detail on BPS (Section 3.2). An example of the measured volume flows during one heating cycle that was measured in the test facility is given in Figure 15. Additionally, the input heating signal, with empirical model calculated valve displacement, and the modelled volume flow are shown. The modelled volume flow was obtained by fitting the theoretical model
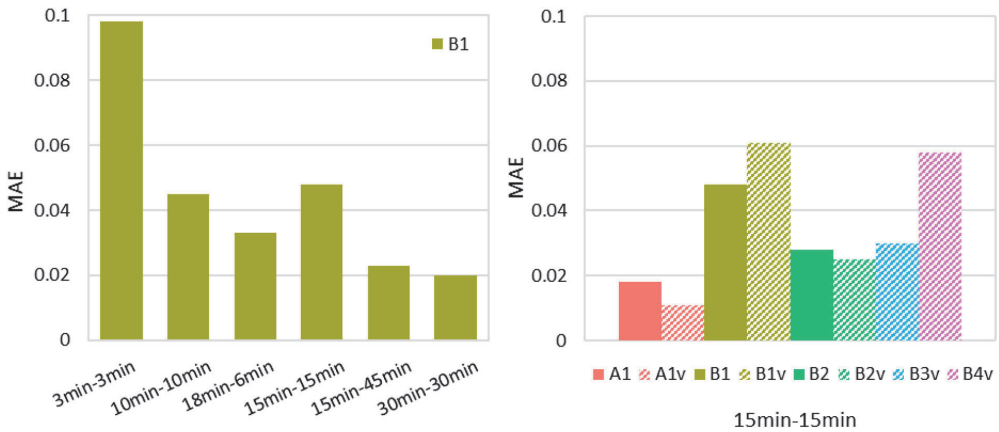

Figure 13. Error estimations for all measured profiles of one motor (left) and for all combinations of one profile (right).
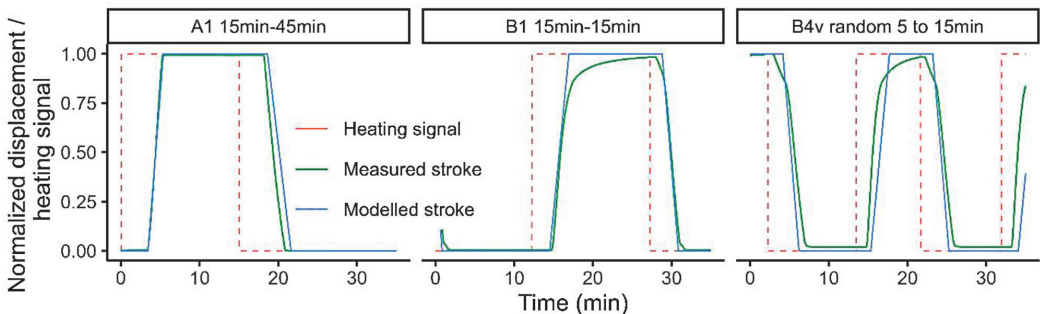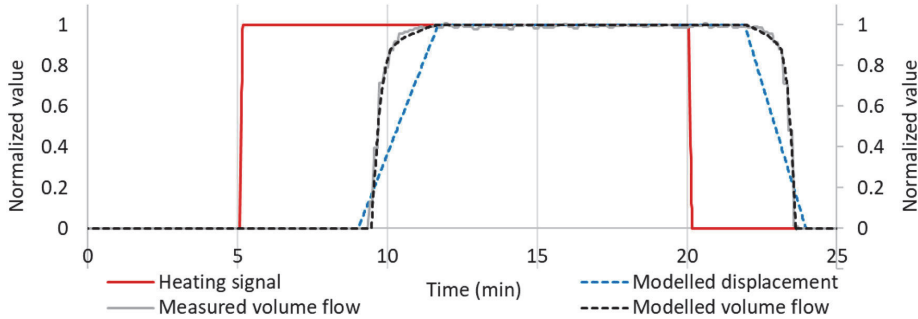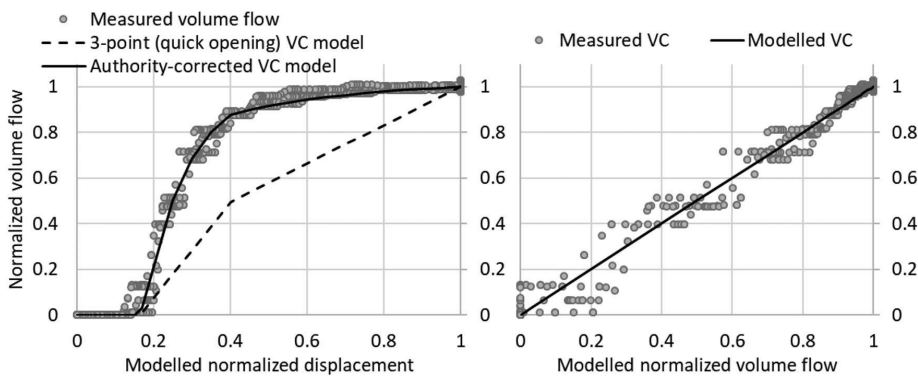

Figure 14. Performance of estimated wax motor model on predicting normalized displacement.

Figure 15. Measured (solid) versus modelled (dashed) volumetric flows, plus heating input signal (red) to the wax motor.

Figure 16. Valve curve modelling process and result on the left; measured versus modelled volume flows on the right.

from Section 3.2.2. The graph of measured and modelled volume flow to displacement is shown in Figure 16, on the left, with estimated valve curves as follows: the theoretical valve curve is shown with dashed line, and the authority-corrected valve curve with solid line. The authority-corrected valve curve matched the measurements the best when the three-point quick opening characteristics were at $h_p = 0.41$, $\dot{V}_p = 0.5$, $h_{min} = 0.17$. For the considered region, the MAE was 1.02%. In the graph on the right, the error between the measured and modelled authority-corrected valve curves is shown.

4.3. Effect on energy performance simulations

In section 3.3, several control scenarios were defined in IDA ICE to quantify the influence of the wax actuator and other elements of control process on energy performance and temperature control accuracy. In this section, we compare the results of the energy performance simulations. We recall that the '0' case was the business-as usual case, namely a simulation model with close-to-ideal control of the UFH system. This ignores the modelling of both wax motors (WM) and exact valve curves VC, while the PI control or On/Off thermostats were represented by parameters that are set to default values commonly used for BPS. The other scenarios use adapted control parameters CP, then sequentially add time delay D to the input signal, a VC; modulation control (MC), and finally, a WM. The level of modelling detail is therefore gradually increased from ideal to WM.

For comparability of energy consumption, air temperature setpoints were shifted so that 20% of the operative temperature remained below 21°C (Section 3.3). The applied setpoint shifts for all the cases, and the resulting energy consumption is shown in Table 5. In the columns, the air temperature shift from 21°C dT and the MAE of the air temperature MAE(T) characterize the temperature fluctuations. Q_h is the floor heating energy consumption per square metre of floor area per observed week, and its relative difference was calculated as $\Delta Q_h = (Q_h - Q_{h,w})/Q_{h,w}$ [%] for the given week. This quantified the consumption under-/ overestimation in

Table 5. Temperature fluctuation and energy consumption results for all cases; air temperature setpoint deviations dT are from 21°C and energy consumption results Q_h are in kWh/m²/week.

ID	Temperature fluctuations				Energy consumption			
	January week		February week		January week		February week	
	dT	MAE(T)	dT	MAE(T)	Q_h	Δ$Q_{h,w}$%	Q_h	Δ$Q_{h,w}$%
O_0	0.49	0.597	0.33	1.092	2.55	5.71%	2.42	4.84%
O_CP	0.05	0.195	-0.03	0.682	2.42	0.36%	2.32	0.41%
O_D	0.05	0.2	-0.03	0.691	2.41	-0.12%	2.32	0.25%
O_VC	0.05	0.2	-0.03	0.69	2.41	-0.12%	2.32	0.21%
O_WM	0.06	0.215	0	0.628	2.41	0.00%	2.31	0.00%
P_0	-0.03	0.128	-0.08	0.637	2.41	0.08%	2.28	0.68%
P_CP	-0.09	0.033	-0.13	0.447	2.37	-1.63%	2.20	-2.75%
P_D	-0.09	0.038	-0.13	0.453	2.37	-1.67%	2.20	-2.71%
P_VC	-0.1	0.044	-0.14	0.462	2.37	-1.67%	2.21	-2.54%
P_MC	-0.07	0.149	-0.11	0.589	2.40	-0.48%	2.24	-0.80%
P_WM	-0.05	0.150	-0.08	0.676	2.41	0.00%	2.26	0.00%

the observed case, compared to the most detailed case O_WM or P_WM, respectively.

The table shows that only adding the wax motor onto the previous level of detail does not change the energy consumption a lot. There are larger changes in one step, such as correcting the parameters or adding modulation. However, the whole process of adding modelling detail, changes the results vividly both in temperature fluctuations and in energy consumption. The changes are discussed in detail in the following sections.

4.3.1. Temperature setpoint changes
The setpoint changes were negative for PI, but close to zero or even positive for On/Off (Table 5). This means that the operative temperature stayed most of the time above the desired 21°C even after lowering the air temperature setpoint below 21°C for PI. In both cases, the operative temperature and air temperature fluctuated similarly, yet with an offset. Regarding the On/Off case, the fluctuations were much larger, and the setpoint had to be higher. An example of this behaviour is shown in Figure 17, where line typology corresponds to air temperature setpoint (dotted), air temperature (solid) and operative temperature (dashed).

Figure 18 portrays all the shifted operative temperatures by cumulating their occurrence durations. While temperatures in January stayed close to the original setpoint for the whole week, except for some hours, the solar gains in February raised the temperatures. These rose over 24°C and were more than a degree over the setpoint for about 20% of the week. The two extra high temperature cases are the O_0 cases for January and February weeks; the others lie closer together, although the solid (On/Off) lines are relatively higher. This agrees with Table 5, where in all cases except

P_WM the temperature fluctuations were clearly smaller for PI than for the corresponding On/Off cases. WM cases are shown in darker colour and thicker lines in Figure 18.

4.3.2. Temperature fluctuations
For On/Off, the source of temperature fluctuations is the dead band (T_{Db}). The setpoint change and MAE of O_0 cases ($T_{Db} = 2$ K) were much higher than for the rest of the cases ($T_{Db} = 0.5$ K). While MAE for On/Off in January is mostly around 0.2 K, it was around 0.6 K for the default (O_0) case. Due to symmetric fluctuations around the air temperature setpoint, the MAE is close to 60% of the dead band in all On/Off cases.

The fluctuations for PI were induced by non-optimal parameters as well as modulation. While non-optimal parameters alter the continuous signal, modulation translates it to On/Off-like signal. The theoretical development of control signal for P_WM was described in Figure 8. From simulation outputs, an excerpt was chosen to visualize this development from PI output signal to valve curve output, and it is shown in Figure 19.

This translation from continuous to binary signal resulted in the PI cases with modulation cases, P_MC and P_WM, having MAEs close to the On/Off cases from 'CP' to 'WM'. The temperature fluctuations for the P_WM and O_WM cases are shown in Figure 20, together with the benchmark cases P_0 and O_0 as well as the improved parameter cases P_CP and O_CP. Significantly higher fluctuations occurred at a greater dead band for On/Off (O_0 case), and the smaller dead band starting from O_CP improved the On/Off control remarkably. Improved PI parameters resulted in an almost ideal control, while modulation and WM delay reintroduced the temperature fluctuations. Altogether, the temperature performance of
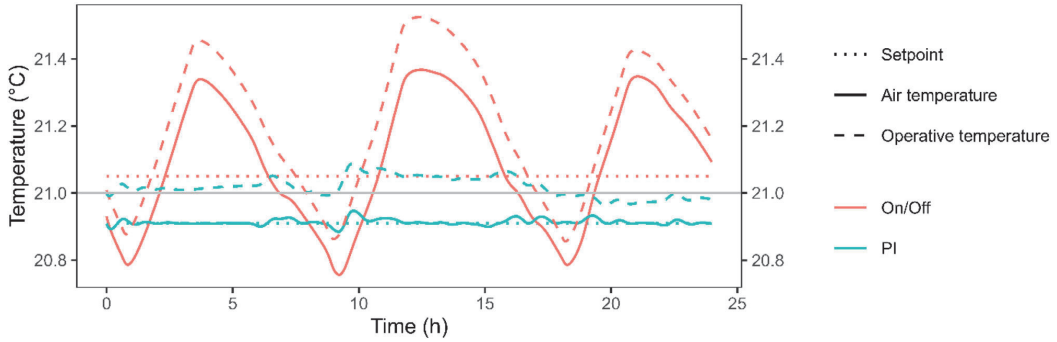
Figure 17. Air and operative temperature comparison during one January day for PI (P_CP) and On/Off (O_CP) cases. Grey line shows 21°C reference.
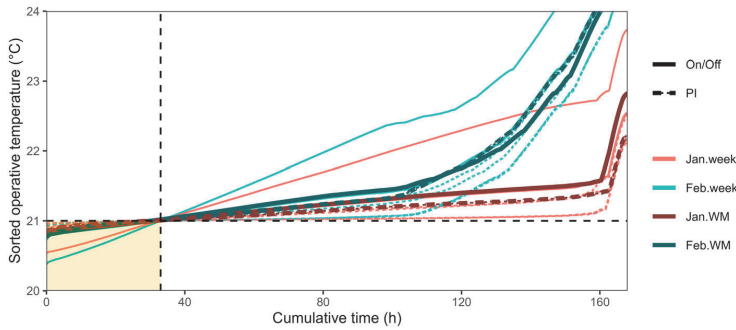
Figure 18. Cumulative operative temperature graphs after setpoint correction for all cases.

cases P_0, O_CP, O_WM, and P_WM was similar, and the WM cases could be substituted by simpler control in simulations. The similarity between On/Off and PI occurred as the PI cases did not perform optimally, while the On/Off cases improved significantly from O_0. In this work, the adapted dead band for On/Off was chosen to be 0.5 K. For this to be realized, the room air temperature sensor must be precise, calibrated, and positioned optimally. The room air should also be ideally mixed. Even though the

vertical gradient for UFH should be small (Maivel, Ferrantelli, and Kurnitski 2018; Võsa, Ferrantelli, and Kurnitski 2019), realizing one single uniform temperature per zone is clearly still an idealization.

4.3.3. Energy consumption
The energy performance in the given scenarios varied significantly across their levels of detail. Simply modelling the wax motor instead of continuous control (VC to WM
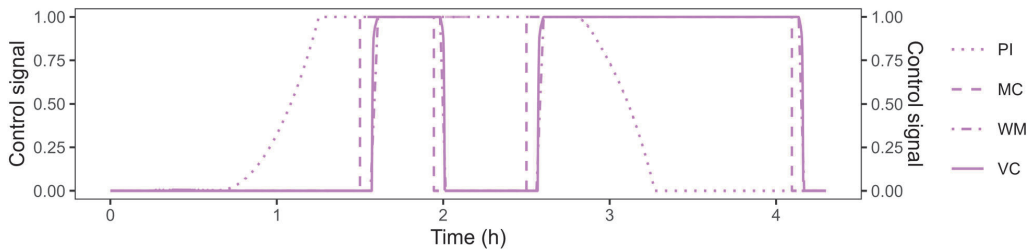
Figure 19. Control signal development for P_WM during 4 hours. Outputs from PI (PI), modulation (MC), wax motor (WM), and valve curve (VC) blocks.
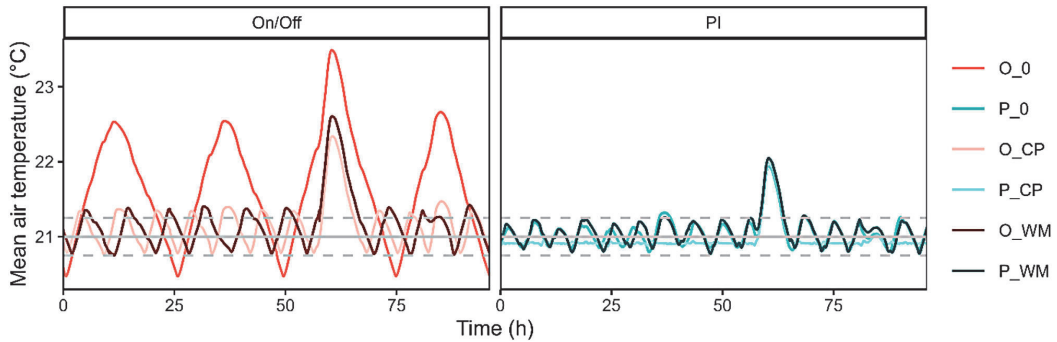
Figure 20. Air temperature fluctuations for detailed cases (O_WM, P_WM) in January, the default cases (O_0, P_0) are shown in comparison as well as the cases with improved parameters (O_CP, P_CP), grey helper lines are at 21 ± 0.25°C.

case) showed up to 2.5% energy consumption difference in the observed weeks, as Table 5 illustrates. This is consistent with the literature, see e.g. Clauß and Georges (2019) and references quoted therein. Extended to an annual basis, this can be a sizeable effect for energy efficiency.

Although the short delays and the modelling of the valve curve had less influence on the total energy performance, these resulted in different load profiles (see the next section). We found that the choice of parameters for both On/Off and PI, as well as the modelling of modulation in the PI case, had a significant effect. All On/Off cases overestimated the energy consumption compared to the most detailed case (O_WM). For the business-as-usual approach (O_0) the difference was 5.7% for On/Off in the January week and 4.8% in the February week. The business-as-usual PI case P_0 with default parameters and no modulation differs from the other simple PI cases (P_CP, P_D, P_VC – optimal parameters, no modulation). Yet, its energy consumption was like that of the modulation cases P_MC and P_WM with optimal parameters and modulation. P_0 overestimated the energy consumption by 0.1% in the January week and 0.7% in February compared to P_WM. However, all the other PI cases underestimated the energy consumption compared to P_WM.

As in most cases, a lower energy consumption was achieved thanks to smaller temperature fluctuations, which enabled a lower temperature setpoint. The step from '0' to 'CP', with reduction of energy use by using improved PI parameters, was over 3.4 percentage points in the February week. The reduction in temperature fluctuation from optimal PI parameters was cancelled out by an increase in fluctuations, which was caused by the conversion of the continuous PI output to binary values, so from P_VC to P_MC, and by wax motor delay, from P_MC to P_WM. The step from '0' to 'CP'

was higher than the 2.5% increase from 'VC' to 'WM', adding modulation and WM, in the February week. This highlights the importance of optimal PI parameters. However, the parameters that were optimized in the business-as-usual situation did not perform optimally together with a modulation approach. The optimized parameters for continuous PI control (without modulation) can thus be potentially used for 0–10 V actuators, while the coupling of modulation with parameters' optimization should be further researched. The PI parameters that were specifically adapted to the applied modulation could potentially improve the performance (Appendix D).

In most occurrences anyway, the PI cases consumed less heating energy than the corresponding On/Off cases. While for On/Off and PI business-as-usual, the PI was almost 6% more efficient for both weeks (2.41 vs. 2.55 and 2.31 vs. 2.42), there was practically no difference in the WM cases. The difference between O_WM and P_WM is generally smaller than the rest, holding at 0.2% in January and 2.1% in February. For the 'CP' through 'VC' cases it approached 2% in January and 5% in February. Therefore, substituting the PI with WM modelling with On/Off as suggested for temperature fluctuations in Section 4.3.2 would not provide the same energy performance. The smallest difference was to O_VC and to P_0.

4.3.4. Load dynamics

All the business-as-usual cases overestimated the energy consumption, leaving the results on the safe side regarding system design. However, it was clear that the volume flows in the circuit are different between the business-as-usual and the WM cases. Both overestimation of energy consumption and inaccurate mass flows could be non-conservative for other applications such as grid balancing, structural thermal storage, etc.

To better understand the development of energy consumption, Figure 21 displays on separate rows the mass flows (row a), water return temperatures (row b), and floor surface heat flux (row c) as cumulative for the January week. The outdoor temperature-dependent supply temperatures were the same for all scenarios and are portrayed as dashed lines in charts 1b and 2b.

For the On/Off scenarios, O_0 stands out from the rest. For PI, the distribution of mass flows, return temperatures as well as heating loads vary between all the cases, including 'CP', 'D', and 'VC'. These otherwise performed similarly, differing by no more than 0.01 K in setpoint, 0.015 K in MAE(T), and by 0.5 percentage points (0.01 kWh/m^2/week) in energy consumption during one given week. This means that adding a 2-min delay to the input signal and correcting the valve curve did not have a significant effect on the air temperature and energy performance. However, it changed the mass flow dynamics. P_MC and P_WM had mass flows like those

of the binary On/Off cases, while the 'CP' and 'D' cases had mass flows mostly at the 25% level. P_0 and P_VC were between the two extremes, with a close to linear flow.

Adding a WM had almost no influence in January compared to the control that was simpler by one step, either O_VC or P_MC. However, the cumulative graphs in Figure 21 show that the return temperatures for the WM scenarios were lower. This would refer to a different timing of the heating periods in relation to outdoor temperatures. Adding the WM in February, the energy consumption decreased for On/Off and increased for PI. For On/Off, the additional delay from the WM reduced the MAE and energy consumption. This could be due to the combination of delay and solar gains, as the two charts on the left side of Figure 22 show. The delay enabled to omit one heating cycle when solar gains emerged, keeping lower solar peak temperatures. For PI, the additional delay generated higher temperature fluctuations
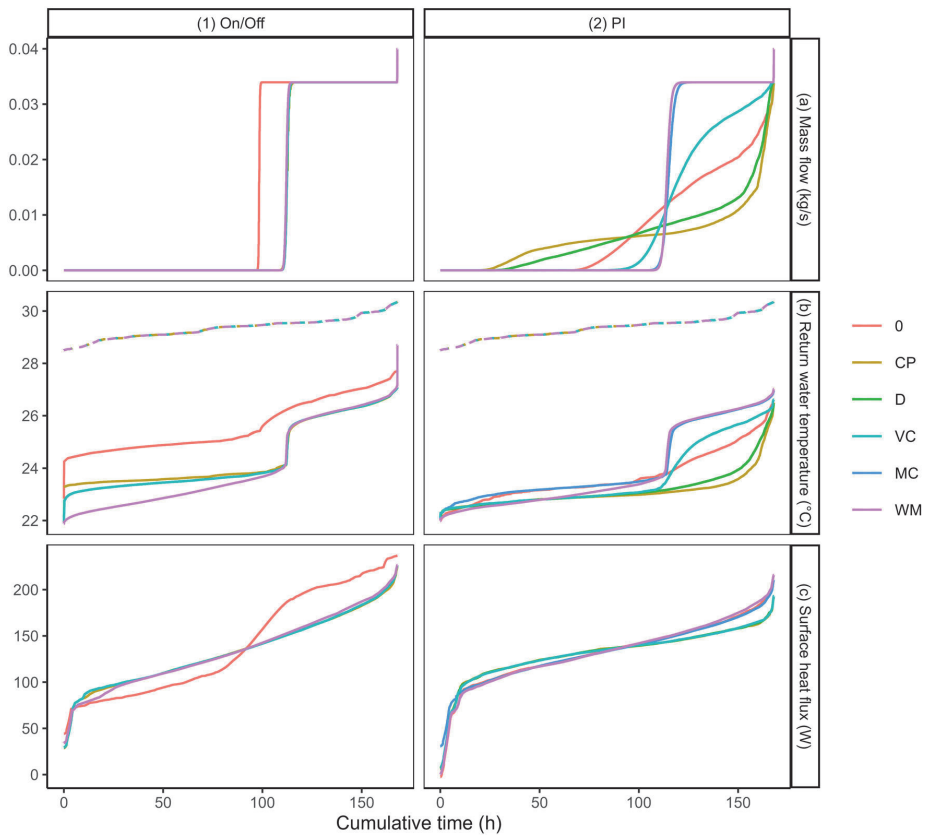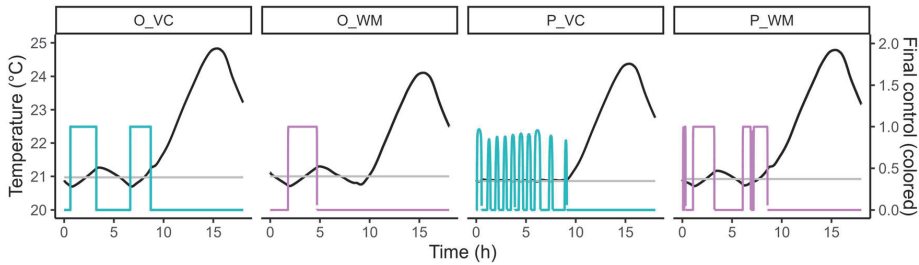

Figure 21. Cumulative performance in the January week.

Figure 22. Control and temperature during a day in February, hours from midnight, grey line showing the shifted setpoint.

and, due to the higher induced setpoint, this increased the consumption (see the two charts on the right in Figure 22).

5. Conclusions

In this paper, we have attempted at shedding light on two aspects of UFH control modelling by

- analysing how a stepwise increase in the modelling detail can affect its performance, regarding both temperature fluctuations and energy consumption,
- proposing an empirical wax motor model, calibrating it with extensive experimental results, and implementing as well as testing it with simulations.

To such aim, an experimentally based empirical model of thermo-electric actuators, or wax motors used in HVAC control was here developed. The experimental aspect was addressed into detail, first by measuring the linear displacement of the attached valve's piston without the rest of the system. Based on these measurements, we defined an empirical model consisting of four sub-models of linear segments that estimated the characteristic times. The final model resulted in an average MAE of normalized linear displacement that stayed below 10%.

The volume flows were then measured within one circuit of an UFH system with a predefined control signal that was applied to the wax motor. Based on the volume flow measurements, the valve curve was calibrated, and the models were finally implemented in the IDA ICE simulation software, for quantifying the effect of the models on BPS results.

Referring to the research questions that were formulated in the Introduction, they can now be answered as follows:

i)   How can we characterize the wax actuators for HVAC in an applicable way?

a.   The developed empirical wax motor model consists of dead time, rise time, hold time, and fall time, which depend on undercooling or overheating times. The dead time was up to 4 min, the rise time up to 3 min, the hold time up to 2.5 or 4 min depending on the motor product. As an exception, the fall time was constant for one product, either 2 or 3 min. Adapting the developed models to new products does not need extensive modelling nor expensive measurements.

ii) How much time does the valve opening with wax motors take? Can it be managed within 5 min, so that it would match the limit imposed by the frequency market for energy grids?

a.   After longer undercooling times, the wax heated up slowly, showing that the full activation time, i.e. the valve opening time, can be larger than 5 min. However, the maximum FAT did not exceed 7 min. Quick-opening valve curves, together with a low valve authority, ensured that nearly maximal flow rates were reached with 50% valve openness. If a shorter FAT is needed, the wax actuators should be continuously kept on standby, thus applying short heating cycles.

iii) How are temperature control accuracy and energy performance affected by the control strategy?

a.   Modelling the control with the empirical wax motor model, including modulation for PI, valve curves, signal delays and realistic parameter values is important for some applications. Compared to including all these options, a business-as-usual BPS overestimated the energy consumption by 5% for On/Off and less than 1% for PI. While for On/Off the temperature fluctuations were reduced by a smaller dead band, for PI these were increased due to modulation. The temperature variations were thus critically affecting the energy balance.

iv) How do wax motor and modulation effects compare to performance differences from other modelling simplifications?

  a. Changing control parameters and adding modulation resulted in the largest changes regarding all the steps taken for detailing the control modelling. The control parameters changed energy consumption by about 2%–5% and adding modulation by 2%–3%. Adding a wax motor when the heating signal was already binary changed the result by less than 1%.

As a practical consideration, it was found that the business-as-usual PI control did not reflect the actual mass flows in the system. The actual behaviour is similar to that of the On/Off behaviour, so the PI simulations could be substituted by On/Off simulations with a small dead band, and an actual valve curve but without the wax motor. However, the temperature setpoint in the simulations had to be set higher than for the PI by at least 0.1 K, to ensure the same energy performance.

The work has some limitations, which should be further analysed in future studies:

- The study can be extended on several aspects, for instance by implementing a physical model for 0–10 V wax actuators, which could also model profiles where the motor does not completely open/close the valve during each period. Experiments to determine properties of the spring, the wax, and the motor cover should be carried out accordingly. The piston movement inside the manifold should be measured as well.
- Also, the implemented empirical model currently uses very small timesteps, making it time-and resource-consuming when used for simulations involving longer time spans. Speeding up the model with a carefully performance-optimized implementation would enable simulating annual energy consumption differences.
- Finally, as the parameters that were optimized in the business-as-usual situation might not work optimally together with a modulation approach, the coupling of modulation with the parameters' optimization should be further researched.

Disclosure statement

No potential conflict of interest was reported by the author(s).

Funding

Data availability statement

ORCID

Tuule Mall Parts ⓘ http://orcid.org/0000-0002-2170-9575
Andrea Ferrantelli ⓘ http://orcid.org/0000-0003-0841-1755
Hendrik Naar ⓘ http://orcid.org/0000-0003-2221-7684
Martin Thalfeldt ⓘ http://orcid.org/0000-0002-9414-2514
Jarek Kurnitski ⓘ http://orcid.org/0000-0003-3254-0637

References

Artelys. 2017. *METIS Technical Note T6 – METIS Power System Module*. Brussels: European Commission.
Beijing MUYY Technologies Co., Ltd. 2023. "Electric Thermal Actuator – TRV Head," [Online]. Accessed 7 February 2023. https://www.muyytec.com/portfolio-items/electric-thermal-actuator/.
Bienvenido-Huertas, D., C. Rubio-Bellido, D. Marín-García, and J. Canivell. 2021. "Influence of the Representative Concentration Pathways (RCP) Scenarios on the Bioclimatic Design Strategies of the Built Environment." *Sustainable Cities and Society* 72: 103042. doi:10.1016/j.scs.2021.103042.
Boßmann, T., and I. Staffell. 2015. "The Shape of Future Electricity Demand: Exploring Load Curves in 2050s Germany and Britain." *Energy* 90 (2): 1317–1333. doi:10.1016/j.energy.2015.06.082.
Burt, S., and M. de Podesta. 2020. "Response Times of Meteorological Air Temperature Sensors." *Quarterly Journal of the Royal Meteorological Society* 146: 2789–2800. doi:10.1002/qj.3817.
CEN. 2008. *EN 15377-1:2008*. Bruxelles: European Committee for Standardization.
CEN. 2019. *EN 16798-2:2019*. Bruxelles: European Committee for Standardization.
Clauß, J., and L. Georges. 2019. "Model Complexity of Heat Pump Systems to Investigate the Building Energy Flexibility and Guidelines for Model Implementation." *Applied Energy* 255: 113847. doi:10.1016/j.apenergy.2019.113847.
Danfoss A/S. 2017. *Actuator ABNM A5 0-10V Proportional For Use with RA2000 Valves*. Nordborg: Danfoss A/S.
Elnaklah, R., I. Walker, and S. Natarajan. 2021. "Moving to a Green Building: Indoor Environment Quality, Thermal Comfort and Health." *Building and Environment* 121: 107592. doi:10.1016/j.buildenv.2021.107592.
EQUA AB. 2020. *IDA Indoor Climate and Energy (IDA ICE, Version 4.8 SP2, Expert edition)*. Solna: EQUA AB.
Fingrid Oyj. 2022. "Reserve Products and Reserve Market Places," Fingrid Oyj. [Online]. Accessed 19 May 2022. https://www.fingrid.fi/globalassets/dokumentit/en/electricity-market/reserves/reserve-products-and-reserve-market-places.pdf.
Goia, F., G. Chaudhary, and S. Fantucci. 2018. "Modelling and Experimental Validation of an Algorithm for Simulation of Hysteresis Effects in Phase Change Materials for

Building Components." *Energy and Buildings* 174: 54–67. doi:10.1016/j.enbuild.2018.06.001.

HBK. 2021. *QUANTUM MX840A Universal Amplifier – Data Sheet.* Halifax: HBK.

HBK. 2022. *QUANTUM CX22B-W/CX22B – Data Sheet.* Egham: HBK.

HBM Finland. 2022. "WI: Inductive Displacement Transducer (Miniature Probe)," HBM Finland. [Online]. Accessed 19 May 2022. https://www.hbm.com/en/3060/wi-inductive-displacement-transducer-miniature-probe/.

Johnson Controls LTD. 2020. *Valve and Actuator Manual.* Cork: Johnson Controls.

Kalamees, T., and J. Kurnitski. 2006. "Estonian Test Reference Year for Energy Calculations." *Proceedings of the Estonian Academy of Sciences. Engineering* 12 (1): 40–58. doi:10.3176/eng.2006.1.04.

Klimeš, L., P. Charvát, and M. Ostrý. 2019. "Thermally Activated Wall Panels with Microencapsulated PCM: Comparison of 1D and 3D Models." *Journal of Building Performance Simulation* 12 (4): 404–419. doi:10.1080/19401493.2018.1543350

Kull, T. M., M. Thalfeldt, and J. Kurnitski. 2019a. "Estimating Time Constants for Underfloor Heating Control." *Journal of Physics: Conference Series* 1343 (1): 012121. doi:10.1088/1742-6596/1343/1/012121.

Kull, T. M., M. Thalfeldt, and J. Kurnitski. 2019b. "Optimal PI Control Parameters for Accurate Underfloor Heating Temperature Control." *E3S Web of Conferences* 111: 01081. doi:10.1051/e3sconf/201911101081.

Kull, T. M., M. Thalfeldt, and J. Kurnitski. 2020. "PI Parameter Influence on Underfloor Heating Energy Consumption and Setpoint Tracking in nZEBs." *Energies* 13 (8): 2068. doi:10.3390/en13082068.

Kull, T. M., M. Thalfeldt, and J. Kurnitski. 2021. "Modelling of Wax Actuators in Underfloor Heating Manifolds." In Cold Climate HVAC & Energy 2021, Tallinn, Estonia.

Kumar, P. 2017. "Valve Trim Design Using Control Valve Performer," 21 October 2017. [Online]. Accessed 9 May 2022. Available: https://www.simulationhub.com/blog/valve-trim-design-using-control-valve-performer.

Le Dréau, J., and P. Heiselberg. 2016. "Energy Flexibility of Residential Buildings Using Short Term Heat Storage in the Thermal Mass." *Energy* 111: 991–1002. doi:10.1016/j.energy.2016.05.076.

Li, Y., N. Nord, H. Wu, Z. Yu, and G. Huang. 2020. "A Study on the Integration of Air-Source Heat Pumps, Solar Collectors, and PCM Tanks for Outdoor Swimming Pools for Winter Application in Subtropical Climates." *Journal of Building Performance Simulation* 13 (6): 662–683. doi:10.1080/19401493.2020.1813198.

Lindab, A. B. 2021. *Lindab Actuators - Actuator 24 V.* Båstad: Lindab AB.

Lindahl, M. 2020. *Grid Flexible Control of Heat Pumps.* HPT - Heat Pumping Technologies.

Maivel, M., A. Ferrantelli, and J. Kurnitski. 2018. "Experimental Determination of Radiator, Underfloor and Air Heating Emission Losses due to Stratification and Operative Temperature Variations." *Energy and Buildings* 166: 220–228. doi:10.1016/j.enbuild.2018.01.061.

Majandus-ja taristuminister. 2015. "Hoone energiatõhususe arvutamise metoodika," 1 July 2015. [Online]. Accessed 13 May 2022. https://www.riigiteataja.ee/akt/109062015021?leiaKehtiv.

Okur, Ö, P. Heijnen, and Z. Lukszo. 2021. "Aggregator's Business Models in Residential and Service Sectors: A Review of Operational and Financial Aspects." *Renewable and Sustainable Energy Reviews* 139: 110702. doi:10.1016/j.rser.2020.110702.

Pedersen, T. H., R. E. Hedegaard, and S. Petersen. 2017. "Space Heating Demand Response Potential of Retrofitted Residential Apartment Blocks." *Energy and Buildings* 141: 158–166. doi:10.1016/j.enbuild.2017.02.035.

Petitjean, R. 1994. *Total Hydronic Balancing: A Handbook for Design and Troubleshooting of Hydronic HVAC Systems.* Ljung: Tour & Andersson AB.

R Core Team. 2020. *R: A Language and Environment for Statistical Computing.* Vienna: R Foundation for Statistical Computing.

Reynders, G., J. Diriken, and D. Saelens. 2017. "Generic Characterization Method for Energy Flexibility: Applied to Structural Thermal Storage in Residential Buildings." *Applied Energy* 198: 192–202. doi:10.1016/j.apenergy.2017.04.061.

Rizzello, G., D. Naso, and S. Seelecke. 2019. "Hysteresis Modeling in Thermal Shape Memory Alloy Wire Actuators: An Irreversible Port-Hamiltonian Approach." In *2019 IEEE 58th Conference on Decision and Control (CDC)*, 7937–7943.

Rogelj, J., et al. 2018. "Scenarios Towards Limiting Global Mean Temperature Increase Below 1.5 °C." *Nature Climate Change* 8 (4): 325–332. doi:10.1038/s41558-018-0091-3.

Sensus Inc. 2021. *PolluStat E - Data Sheet.* Morrisville: Sensus Inc.

Siemens, A. G. 2021. *LOGO! 24CE Logic Module, 6ED1052-1CC08-0BA1.* Munich: Siemens AG.

The Underfloor Heating Site. 2023. "Reliance Manifold Thermoelectric Head." [Online]. Accessed 7 February 2023. https://theunderfloorheatingsite.co.uk/shop/water-underfloor-heating/accessories/actuators/manifold-thermoelectric-head/.

Ventilation Control Products Sweden AB. 2022. "Thermoelectric Valve Actuators and Valve Adaptors for Different Valve Brands," 2011-2022. [Online]. Accessed 23 October 2022. http://www.ventilationcontrolproducts.net/actuators-and-valve-adaptors.

Vernatherm. 2023. "Thermal Actuators (Wax Motors)." [Online]. Accessed 7 February 2023. Available: https://www.vernatherm.com/thermal_actuators.html.

Võsa, K.-V., A. Ferrantelli, and J. Kurnitski. 2019. "Experimental Study of Radiator, Underfloor, Ceiling and Air Heater Systems Heat Emission Performance in TUT nZEB Test Facility." *E3S Web of Conferences* 111: 04005. doi:10.1051/e3sconf/201911104005.

Wen, J., and T. F. Smith. 2001. "Effect of Thermostat Time Constant on Temperature Control and Energy Consumption." SIcon/01. Sensors for Industry Conference. Proceedings of the First ISA/IEEE. Sensors for Industry Conference (Cat. No.01EX459), 252–257.

Wetter, M.. 2009. "A Modelica-based Model Library for Building Energy and Control Systems". Lawrence Berkeley National Laboratory. 11th International Building Performance Simulation Association Conference - Building Simulation '09, Glasgow, Scotland, July 27–30.

Wolisz, H., T. M. Kull, D. Müller, and J. Kurnitski. 2020. "Self-learning Model Predictive Control for Dynamic Activation of Structural Thermal Mass in Residential Buildings." *Energy And Buildings* 207: 109542. doi:10.1016/j.enbuild.2019.109 542.

Wolisz, H., C. Punkenburg, R. Streblow, and D. Müller. 2016. "Feasibility and Potential of Thermal Demand Side Management in Residential Buildings Considering Different Developments in the German Energy Market." *Energy Conversion and Management* 107: 86–95. doi:10.1016/j.enconman.2015. 06.059.

Zhang, L., N. Good, and P. Mancarella. 2019. "Building-to-Grid Flexibility: Modelling and Assessment Metrics for Residential Demand Response from Heat Pump Aggregations." *Applied Energy* 233–234: 709–723. doi:10.1016/j.apenergy.2018. 10.058.

Appendices

A. Measured actuators, heating profiles, and error estimates

Table A1. The error estimations for all profiles.

Combination	Producer	Motor specimen	Valve included?	Heating profiles measured (signal On-Off)	Duration (min)	MAE	RMSE
A1	A	1	no	15 min–45 min	515	0.014	0.042
A1	A	1	no	15 min–15 min	362	0.018	0.047
A1	A	1	no	5 min–5 min	454	0.058	0.089
A1v	A	1	yes	15 min–15 min	2774	0.011	0.019
B1	B	1	no	15 min–45 min	1241	0.023	0.047
B1	B	1	no	30 min–30 min	720	0.020	0.037
B1	B	1	no	10 min–10 min	646	0.045	0.097
B1	B	1	no	18 min–6 min	711	0.033	0.050
B1	B	1	no	15 min–15 min	1049	0.048	0.079
B1	B	1	no	3 min–3 min	141	0.098	0.122
B2	B	2	no	15 min–15 min	1110	0.028	0.048
B1v	B	1	yes	15 min–15 min	118	0.061	0.153
B2v	B	2	yes	15 min–15 min	1090	0.025	0.042
B2v	B	2	yes	15 min–45 min	1486	0.019	0.036
B3v	B	3	yes	15 min–15 min	144	0.030	0.056
B4v	B	4	yes	15 min–15 min	136	0.058	0.106
B4v	B	4	yes	random 5 to 15 min	482	0.086	0.148
B4v	B	4	yes	15 min–45 min	416	0.043	0.090

B. Heating curve for UFH supply water temperature in simulations
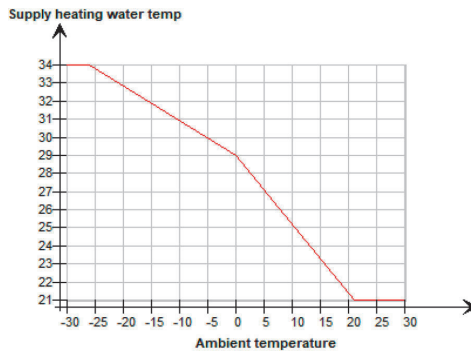
Figure B1. Heating temperature curve used in simulations.

C. Model fitting results for the characteristic times

Table C1. The process of fitting the empirical models to the characteristic times estimated from the measurements.
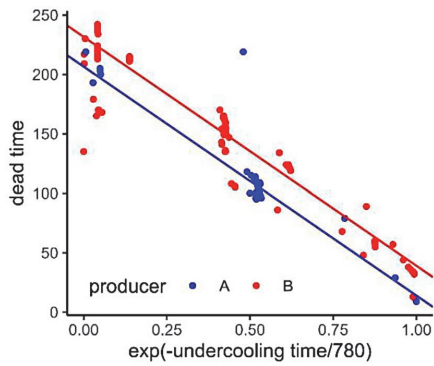
The estimated dead times had a clear dependence on the undercooling time of the previous period, therefore tdead,i = f(tuc,i-1). The negative exponent model was fitted as given in Equation (1). The time constant value $\tau = 780$ s had the highest correlation, with R-squared between the negative exponent and the dead time equalling 0.885. However, the linear model resulted in maximum residuals of over 1.5 min. To improve the performance, a linear multi-level model was tested and chosen for separate products, which constrained the residuals to maximum 10 s. In the figure, blue is the model for product A and red for the product B.
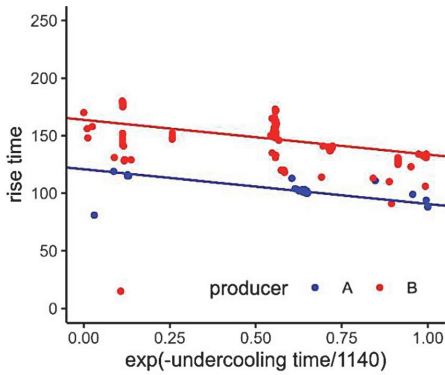
The rise times varied between 100 s and 180 s and it was therefore not constant as expected. The null hypothesis of rise time depending on room temperature was not confirmed as the ambient temperature varied in a very small range during the measurements. Instead, there was a slight dependence on the undercooling time's negative exponent similarly to the dead time. Therefore, trise,i = f(tuc,i-1) where the most suitable τ was 1140 s. The parameter k was small but clearly significant (p < .001). The residuals were over two minutes, so instead, a motor-specific solution was again identified using multi-level modelling.
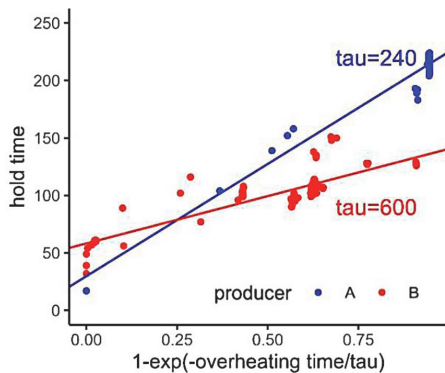
The hold time did depend on the overheating time, as expected in Equation (2). However, the dependence was not significant. As the hold time could be quite different for the motors, as Figure 11 shows. Thus, a producer-separated model was generated. As the intercept was insignificant for lme, separate linear models were fitted. Moreover, as in this case there is no reason to assume the same time constants and parameters, we searched for separate τ values. These resulted to be $\tau = 240$ s for product A and $\tau = 600$ s for product B.

Table C2. Continued

The fall time was constant for a product, as the standard deviation was around 10 s. No room temperature dependence was seen in the data. In the figure, the order of magnitude of the overheating time is shown in three colours for the two products.
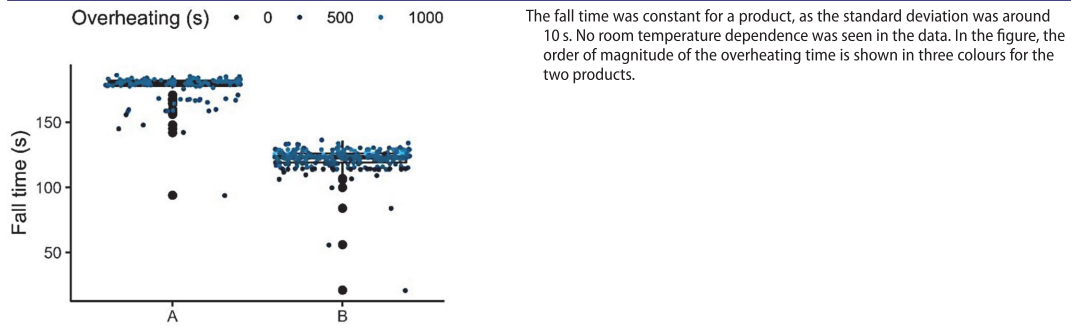
D. PI parameters optimized for continuous and modulated output
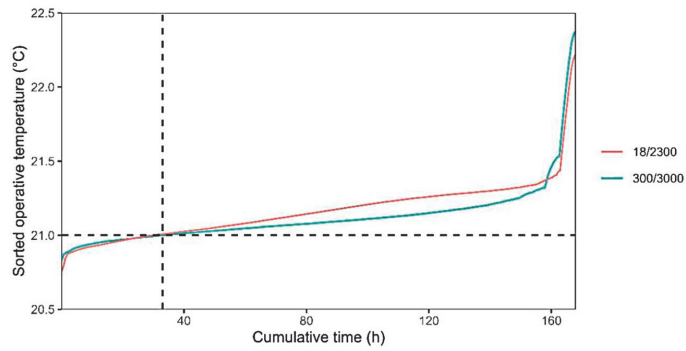
Figure D1. The cumulative temperature graphs for P_WM case (18/2300) and the same case with PI parameters adapted for the modulation (300/3000).

Publication IV

Kull, T. **M.**, Thalfeldt, M., and Kurnitski, J. (2021) Modelling of Wax Actuators in Underfloor Heating Manifolds, in E3S Web of Conferences, pp. 1–8. doi: 10.1051/e3sconf/202124611009

Modelling of Wax Actuators in Underfloor Heating Manifolds

Tuule Mall Kull[1*]*, Martin* Thalfeldt[2,1], and *Jarek* Kurnitski[2,1,3]

[1]Nearly Zero Energy Buildings Research Group, Tallinn University of Technology, Ehitajate tee 5, 19086 Tallinn, Estonia
[2]Smart City Center of Excellence, Tallinn University of Technology, Ehitajate Tee 5, 19086 Tallinn, Estonia
[3]Department of Civil Engineering, Rakentajanaukio 4 A, Aalto University, FI-02150 Espoo, Finland

Abstract. Finding sources for power grid balancing has become increasingly important with more renewables used for production. In buildings, heat pumps could be utilized among other electrical appliances. The heat pumps would work at full power to balance the overproduction in the grid. However, short-term grid flexibility announces the consumption need up to 5 minutes in advance, which can prove a problem to control. When there is no current energy need in the building, all valves are closed. That means that when a heat pump with overridden control starts working at the maximum frequency, its full power heats up the local circuit very fast, especially when there is no storage tank. Whether the heat pump overheats and cannot be used for balancing the grid or the whole system opens for heating depends on the regulating valves and their opening speed. For underfloor heating systems, the valve opening speed is slower than for other systems as wax actuators are used. This paper focuses on how to model these wax actuators and determine the opening time to provide input for further studies on flexibility. A physical and a linear segment model are parameterized and the results show that the wax actuator fully opens the valve in six minutes.

1 Introduction

Power grid that is rich in renewable energy, faces an increasingly difficult challenge of ensuring the grid power frequency at the needed 50 Hz level. The frequency stays constant when production and demand are in balance. When production changes rapidly, it can be faster and cost-efficient to change the demand rather than switch on or off other production sources. In demand side management, large consumers such as factory lines are a logical option. However, as the building sector consumes 30 % of electrical energy globally [1], buildings cannot be omitted as a possible flexibility source. It could be possible to switch household electrical appliances, but the increasing use of heat pumps allows using thermal energy storage in buildings to balance the power grid as well [2]. Energy flexible buildings have been discussed in detail in IEA EBC Annex 67 project [3]. Several control methods have been developed to utilize either the storage tank or structural thermal storage in buildings for flexibility [4].

However, the grid changes are quick and in the solution where many heat pumps are aggregated to an overhead system, the individual heat pumps get the signal to create demand only about 5 min in advance [5]. The control would overrun the default approach and the frequency would be set manually [6]. While small inverter based heat pump systems do not need large storage tanks, the system volume is very small when valves towards the rooms are closed. This could result in overheating or -cooling when the heat pump is started at full power. Therefore, to accurately predict what happens in the heat pump circuit, the slowest components have to be modelled precisely. Next to the heat pump itself, the only variable that controls the circuit are the actuators on the regulating valves. For underfloor heating, these are wax actuators in the manifold's return side.

Wax actuators are electrically controlled PCM (phase change material) actuators where paraffin wax is heated by a PTC (positive temperature coefficient) heater. These actuators are also called wax pellet actuators [7], thermal actuators, wax motors [8]. The actuator is screwed to the valve, which is therefore normally closed. When the voltage is applied, the wax starts to melt and expands. This expansion moves the piston, and with a system of springs, the actuator inner height reduces, which opens the valve. This type of actuators have been widely used for fan coils and in manifolds for TABS systems as well as hydronic underfloor heating for a long time as they are silent and strong. The core of the wax actuator is shown in **Figure 1** (a) and the cross-section of the wax actuator in **Figure 1** (b).

Actuators are mostly omitted in building energy performance simulations as their time constant is in orders of magnitude smaller than for the whole system. Sometimes these are modelled in a simplified mathematical way as a delay [9]. In other fields, wax actuators have mostly been modelled for microfluid systems in the scientific literature, however with nonmoving parts and therefore with an upscaling challenge [10]. In the actuator industry, it is common to model the actuator movement as hysteresis [8]. The

---

* Corresponding author: tuule.kull@taltech.ee

PCMs have been modelled in building structures as a thermal hysteresis as well [11]. The characteristics of the paraffin wax used in the actuators have been analysed in several articles [12]–[14]. However, wax actuator models that are more detailed than delay models are not discussed in the scientific literature for buildings and HVAC until now.

For grid flexibility, a timescale of 5 minutes has to be analysed and wax actuators are in that range. Therefore, the wax actuators should be modelled more precisely. In the current paper, we compare the physical and mathematical models for wax actuator. The main novelty of this paper is in the detailed modelling of the wax motor together with the valve and calibrating these in an actual system. This paper applies the wax motor model developed by Lars Eriksson in EQUA's IDA ICE software library [15] for the first time in the scientific literature. Moreover, in the HVAC science, possible parameters for wax motor have not been published before.
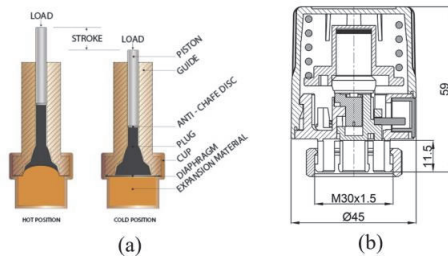
Figure 1. (a) Wax pellet actuator core [8] and (b) a cross-section how it is reversely implemented in a wax motor [16].

2 Methods

2.1 Experiment setup

The experiments are carried out in two phases to determine the effect of actuator only and actuator together with a valve. Initially, the wax actuator was unmounted from the valve and the change in its height with periodic applying of voltage was measured. In the second phase, the wax actuator was mounted in an underfloor heating manifold and the height could not be directly measured but the mass flow through the system could be.

2.1.1 Phase 1 : Linear movement of the actuator

A commercial 24V wax actuator produced and installed in 2013 was placed between a digital calliper with data logging capability. A metal piece was added between the calliper and the wax motor bottom to enable measuring the change in height. The calliper was fixed with a rubber band so that when the actuator's height reduces, the calliper would keep contact with the actuator and measure the change in height. Clearly, the measuring method and devices could be improved, especially as the force applied on the actuator by the

calliper was not measured. However, this force is small and presumably has no major effect. Therefore, this approach can be used for this preliminary study.

The wax actuator was controlled by a 24 V DC on-off signal with 15 minutes ON and 15 minutes OFF, periodically for 10 hours. The voltage control was implemented and logged in Siemens LOGO! 24CE controller [17]. The first hour was not used for parameter fitting.

2.1.2 Phase 2 : Mass flow through the valve

In the second phase, the wax actuator was mounted on a regulating return valve in an underfloor heating manifold. It is a typical hydronic underfloor heating manifold with 8 circuits in a small residential house. Its water is heated by a heat pump to a storage tank. From the tank, a pump in the mixing valve circulates the water through the manifold and circuits. In the mixing station, the thee-way valve is set to fully open with no recirculation. Pump speed was set to be constant. The setup consists of commercial products, so it is not exactly known what is inside each component. All parameter estimates depend on the documentation of the products.

To enable measuring the mass flow through one valve only, all but one valve in the manifold were closed by a commercial controller by setting the setpoints for the corresponding rooms (circuits) very low. The observed wax actuator on the last valve was again controlled by the Siemens LOGO controller. As the linear opening could not be directly measured, the mass flow through the manifold was measured by a heat meter. As additional measures, the surface temperature of the wax actuator was measured as well as the opening indicator on the cover was filmed for some cycles.

For surface temperature measurement, a PT100 sensor with data logging was glued to the plastic cover of the actuator on the side with thermal paste improving the thermal contact. The sensor was not insulated from the ambient air as otherwise the motor would cool down and close much slower than without it.

This time the wax actuator was observed for 3.5 days, the first two days the actuator was controlled with a signal of 15 minutes ON and 45 minutes OFF, and the last two days the signal was 15 minutes ON and 15 minutes OFF.

2.2 Modelling

The actuator was described by two models:
  • Characteristic curve model
  • Physical model
Both models calculate the linear position of the piston based on the voltage applied to the wax actuator. Pure hysteresis model was not included in this paper but should be analysed in future works.

The valve model was used to translate the linear piston movement of the actuator into mass flow through the valve.

2.2.1 Actuator: characteristic curve

The characteristic curve model is a linear segment model determined by four parameters: dead time, rise time, hold time, and fall time. The principle graph is shown in **Figure 2**. The model has four parameters. The dead time occurs when the voltage is turned on and therefore the PTC heater has started to heat the wax but the wax has not reached the melting point yet. During the rise time, the wax melts and expands, which moves the piston. When all wax has melted, its temperature increases but it does not expand and move the piston further. When the voltage turns off, the wax cools down. Before it reaches the melting point, it does not start to contract. This time is called hold time. When the solidification and therefore contraction starts, the hold time ends and fall time starts. Fall time ends when the actuator reaches its cold height. All four parameters were determined for each heating cycle in Phase 1. Average parameter value over all cycles was used for comparison simulations.
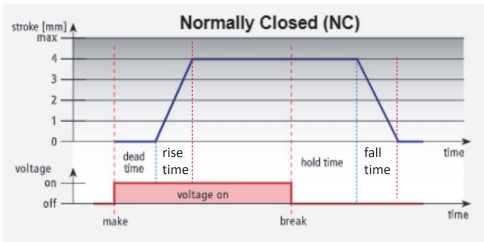
Figure 2. Characteristic curve model of linear segments for the actuator, adapted from [18]

2.2.2 Actuator: physical model overview

The physical model is based on first principles and was developed by Lars Eriksson at EQUA AB in 2017 for a private company. It has been published together with IDA ICE software. However, to keep the company's secret, the original parameter values were deleted. The adjustable parameters, their default and potential value ranges are discussed in the next section. The model uses enthalpy levels to keep track of the wax state in the motor. The model implementation is shown in **Figure 3**.

The main limitations of the model include the lack of modelling all springs in the system and that the heat transfer to the ambient is greatly simplified. The heat exchange with ambient is modelled with only resistance without capacitance and the ambient temperature is only an input not enabling the generation of heat balance. Therefore, the heat transfer to ambient is just dependent on the input temperature from the ambient and the resistance. To use the air temperature in the room where the manifold is situated, the resistance would have to be large. Moreover, the delays due to the capacity of the plastic cover cannot be described. Not modelling springs increases the same effect. For improvement, the surface temperature can be used as input. As the surface temperature is not measured in typical applications, it

was not included in Phase 1. However, it was added in Phase 2 to enable calibration.

The lack of surface temperature in Phase 1 was solved with the measured room air temperature plus a second-order transfer function from the heating signal. Its parameters gain k, damping D, and angular frequency w were fit to Phase 2 experimental surface temperature via IDA ICE parametric runs connection to GenOpt [19]. The possible value ranges were estimated from time constants as we expect the first time constant to be close to an hour and the second time constant to be close to a minute. As transfer function denominator:

$$(\tau_1 s + 1)(\tau_2 s + 1) = (s/w)^2 + 2D(s/w) + 1 \qquad (1)$$

Then:

$$w = 1/\sqrt{\tau_1 \tau_2} \qquad (2)$$

$$D = w(\tau_1 + \tau_2)/2 \qquad (3)$$

These give the initial estimates of w and D to be around 0.002 and 4. Gain represents the temperature change between the room and wax temperature.

2.2.3 Actuator: physical model parameter estimation

The parameters and their possible values for the physical model are shown in Table 1. N describes how many different ambient temperatures and resistances are modelled. This was kept at one. U defines the input voltage at signal 1, which for the used actuators is 24 V. Maximum displacements of the valve and actuator were set to the same values to initially exclude the valve effect. The displacement of 3.25 mm was determined from the Phase 1 measurements, although when defined equal, this effect is eliminated as the output of the model is the position in decimal percentage. This will be later multiplied with the known maximum displacement for error evaluation. The last parameter set to a constant is T_{H0}. It is described as „*Temperature at which H = 1E5 J/kg (default initial value of H). If initial value of H isn't changed, T_H0 becomes initial value of T.*" [15] As the initial value of H was not changed and the absolute values of enthalpy are not of interest only the relative differences, this can be fixed to some chosen value. Default value was used.

As wax motors are declared to work in ambient temperatures up to 60 degrees [18], [20], the melting temperature T_MELT has to be higher than this. Specific heat capacity in solid state CP_SOL can be according to different sources, for example, 2384 or 2604 J/(kg K) and for liquid state (CP_FLU) 2981 J/(kg K) [21], or 2100 J/(kg K) for both [22]. These values were included in the chosen range for both parameters. The melting heat should vary from 200 to 220 J/g [21]. Estimating that there should be around 1 cm³ of wax with a density of 0.8 g/cm³ [21], the mass range M can be guessed.

The parameters R_25 and T_CURIE describe the PTC heater. T_CURIE is the temperature where the resistance becomes infinite large, ranging from 60 to

140 °C, for thermal actuators is typically at 90 °C [23]. R_25 is the resistance at 25°C, a possible value from the literature is 50 K/W [24]. Between the surface temperature and the wax, the materials and air result in a thermal resistance described by R. Assuming only insulation, this would be 100 K/W and only plastic 0.3 K/W.

Suitable values for all parameters were found with GenOpt (through IDA ICE Parametric Runs) minimizing the MAE (mean absolute error) between the measured and simulated linear piston movement.

```
CONTINUOUS_MODEL RadWaxA

ABSTRACT "Wax actuator modelled using enthalpy formulation for the
solidification/melting.

Thermal resistances to multiple temperatures and source term describing
the effect dissipated in the PTC resistance. Source term is switched on/off
according to insignal.
Outsignal is normalized lift.

Date:       July 5, 2017

By:         LE at EQUA

Calls:      none

Revision history:

"

EQUATIONS

/* heat balance */

    T := IF        H < H_sol THEN
             T_melt + (H - H_sol) / cp_sol
         ELSE_IF H < H_flu THEN
             T_melt
         ELSE
             T_melt + (H - H_flu) / cp_flu
         END_IF ;

    Q := IF     T < T_curie THEN
             Insignal * U**2 * (1 - (T - 25) / (T_curie - 25)) / R_25
         ELSE
             0
         END_IF ;

    M * H' = SUM i = 1, N  (T_in[i] - T) / R[i]   END_SUM + Q ;

    OutSignal = IF       mode_as == 0 THEN
                   0
                ELSE_IF mode_as == 1 THEN
                   max( 0.0, min( 1.0, (H - H_sol) / (L_solid * RatVlvAct)))
                ELSE
                   1
                END_IF ;

    mode := IF       event(G0, H - H_sol ) < 0 THEN
                0
            ELSE_IF event(G1, H - H_open) < 0 THEN
                1
            ELSE_IF event(G2, H - H_flu ) < 0 THEN
                2
            ELSE
                2
            END_IF ;

    mode_as := mode ;

PARAMETER_PROCESSING

    IF     T_melt > T_H0 THEN
       H_sol := cp_sol * (T_melt - T_H0) + 1.0E5 ;
       H_flu := H_sol + L_solid          ;
    ELSE_IF T_melt < T_H0 THEN
       H_flu := cp_flu * (T_melt - T_H0) + 1.0E5 ;
       H_sol := H_flu - L_solid          ;
    ELSE
       CALL NMF_ERROR("T_H0 must be different from T_melt");
    END_IF ;

    RatVlvAct := MaxDispVlv / MaxDispAct ;

    H_open := H_sol + RatVlvAct * L_solid ;

END MODEL
```

Figure 3. The implementation of wax actuator in IDA ICE, the definition of all links, variables, and parameters has been omitted here for conciseness

2.2.4 Valve model

Modelling the actuator and valve together would need to transform the linear piston movement from the actuator model into water flow. This is characterized by a valve characteristic that maps the piston position to the

percentage of nominal flow. Manifold valves should mostly be quick opening valves, as indicates the shape of valve (5) in **Figure 4** (a). Quick opening is not very clearly defined, so the shape of the characteristic curve has to be determined experimentally.

In addition, valve authority distorts the valve characteristic in an experimental setting. Both curves are shown in a hypothetical example in Figure 4 (b). Valve authority is defined as the ratio of valve pressure drop to total pressure drop. In the observed system, the circuit starting from the storage tank can be observed as a separate system and therefore, the components towards the heat pump are not taken into account for pressure drop analysis.

The whole system has been balanced for 800 l/h with a balancing valve Comap DN 25 1" at 3 kPa the position 28 has been chosen (but zero has shifted, so the actual position was 27) using the producer's nomograms [25]. When closing all other circuits, the balancing valve position was adapted to 9, and the volume flow of a maximally open valve is at $G_{max} = 240$ l/h. The component wise pressure drops are estimated via various sources [26] and shown in Table 2. The estimation of all components started from the assumption that the pump pressure head stays constant, which is approximately valid as the pump curve at average speed and volume flow below 800 l/s varies less than 1 kPa [27]. All other components add up to $dp_{sys} = 27.2$ kPa pressure drop. Therefore, the valve pressure drop is 2.9 kPa and the K_v of the regulating valve is estimated to be:

$$K_v = \frac{0.01 \cdot \dot{V}}{\sqrt{dp_{valve}}} \approx 1.4 \qquad (4)$$

and valve authority

$$N = \frac{dp_{valve}}{dp_{valve} + dp_{sys}} \approx 0.1 \qquad (5)$$

The valve authority is very low, which is a result of observing only one circuit in a system which is designed for several circuits.

The actual volume flow is the volume flow from the valve curve distorted by the authority, which can be calculated from [28]:

$$G_\% = \sqrt{\frac{\frac{1}{N}}{\frac{1}{N} - 1 + \frac{1}{k^2}}} \qquad (6)$$

where $G_\%$ is the actual flow rate (in decimal percentage), N is the valve authority calculated for the given linear valve position, and k is the ratio of nondistorted and maximal flow rates. As the valve authority changes for the regulating valve during its opening and closing, the calculation was reversed. We assumed $G_\%$ from 0 to 1, and at each step calculated N. As $dp_{valve} + dp_{sys} = dp_{pump}$, valve authority can be calculated at any valve openness:

$$N = \frac{dp_{pump} - dp_{sys}}{dp_{pump}} = 1 - \frac{dp_{sys}}{dp_{pump}} = 1 - \frac{\left(G/K_{v,sys}\right)^2}{dp_{pump}} \qquad (7)$$

Where G is the actual volume flow $G_\% G_{max}$ and $K_{v,sys}$ is calculated from dp_{sys}, and G_{max}. Now k can be derived from Eq. (6:

$$k = \sqrt{\frac{1}{\frac{1}{N G_\%^2} - \frac{1}{N} + 1}} \qquad (8)$$

And therefore, we have derived the nondistorted volume flow from the distorted as $G_{vc} = k(G_\%) \cdot G_{max}$. Assuming that the quick opening pattern is similar to a logarithmic curve, usually the volume flow would be calculated from the stroke percentage $h_\%$ as:

$$G_{vc} = \frac{\ln(h_\%)}{\ln(100\ \%)} G_{max} \qquad (9)$$

Therefore, now we can calculate backwards:

$$h_\% = e^{k \cdot \ln(100)} \qquad (10)$$

When the mapping was once calculated as reversed, it was numerically saved and could be later used for calculating the volume flow from the piston linear position.

Table 1. The parameters and their value ranges of the physical model, bold values were fixed, based on prior knowledge

Name	Default	Initial value (limits)	Unit
N	1	**1**	items
M	0.0005	0.0008 (0.0005 to 0.002)	kg
CP_SOL	1200	2100 (2100 to 3000)	J / (kg K)
CP_FLU	1200	2100 (2100 to 3000)	J / (kg K)
L_SOLID	200000	210000 (200000-220000)	J/kg
T_H0	20	**20**	°C
T_MELT	75	75 (60 to 80)	°C
U	230	**24**	V
MAXDISPVLV	1.5	**3.25**	mm
MAXDISPACT	3.5	**3.25**	mm
T_CURIE	90	**90**	°C
R_25	290	50 (5 to 300)	K/W
R	13	13 (0.1 to 100)	K/W

Table 2. Pressure difference across components in the hydraulic system with data sources, the pump head should be the sum of all other pressure drops

Component	dp, kPa
Pump [27]	30
Circuit balancing valve on supply side	3.6
Circuit [29]	1.1
Regulating valve (calculated)	2.9
Heat meter [26]	4.5
Balancing valve [25]	10.8
10 knees [29]	7.1
Three-way valve in mixing station (Kv=8)	0.1

(a)   (b)
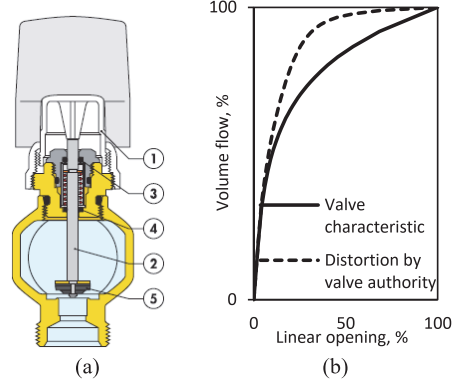
Figure 4. (a) Valve cross-section showing the valve shape (5) to indicate quick-opening valve [30] and (b) the corresponding (theoretical) valve characteristic curve, also distorted by valve authority

Table 3. Configuration of initial values and tested value ranges of input parameters for surface temperature optimization

Name	Value	Unit	OK range	Distribution	Resolution
k	10.0		[1 30]	UNIFORM	101
w	1.0E-4		[1.0E-4 0.1]	UNIFORM	101
D	1.0		[0.1 10]	UNIFORM	101
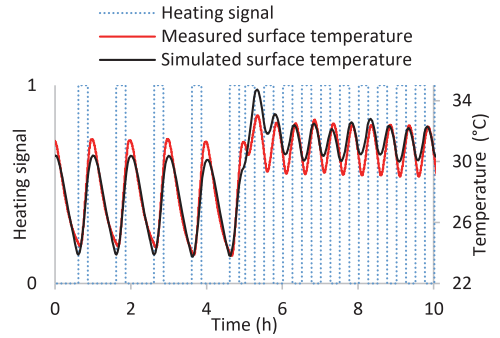
Figure 5. Actuator surface temperature fitting results

3 Results

3.1 Surface temperature estimation

The GenOpt optimization parameters for calibrating wax motor surface temperature were set up as shown in Table 3. The found optimal values were k=18.5, D=0.56, and w=0.0011. The MAE (mean absolute error) for the simulated period was 0.67 K. Comparison of fitted and measured temperatures is shown in Figure 5.

3.2 Actuator model

3.2.1 Physical model parameters

The temperature model from the previous section was included for calibrating the physical model to Phase 1 data. The wax motor parameters were defined for the optimization of linear piston movement as shown in **Table 4**. The minimal stroke MAE of 0.14 mm was reached at melting temperature 72 °C, specific heat for fluid 2910 and for solid 2930 J/kgK. Melting heat was achieved at 203 J/g. The thermal resistance to ambient was set to 52 K/W, PTC resistance at 25°C to 97 K/W. The wax mass value of 1g was reached. The comparison with measurements will be shown in Section 3.2.3. Running the optimization with different sets of variables and fixed parameters as well as different ranges, orders, and initial values, different results can be achieved. Further analysis would be needed in the future to detect an even better combination of parameters.

Table 4. Optimization parameters for piston movement calibration

Name	Value	Unit	OK range	Distribution	Resolution
◼ T_MELT	75.0	°C	[60 80]	UNIFORM	21
◼ CP_FLU	2100.0	J/(kg K)	[2100 3000]	UNIFORM	21
◼ CP_SOL	2100.0	J/(kg K)	[2100 3000]	UNIFORM	21
◼ L_SOLID	210000.0	J/kg	[200000 220000]	UNIFORM	21
◼ R[1]	13.0	K/W	[0.1 100]	UNIFORM	21
◼ R_25	50.0	K/W	[5 300]	UNIFORM	21
◼ M	8.0E-4	kg	[5.0E-4 0.002]	UNIFORM	21

3.2.2 Characteristic curve parameters

The characteristic curve parameters measured for each period in the 8-hour experiment in Phase 1 are shown in **Figure 6**. We can see that in total, the actuator is fully opened 5.6 minutes after the heating starts and fully closed 4.4 minutes after the heating has stopped. In this test, the operation was periodic, but in the future, different patterns of heating should be applied to determine the effect of initial temperature on the characteristic curve parameters.

3.2.3 Comparison

We compare both the characteristic curve and the physical model in the same period of measurements. The results are shown in **Figure 7**. The MAE for the characteristic curve was 0.05 and for the physical model 0.07 mm. This is less than 5 % of the absolute maximum value but 10 % and 8 % of the average stroke, respectively, during the test. However, according to the physical model, the actuator piston started moving more than 1 minute earlier both at opening and closing than seen in measurements. Character curve performed very well as it had been fit to the same data. Both models should also be tested on new data.
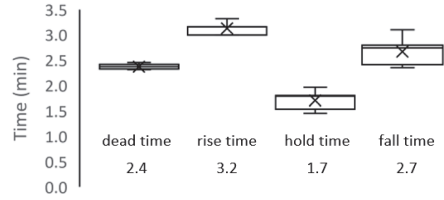
Figure 6. Characteristic curve parameters fitted to Phase 1 experimental data
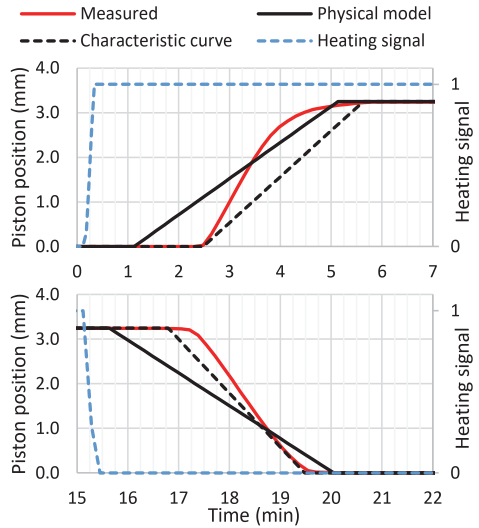
Figure 7. Stroke according to the two models compared to measurements during wax expansion (top) and contraction (bottom)
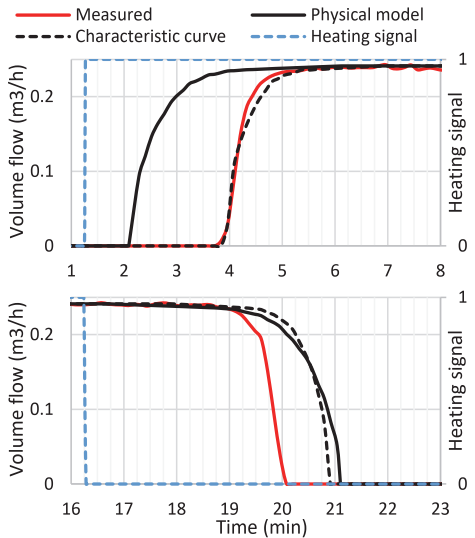
Figure 8. Volume flow according to the two models compared to measurements during wax expansion (top) and contraction (bottom)

3.3 Volume flow comparison

The resulting valve characteristic and its distortion due to valve authority were the same that are shown in Figure 4 (b). Applying these to the stroke calculated from the two actuator models, we can compare the resulting volume flow dynamics. These results are shown in **Figure 8**. MAE of the physical model is 19 % of the average volume flow during the period and the characteristic curve has MAE of 7 %. Characteristic curve seems to predict the increase of volume flow precisely, while with the physical model, currently almost 2 minute shift can be observed. In the cool-down, both models are a minute late.

4 Discussion and conclusions

The opening of the wax actuator and therefore the underfloor heating circuit from fully closed to fully open took 5.6 minutes in this study. The opening started at around 2.4 minutes (dead time). If the signal to start heating comes 5 minutes in advance from the power grid, the valves could be mostly open at the time the heating actually starts. However, it is not clear whether the 5-minute warning will be the reality and whether the opening speed of the valves is enough to ensure the heat pump would not overheat.

Both the physical and characteristic curve fit the measured data well, missing opening and closing times by maximally one minute. The translation to volume flow has larger error than modelling only the linear movement of the actuator piston. Although the mistake is small, this one or two minutes can be crucial for grid balancing. As the valve characteristic was not exactly known, the discrepancy in volume flow could be improved when the exact valve curve of the valve is known.

The main limitations of the physical model are the current implementation of heat transfer to ambient, which does not include capacity. This leads to the need of measured surface temperature of the motor, which is usually not available. Another limitation of this model is that the springs in the motor are not modelled. These could explain the delay effect as well.

In the current paper, the physical and the characteristic curve parameter estimation is preliminary. The physical model parameters were estimated by GenOpt but there was a large range of many parameters tested and there could have been many optimums. What is more, the experiments were short and did not include a large variety of different situations. In future, the characteristic curve parameters would need to be calculated for different situations and if needed, made dependent on the initial situation. In the future, the pure hysteresis model used in the actuator industry should be analysed as well.

References

[1]   IEA and UNEP, *2019 Global Status Report for Buildings and Construction*, vol. 224. 2019.

[2]   G. Reynders, T. Nuytten, and D. Saelens, "Potential of structural thermal mass for demand-side management in dwellings," *Build. Environ.*, vol. 64, pp. 187–199, Jun. 2013.

[3]   S. Ø. Jensen *et al.*, "IEA EBC Annex 67 Energy Flexible Buildings," *Energy Build.*, vol. 155, pp. 25–34, Nov. 2017.

[4]   H. Wolisz, T. M. Kull, D. Müller, and J. Kurnitski, "Self-learning model predictive control for dynamic activation of structural thermal mass in residential buildings," *Energy Build.*, vol. 207, p. 109542, 2020.

[5]   L. Zhang, N. Good, and P. Mancarella, "Building-to-grid flexibility: Modelling and assessment metrics for residential demand response from heat pump aggregations," *Appl. Energy*, vol. 233–234, pp. 709–723, Jan. 2019.

[6]   M. Lindahl, "Grid Flexible Control of Heat Pumps," *HPT - Heat Pumping Technologies*, 2020.

[7]   S. Tibbitts, "High output paraffin actuators: utilization in aerospace mechanisms," 1988.

[8]   "Thermal Actuators - Wax Motors - Thermostatic wax powered linear actuators." [Online]. Available: https://www.vernatherm.com/thermal_actuators.html. [Accessed: 11-Mar-2021].

[9]   M. Wetter, "A Modelica-based Model Library for Building Energy and Control Systems," 2009.

[10] A. Mann, T. Germann, M. Ruiter, and P. Groche, "The challenge of upscaling paraffin wax actuators," *Mater. Des.*, vol. 190, p. 108580, May 2020.

[11] F. Goia, G. Chaudhary, and S. Fantucci, "Modelling and experimental validation of an algorithm for simulation of hysteresis effects in phase change materials for building components," *Energy Build.*, vol. 174, pp. 54–67, Sep. 2018.

[12] J. I. Lipton, S. Angle, and H. Lipson, "3D Printable Wax-Silicone Actuators."

[13] J. I. Lipton, S. Angle, R. E. Banai, E. Peretz, and H. Lipson, "Electrically Actuated Hydraulic Solids ," *Adv. Eng. Mater.*, vol. 18, no. 10, pp. 1710–1715, Oct. 2016.

[14] A. Mann, C. Bürgel, and P. Groche, "A

Modeling Strategy for Predicting the Properties of Paraffin Wax Actuators," *Actuators*, vol. 7, no. 4, p. 81, Nov. 2018.

[15]   "IDA Indoor Climate and Energy 4.8." Equa Simulations AB, 2018.

[16]   "Electric Thermal Actuator - TRV head|Balancing valve|Thermal Actuator|Manifolds|PICV." [Online]. Available: https://www.muuytec.com/portfolio-items/electric-thermal-actuator/. [Accessed: 11-Mar-2021].

[17]   T. Kalema, G. Johannesson, P. Pylsy, and P. Hagengran, "Accuracy of Energy Analysis of Buildings: A Comparison of a Monthly Energy Balance Method and Simulation Methods in Calculating the Energy Consumption and the Effect of Thermal Mass," *J. Build. Phys.*, vol. 32, no. 2, pp. 101–130, Oct. 2008.

[18]   Polytherm Heating Systems, "OEM-Actuator 24V."

[19]   M. Wetter, "GenOpt® -- A Generic Optimization Program," in *Seventh International IBPSA Conference*, 2001.

[20]   Danfoss, "Actuator ABNM A5 0-10 V Proportional For Use with RA2000 Valves."

[21]   N. Ukrainczyk, S. Kurajica, and J. Šipušić, "Thermophysical comparison of five commercial paraffin waxes as latent heat storage materials," *Chem. Biochem. Eng. Q.*, vol. 24, no. 2, pp. 129–137, 2010.

[22]   M. Freund, R. Csikós, S. Keszthelyi, and G. Y. Mózes, *Paraffin Products Properties, Technologies, Applications*, vol. Volume 14. 1982.

[23]   "Thermometrics Product Line PTC Thermistors Positive Temperature Coefficient Thermistors," 2015.

[24]   R. Components, "Thermistors," 1997. [Online]. Available: https://www.thierry-lequeu.fr/data/NTC-RS.pdf. [Accessed: 11-Mar-2021].

[25]   Comap, "750 Static balancing valve," 2014.

[26]   Sensus, "Ultrasonic Meter for heating and cooling energy nominal sizes q p 0.6 to 60 m 3 /h PolluStat E," 2016.

[27]   Grundfos, "ALPHA2 Installation and operating instructions," 2012.

[28]   J. C. Inc., "Valve and Actuator Manual, Section Vb1: Valves," 1994.

[29]   T. Kalamees *et al.*, "Korterelamute välispiirete lisasoojustamise sõlmejoonised ja tüüpkorterite ventilatsioonilahendused," 2015.

[30]   "Pre-assembled distribution manifolds for radiant panel systems series 663 & 668S1 Function."

Publication V

Kull, T. M., Simson, R., and Kurnitski, J. (2018). Setback Efficiency of Limited-Power Heating Systems in Cold Climate. In: Johansson, D., Bagge, H., Wahlström, Å. (eds) *Cold Climate HVAC 2018. CCC 2018. Springer Proceedings in Energy. Springer, Cham.* https://doi.org/10.1007/978-3-030-00662-4_8

Setback Efficiency of Limited-Power Heating Systems in Cold Climate

Tuule Mall Kull, Raimo Simson and Jarek Kurnitski

Abstract The main aim of this work is to analyse the energy saving potential and peak power impact resulting from the temperature setback approach. This paper analyses low energy buildings incorporating high-efficiency heating systems with limited power, as additional power for district heating and heat pump systems will need costly investments. The setback efficiency is estimated for different types of heating systems. Underfloor heating is compared to radiators both for limited and excess power. Based on estimated time constants, suitable heat-up time is calculated to minimise the time when temperatures stay below setpoint during occupancy. The energy saving potential of night-time and weekend setback periods in an office are analysed. It is found that the energy saving potential of setback is low under given constraints. Therefore, for modern buildings the cost-optimality has to be assessed separately for specific cases.

1 Introduction

The method of periodically decreasing the set temperature of heating systems in buildings when the rooms are vacant, often called intermittent heating or the setback approach is a widely used method for energy saving. In several studies [1–3] energy saving potentials of up to 20% were identified. In single cases, the observed reductions are much higher [4] or much lower [5]. In the mentioned studies, mostly moderately insulated buildings are considered with simple setback control mechanisms based on pre-defined set-temperature schedules. However, such an approach

T. M. Kull (✉) · R. Simson · J. Kurnitski
Tallinn University of Technology, Ehitajate tee 5, 19086 Tallinn, Estonia
e-mail: tuule.kull@ttu.ee

J. Kurnitski
School of Engineering, Aalto University, Rakentajanaukio 4A, 02150 Espoo, Finland

generates discomfort during the times when people arrive and the temperature has not achieved its set value. In recent years, most intermittent heating control systems for low energy buildings include advanced control methods to solve this problem [6]. However, these are not simple to apply. Applying setback temperatures requires over-dimensioned heating systems to enable fast heat up times [7]. However, a typical advantage of modern low energy buildings is the utilization of low peak-power heating systems which reduces the building's investment cost.

Our assumption is that only very low energy savings can be achieved by temperature setback in modern well insulated buildings and therefore the required investment in over-sized heating systems is not profitable. Therefore, the efficiency of intermittent heating in modern and old buildings is compared in this work.

2 Approach

2.1 The Building Description

Envelope. The room model used for the simulations is a 13.3 m^2 office with a 3-m^2 window facing north. We have previously described this model with all construction specifications for modern and old buildings as well as heavy and light construction types in [8]. The room has one external wall and an external floor over outdoor air, therefore, its heating demand is larger than for an average office building. This case is defined as 'standard' office. For comparison, a similar office room with less insulation is defined as 'old' office. The third configuration is referred to as 'modern' as it has standard constructions but its floor is adiabatic and the window is south-facing. The total heat loss coefficient (without ventilation system) is 7, 9 or 18 W/K for modern, standard, and old buildings respectively.

Ventilation and internal gains. We have redefined the internal loads and ventilation control according to the Estonian norms for office simulations [9], meaning that the ventilation airflow is 2 l/s/m^2 during the occupancy hours (7 a.m. to 6 p.m. at workdays) and 1 h before and after this timeframe. The usage profile is depicted in Fig. 1. These usage factors are multiplied with 5.8 W/m^2 for occupant heat gain, and 9.5 W/m^2 for heat gains from lighting and electrical appliances. During the weekends and holidays the building is not in use. The supply air temperature of the ventilation is 18 °C. For the modern offices, 80% heat recovery from the exhaust air is assumed, whereas the old building has no heat recovery at all. The infiltration in modern buildings is 1.3 l/s; in the old buildings, it is included in the ventilation.

Heating systems. Two types of limited power heating systems are simulated: ideal heaters and electric floor heaters. Ideal heaters represent radiators (Rad) supplied by a district heating system, while electric floor heating represents underfloor heating (UFH) supplied by a heat pump. Using the electric/ideal systems replaces here the function of raising the heating curve to achieve maximum output power of the systems during the heat-up. The nominal power of the modern systems is 273 W,
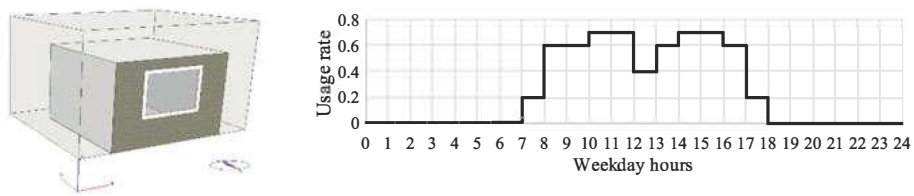
Fig. 1 The isometric view of the simulated zone (on the left, screenshot from software IDA-ICE) and the usage factor profile

of standard systems 437 W, and for old systems 1656 W. For the comparison with a gas boiler supplied radiator-based heating system, which can be easily over dimensioned without distinct cost increase, ideal heater cases with 684 W in standard light and 1367 W in heavy offices are simulated and defined as 'over-dim-Rad'. These are dimensioned according [7] to weekend setbacks.

Simulation. The building is simulated in IDA-ICE 4.7.1 software [10] using Estonian TRY [11] as climate data. The heating season is assumed to be from 1st of October to 30th of April.

2.2 The Control Description

Reference case. The performance of the setback control is evaluated by comparing the required heating energy demand against the demand of a reference case, where a constant temperature of 21 °C is maintained by a proportional-integral (PI) controller in the same room. Here, the performance is defined as the heating demand for both space heating and supply air heating by the air-handling unit.

Control algorithm. The setback control also keeps the air temperature during the occupancy hours at 21 °C with PI control, only it is reduced to 18 °C during unoccupied hours. However, to ensure comfort conditions when occupancy starts the required heat-up time, until comfort temperature is reached, is calculated.

   If that calculated heat-up time is longer than the actual time left to the start of occupancy hours, the set temperature is changed to 21 °C overriding the initial PI control. If the temperature rises faster than estimated, the set temperature is turned back to 18 °C again.

Heat-up time calculation. The heat-up time is the time the system needs to heat the room up to 21 °C again from setback. It is calculated every 5 min. For that, the one-time-constant model for the building is used. From the heat balance equation of

$$C\frac{d\theta_{in}}{dt} = H(\theta_{out} - \theta_{in}) + \Phi \tag{1}$$

Table 1 Calculated input parameters used for preheat-control in intermittent heating

Energy-efficiency level	Str. mass	Heat emitter	Abbrev.	τ_n (h)	τ_{wnd} (h)	Φ (W)	H (W/K)	C_{20mm} (kJ/K)
Standard	Heavy	UFH	S_H_UFH	50	225	437	9	1677
Standard	Heavy	Rad	S_H_Rad	50	225	437	9	1677
Standard	Light	UFH	S_L_UFH	50	150	437	9	1561
Standard	Light	Rad	S_L_Rad	50	150	437	9	1561
Old	Heavy	Rad	O_H_Rad	25	125	1656	18	1677
Old	Light	Rad	O_L_Rad	25	75	1656	18	1561
Modern	Heavy	UFH	M_H_UFH	50	300	273	7	1677
Modern	Heavy	Rad	M_H_Rad	50	300	273	7	1677
Standard	Heavy	Over-dim Rad	S_H_O_Rad	50	225	1367	9	1677
Standard	Light	Over-dim Rad	S_L_O_Rad	50	150	684	9	1561

for the indoor temperature θ_{in}, the solution for the heat-up time is derived:

$$t = -\tau \cdot \ln\left(\frac{\Phi/H - \theta_{set} + \theta_{out}}{\Phi/H - \theta_{in} + \theta_{out}}\right). \tag{2}$$

Φ is the heating power in watts, H is the heat loss coefficient (W/K), θ_{out} is the exterior air temperature, θ_{set} is 21 °C and θ_{in} is the current indoor air temperature. τ is the time constant in seconds, however in this work it is always converted to hours. It is calculated as $\tau = C/H$. C represents the heat capacity of the air and structures (J/K). For the calculation of time constant for night setback, the surface layers up to 20 mm depth are included into the heat capacity calculation. The active layer depth of 100 mm is used for weekend setback [12]. The time constants are quantized; they are rounded to the closest 25 h. This is done to use approximate values, as the exact values are not known in real cases. The used values are shown in Table 1. The 100 mm heat capacity values are approximately four times higher than the 20 mm values shown in the table (7449 kJ/K for heavy and 5002 kJ/K for light).

3   Results and Discussion

3.1   *Energy Performance*

The simulated energy demands for all observed cases are shown in Table 2. It can be seen that the energy consumption in the air-handling unit is almost equal for all the modern and standard cases; it is zero for old buildings, as the supply air is not heated. The total reduction of energy demand resulting from the intermittent heating

Table 2 Energy need results for constant temperature and setback control cases

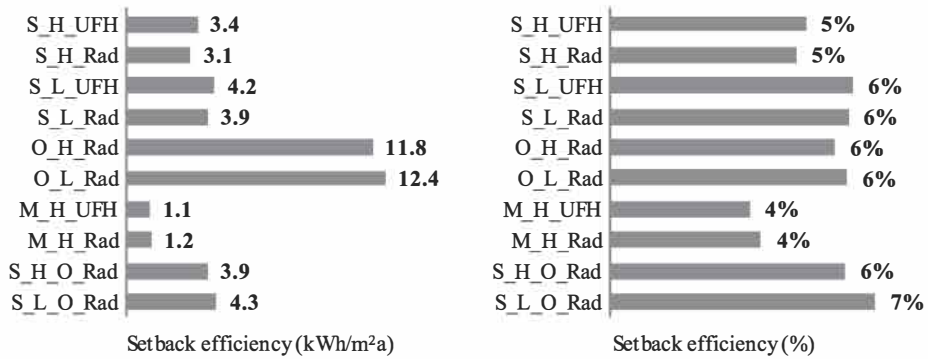|	Space heating [kWh/(m^2 a)]		Air handling unit [kWh/(m^2 a)]		Total [kWh/(m^2 a)]	
	21 °C	Setback	21 °C	Setback	21 °C	Setback
S_H_UFH	52	47	15	17	68	64
S_H_Rad	48	44	16	17	65	62
S_L_UFH	53	47	15	17	68	64
S_L_Rad	48	43	16	17	64	60
O_H_Rad	207	195	0	0	**207**	**195**
O_L_Rad	206	194	0	0	**206**	**194**
M_H_UFH	17	15	14	15	*31*	*30*
M_H_Rad	15	13	15	16	*30*	*29*
S_H_O_Rad	49	44	16	17	65	61
S_L_O_Rad	48	42	16	17	64	60

operation is shown in Fig. 2. All observed cases result in heating demands reduced by approximately 4–7% when setback control is compared against the constant temperature reference cases. However, the absolute reduction differs significantly between construction types, as the net heat demand between the evaluated cases ranges from 29 to 195 kWh/(m^2 a). While for the old buildings the reduction is about 12 kWh/(m^2 a), then for the south-oriented low energy buildings the reduction is only 1 kWh/(m^2 a). For heavy construction, setback efficiency is in all cases marginally less than for the corresponding light construction case.

3.2 Temperature Performance

Weekly fluctuations. The resulting air temperatures in the observed office during a two-week period in winter are depicted for all simulated cases in Fig. 3. In Fig. 3a, we can see that for the well-insulated room, air temperatures do not decrease to 18 °C (lower horizontal interrupted line), staying even for weekend setback above 19 °C. Moreover, the graph shows that the PI-control cannot hold a constant temperature during the day (set temperature level of 21 °C shown in upper horizontal dashed line) and the room overheats for the floor-heating case.

Figure 3b illustrates the known observation that a room with higher heat capacity cools down slower. In case of a light building structure, the temperature can decrease to 18 °C even for the floor heating case the Fig. 3b shows. Still, the temperature change is slow and the set temperatures difficult to maintain.

Compared to these, changes in temperature for radiator cases in Fig. 3c are faster. PI control with the radiators maintains the temperature setpoint well. However, during the heat-up fluctuations occur.

S_H_UFH	3.4
S_H_Rad	3.1
S_L_UFH	4.2
S_L_Rad	3.9
O_H_Rad	11.8
O_L_Rad	12.4
M_H_UFH	1.1
M_H_Rad	1.2
S_H_O_Rad	3.9
S_L_O_Rad	4.3
Setback efficiency (kWh/m²a)	

|	
S_H_UFH	5%
S_H_Rad	5%
S_L_UFH	6%
S_L_Rad	6%
O_H_Rad	6%
O_L_Rad	6%
M_H_UFH	4%
M_H_Rad	4%
S_H_O_Rad	6%
S_L_O_Rad	7%
Setback efficiency (%)	

Fig. 2 Energy performance of the intermittent heating, absolute difference from the reference cases on the left and relative on the right. The abbreviations in the labels are explained in Table 1

In Fig. 3d, we can see that the over-dimensioned radiators allow for stronger room temperature reductions than in the corresponding cases with regular heating dimensioning in Fig. 3c. However, Table 2 shows that the resulting reduction of energy demand is not higher than 1 kWh/m² a.

Figure 3e shows that in old buildings the temperature drops to 18 °C almost immediately and, due to the high available heating power, raises up to 21 °C fast as well. Therefore, in the old building case, the setback potential is fully exploited.

Heat-up performance. In all the temperature graphs (Fig. 3), we can see that for the heavy building cases the temperatures fluctuate before reaching the set temperature. This is because the actual temperature increase is significantly faster than modelled and the system lets the room cool down again until it calculates that heat-up should be started again. In Fig. 4. we can see that the fluctuation after weekend setback (on Monday) is more significant than after night-setback (Friday). While on Friday, the setpoint (21 °C) is reached by the start of occupancy in most of the evaluated office rooms, it is not the case on Monday. However, the temperatures are above 20 °C when occupancy begins in all observed scenarios. On Friday, as an exceptional case, S_L_UFH cools down fast but does not manage to heat up on time.

Heating season. The overall temperature performance during the heating season is depicted in duration graphs in Fig. 5. Figure 5a illustrates the difference between the two heat emitters. We can see that the floor heating is not keeping the given set temperatures, as the graphs are smooth, whereas the plateaus in the radiator graphs show that to some extent set temperatures are maintained. In Fig. 5b, we can see that there is a very clear difference between the different insulation levels. While the plateaus are very clear in the old house case, the modern south-oriented building has very small energy losses and it has significantly higher temperatures. The standard cases can be found between these two extremes. Figure 5c compares heavy and light structures in old and modern buildings. The slower cool-down of the heavy buildings results in higher temperatures in the duration graph.
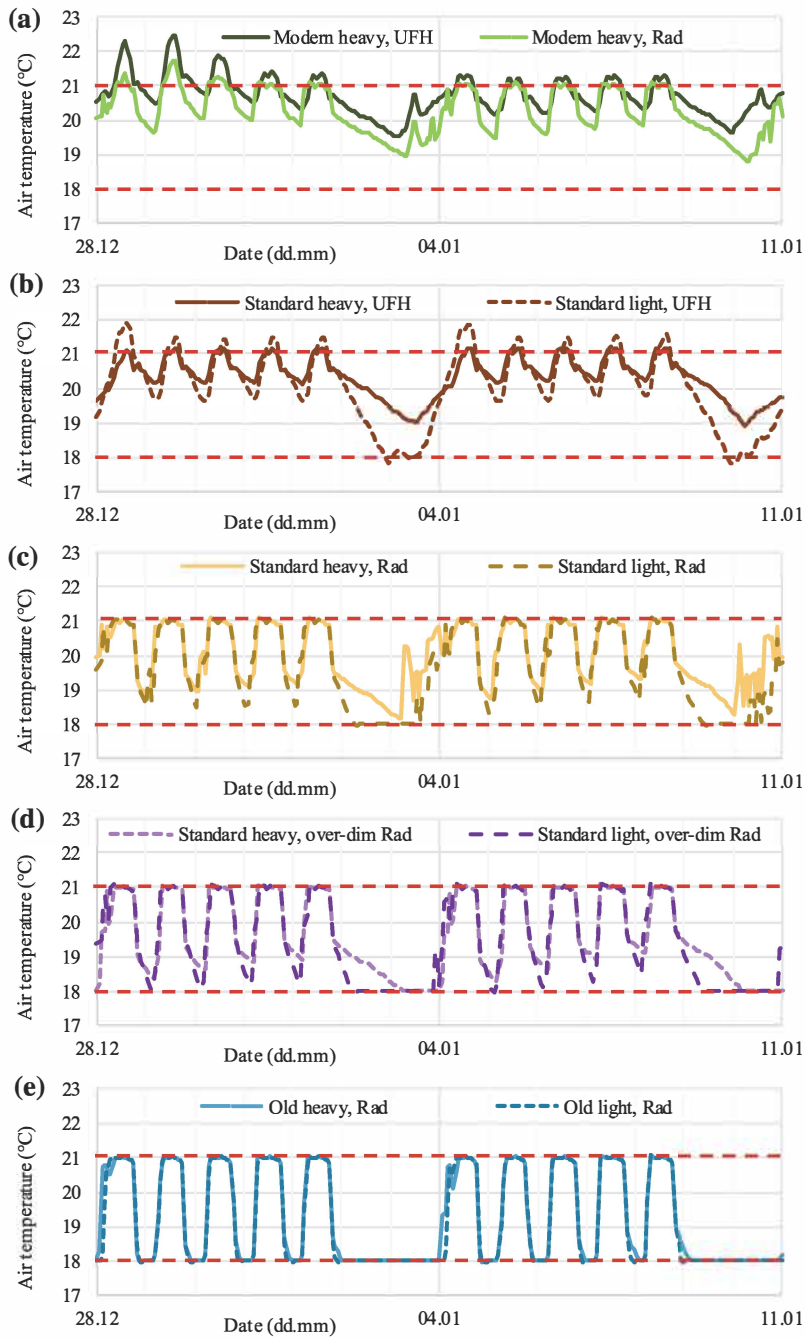
Fig. 3 Air temperature fluctuations during two winter weeks for all simulated cases
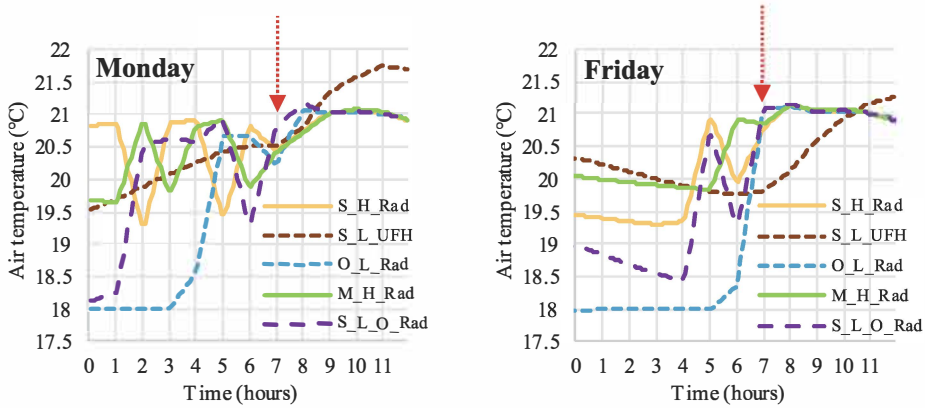
Fig. 4 Temperature performance during heat-up times in the first 12 h on Monday, January 4 (left) and Friday, January 8 (right). Occupancy start at 7 a.m. and is marked with arrows
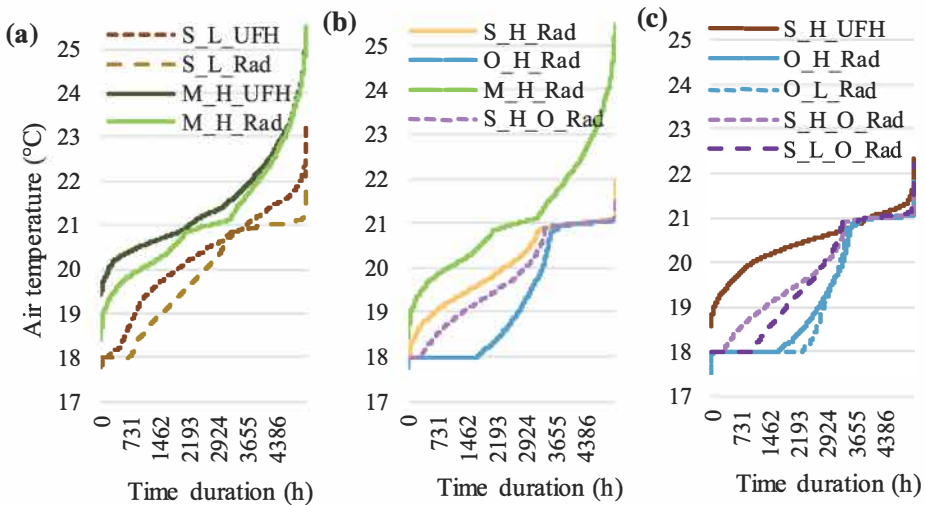
Fig. 5 Temperature duration graphs over the heating season

4 Conclusion

This research shows that the absolute setback efficiency in modern office buildings is significantly lower than in old buildings. This is mainly because the air temperature does not drop as fast and it stays above allowed minimal limit during the nighttime setbacks. For floor heating cases, this applies even for weekend setbacks. It has been shown that buildings with lower thermal mass and faster reacting heating system have higher energy conservation potential when applying intermittent heating operation. The setback control for old office buildings is always

profitable. However, for modern and especially modern buildings with slow reacting heating system, the benefits of setback control are low, especially in absolute numbers. Before applying, the saving needs to be weighed against potential discomfort and additional cost for every specific case.

References

1. B. Xu, S. Zhou, W. Hu, An intermittent heating strategy by predicting warm-up time for office buildings in Beijing. Energy Build (2017)
2. J.W. Moon, S.H. Han, Thermostat strategies impact on energy consumption in residential buildings. Energy Build. **43**(2–3), 338–346 (2011)
3. W. Wang, J. Zhang, W. Jiang, B. Liu, Energy performance comparison of heating and air-conditioning systems for multi-family residential buildings. HVAC&R Res. **17**(3), 309–322 (2011)
4. W. Guo, D.W. Nutter, Setback and setup temperature analysis for a classic double-corridor classroom building. Energy Build. **42**(2), 189–197 (2010)
5. Z. Wang, B. Lin, Y. Zhu, Modeling and measurement study on an intermittent heating system of a residence in Cambridgeshire. Build. Environ. **92**, 380–386 (2015)
6. Y. Wang, J. Kuckelkorn, Y. Liu, A state of art review on methodologies for control strategies in low energy buildings in the period from 2006 to 2016. Energy Build. **147**, 27–40 (2017)
7. Energy performance of buildings—Method for calculation of the design heat load—Part 1: Space heating load. FprEN 12831-1, European Standard (2016)
8. T.M. Kull, R. Simson, M. Thalfeldt, J. Kurnitski, Influence of time constants on low energy buildings' heating control, pp. 11–14 (2017)
9. Estonian Regulation No 58: Methodology for calculating the energy performance of buildings. Ministry of Economic Affairs and Communications (2015)
10. "IDA Indoor Climate and Energy 4.7.1." Equa Simulations AB, 2016
11. T. Kalamees, J. Kurnitski, Estonian test reference year for energy calculations. Proc. Est. Acad. Sci. Eng. **12**(1), 40–58 (2006)
12. Energy performance of buildings—Calculation of energy use for space heating and cooling, vol. 2008. ISO 13790, International Standard (2008)

Appendix 2

Implementation of wax motor in IDA ICE by Lars Eriksson

```
CONTINUOUS_MODEL RadWaxA

ABSTRACT "Wax actuator modelled using enthalpy formulation for the
solidification/melting.

Thermal resistances to multiple temperatures and source term describing
the effect dissipated in the PTC resistance. Source term is switched on/off
according to insignal.
Outsignal is normalized lift.

Date:        July 5, 2017

By:          LE at EQUA

Calls:       none

Revision history:

"

EQUATIONS

/* heat balance  */

   T := IF        H < H_sol THEN
           T_melt + (H - H_sol) / cp_sol
        ELSE_IF H < H_flu THEN
           T_melt
        ELSE
           T_melt + (H - H_flu) / cp_flu
        END_IF ;

   Q := IF     T < T_curie THEN
           Insignal * U**2 * (1 - (T - 25) / (T_curie - 25)) / R_25
        ELSE
           0
        END_IF ;

   M * H' = SUM i = 1, N  (T_in[i] - T) / R[i]  END_SUM + Q ;

   OutSignal = IF        mode_as == 0 THEN
                   0
               ELSE_IF mode_as == 1 THEN
                   max( 0.0, min( 1.0, (H - H_sol) / (L_solid * RatVlvAct)))
               ELSE
                   1
               END_IF ;

   mode := IF        event(G0, H - H_sol ) < 0 THEN
               0
           ELSE_IF event(G1, H - H_open) < 0 THEN
               1
           ELSE_IF event(G2, H - H_flu ) < 0 THEN
               2
           ELSE
               2
           END_IF ;

   mode_as := mode ;

LINKS

/* type          name          variables */

FOR i = 1, N
   T              Surtemp[i]   T_In[i];
END_FOR;
```

```
    GENERIC    OutSignalLink   OutSignal (output);

    GENERIC     InSignalLink    InSignal (input);

VARIABLES

/* type         name        role  def       min    max   description */

   Temp          T           LOC    20 ABS_ZERO   BIG   "Temperature"
   Temp          T_in[N]     IN     20 ABS_ZERO   BIG   "Temperature at surrounding
   Enthalpy      H           OUT   1.0E5   -BIG   BIG   "Enthalpy"
   HeatFlux      Q           LOC     3        0   BIG   "Heatflux"

   Generic       OutSignal   OUT     0        0     1   "Outsignal, between 0 and 1"
   Generic       InSignal    IN      0        0     1   "Insignal, 0 or 1"

   Generic       G0          A_S     0     -BIG   BIG   ""
   Generic       G1          A_S     0     -BIG   BIG   ""
   Generic       G2          A_S     0     -BIG   BIG   ""
   Generic       mode_as     A_S     0        0     1   "mode of operation, 0 = , 1
   Generic       mode        LOC     0        0     1   "mode of operation, 0 = , 1

MODEL_PARAMETERS

/* type         name        role  def       min    max   description */

   Int           N           SMP     1        1 BIGINT  "Number of surrounding eleme

PARAMETERS

/* type         name        role  def       min    max   description */

   Mass          M           S_P  0.5E-3 SMALL   BIG   "Mass"
   HeatCapM      cp_sol      S_P  1.2E3  SMALL   BIG   "Specific heat of solid phas
   HeatCapM      cp_flu      S_P  1.2E3  SMALL   BIG   "Specific heat of fluid phas
   Enthalpy      L_solid     S_P  2.0E5      0   BIG   "Melting heat"
   Temp          T_H0        S_P    20  ABS_ZERO  BIG   "Temperature at which H = 1E
                                                         If initial value of H isn't
   Temp          T_melt      S_P    75  ABS_ZERO  BIG   "Temperature at which meltin
   HeatRes       R[N]        S_P    13      SMALL   BIG   "Thermal resistances to surr
   Voltage       U           S_P   230         0   BIG   "Tension"
   Generic       MaxDispVlv  S_P   1.5     SMALL   BIG   "Max displacement of valve (
   Generic       MaxDispAct  S_P   3.5     SMALL   BIG   "Max displacement of actuato
   Temp          T_curie     S_P    90  ABS_ZERO  BIG   "PTC switch temperature wher
                                                         infinite large"
   HeatRes       R_25        S_P   290     SMALL   BIG   "PTC resistance at 25 C"

   Factor        RatVlvAct   C_P  0.43     SMALL   BIG   "Max displacement ratio valv
   Enthalpy      H_sol       C_P    12      -BIG   BIG   "Enthalpy at which melting s
   Enthalpy      H_flu       C_P    12      -BIG   BIG   "Enthalpy at which solidific
   Enthalpy      H_open      C_P    12      -BIG   BIG   "Enthalpy at which actuator

PARAMETER_PROCESSING

  IF       T_melt > T_H0 THEN
     H_sol := cp_sol * (T_melt - T_H0) + 1.0E5 ;
     H_flu := H_sol + L_solid               ;
  ELSE_IF T_melt < T_H0 THEN
     H_flu := cp_flu * (T_melt - T_H0) + 1.0E5 ;
     H_sol := H_flu - L_solid               ;
  ELSE
     CALL NMF_ERROR("T_H0 must be different from T_melt");
  END_IF ;

  RatVlvAct := MaxDispVlv / MaxDispAct ;

  H_open := H_sol + RatVlvAct * L_solid ;

END_MODEL
```

Curriculum vitae

Personal data

Name:	Tuule Mall Parts (née Kull)
Date of birth:	16.12.1991
Place of birth:	Tartu, Estonia
Citizenship:	Estonian

Contact data

E-mail:	tuule.parts@taltech.ee

Education

2016–2023	Tallinn University of Technology, Civil engineering and architecture, PhD
2013–2016	RWTH Aachen University, Simulation Sciences, MSc
2010–2013	University of Tartu, physics, BSc *cum laude*
1998–2010	Miina Härma Gymnasium, Secondary education

Language competence

Estonian	Native language
English	Fluent
German	Intermediate
Russian	Basic

Academic employment

2022–…	R8 Technologies, engineer
2016–…	Tallinn University of Technology, Estonia, Institute of Civil Engineering and Architecture, nZEB Research Group, junior researcher/expert
2018–2019	Amenti AG, programmer and data scientist
2016–2018	Swiss Property, building physics specialist
2016	Institute of Building Research & Innovation, Austria, researcher
2014–2016	RWTH Aachen University, Germany, Institute for Energy Efficient Buildings and Indoor Climate, research assistant
2012–2013	University of Tartu, Estonia, Institute of Computer Science, lab tutor in programming
2010–2013	University of Tartu, Estonia, Institute of Technology, Energy efficient building core laboratory, specialist

Scientific publications

Parts, Tuule Mall; Ferrantelli, Andrea; Naar, Hendrik; Thalfeldt, Martin; Kurnitski, Jarek (2023). Wax actuator's empirical model development and application to underfloor heating control with varying complexity of controller modelling detail. Journal of Building Performance Simulation, 1–25. DOI: 10.1080/19401493.2023.2201818.

Parts, Egert-Ronald; Pikas, Ergo; Parts, Tuule Mall; Arumägi, Endrik; Liiv, Innar; Kalamees, Targo (2023). Quality and accuracy of digital twin models for the neighbourhood level building energy performance calculations. E3S Web of Conferences, 396: The 11th International Conference on Indoor Air Quality, Ventilation & Energy Conservation in Buildings (IAQVEC2023), Tokyo, Japan, May 20-23, 2023. EDP Sciences. DOI: 10.1051/e3sconf/202339604021.

Vihman, Lauri; Parts, Tuule Mall; Aljas, Hans Kristjan; Thalfeldt, Martin; Raik, Jaan (2023). Algorithms for online CO2 baseline correction in intermittently occupied rooms. Healthy Buildings 2023 - Europe: Beyond disciplinary boundaries : Proceedings: 18th Healthy Buildings Europe Conference, Aachen, Germany, 11th–14th June, 2023. Emerald.

Aljas, Hans Kristjan; Parts, Tuule Mall; Thalfeldt, Martin (2023). Whole building algorithm for indoor air quality classification based on measured CO2 data. Healthy Buildings 2023 - Europe: Beyond disciplinary boundaries : Proceedings: 18th Healthy Buildings Europe Conference, Aachen, Germany, 11th–14th June, 2023. Emerald.

Alimohammadi, H.; Vassiljeva, K.; Petlenkov, E.; Kull, T. M.; Thalfeldt, M. (2022). Predict the remaining useful life in HVAC filters using a hybrid strategy. CLIMA 2022 The 14th REHVA HVAC World Congress: Rotterdam, The Netherlands, 22nd – 25th May. CLIMA 2022 conference, 1–8. DOI: 10.34641/clima.2022.273.

Erfani, A.; Yu, X.; Kull, T.M.; Bacher, P.; Jafarinejad, T.; Roels, S.; Saelens, D. (2022). Analysis of the impact of predictive models on the quality of the model predictive control for an experimental building. Building Simulation Conference Proceedings. IBPSA, 302–309. DOI: 10.26868/25222708.2021.30566.

Häring, T.; Kull, T. M.; Ahmadiahangar, R.; Rosin, A.; Thalfeldt, M.; Biechl, H. (2021). Microgrid Oriented modeling of space heating system based on neural networks. Journal of Building Engineering, 43, 103150. DOI: 10.1016/j.jobe.2021.103150.

Hamburg, A.; Mikola, A.; Parts, T. M.; Kalamees, T. (2021). Heat Loss Due to Domestic Hot Water Pipes. Energies, 14 (20). DOI: 10.3390/en14206446.

Kull, T. M.; Mikola, A.; Tukia, A.; Köse, A.; Petlenkov, E.; Thalfeldt, M. (2021). Continuous automated ventilation heat recovery efficiency performance assessment using building monitoring system. E3S Web of Conferences, 246. EDP Sciences. DOI: 10.1051/e3sconf/202124610006.

Alimohammadi, H.; Vassiljeva, K.; Petlenkov, E.; Thalfeldt, M.; Mikola, A.; Kull, T.M.; Köse, A. (2021). Gray Box Time Variant Clogging behaviour and Pressure Drop Prediction of the Air Filter in the HVAC System. E3S Web of Conferences, 246. DOI: 10.1051/e3sconf/202124610002.

Kull, T. M.; Thalfeldt, M.; Kurnitski, J. (2021). Modelling of Wax Actuators in Underfloor Heating Manifolds. E3S Web of Conferences, 246: Cold Climate HVAC & Energy 2021, Tallinn (virtual), 20-21 April 2021. EDP Sciences. DOI: 10.1051/e3sconf/202124611009

Wolisz, H.; Kull, T. M.; Müller, D.; Kurnitski, J. (2020). Self-learning model predictive control for dynamic activation of structural thermal mass in residential buildings. Energy and Buildings, 207, 109542. DOI: 10.1016/j.enbuild.2019.109542.

Kull, T. M.; Thalfeldt, M.; Kurnitski, J. (2020). PI Parameter Influence on Underfloor Heating Energy Consumption and Setpoint Tracking in nZEBs. Energies, 13. DOI: 10.3390/en13082068.

Kull, T. M.; Penu, K.-R.; Thalfeldt, M.; Kurnitski, J. (2020). Energy saving potential with smart thermostats in low-energy homes in cold climate. In: E3S Web of Conferences: 12th Nordic Symposium on Building Physics (NSB 2020). EDP Sciences. DOI: 10.1051/e3sconf/202017209009.

Häring, T.; Kull, T. M.; Helguero, J.; Rosin, A.; Biechl, H. (2020). Thermal Modelling of a Control Center for Flexibility Analysis in nZEB Nanogrids. 2020 IEEE 61st International Scientific Conference on Power and Electrical Engineering of Riga Technical University (RTUCON), Riga, Latvia, Nov. 5-7, 2020. IEEE. DOI: 10.1109/RTUCON51174.2020.9316568.

Kull, T. M.; Simson, R.; Kurnitski, J. (2019). Setback Efficiency of Limited-Power Heating Systems in Cold Climate. In: Johansson, D.; Bagge, H.; Wahlström, Å. (Ed.). Cold Climate HVAC 2018: Sustainable Buildings in Cold Climates. (87–95). Springer, Cham. (Springer Proceedings in Energy). DOI: 10.1007/978-3-030-00662-4_8.

Kull, T. M.; Thalfeldt, M.; Kurnitski, J.; (2019). Optimal PI control parameters for accurate underfloor heating temperature control. 111: Clima 2019 Congress, Rumenia. E3S Web of Conferences. DOI: 10.1051/e3sconf/201911101081.

Kull, T. M.; Thalfeldt, M.; Kurnitski, J. (2019). Estimating time constants for underfloor heating control. Journal of Physics: Conference Series, 1343: CISBAT 2019 | Climate Resilient Cities – Energy Efficiency & Renewables in the Digital Era 4–6 September 2019, EPFL Lausanne, Switzerland. IOP Publishing Ltd, 012121. DOI: 10.1088%2F1742-6596%2F1343%2F1%2F012121.

Võsa, K.-V.; Ferrantelli, A.; Kull, T.-M.; Kurnitski, J. (2018). Experimental analysis of emission efficiency of parallel and serial connected radiators in EN442 test chamber. Applied Thermal Engineering, 132, 531–544. DOI: 10.1016/j.applthermaleng.2017.12.109.

Kull, T. M.; Simson, R.; Thalfeldt, M.; Kurnitski, J. (2017). Influence of time constants on low energy buildings' heating control. Energy Procedia: 11th Nordic Symposium on Building Physics, NSB2017, 11-14 June 2017, Trondheim, Norway. Ed. S. Geving and B. Time. Elsevier, 75–80. (132). DOI: 10.1016/j.egypro.2017.09.640.

Kull, Tuule Mall; Mauring, Tõnu; Tkaczyk, Alan Henry (2015). Energy balance calculation of window glazings in the northern latitudes using long-term measured climatic data. Energy Conversion and Management, 89, 896–906. DOI: 10.1016/j.enconman.2014.10.058.

Wolisz, Henryk; Kull, Tuule Mall; Streblow, Rita; Müller, Dirk (2015). The effect of furniture and floor covering upon dynamic thermal building simulations. Energy Procedia, 78: 6th International Building Physics Conference, IBPC 2015. Elsevier, 2154–2159. DOI: 10.1016/j.egypro.2015.11.304.

Elulookirjeldus

Isikuandmed

    Nimi: Tuule Mall Parts (np. Kull)
    Sünniaeg: 16.12.1991
    Sünnikoht: Tartu, Eesti
    Kodakondsus: Eesti

Kontaktandmed

    E-post: tuule.parts@taltech.ee

Hariduskäik

2016–2023	Tallinna Tehnikaülikool, ehitus ja arhitektuur, PhD
2013–2016	RWTH Aacheni Ülikool, simulatsiooniteadused, MSc
2010–2013	Tartu Ülikool, füüsika, BSc *cum laude*
1998–2010	Miina Härma Gümnaasium, keskharidus, hõbemedal

Keelteoskus

Eesti keel	Emakeel
Inglise keel	Sorav
Saksa keel	Kesktase
Vene keel	Algtase

Teenistuskäik

2022–…	R8 Technologies, insener
2016–…	Tallinna Tehnikaülikool, Ehituse ja arhitektuuri instituut, Liginullenergiahoonete uurimisrühm, nooremteadur/ekspert
2018–2019	Amenti AG, programmeerija ja andmeteadlane
2016–2018	Swiss Property, ehitusfüüsika spetsialist
2016	*Institute of Building Research & Innovation*, Austria, teadur
2014–2016	RWTH Aacheni Ülikool, Saksamaa, *Institute for Energy Efficient Buildings and Indoor Climate*, teadustöö assistent
2012–2013	Tartu Ülikool, Arvutiteaduste instituut, programmeerimise praktikumijuhendaja
2010–2013	Tartu Ülikool, Tehnoloogiainstituut, Energiatõhusa ehituse tuumiklabor, spetsialist

Teaduspublikatsioonid

Nimekiri teaduspublikatsioonidest on esitatud inglise keelse elulookirjelduse all.